



Modélisation semi-analytique des contacts mécaniques complexes : application aux problèmes inclusionnaires et à l'usure des surfaces revêtues

Benjamin Fulleringer

► To cite this version:

Benjamin Fulleringer. Modélisation semi-analytique des contacts mécaniques complexes : application aux problèmes inclusionnaires et à l'usure des surfaces revêtues. Other. INSA de Lyon, 2011. English. <NNT : 2011ISAL0061>. <tel-00684944>

HAL Id: tel-00684944

<https://tel.archives-ouvertes.fr/tel-00684944>

Submitted on 3 Apr 2012

HAL is a multi-disciplinary open access archive for the deposit and dissemination of scientific research documents, whether they are published or not. The documents may come from teaching and research institutions in France or abroad, or from public or private research centers.

L'archive ouverte pluridisciplinaire **HAL**, est destinée au dépôt et à la diffusion de documents scientifiques de niveau recherche, publiés ou non, émanant des établissements d'enseignement et de recherche français ou étrangers, des laboratoires publics ou privés.

PhD. THESIS

Semi-analytical modeling of complex mechanical contacts: Application to inclusions and wear of coated surfaces

Presented at

Institut National des Sciences Appliquées de Lyon

To obtain

The title of Doctor

Doctoral school :

Mécanique, Énergétique, Génie Civil, Acoustique (MEGA)

Speciality :

MECHANICAL AND CIVIL ENGINEERING

By

Benjamin FULLERINGER

Engineer of INSA Lyon

Defended on examination commission, the 1st of July 2011

Jury Members

PROF. Gery de Saxce (Université de Lille)	Reviewer
DR. Daniele Dini (Imperial college, UK)	Reviewer
PROF. Georges Cailletaud (ENSMP)	Chairman
PROF. Timothy Ovaert (University of Notre-Dame, USA)	Examiner
PROF. Marie-Christine Baietto (INSA Lyon)	Examiner
PROF. David Dureisseix (INSA Lyon)	Examiner
PROF. Daniel Nelias (INSA Lyon)	Phd supervisor
DR Juan-Antonio Ruiz-Sabariego(SNECMA)	Examiner

LaMCoS - UMR CNRS 5259 - INSA de Lyon
20, avenue Albert Einstein, 69621 Villeurbanne Cedex (FRANCE)

INSA Direction de la Recherche - Ecoles Doctorales 2011

SIGLE	ECOLE DOCTORALE	NOM ET COORDONNEES DU RESPONSABLE
CHIMIE	<u>CHIMIE DE LYON</u> Insa : R. GOURDON	M. Jean Marc LANCELIN Université Claude Bernard Lyon 1 Bât CPE 43 bd du 11 novembre 1918 69622 VILLEURBANNE Cedex Tél : 04.72.43 13 95 Fax : directeur@edchimie-lyon.fr
E. E. A.	<u>ELECTRONIQUE, ELECTROTECHNIQUE, AUTOMATIQUE</u> Secretariat: M.C. HAVGOUDOUKIAN eea@ec-lyon.fr	M. Gerard SCORLETTI Ecole Centrale de Lyon Bâtiment H9 36 avenue Guy de Collongue 69134 ECULLY Tél : 04.72.18 60 97 Fax : 04 78 43 37 17 eea@ec-lyon.fr Secrétariat : M.C. HAVGOUDOUKIAN
E2M2	<u>EVOLUTION, ECOSYSTEME, MICROBIOLOGIE, MODELISATION</u> INSA : H. CHARLES	M. Gundrun BORNETTE CNRS UMR 5023 LEHNA Université Claude Bernard Lyon 1 Bât Forel 43 bd du 11 novembre 1918 69622 VILLEURBANNE Cédex Tél : 04.72.43.12.94 e2m2@biomserv.univ-lyon1.fr
EDIIS	<u>INTERDISCIPLINAIRE SCIENCES- SANTÉ</u> Secretariat: Safia AIT CHALAL INSA : M. LAGARDE	M. Gerard SCORLETTI Hôpital Louis Pradel, Bâtiment Central 28, Avenue Doyen Lépine 69500 BRON Tél: 04.72.68.49.09 Fax: 04.72.35.49.16 Didier.revel@creatis.univ-lyon1.fr
Materiaux	<u>MATERIAUX DE LYON</u> Secretariat: M. Laboune PM: 71.70 Fax: 87.12 Bat. Saint Exupéry	M. Jean-Yves BUFFIERE INSA de Lyon, MATEIS Bâtiment Saint Exupéry 7 avenue Jean Capelle 69621 VILLEURBANNE Cédex Tél: 04.72.43.83.18 Fax: 04.72.43.85.28 jean-yves.buffiere@insa-lyon.fr
INFOMaths	<u>MATHEMATIQUES ET INFORMATIQUE FONDAMENTALE</u>	M. Johannes KELLENDONK Université Claude Bernard Lyon 1 - LIRIS - INFOMATHS Bâtiment Nautibus 43 bd du 11 novembre 1918 69622 VILLEURBANNE Cédex Tél: 04.72.43.19.05 Fax: 04.72.43.13.10 infomaths@bat710.univ-lyon1.fr
MEGA	<u>MECANIQUE, ENERGETIQUE, GENIE CIVIL, ACOUSTIQUE</u> Secretariat: M. Laboune PM: 71.70 Fax: 87.12 Bat. Saint Exupéry mega@insa-lyon.fr	M. Philippe BOISSE INSA de Lyon, LAMCOS Bâtiment Jacquard 25 bis avenue Jean Capelle 69621 VILLEURBANNE Cédex Tél: 04.72.43.71.70 Fax: 04.72.43.72.37 philippe.boisse@insa-lyon.fr
ScSo	<u>Sciences Sociales</u> Secrétariat: Viviane POLSINELLI INSA : J.Y. TOUSSAINT	M. Lionel OBADIA Université Lyon 2 86 rue Pasteur 69365 Lyon Cedex 07 Tél: 04.78.69.72.76 Fax: 04.37.28.04.48 lionel.Obadia@univ-lyon2.fr

Acknowledgment

Je tiens tout d'abord à remercier toutes les personnes ayant participé au groupe de travail fretting avec Snecma, et tout particulièrement Stéphane Deyber qui m'a accueilli en stage de fin d'étude et a eu confiance en moi pour débiter une thèse avec Snecma. Son successeur au sein du groupe de travail, Juan-Antonio Juiz-Sabariego, s'est révélé tout aussi compétent et compréhensif. Je citerai également:

- la composante expérimentale avec Siegfried Fouvry de l'École Centrale de Lyon et ses doctorants qui se sont succédés : Christophe Paulin, Jocelyn Arthaud, Caroline Mary et Jean Meriaux ;
- la composante dynamique numérique : Loïc Salles et Laurent Blanc également de l'ECL ;
- le partie modélisation des matériaux de l'École des Mines : Georges Cailletaud, Thomas Dick et Eva Héripé ;
- la branche Snecma : Juan-Antonio Juiz-Sabariego, Stéphane Deyber, Bénédicte Bonnet et Nathalie Serres.

Évidemment j'ai une infinie reconnaissance en mon directeur de thèse, Daniel Nélias. Il m'a donné l'immense opportunité de participer à de nombreux congrès pendant ces trois années, me permettant ainsi de perfectionner mon anglais. Il aura dans un premier temps cherché à améliorer mes compétences pédagogiques et oratoires, et dans un second temps cherché à comprendre mes états d'âme. Il a toujours su maintenir une bonne ambiance et je n'oublierai pas ses dîners à la campagne.

Timothy Ovaert a quant à lui su me montrer le meilleur du Middle-West. Ca restera de loin la plus belle expérience que j'ai vécue, dans ce que j'ai considéré comme ma "nouvelle famille". Grâce à lui, à ce petit coin de paradis perdu, j'ai pu trouver la paix pendant six mois.

Enfin je remercie tous mes amis du laboratoire. Je souhaite du courage à l'équipe travaillant sur le code UncleSAM (Semi Analytical method), et ne doute aucunement que ses membres sauront s'avérer efficaces dans la poursuite de ce travail. Ces trois années de thèse auraient été différentes sans Daniel, Thibaut, Julien et Caroline. Je remercie tout particulièrement Julien qui a su me faire rajeunir de quelques années.

Mes derniers mots vont à mes parents qui ont sacrifié une partie de leur vie pour rendre la mienne la plus agréable possible. Je leur dédie ce mémoire.

Résumé

Les pieds d'aubes de souffantes de turboréacteurs font face à des sollicitations de type fretting. Il en résulte deux types d'endommagements: (i) l'amorçage et la propagation de fissures, (ii) l'usure des surfaces en contact. Afin de fournir les outils permettant de répondre à la problématique industrielle, un code semi-analytique permettant de traiter des problèmes hétérogènes de contacts élasto-plastiques est développé à partir d'éléments existants et de solutions analytiques et numériques novatrices.

La structure est simplifiée en supposant un contact entre deux massifs élastiques semi-infinis. Des solutions analytiques donnant, pour les déplacements en surface:

- les contributions élémentaires de chargements normaux et tangentiels constants sur une surface rectangulaire pour obtenir par sommation les déplacements élastiques de la surface chargée;
- les contributions élémentaires de déformations plastiques supposées constantes sur un volume parallélépipédique pour obtenir par sommation les déplacements résiduels en surface;
- les contributions élémentaires de déformations d'incompatibilité liées à un problème hétérogène (inclusions, revêtements, endommagement,...) supposées constantes sur un volume parallélépipédique pour obtenir par sommation les déplacements résiduels en surface;

Les déplacements en surface sont alors exprimés en utilisant des produits de convolution discrets entre des coefficients d'influence et la source surfacique (chargements en surface) ou volumique (déformations plastiques ou d'incompatibilité). Le problème normal et le problème tangentiel en glissement total ou en glissement partiel peuvent alors être résolus, en prenant en compte les effets plastiques et hétérogènes. L'algorithme d'optimisation sous contrainte utilisé est celui développé par L.Gallego.

Des solutions analytiques donnant, pour les contraintes dans le volume:

- les contributions élémentaires de chargements normaux et tangentiels constants sur une surface rectangulaire pour obtenir par sommation les contraintes de contact dans le volume
- les contributions élémentaires de déformations plastiques supposées constantes sur un volume parallélépipédique pour obtenir par sommation les contraintes résiduelles dans le volume
- les contributions élémentaires de déformations d'incompatibilité liées à un problème hétérogène (inclusions, revêtements, endommagement,...) supposées constantes sur un volume parallélépipédique pour obtenir par sommation les contraintes d'incompatibilité dans le volume

De la même manière, les contraintes dans le volume sont exprimées en utilisant des produits de convolution discrets entre des coefficients d'influence et la source surfacique. Pour accélérer les calculs, les transformées de Fourier rapides (2D-FFT et 3D-FFT) sont utilisées pour effectuer les produits de convolution.

Les solutions élémentaires sont validées, puis le code est validé à partir de solutions analytiques ou numériques trouvées dans la littérature pour des cas simples. Des simulations avec plasticité, inclusions ou revêtements sont effectuées pour un contact sphère-plan en glissement total ou en glissement partiel. Des simulations d'usure avec revêtement sont par la suite effectuées, et certaines applications potentielles sont brièvement traitées.

MOTS CLÉS: plasticité, inclusions, revêtement, usure, contact, stick-slip, fretting, tribologie, modélisation numérique

Table of contents

Table of contents	i
List of figures	v
List of tables	xi
Introduction	1
1 Contacts in the Aeronautical Field	3
1.1 Context and motivations	5
1.1.1 Aircraft engines	5
1.1.2 Dovetail joints in aircraft engines	5
1.1.3 Needs in contact modeling	8
1.2 Fretting	10
1.3 Hardening in contacts	11
1.3.1 Nano-indentation	11
1.3.2 Hardening in rough surfaces	12
1.3.3 Peening processes and residual stress layers	13
1.4 Inclusions and metal cleanliness	16
1.4.1 Aeronautical alloys	16
1.4.2 Inclusions as a stress raiser	17
1.4.3 Numerical methods	18
1.5 Coatings and other applications	19
1.5.1 Coatings	19
1.5.2 Fiber reinforcements	21
1.5.3 Damage in brittle materials	23
1.6 Methods used in contact mechanics	24
1.6.1 Analytical solutions	24
1.6.2 Numerical methods	25
1.7 Conclusion	26
2 The elastic-plastic contact	29
2.1 The elastic contact	31
2.1.1 Contact kinematic	31

2.1.2	Loadings transmitted into the contact	33
2.1.3	The half-space	34
2.1.4	Discretization of surface loadings	41
2.1.5	Normal problem	43
2.1.6	Tangential problem	46
2.1.7	Coupling between the normal and tangential problem	49
2.2	The elastic-plastic half-space	51
2.2.1	Elastic-plastic algorithm	51
2.2.2	Plasticity model	52
2.2.3	Residual stress calculation	53
2.2.4	Maxwell-Betti's reciprocal theorem	56
2.2.5	Normal residual displacements [JAC 01]	57
2.2.6	Tangential residual displacements [FUL 09]	59
2.2.7	Validations using a Finite Element model	61
2.2.8	Comparison between the FEA and analytical results	62
2.2.9	Validation using a finite element model without friction	65
2.3	Numerical methods and improvements	66
2.3.1	Weak formulation	66
2.3.2	Conjugate Gradient Method (CGM)	67
2.3.3	Convergence of the tangential contact solver	68
2.3.4	Discrete Continuous Fast Fourier Transforms (DC-FFT)	70
2.3.5	2D-FFT Algorithm	74
2.3.6	3D-FFT Algorithm	74
2.3.7	2.5D-FFT Algorithm	76
2.3.8	Instability on plastic strains	77
2.3.9	Conclusion	79
2.4	Fretting considering the elastic-plastic regime	80
2.4.1	Fretting modes and material properties	80
2.4.2	Fretting mode II: Indentation	81
2.4.3	Fretting mode I: Sliding	92
2.4.4	Conclusion	96
2.5	Conclusion	98
3	Inclusions	99
3.1	The Equivalent Inclusions Method (EIM) of Eshelby and developments	101
3.1.1	The Equivalent Inclusions Method (EIM) of Eshelby	101
3.1.2	Determination of ϵ^* and ϵ	103
3.1.3	Potentials ϕ and ψ for a sphere	104
3.1.4	Eshelby's tensor of a spherical inclusion	105
3.1.5	Eshelby's tensor for a cubical inclusions	106
3.1.6	Infinite half space using a 3D-FFT algorithm	107
3.1.7	The non-homogeneous solver	109
3.1.8	Non-homogeneous problems considering frictional aspects	110

3.1.9	Non-homogeneous problems with plastic behaviors	112
3.2	Validation of elementary solutions	114
3.2.1	Misfit stresses caused by a spherical inclusion	114
3.2.2	Misfit displacements caused by a spherical inclusion	117
3.2.3	Misfit stresses around a parallelepipedic inclusion	120
3.2.4	Misfit displacements caused by a cuboidal inclusion	120
3.3	Influence of non-homogeneities on contact conditions considering no gradient	123
3.3.1	Influence of the Young's modulus using a cluster of inclusions	124
3.3.2	Influence of the inclusion's radius using a unique inclusion	126
3.3.3	Influence of the Poisson's ratio using a cluster of inclusions	129
3.3.4	Influence of the inclusion's depth using a unique inclusion	131
3.3.5	Mutual interactions	131
3.3.6	Summary	135
3.4	Inclusions considering gradients	137
3.4.1	Enrichment of a complete half-space	137
3.4.2	Inclusions discretized in many cubes	139
3.4.3	Inclusions when considering gradients	142
3.5	Conclusion	143
4	Coatings and other applications	145
4.1	Coatings	147
4.1.1	Elastic layers of uniform thickness using cubical inclusions	147
4.1.2	Enrichment techniques using spherical inclusions	149
4.1.3	Proposed technique for coating computations	153
4.1.4	Coatings under fully-sliding conditions	156
4.1.5	Coating thickness	161
4.1.6	Conclusion	163
4.2	Applications	164
4.2.1	Indentation of coated surfaces considering friction	164
4.2.2	Partial sliding over coated surfaces	167
4.2.3	Wear of coatings	175
4.2.4	Wear of coatings: fully sliding contacts	178
4.2.5	Fretting-wear of coatings: stick-slip conditions	185
4.2.6	Concrete used in civil engineering	194
4.2.7	Nano indentation of human bones	197
4.3	Conclusion	200
	Conclusion and perspectives	203
	Bibliography	207

List of figures

1.1	Schematic diagram illustrating the operation of turbojets	5
1.2	Schematic diagram illustrating the operation of turbofans	6
1.3	Blade and disk linked together using a dovetail joint	6
1.4	Loadings observed at the blade-disk interface	7
1.5	Composition of the blade-disk interface	7
1.6	Pressure field observed at the blade-disk interface	8
1.7	Fretting issues observed in blade-roots: wear and fatigue	9
1.8	Indentation: normal displacement versus applied force curve	11
1.9	Effect of an indented groove in a ball bearing	12
1.10	Shots bombarding an helicoidal gear	13
1.11	Shot peening generates a compressive layer below the surface	13
1.12	A semi-analytical solver can describe the shot peening process [CHA]	14
1.13	Laser peening used in aeronautical applications	15
1.14	Whitening effect around a spherical inclusion	17
1.15	Metal coming off in plates and chipped surface	17
1.16	Crack initiation and propagation using FE and X-FE methods	18
1.17	Multi-coatings at the blade-disk interface	19
1.18	Chronology and wear of multi-coating systems	20
1.19	Composite materials are used in RTM fans of modern engines	21
1.20	Modulus and strength variations observed for a damaged material	23
1.21	Tresca's stress around a spherical cavity and a stiff particle	27
2.1	Rigid body displacements	32
2.2	Forces and moments transmitted into the contact	33
2.3	Elastic deflections induced by a normal loading	36
2.4	Elastic deflections induced by a tangential loading	38
2.5	Normal load discretized in rectangles of uniform pressure	41
2.6	The elastic normal problem	43
2.7	Residual displacements used in the normal problem	45
2.8	The elastic tangential problem	46
2.9	Residual displacements used in the tangential problem	49
2.10	Flow chart of the actual fully coupled elastic-plastic contact code	52
2.11	Plastic strains in a half-space decomposed in three elementary problems	53

2.12	Cuboïd of uniform plastic strain	57
2.13	Cuboïd of uniform plastic strain	59
2.14	Finite Element Model	61
2.15	Normal displacements induced by a unique plastic cube (FEM vs. SAM) .	63
2.16	Tangential displacements induced by a unique plastic cube (FEM vs. SAM)	64
2.17	Indentation curves found using both a FEM and a SAM	65
2.18	Errors encountered considering no relaxation or a fixed relaxation	69
2.19	Convergence anomalies considering no relaxation or a fixed relaxation . .	69
2.20	Errors and corresponding convergence anomalies for an adaptative relaxation	70
2.21	Convolution of P and K_z^p in the frequency domain	72
2.22	wrap-around and zero-padding for pair coefficients	73
2.23	Use of the 2D-FFT in the actual code	75
2.24	Decomposition of the half-space in three subproblems	75
2.25	Use of the 3D-FFT	76
2.26	3D-FFT techniques for inclusions far from the surface	76
2.27	3D-FFT techniques for inclusions close to the surface	77
2.28	Stresses instability typically found with a poor discretization	78
2.29	Three modes of fretting defined by Mohrbacher [MOH 95]	80
2.30	Second mode of fretting creates radial slips	81
2.31	Sticking radii in the elastic-plastic regime [SPE 75]	82
2.32	Critical load and depth at the onset of yielding while indenting	83
2.33	Equivalent plastic strain for an indentation test	84
2.34	Von Mises stress for an indentation test ($P_0/S_y=2$)	85
2.35	Influence of friction on the maximum plastic strain for $P_0/S_y=2$	86
2.36	Evolution of sticking radii with the coefficient of friction	86
2.37	Residual prints for an indentation test	87
2.38	Shape of the tangential residual displacements	88
2.39	Influence of plasticity on the contact regime	89
2.40	Von Mises residual stress for an indentation test ($P_0/S_y=2$)	90
2.41	Hydrostatic residual stress for an indentation test ($P_0/S_y=2$)	91
2.42	First mode of fretting creates slips along one direction	92
2.43	Stick-slip regime considering plasticity:loadings	92
2.44	Equivalent plastic strains after 1 cycles	93
2.45	Influence of plasticity on the contact regime	94
2.46	Residual prints for $Q=0.5P$	95
2.47	Equivalent plastic strains after 1 cycles	95
2.48	Residual prints for $Q=0.5P$ after 1 fretting-cycle	96
2.49	Influence of plasticity on the contact regime	97
3.1	Ellipsoidal heterogeneity surrounded by an infinite volume	101
3.2	Strains defined herebefore, for an ellipsoidal inclusion	101
3.3	Strains for an ellipsoidal inclusion in a strain field	102
3.4	Strains for an inclusion equivalent to non-homogeneity	102

3.5	Geometries requiring an elementary solution	104
3.6	Decomposition of the half-space problem into three subproblems	108
3.7	Flow chart of the misfit stresses algorithm	109
3.8	Flow chart of the actual heterogeneous-elastic contact solver	111
3.9	Flow chart of the misfit displacement algorithm	112
3.10	Flow chart of the actual heterogeneous-elastic-plastic contact solver	113
3.11	Stress distribution for a spherical inclusion in an infinite space	115
3.12	Stress distribution for a spherical inclusion in a half-space	115
3.13	Stress distribution for a spherical inclusion in a half-space	116
3.14	Normal displacements for a spherical inclusion at a certain depth	118
3.15	Tangential displacements for a spherical inclusion at a certain depth	119
3.16	Normal displacements for a plastic cube at a certain depth	121
3.17	Tangential displacements for a plastic cube at a certain depth	122
3.18	Normal loading of a half-space containing multiple inclusions	123
3.19	Representation of the inclusion pattern in the (Oxz) plane	124
3.20	Contact pressure distribution for inhomogeneities of various stiffnesses	124
3.21	Contact pressure profile for inhomogeneities of various stiffnesses	125
3.22	Contact pressure and von Mises stress vs. the ratio $\gamma = E_i/E_m$	125
3.23	Non-homogeneity tangent to the surface or far away from the surface	126
3.24	Pressures for an inhomogeneity of different radii tangent to the surface	127
3.25	Pressures for an inhomogeneity of different radii below the surface	128
3.26	Maximum contact pressure and von Mises stress vs. the inclusion radius	128
3.27	Contact pressure for a cluster of spherical inhomogeneities	129
3.28	Maximum pressure and von Mises stress vs. the inclusion Poisson's ratio	130
3.29	Pressures for soft or stiff inhomogeneities and various Poisson's ratio	130
3.30	Pressures for a set of 49 inhomogeneities equally spaced	131
3.31	Maximum pressures and von Mises stress vs. the depth of inclusions	132
3.32	Representation of two inhomogeneities in the elastic half-space	132
3.33	Pressure on the top of two inclusions of various stiffnesses	133
3.34	Maximum shear stress vs. the spacing between inclusions $h=0.23a$	134
3.35	Maximum shear stress vs. the spacing between inclusions $h=0.5a$	135
3.36	Validation of the solutions by enriching a whole half-space	137
3.37	Pressure field obtained while enriching a whole half-space	138
3.38	Stress distribution for an inclusion in an infinite space [MUR 79]	139
3.39	Discretized spherical and ellipsoidal inclusions onto the free surface	139
3.40	Stress distribution for an inclusion in a half-space [MUR 79]	140
3.41	Discretized spherical and ellipsoidal inclusions below the surface	141
3.42	Stress distribution for an inclusion in a half-space [MUR 79]	141
3.43	Maximum stress for various ellipticity ratios [MUR 79]	142
3.44	Spherical inclusion discretized in cubes accounting for gradients	143
4.1	Spherical indentation of an elastic coating [O'S 88]	147
4.2	Pressure fields for different coatings	148

4.3	Validations of stress fields for three elements considering $\epsilon_{11}^*=1$ and $\epsilon_{33}^*=1$	151
4.4	Validations of stress fields for three elements considering $\epsilon_{12}^*=1$ and $\epsilon_{13}^*=1$	152
4.5	Proposed technique for coatings using an enrichment of the substrate . . .	153
4.6	Pressure normalized by the Hertzian pressure for different coatings	154
4.7	Normalized indentation curves for different coatings	155
4.8	Von Mises stress for different coatings	155
4.9	Sphere sliding over an elastic coating [O'S 88]	156
4.10	Von Mises stress for different coatings and friction coefficients	158
4.11	Stresses under combined normal loading and sliding for $\mu = 0.25$ [O'S 88]	159
4.12	Stresses σ_{zx} under combined normal and tangential loading for various frictions	160
4.13	Maximal normal pressure variations depending on the coating thickness .	161
4.14	Contact area size variations depending on the coating thickness	162
4.15	Indentation of coatings: normal loading	164
4.16	Von Mises stress and contact conditions for frictionless vs. frictional contacts	165
4.17	Evolution of the sticking radius c/a for various coatings	166
4.18	Fretting cycle considering a coated surface	167
4.19	Stick-slip regime for a coated surface: normal and tangential loadings . .	168
4.20	Fretting loop obtained for various coating properties	169
4.21	Von Mises stresses for a fretting loading of small amplitude	169
4.22	Von Mises stresses, pressures, shears and slips when partially sliding . . .	170
4.23	Onset of the gross-slip regime: normal and tangential loadings	171
4.24	Fretting loop obtained for various coating properties	172
4.25	Von Mises stresses for a fretting loading of large amplitude	172
4.26	Von Mises stresses, pressures, shears and slips at the onset of gross-slip .	173
4.27	Techniques used to model rough surfaces	175
4.28	Worn coatings considering a moving surface or a moving interface	176
4.29	The weight tensor \mathbf{W} used to define the moving interface	177
4.30	Coated sphere sliding over a rigid flat	178
4.31	Dissipated energy: Wear volume vs. the number of cycles	179
4.32	Maximum wear depth vs. the number of cycles	180
4.33	Maximum pressure vs. the number of cycles	180
4.34	Wear depth and associated pressure fields for various coatings	181
4.35	Contact surface vs. the number of cycles	182
4.36	Example of sphere of radius 0.2mm unworn and worn	182
4.37	Von Mises stress for various coatings and wear rates	183
4.38	Issues observed for highly worn geometries	184
4.39	Fretting cycle considering a coated surface	185
4.40	Wear of coatings in the stick-slip regime: normal and tangential loadings .	185
4.41	Dissipated energy and maximum wear for worn coatings: large amplitudes	186
4.42	Wear profiles at the onset of the gross-slip regime	187
4.43	Maximum pressure and evolution of the contact surface for worn coatings	187
4.44	Fretting loops for worn coatings and small amplitudes of sliding	188
4.45	Von Mises stress and shears for various coatings and wear rates	188

4.46	Dissipated energy and maximum wear for worn coatings: large amplitudes	189
4.47	Wear profiles at the onset of the gross-slip regime	189
4.48	Maximum pressure and evolution of the contact surface for worn coatings	190
4.49	Fretting loops for worn coatings and large amplitudes of sliding	190
4.50	Von Mises stress and shears for various coatings and wear rates	191
4.51	Fretting loops considering a coated surface highly worn	191
4.52	Evolution of wear rates	192
4.53	Evolution of fretting loops considering severe wear	193
4.54	Structure of a reinforced or prestressed concrete	194
4.55	Von Mises stress in a pre-stressed concrete	195
4.56	Von Mises stress in a pre-stressed concrete under contact loading	195
4.57	Pressure field for a loaded pre-stressed concrete	196
4.58	Trabecular and cortical bone structure	197
4.59	Elastic-plastic damage properties of cortical bone [ZHA 08]	198
4.60	Plastic-damage model vs. a bone-indentation experimental curve [ZHA 08]	199
4.61	Plastic-damage model results vs. plastic model results	200

List of tables

2.1	Variables of the normal problem	44
2.2	Variables of the tangential problem	48
2.3	Boundary conditions of the FE Model	62
2.4	Material properties used in elastic-plastic simulations	80
2.5	Normal loading simulations considering a plastic behavior	82
3.1	Elementary solutions required when dealing with cubical inclusions	106
3.2	Existing analytical solutions of infinite and semi-infinite spaces	110
3.3	Different configurations to study the influence of each inclusion parameters	123
4.1	Existing semi-analytical solutions for spherical or cubical inclusions	149
4.2	Validations of stress fields inside/outside of a spherical element	149
4.3	Validations of stress fields inside/outside of an element made of 8 spheres	150
4.4	Validations of stress fields for a cubical element while enriching the substrate	153
4.5	Material properties used for coating simulations	156
4.6	Wear of coating in the gross-slip regime: material properties	178

Introduction

Tribology is a branch of mechanical engineering where interacting surfaces in relative motion are studied. It includes the study and applications of the principles of friction, wear, solid and fluid lubrication.

Numerous industrial applications are concerned with contacting surfaces submitted to a mechanical load which may result in a loss of material, which is known as "wear". This phenomenon becomes critical for some high speed applications such as for aeronautical turbine engines, and requires a better understanding of the state of stress in the contact. In a previous approach a homogeneous and purely elastic analysis [GAL 07a] was carried out to simulate fretting wear. This method worked very well, however it was limited to elastic, isotropic and homogeneous contact problems. When other aspects are considered (plasticity, metal cleanliness, solid lubricants), the state of stress in the contact and wear profiles become obsolete. Since metal cleanliness is becoming an issue when trying to extend the working life, and solid lubricants have been used for a long time in aeronautical contacts, problems are no longer homogeneous. Moreover metal working processes induce some residual stresses, and edges of contacts can still induce some plastic deformation, making elastic analyses inaccurate.

The first part presents the context and motivations. The contact of interest corresponds to the dovetail joint. This joint is critical and there is an increasing need in contact modeling. Various phenomena are considered and constitute the main chapters of this thesis:

- hardening
- inclusions
- coatings and wear of coatings

Some mechanical issues observed and techniques used in the aeronautical field that may require one or all of those aspects are then detailed. Finally, various analytical and numerical methods used in contact mechanics are shown. Weaknesses and advantages of each method (including semi-analytical methods) are then exposed.

The second part deals with the contact model, based on the work of L.Gallego and C.Jacq and V.Boucly. On the first hand, the initial work of L.Gallego [GAL 07a] focused on a purely elastic analysis of frictional contacts, where contact conditions are determined at every step. On the other hand, the combined work of C.Jacq [Jac 01, Jac 02] and

V. Boucly [BOU 08] focused on an elastic-plastic analysis of frictionless contacts, where pressure is determined at every step. Because Ambrico and Begley [AMB 00, AMB 01] have highlighted the role of macroscopic plastic deformation in fretting fatigue life predictions, and it is assumed that plastic deformations also play a role in fretting-wear, contact conditions and state of stress, plasticity will be considered in this model, allowing many other potential applications. The contact problem is composed of (i) the normal problem and (ii) the tangential problem. Both sub-problems are exposed and extended to the elastic-plastic contact when considering friction. Most of elementary solutions are available in [JOH 85] and briefly expressed, others are detailed and validated using a finite element analysis.

Structures of contact algorithms remain globally unchanged and are not detailed in this document (See [GAL 07a]). However, numerical methods used are detailed, including initial methods (CGM, 2D-FFT) and new methods (CGM with an adaptive relaxation, 3D-FFT, ...). Finally, the contact code is validated using three modes of fretting and results given by L. Gallego. Fretting modes when considering hardening is then investigated and compared to the elastic case.

The third part presents the Eshelby's theory, and the way it has been used in the code in order to take non-homogeneous aspects into account. Spherical and cubical non-homogeneities are later considered, and elementary solutions are given and validated using results found in the literature. Influence of the metal cleanliness has been investigated using various clusters of spherical inclusions under normal contact conditions. No gradient has been considered in this study, but results are still accurate when considering small inclusions. The size and the effect of those inclusions will be discussed.

Another way is to mesh an inclusion in many small cuboids. Using this technique, elementary solutions used are relative to a cube, but any inclusion's shape can be treated. This is of a great importance when fiber reinforcements, polyhedral or ellipsoidal inclusions have to be considered. This technique has been validated considering results found for a spherical and an elliptical inclusion in [MUR 79] and can be used when gradients can not be neglected at the inclusions' scale, when large inclusions are considered for instance.

Finally, a short study is made considering a large and unique spherical inclusion under rolling conditions or an oscillating sliding. Gradients are taken into account considering the relative size of the inclusion. Unlike most of other works, the non-homogeneous, the normal and the tangential problems are coupled together.

The last part highlights the efficiency of this code when dealing with coatings in frictional contacts. Results obtained using the semi-analytical methods are compared to published data [O'S 88]. In addition, the effect of the coating thickness on the maximal pressure and the contact size has been compared to existing results [PLU 98]. Considering validations made in parts two, three and four, many other fields of application can be envisioned. For instance, non-homogeneous properties of materials can be modified in order to deal with damage of brittle materials, such as bones. Fiber reinforcements can even be considered in such brittle material, such as in prestressed concrete. As example, some results are given for both applications.

Chapter 1

Contacts in the Aeronautical Field

This chapter is an introduction to contact problems encountered in jet engines. Modeling in contact mechanics, including fretting-wear and hardening issues are briefly exposed.

Contents

1.1	Context and motivations	5
1.1.1	Aircraft engines	5
1.1.2	Dovetail joints in aircraft engines	5
1.1.3	Needs in contact modeling	8
1.2	Fretting	10
1.3	Hardening in contacts	11
1.3.1	Nano-indentation	11
1.3.2	Hardening in rough surfaces	12
1.3.3	Peening processes and residual stress layers	13
1.4	Inclusions and metal cleanliness	16
1.4.1	Aeronautical alloys	16
1.4.2	Inclusions as a stress raiser	17
1.4.3	Numerical methods	18

1.5	Coatings and other applications	19
1.5.1	Coatings	19
1.5.2	Fiber reinforcements	21
1.5.3	Damage in brittle materials	23
1.6	Methods used in contact mechanics	24
1.6.1	Analytical solutions	24
1.6.2	Numerical methods	25
1.7	Conclusion	26

1.1 Context and motivations

1.1.1 Aircraft engines

Airbreathing jet engines are gas turbines optimized to produce thrust from the exhaust gases, or from ducted fans connected to the gas turbines. Engines were initially composed of three core components (compressor, combustor, turbine). Air flow is compressed in the first core with an inlet and a compressor. Compressed air and fuel are mixed together in the combustion chamber. Hot and high pressure burning mixture passes through a turbine and a nozzle. The compressor is powered by the turbine, which extracts energy from the expanding gas passing through it. Actually, better results were obtained when considering a two-spool configuration. Two shafts are running concentrically with a low-pressure compressor and a low-pressure turbine for the first one, and a high-pressure compressor and a high-pressure turbine for the second one. Using such configuration, the high pressure compressor can rotate faster, increasing its efficiency.

In turbojets, all the air ingested by the inlet passes through the compressor, combustor and turbine. Thrust is primarily produced from the direct impulse of exhaust gas. (cf. FIG.1.1). Those engines give good efficiency at speeds above the speed of sound, and are used in military jet fighters.

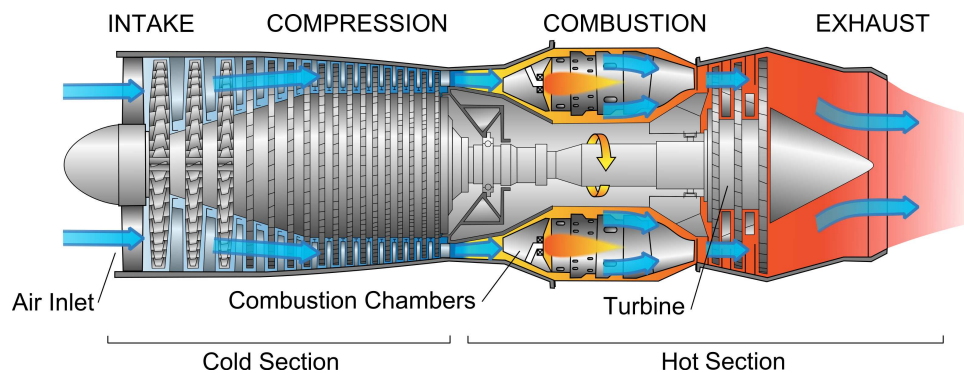


Figure 1.1: Schematic diagram illustrating the operation of turbojets

In turbofans, some of the flow bypasses the gas generator core and is accelerated by the fan. This bypassed flow is cold and at lower velocities, but a higher mass, making thrust by the fan (80% of the thrust) more important than the thrust produced by the core (cf. FIG.1.2). Most of the airbreathing jet engines that are in use are turbofan jet engines which give good efficiency at speeds just below the speed of sound. They are in use on most of commercial flights.

1.1.2 Dovetail joints in aircraft engines

The fan (cf. FIG.1.3) is composed of a disk and many blades. Blade and disk are linked together using a dovetail joint, which is basically made of two interfaces (other stages may

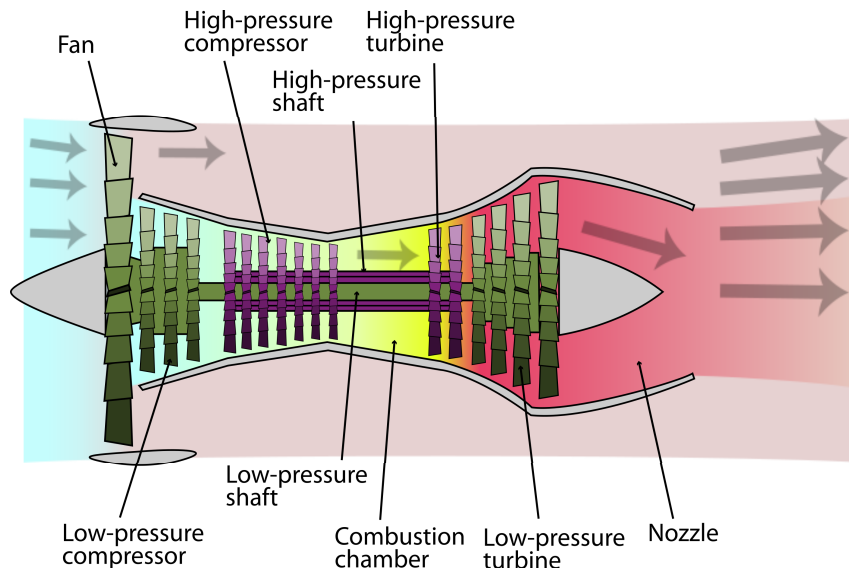


Figure 1.2: Schematic diagram illustrating the operation of turbofans

contain more than two interfaces for each blade). Because of the rate of rotation, blades and disk experience a high centrifugal force. Parts are strained and geometries may vary. High intensity and low-frequency loadings are then observed in both interfaces. Loadings are micro-displacements, pressure and shears (cf. FIG. 1.4). Those are directly induced by the rate of rotation and are often simplified by a unique loading when starting the engine, a long holding phase during flight, and unique unloading after landing. One flight is then equal to one low-frequency cycle. Blades and disk also experience aerodynamic instabilities and structural vibrations. Those loadings are high-frequency but low-amplitude.



Figure 1.3: Blade and disk linked together using a dovetail joint

Repeated relative motion of normally loaded surfaces will induce damage, and is

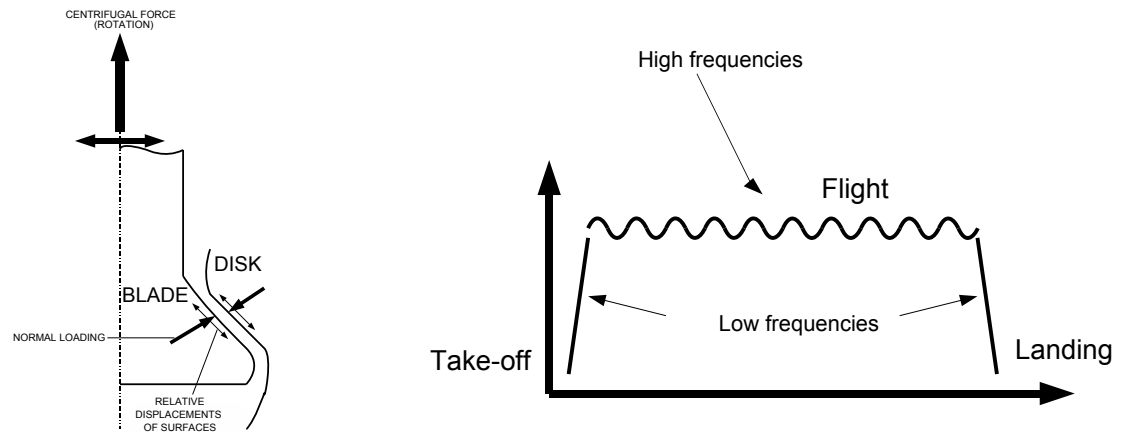


Figure 1.4: Loadings observed at the blade-disk interface

called "fretting". Fretting activates two damage mechanisms: wear of surfaces and fatigue of materials leading to crack nucleation and propagation. Wear modifies geometries of parts which may affect the aerodynamic efficiency of engines, involving important servicing costs because of premature part changes. However, it is not typically critical. Fretting-fatigue is much more critical, and crack propagation in the dovetail blade-root can lead to an in-flight loss of fan blade, compromising passengers' safety. Both mechanisms are heavily studied in order to constantly improve safety of flights. Material used for the manufacture and processing of blades and disks is typically a titanium alloy: Ti-6Al-4V. This alloy is light, strong and resists to oxidation. Blade and disks are forged and machined, while future contact interfaces are reinforced using a shot peening process. This process adds compressive residual stresses on the surface, which reduces the crack nucleation and propagation.

However, titanium has poor tribologic properties. In order to improve the interface lifespan, a coating of about $150\mu\text{m}$ and made of copper-nickel-indium (Cu-Ni-In) is sprayed over the blade contact using a plasma. Then, a solid lubricant called Molydag (MoS₂) is roughly settled. It is used to drastically reduce the coefficient of friction in the contact but is actually rapidly worn (cf. FIG.1.5).

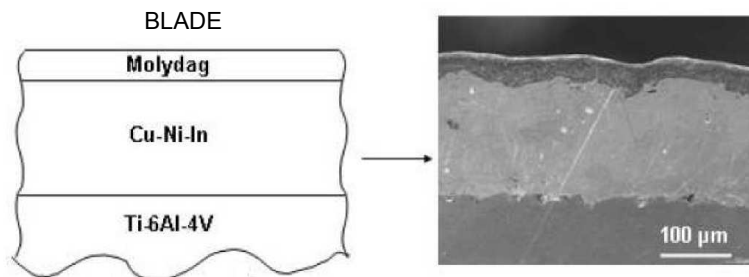


Figure 1.5: Composition of the blade-disk interface [PAU 06]

1.1.3 Needs in contact modeling

Lifespan of blades and disks was initially extended thanks to experiments and a better understanding of materials and manufacturing processes. Because fretting-wear is a long-term and complex phenomenon, it was not taken into account in previous blade and disk designs. In order to improve reliability it is necessary to determine wear kinetics by numerical simulations using various numerical methods such as Finite Element (FE) and Semi Analytical (SA) methods. Actually, modeling could improve our vision of designing dovetail joints by reducing stresses, gradients and micro-slidings. A very typical method used is the Finite Elements Methods (FEM) but FEM are cumbersome, and discretization in contacts is often limited (FIG.1.6).

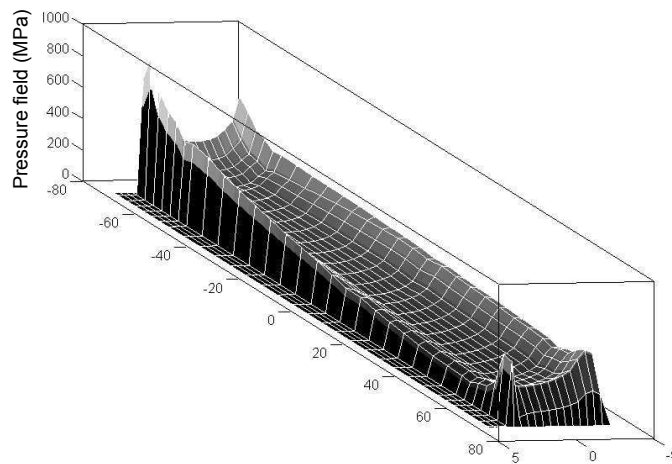


Figure 1.6: Pressure field observed at the blade-disk interface

Lifespan estimations are basically based on the maximum true stress. Maximum true stress can be actively lowered by a poor mesh, when gradients are locally important for instance. Many phenomena will be taken into account, in order to correctly describe the aeronautical contact. Each chapter of this thesis will study some of the following phenomena.

- Geometry of the contact may localize pressure and shears, especially at the edge of the contact zone. In blade-disk contacts, crack initiation are commonly observed at the edge of the contact and local refinements are required. Multi-scale techniques are also used in more complete studies using FE methods. The actual work is based on a semi-analytical contact code and allows fine meshes.
- Hardening occurs during the shot peening process. In consequence, residual stress fields can be observed below the contact and will significantly reduce the tensile stresses responsible for the crack opening. Moreover, due to high pressure and

shears observed at the edge of the contact, a plastic analysis may be required in aeronautical contacts.

- Material impurities such as oxyds inclusions, act as privileged crack initiation sites, increasing the local stress. FE methods commonly ignore such impurities because local refinements at such scale would be unaffordable when dealing with a complete contact. Because semi-analytical methods do not require any mesh generation, material impurities could be considered more easily.
- Coatings are applied to improve surface properties of the substrate. Multiple coatings of non-uniform thickness should be considered. Models become even more complicated when a coating is worn so the substrate or a sub-layer appears locally into the contact zone. Various coefficients of friction could be considered in the same contact area.
- Wear alters contact geometries and structural response, sensibly affecting lifespan estimations. A smooth iterative process even more cumbersome is then required in order to define the worn surface properly. FE methods are experiencing some troubles when dealing with rough surfaces, and discrepancies are commonly observed. Computations can take many weeks before they crash due to a contact instability. Advantages of a fast-computing method become clear.
- Frictional heating of worn surfaces is inevitable and is often responsible for failures such as scuffing, seizure and cracking. Raising temperature also modifies material properties locally. This aspect will not be treated in this work considering very low-speed slidings observed during low-frequency cycles. But it could have a major effect when dealing with high-frequency cycles caused by the aerodynamic response and structural vibrations.

Considering this, accuracy and feasibility of such computation using FE methods could be discussed. The actual work is based on a challenging method called semi-analytical method. An existing elastic contact solver will be used, and additional effects shown above will have to be taken into account. This solver will remain a robust and fast-computing tool, allowing iterative processes and fine discretizations.



Figure 1.7: Fretting issues observed in blade-roots: wear (left) and fatigue (right)

1.2 Fretting

Fretting refers to wear, fatigue and sometimes corrosion damage of the contact. This damage is induced under load and in the presence of repeated relative surface motion. The amplitude of the relative sliding motion is often in the order of micrometers. It can be induced by vibrations (aerodynamic or mechanic), or a repeated contact loading (low-frequency loadings in jet engines). Fretting wear is currently observed in most of quasi-static industrial contacts. In the aerospace industry, the dovetail blade-root connection and rotation splines on driveshafts experience fretting (See Figure 1.7). Bolted and riveted assemblies or sheathed cables also have fretting issues.

Mechanical wear (fretting-wear) is often followed by oxidation of both the metallic debris and the freshly-exposed metallic surfaces. Because oxides (fretting-corrosion) are often much harder than the surfaces from which they come, it often acts as an abrasive agent that increases the rate of both fretting and mechanical wear. We call this abrasive agent "the third body". Fretting also decreases fatigue strength of materials operating under cycling stress (fretting-fatigue), resulting in the nucleation of cracks that can propagate into the material.

In fine, wear can be understood through the energetic balance. Friction is a dissipative phenomenon, and a part of this energy is consumed by different processes (material transformations, physical-chemical processes, third body formation) that conduct to wear. Those phenomena are not explicitly taken into account, but estimations of wear kinetics and worn surfaces remain possible using an empirical wear law that implicitly accounts for all those aspects. The wear law used in this work is based on the Archard's law, modified by Fouvry and Paulin [PAU 05, PAU 06], and is based on the friction dissipated energy. After N cycles dissipating Ed , the worn volume V will be:

$$V = \alpha \sum_N Ed \quad (1.1)$$

In fretting applications, the wear coefficient α is a consequence of debris formation and debris ejection, because the fretting tangential displacement δ_o relative to the reference fretting test amplitude is responsible for the debris ejection, the wear law used derived from:

$$V = \alpha_{ref} \frac{\delta_o}{\delta_{ref}} \sum_N Ed \quad (1.2)$$

Finite element models have been used for wear computations and consist in computing one fretting cycle, using the contact data fields in order to obtain a wear depth field, updating the mesh by moving the node using various techniques, and restarting the procedure iteratively until a certain wear depth. While surfaces become rough, finite element solvers experience some discrepancies making results less reliable. In addition, three dimensional fan blades models require a fine mesh at the contact interface and lead to high computing costs, incompatible with an industrial design process [GAL 07c, GAL 07b, GAL 10].

1.3 Hardening in contacts

1.3.1 Nano-indentation

Indentation tests are the most commonly applied means of testing the mechanical properties of materials, elastic-plastic properties of metals for instance. A very hard tip, frequently made of diamond, is pressed into a sample whose properties are unknown. The load placed on the indenter tip is increased as the tip penetrates further into the sample, and then removed. A record of the depth of penetration is made during the experiment, and the area of the indent is determined using the known geometry of the indentation tip. The load versus displacement curve can be used to extract mechanical properties of the material. For instance, the slope of the curve dP / dh upon unloading (See Figure 1.8), is indicative of the stiffness S and can be used to calculate the Young's modulus of the sample considering the onset of unloading totally elastic.

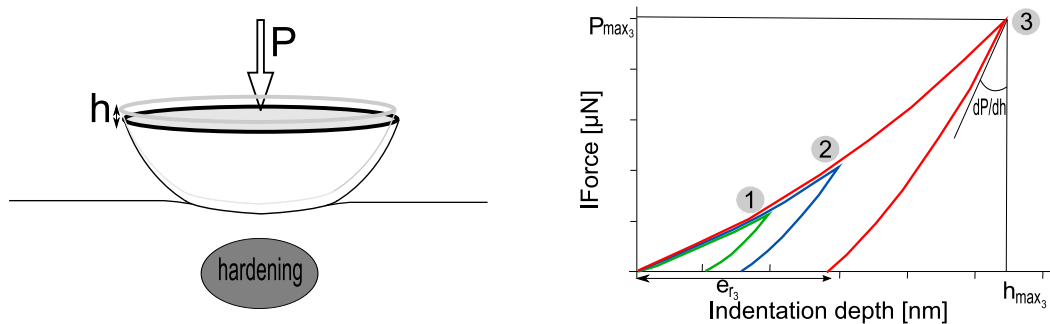


Figure 1.8: Indentation: normal displacement versus applied force curve

When considering elastic-plastic materials, the indentation process can be repeated many times, with each time a higher load. The remnant displacements versus the maximum normal load for each indentation test is then used to determine the hardening parameters using an inverse method and considering that a hardening law has been chosen. The commonly used stress-strain curve can be plotted using hardening parameters and the young's modulus.

Macro and micro indentations are limited due to large tip and varied tip shapes. Comparison across experiments is often difficult, while the area to be indented is very hard to specify accurately. But nano-indentation tests have a higher reliability. By indenting on the nano-scale with a very precise tip shape, such as a Berkovich tip which has a three-sided pyramid geometry, the nano-indentation gives high spatial resolutions to place the indents and a great stability across experiments. Moreover, nano-indentation provides real-time load-displacement data. However, it also presents new problems as the contact area is not easily found at this micro or even nano-scale.

Experimentally, results obtained using a spherical indenter are less stable than using a Berkovich indenter, but spherical indentations are still widely used. High plastic strains are localized at the tip of the Berkovitch indenter, while plastic strain fields are smoother

and are mainly observed below the surface with a spherical indenter. Spherical indentations will be widely used in this thesis.

1.3.2 Hardening in rough surfaces

Several damage mechanisms affect vital machine parts such as bearings, gears and blade-disk joints. The presence of geometrical singularities, such as dents, roughness, metal impurities and even edges of a contact induces the generation of elastic pressure peaks when loaded, increasing locally the stress level. Because of this high stress level, the material will undergo irreversible deformations caused by atomic reorganizations of the metallic crystals [JAC 02, BOU 07, NEL 07b, NEL 07a, ANT 08].

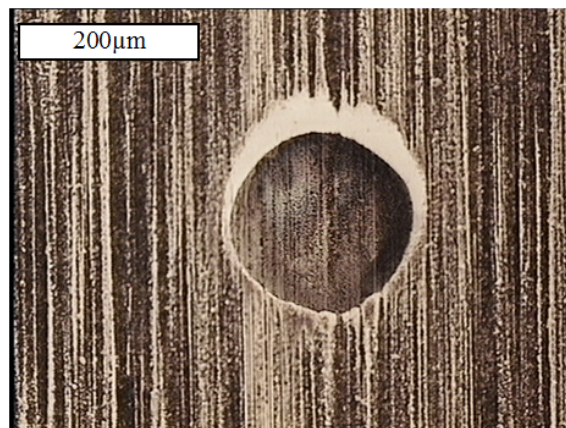


Figure 1.9: Effect of an indented groove in a ball bearing

The geometry of contacts play a key role in studies of friction, solid lubrication and wear. This geometry is affected by elastic and plastic deformations that may extend well below the surface. Those deformations are of a great importance and may lead to local hardening, heating and wear that limit lifetime estimations' accuracy.

For instance, a dent is a residual print caused by an indentation process that created plastic deformations below the surface. The contact surface is now dented, the geometry changed significantly and peaks of pressure occur at the base of the dent's shoulder when rolled over by a rolling body, leading to local hardening (See Figure 1.9).

Moreover, there is a high probability that crack will initiate where high stresses are localized (dent's shoulder, metal impurities, edges of a contact, ...). Cracks might initiate at the sub-surface or surface level, propagate and lead to a critical failure. In the ball-bearing industry for instance, the rolling contact fatigue (RCF) is the most common and dangerous phenomenon and is considerably accelerated by the formation of surface cracks, leading to surface initiated spalls. Even if uncontrolled hardening may result in a critical failure, controlled hardening is used in many applications in order to determine the elastic-plastic properties or to modify mechanical properties of metals and provide a considerable increase in part life.

1.3.3 Peening processes and residual stress layers

Shot peening is a cold working process in which small spherical media (round metallic, glass or ceramic particles) bombard the surface of a part. Each sphere that strikes the material at high speed acts as a tiny peening hammer. This process operates by the mechanism of plasticity which produces a compressive residual stress layer and modifies mechanical properties of metals.



Figure 1.10: Shots (left) bombarding an helicoidal gear (right)

Plastic deformation induces a residual compressive stress in a peened surface, along with tensile stress in the interior. Nearly all fatigue and stress corrosion failures originate at the surface of a part, due to the contact loading or gas surrounding. Because cracks do not initiate or propagate in a compressively stressed zone, shot peening provides considerable increases in part life. Therefore, shot peening is used in many industrial applications, especially in aeronautics, such as gear parts which experience fatigue and dovetail roots of blades which experience fretting-fatigue. It is also called for in aircraft repairs to relieve tensile stresses built up in the grinding process, replacing them with beneficial compressive stresses.

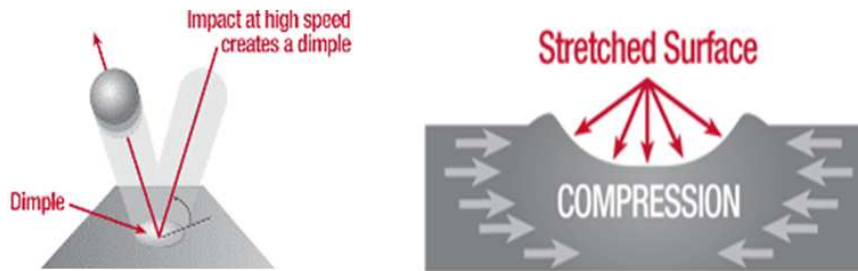


Figure 1.11: Shot peening generates a compressive layer below the surface

The tensile stresses deep in the part are not as problematic as tensile stresses on the surface because cracks are less likely to start in the interior. Shot peening has proved its effectiveness in extending the service life and enhancing the performance of metal components by protecting them against fatigue, fretting-fatigue, stress corrosion cracking and a variety of other failure mechanisms. Depending on part geometry, part and shot

material, shot quality, shot intensity and shot coverage, shot peening can increase fatigue life from 0% to 1000%.

Size, weight and speed of shots are key parameters, controlling the intensity of the shot peening process. The angle of the shot blast stream relative to the workpiece surface is another parameter. Moreover, stream is cone-shaped, thus, shot arrives at varying angles. Processing the surface with a series of overlapping passes improves coverage. A continuous compressively stressed surface of the workpiece has been shown to be produced at less than 50% coverage but falls as 100% is approached. Optimizing all those parameters for the process being performed is important for producing the desired surface effect.

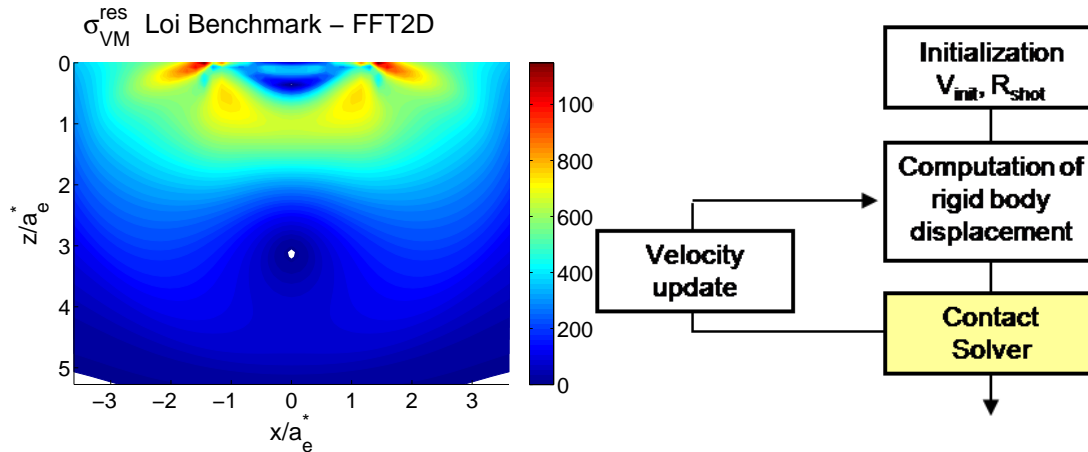


Figure 1.12: A semi-analytical solver can describe the shot peening process [CHA]

Shot peening process can be studied using numerical or semi-analytical methods in order to get a better understanding of key parameters. Plastic strains and residual stress fields are then obtained. The contact solver developed has been used by T.Chaise so that single and multiple shots can be treated. Those shots are still normal to the surface. However, recent improvements presented in this thesis allow us to consider both friction and plasticity, so that any angle of the shot blast stream could be treated.

While shot peening is the most economical and practical method of ensuring surface residual compressive stresses, other methods exist including ultrasonic peening, wet peening and laser peening. Laser technology is still expensive and requires a very high energy laser, but is expected to produce major savings in maintenance of commercial aircraft parts. In 2003, GE Aviation's F-110, P&W F-119 and F-135 military engines already used this technology. In 2004, Rolls-Royce also laser peened critical fan blade components installed in over 250 Rolls-Royce Trent 800 and Trent 500 commercial engines. Today, this working process is used in the new Boeing 747-8 and many other aeronautical systems.

A neodymium-doped glass laser is often used to produce high energy beams to create pressure pulses on the metal surface, which generate shock waves that travel into the metal and compress it. Each laser pulse creates an intense shock wave over a roughly 5x5-millimeters area that drives a residual compressive stress approximately 1 to 2 millimeters



Figure 1.13: Laser peening used in aeronautical applications

deep into the base metal. In conventional peening, this compressed layer is approximately 0.25 millimeters deep. Due to the deeper compressive residual stress imparted by the laser peening process, components are more resistant to fatigue, improving the cost effectiveness of the operation of the component in terms of increased life and reduced maintenance costs.

In addition to the understanding of the shot peening process, plastic strains induced by shot peening, laser peening (replacing shot peening in many applications) or any metal working process, e.g. milling or surface finishing, should be taken into account in blade-disk contact analysis, in order to account for prestressed media. Taking this compressive stress layer into account will significantly modify the maximum stress observed in the contact during flight, increasing lifespan estimations and avoiding unnecessary maintenance schedulings.

1.4 Inclusions and metal cleanliness

Materials used in construction are often considered flawless, which is sufficient at a macro-scale. However, aeronautics and many other fields require a finer approach in order to reduce risks and increase lifetime of parts. Soft and hard inclusions act as a stress raiser, i.e. media surrounding such inclusion experiences a local increase in the intensity of the stress field. Size, shape, chemical and physical characteristic of those impurities become of a great importance when long-term failure modes are considered. Because inclusions are responsible for most of fatigue failures initiated in the media, considering the metal purity in lifespan estimations becomes compulsory.

1.4.1 Aeronautical alloys

Engines construction typically requires the use of superalloys, Titanium superalloys e.g. Ti-6Al-4V are basically used for cold-stages, whereas nickel-chromium based superalloys e.g. Inconel 600 are used for hot-stages.

Ti-6Al-4V has a chemical composition of 6% aluminum, 4% vanadium, less than 0.25% iron, less than 0.20% oxygen, and the remainder titanium. This alloy is considered to be the workhorse of the titanium alloys due to an excellent combination of density, strength, corrosion resistance, weld and fabricability (4500 kg/m³, E=110 GPa, TS=1000 MPa). Generally, it is used in applications up to 400 °C, such as cold-stages of engines. Titanium alloys, except the most carefully purified, has a significant amount of dissolved oxygen, and so may be considered an oxide precipitate Ti-O. Ti-6Al-4V only contains small amounts of oxide precipitates and iron inclusions so the toughness of this alloy is not altered, but those inclusions can still act as a stress raiser and activate some long-term failure modes.

Inconel 600 has a chemical composition of more than 72% nickel, 14 to 17% chromium, 6 to 10% iron, 1% Manganese, less than 0.5% copper, less than 0.5% silicon, less than 0.15% carbon and no more than 0.015% sulfurs. Sulfur precipitates, copper, carbon and silicon may also act as a stress raiser. Other Inconel alloys have widely varying compositions and may include molybdenum, niobium, cobalt, aluminum, titanium, etc. Inconel alloys are oxidation and corrosion resistant and well suited for service in extreme environments and stay attractive for high temperature applications such as turbine blades, seals and combustors.

More classically, inclusions can be metallic (Tungsten, copper, etc), partially metallic (Oxides and sulfurs) and non-metallic (Carbon, Silicon, etc). Various shapes are encountered, such as spherical and elliptical inclusions, but polyhedral inclusions are also encountered when a crystal acts as an inclusion. It is of a great importance to consider those inclusions and their elastic-plastic properties in some cases, when the maximum true stress has to be found in order to prevent some phenomena initiated around inclusions.

1.4.2 Inclusions as a stress raiser

True elastic limit is easily exceeded and micro-structural transformations can be observed around inclusions at a very early stage. Dislocations start moving, and a whitening effect is even observed in ball-bearing steels (martensite). The angle of the whitening effect relative to the rolling direction is often equal to 45° due to the maximum shear stress.

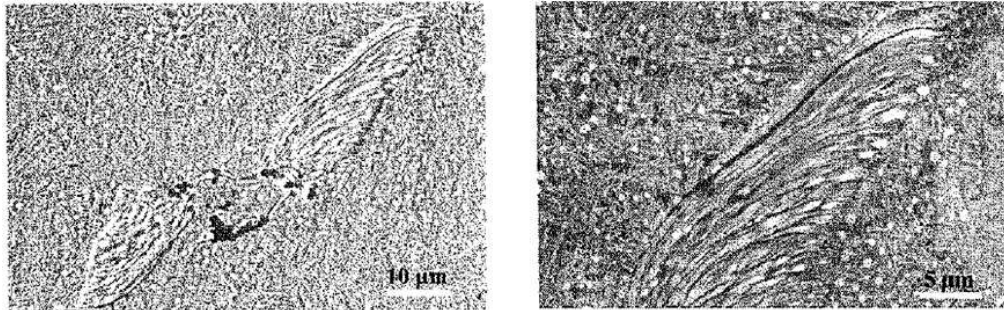


Figure 1.14: Whitening effect around an inclusion (left) and crack initiation (right)

Dislocations play a major role in the fatigue crack initiation phase. When enough dislocations are produced, a crack may initiate. If the repeated contact loading is sufficient, crack may propagate through the media and finally arise in the contact. Chipping of ball-bearings and gears (cf. FIG.1.15) is typically initiated around inclusions just below the surface and is a dangerous kind of damage where metal comes off in plates, but it is only one example among many that are initiated in the media around inclusions.

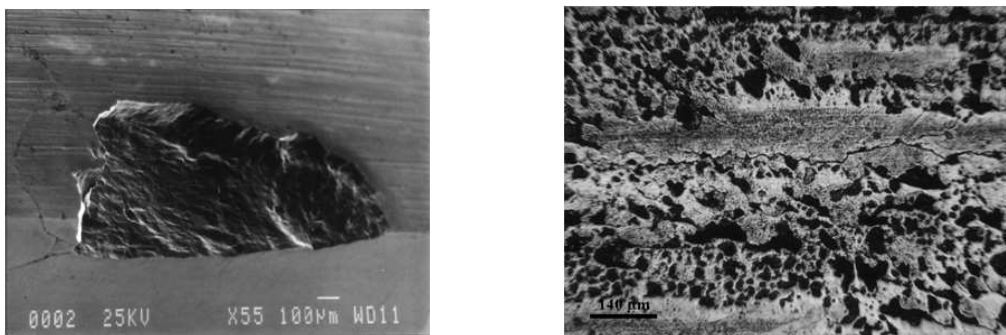


Figure 1.15: Metal coming off in plates (left) and chipped surface (right)

Because defects such as pores, inclusions and induced cracks are important for the structural integrity and durability of components, they have been intensively studied for decades using both analytical and numerical methods. Analytical methods based on the pioneering work of J.D. Eshelby [ESH 06] will be detailed and used later in this thesis. However, those analytical methods are still limited to a simple stress-analysis, used as a crack initiation indicator. Numerical methods, such as FEM and X-FEM, may also predict the crack propagation around an inclusion. But they are most of the time 2-dimensional and limited to small models with only few inclusions.

1.4.3 Numerical methods

In the finite-element method, the presence of flaws or inhomogeneities such as cracks, voids, and inclusions must be taken into account in the mesh generation process since edges of the element must conform to these geometric entities. This implies:

- Mesh has to be refined around each inclusion, especially when considering non-polyhedral inclusions, increasing the computing time. Moreover, meshing a distribution of defects and inclusions is a time-consuming and burdensome task, while semi-analytical methods do not require any mesh. (See Figure 1.16a)
- Mesh has to be re-generated each time the crack propagates. An automatic mesh generation is possible around the crack tip after the crack propagation, by refining locally the mesh and by increasing the number of elements. This also sensibly increases the computing time.

An alternative solution is the extended finite-element method or X-FEM. This aims to alleviate much of the burden associated with mesh generation for problems with voids and interfaces by not requiring the finite-element mesh to conform to internal boundaries. For instance, a crack may propagate through the media because of the stress concentration factor of a void without having to re-mesh the model. (See Figure 1.16b) The essence of the X-FEM lies in sub-dividing a model into two distinct parts: mesh generation for the domain (excluding internal boundaries); and enriching the finite-element approximation by additional functions that model the internal boundaries.

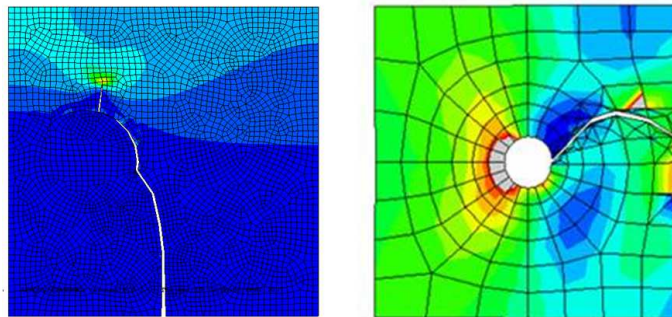


Figure 1.16: Crack initiation and propagation using FE (left) and X-FE (right) methods

Those techniques are widely used in fatigue life predictions when considering the metal purity. It allows a propagation of cracks through the media and the decohesion at the inclusion/matrix interface, but they are still limited to small models and few inclusions and are time-consuming. Semi-analytical methods are simpler and do not allow a propagation of cracks at this time. However, larger models can be considered and influence of a cluster of inclusions under contact conditions is not an issue.

1.5 Coatings and other applications

1.5.1 Coatings

Motivations In many engineering applications, protective coatings are increasingly used to extend the fatigue life of mechanical components in contact [CHA 90] and to provide low friction coefficients and wear resistance of tribological surface properties [KOM 88]. A great deal of research is to evaluate the performance of coatings and their failure mechanisms, while optimizing coatings may result in lifespan extensions.

Principle Material used for the manufacture and processing of blades and disks is typically a titanium alloy, Ti-6Al-4V, which is light, strong but has poor tribologic properties. Considering the surface-environment interactions to which some components of the aircraft industry are exposed, wear will slowly modify geometries of parts 1.7, affecting the aerodynamic efficiency of engines and involving important servicing costs because of premature part changes. In consequence, the study of protection against wear and corrosion induced by the use of coatings is an important research field in aeronautical engineering.

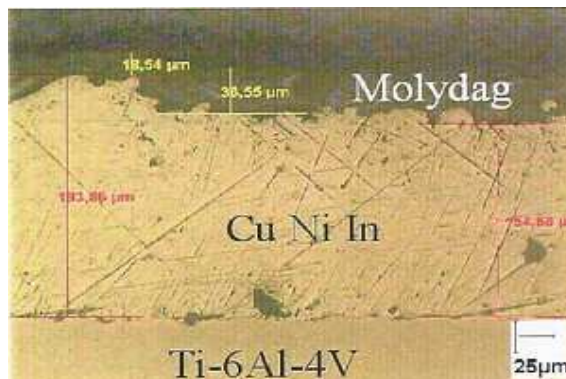


Figure 1.17: Multi-coatings at the blade-disk interface

In order to protect components from fretting, blade contact surfaces are usually covered by a thick and soft CuNiIn coating (100-150 μm), on top of which a solid lubricant is deposited (See Figure 1.17). Because this system is subjected to high contact pressure (up to 600MPa) and high temperatures (up to 500 $^{\circ}\text{C}$). The CuNiIn coating is chosen for its great capacity of accommodation by plastic deformation and acts as a sacrificial barrier to prevent titanium surfaces from coming into contact, while the solid lubricant promotes sliding and decreases the friction coefficient.

However, it had been observed that the solid lubricant has a limited life and this multi-layer system rapidly led back to a Ti/CuNiIn contact. Titanium may finally arise into the contact for severe wear depth (See Figure 1.18). Since it is generally the uncoated Ti part (corresponding to the compressor disk) that must be protected against wear, the CuNiIn/MoS₂ surface degradation process plays a key role in the preservation of the most critical parts.

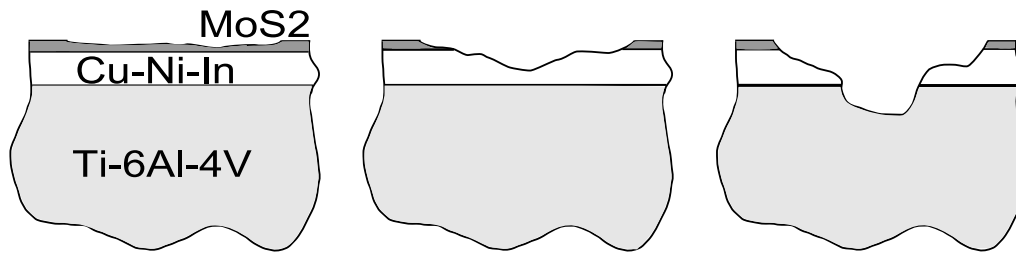
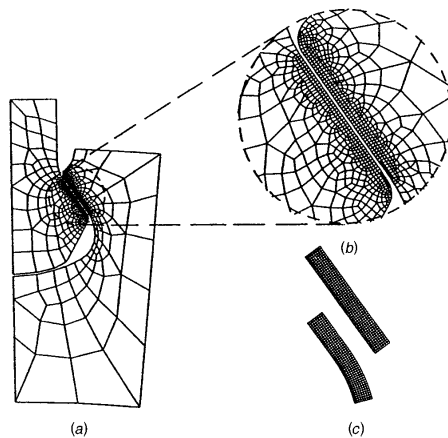


Figure 1.18: Chronology and wear of multi-coating systems

In consequence, the development of numerical tools able to analyse the frictional elastic-plastic contacts and internal stresses in a multi-layered body is therefore of a great practical importance since optimizing coatings may result in lifespan extensions.



Numerical methods The finite element method (FEM) has been extensively used by many researchers to perform the numerical studies of elasto-plastic problems layered materials. The FEM is flexible enough to solve the problems with complicated geometries and material constitutive responses. However, a large number of elements is needed to mesh the entire layered body, which may increase the computation burden significantly.

Wear simulations are an iterative process requiring an update of the contact geometry by moving each node. It becomes prohibitive and 2-dimensional simulations are often considered, while 3-dimensional simulations would require supercomputer capabilities for days.

A three-dimensional model of an elastic multilayered body, loaded both normally and tangentially against an elliptical rigid body (partial sliding, rolling/sliding conditions) has been presented by Plumet et Al. [PLU 98]. This kind of method can be used to guide the choice of coatings and has become very classical [O'S 88, LER 89, LIU 02, LIU 05b, LIU 07, POL 00b, POL 01]. Although, most of these theories take into account a uniform layer over an elastic substrate, there is a lack of models for solving the elastic-plastic contact problem of non-uniform coatings under normal and tangential loading conditions. This thesis will focus on a theory enabling this kind of studies.

1.5.2 Fiber reinforcements

In choosing new materials for airframe applications, it is essential to ensure there are no compromises in the levels of safety achievable with conventional alloys. This implies a perfect modelling of physical and chemical mechanisms occurring at each level of the composite structure.

Motivations Composites provide the opportunity of additional weight savings, complex geometries (See Fig 1.19b) and many other advantages. But, despite the growth in the use of composites, the reality is that airframes and engines will continue to be a mix of materials. These will include composites of various types and a range of metal alloys, the balance depending on structural and economic factors.

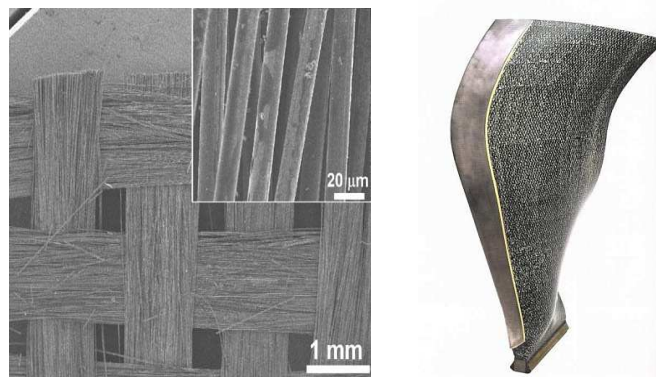


Figure 1.19: Composite materials are used in RTM fans of modern engines

Principle The approach is to use strong, stiff fibers to reinforce a relatively weaker, less stiff matrix. Both the fiber and matrix can be a polymer, a metal, or a ceramic. Fibers can be made from carbon, silica-based glasses or organic materials such as aramid (Kevlar) (See Fig 1.19a). Textile technology has been developed to produce special reinforcing fabrics from continuous fibers using several techniques including weaving, three-dimensional weaving, braiding and knitting.

The matrix forms the shape of the component and serves the following functions:

- transfer load into and out of the fibers: stresses at the fiber/matrix interface
- separate the fibers to prevent failure of adjacent fibers when one fails: crack propagation in a composite material
- protect the fiber from the environment: chemical aspect

Economic production requires that the techniques used for matrix introduction allow simple low-cost formation of the composite without damaging or misaligning the fibers. The simplest method is to infiltrate an aligned fiber bed with a low-viscosity liquid that is then

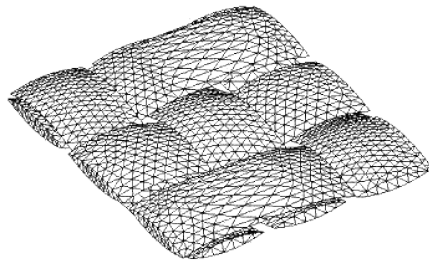
converted by chemical reaction or by cooling to form a continuous solid matrix with the desired properties (Resin-transfer molding or RTM).

PMCs Polymer matrix composites or PMCs are extensively used in aerospace structures; however, carbon/epoxy is by far the most exploited. Blades of modern engines are 3D-woven RTM CRFP blades with titanium bird cutters on the leading edge.

MMCs Potential aircraft applications of the metal matrix composites or MMCs include engine component, such as fan and compressor blades, shafts, and possibly discs, airframe components. Titanium alloys are used to form high-performance metal-matrix composites, offering the possibility of higher temperature service capabilities (>700 °C). But MMCs remain limited in temperature by fiber/matrix chemical and thermal incompatibilities.

CMCs While modern turbfans are reaching the limits of metallic survival, ceramic-matrix composites (CMCs) offer the main long-term promises for high-temperature applications in turbines and for high-temperature airframe structures, although there are formidable problems to be overcome. The main requirement is for lightweight blades able to operate uncooled in environments around 1400°C .

For the first time, GE has tested in 2010 a ceramic matrix composite (CMC) turbine blade in a working engine (a modified General Electric F414 engine). CMC materials have been used in various aerospace applications before, in static parts of the GE/Rolls-Royce F136 engine for instance or the GE/Snecma Leap-x turbine nozzles, but the recent F414 tests represents the first application of CMC materials in rotating engine parts. On turbine blades, CMCs are lighter than metallic turbine alloys and require a smaller cooling system. A GE90-sized engine of the next-generation could be 6% lighter than the actual GE90-115. It is now clear that the key potential benefit is weight saving and CMCs are now eligible to be incorporated in next generation of commercial and military engines, improving fuel efficiency rates in future generation of engines.



Numerical methods This thesis is not dealing with composite materials but with heterogeneous materials. It can be porous materials, materials containing multiple inclusions, multi-layered half-spaces, plastic-damage materials or it could also be reinforced materials. J.Leroux, is now investigating this problem using the same numerical and analytical framework.

1.5.3 Damage in brittle materials

Damage causes a progressive degradation of material continuity, which distinguishes it from other types of inelastic material behavior [LEM 90]. The loss of integrity can have an adverse effect on mechanical properties, and can be attributed to microscopic cracks and/or voids. Most materials contain initial voids and other non-homogeneities that are naturally occurring and distinct from damage. However, when subjected to mechanical loading, such as indentation, further damage accumulation may occur and a change in modulus and strength would basically be observed (See Figure 1.5.3).

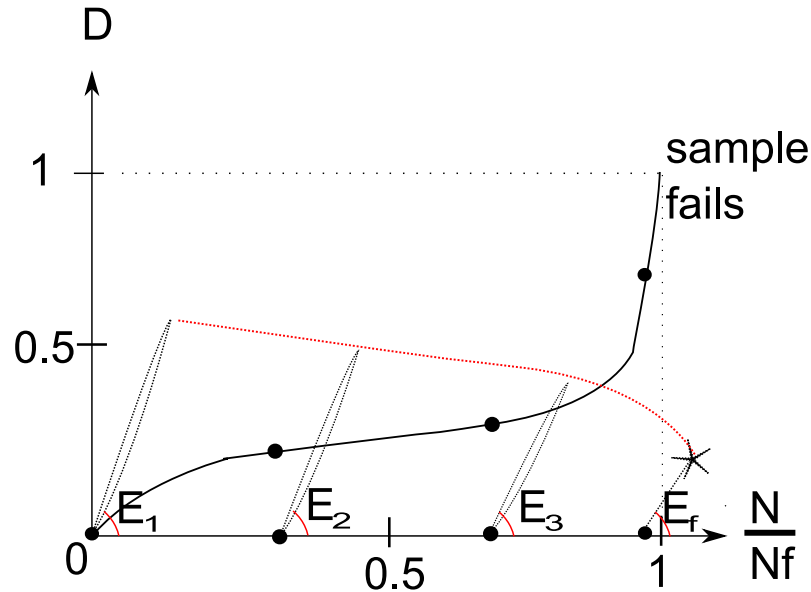


Figure 1.20: Modulus and strength variations observed for a damaged material

In section 4.2.7, the damage rate D will refer to a change in the initial Young's modulus E_{init} only, and the Young's modulus E will be defined by $E = E_{init} \cdot (1 - D)$.

Bones (See section 4.2.7) and concretes (See section 4.2.6) are brittle, meaning that damage may occur. Taking this damage into account in numerical simulations is essential. In aeronautical materials, ceramics provide a high-modulus matrix but also have a high brittleness, while the fibers provide little stiffening; their purpose is to increase toughness. This is achieved mainly by blunting and deflecting cracks in the matrix and contributing to increased fracture energy through the various energy-absorbing mechanisms, such as crack propagation. Only the embedding of fibers proved capable of increasing the resistance to cracks and ductility, breakage strength and thermal shock resistance, sometimes drastically. Typical applications are brake disks and friction pads for clutches in the automotive industry.

1.6 Methods used in contact mechanics

1.6.1 Analytical solutions

Hertzian contact Contact mechanics dates back to 1882 with the original work of Heinrich Hertz *On the contact of elastic solids* [HER 82]. Hertz solved the problem involving contact between two elastic bodies with curved surfaces we call the hertzian contact. Surfaces are supposed continuous and non-conforming. Hertzian theory considers the following assumptions:

- contact zone is elliptical ;
- problem does not account for friction ;
- half-spaces are considered ;

The area of contact must be much smaller than the characteristic radius of the body so that stresses are concentrated in the contact region and are not altered by boundary conditions. Because half-spaces are considered, theory of elasticity in elastic half-spaces can be used. Hertzian theory is quite restrictive because of those assumptions but is still relevant and provides a description of the contact pressure, contact dimension, displacements and stresses within the mating bodies.

Non-Hertzian contacts Additional complications arise when some or all these assumptions are violated and such contact problems are usually called non-hertzian. Those non-hertzian contacts have been extensively studied and are presented in the Johnson book [JOH 85]. Many solutions exist for conforming geometries, when contacts are not elliptical, even if solutions are still based on half-space theory. Some solutions exist for contact against a sheet or a shell. Finally, many solutions are given when geometric discrepancies are considered, such as sharp edges, etc. However, many of those solutions are only two-dimensional. Most of three-dimensional solutions are limited to axisymmetric geometries or other particular geometries. When Hertzian theory assumptions are removed, solutions often have to be found using cutting edge mathematics. It is the case when considering « singular integral equations » used by Muskhelishvili [MUS 53], then by Mikhlin [MIK 57], Galin [GAL 53] and Aleksandrov [ALE 86]. « Integral transforms » are also used, such as the Fourier transform [SNE 51]. Westergaard [WES 39] used it in rough contacts if roughness is a sine function. Greenwood & Willamson [GRE 66] proposed a theory of elastic contact mechanics of rough surfaces which is today the foundation of many theories in tribology (friction, adhesion, thermal and electrical conductance, wear, etc.).

Non-elastic behavior or non-homogeneous bodies Analytical solutions for a uniform coating do exist, if both the coating and the substrate are elastic [MEI 68]. Integral methods are also used [GLA 80]. However little work has been done concerning non-uniform

coatings considering the complexity of such problem [MAN]. Non-elastic behaviors, such as plasticity, are also studied. However, most analytical studies are limited and consider a perfectly plastic behavior. Indentation process is particularly studied and solutions exist for a conical, spherical and pyramidal tip indenter [JOH 85]. But spatial displacements in the media are assumed to be radial. It is clear that fully analytical methods are limited when considering non-elastic behaviors and non-uniform coatings.

Frictional contacts Coulomb's law of friction is used in most existing analytical solutions. When contact is considered fully sliding, shears are directly obtained from the hertzian pressure. Stresses for a cylindrical contact are given by McEwen [MCE 49] while stresses for a spherical contact are given by Hamilton [HAM 63]. Those solutions are extended to elliptical contacts by Sackfelds & Hills [SAC 83]. Cattaneo [CAT 38] and Mindlin [MIN 49] were considering a sphere normally and tangentially loaded. Tangential force is lower or equal to the limit fixed by the Coulomb's law in fully-sliding conditions. Because the Coulomb's law must be observed at each point within the contact area, sliding will appear at the edge of the contact creating a slip annulus. Mindlin & Deresiewicz [MIN 53] also studied this spherical contact when tangential force is a linear function of the normal force. The very popular Cattaneo-Mindlin Concept has been extended to any two dimensional geometry by Ciavarella [CIA 98a, CIA 98b], but analytical solutions are still limited when dealing with any three-dimensional geometry and loading.

1.6.2 Numerical methods

Finite element method The finite element method (FEM) is a numerical technique for finding approximate solutions of partial differential equations (PDE) as well as of integral equations. It is largely used in mechanics for complicated domains changing over time, and several modern FEM packages also include specific components (dynamic, thermal, electromagnetic, plasticity, viscosity, etc). But time consumption can be important, depending on the level of accuracy required. When contacts and inclusions are considered, using a finer mesh at the interface is imposed by the gradients that are expected, drastically increasing the computing time. For this reason, FEM is not a fast-computing method we have chosen for solving complex contact problems.

Semi-analytical methods When analytical solutions are way too complicated, it is possible to discretize the full-problem in a sum of elementary problems. Then, the solution is the numerical summation of analytical solutions for each elementary problem. Semi Analytical methods, or SA methods, have been intensively used in contact mechanics but numerical techniques can be different from an author [KAL 90] (Newton-Raphson algorithm) to an other [JAE 04] (Gauss-Seidel Algorithm). Today, most authors use Fast Fourier Transform (FFT) techniques [POL 00a, LIU 00] and a Conjugate Gradient Method (CGM) algorithm [POL 99] to perform their computations. Domains are large enough to consider the roughness of contacts [AI 99], elastic coatings of uniform thickness are even possible [PLU 98]. Frictional [GAL 07a], thermal-elastic

[LIU 02, LIU 01], plastic [JAC 01, NEL 06, SAI 02, ANT 04, ANT 05] and thermal-elastic-plastic analysis [BOU 05, BOU 04] have been investigated and proved the efficiency of SA methods.

1.7 Conclusion

Semi-analytical methods are still limited compared to finite element methods, and further developments are still needed. This PhD is based on C.Jacq, V.Boucly, E.Antaluca and L.Gallego SA codes developed at the LaMCoS. E.Antaluca [ANT 04, ANT 05] considered a sliding contact but the contact problem was not solved, nor coupled. Analytical solutions are then found so an elastic-plastic analysis of a frictional contact becomes possible. The contact becomes fully-sliding or partially sliding depending on the contact problem and considering a full coupling between the normal, tangential and plastic effects. Fretting modes are then briefly investigated considering plasticity. This work is also used in T.Chaise thesis while treating shot peening impacts.

Those models were still homogeneous, while the metal cleanliness, coatings and fiber reinforcements are found in some FE analysis. Semi-analytical contact algorithm found in the literature may already consider multiple effects:

- spherical and elliptical inclusions, but the contact problem was not solved, nor coupled to the non-homogeneous problem, and a hertzian pressure was applied over the surface [Cou 03];
- coatings of uniform thickness, which is not sufficient with worn geometries [PLU 98];
- fiber reinforcements are not treated at this time;

In fine, developing a unique method accounting non-homogeneous has been preferred in this work. The technique acts as an enrichment technique and is based on the pioneering work of J.D.Eshelby [ESH 06]. Spherical and cuboidal enrichment "elements" are then considered:

- Spherical inclusions are first used to perform some inclusion related simulations. This technique remains valid, even when inclusions are relatively small compared to the mesh size, so the influence of multiple spherical inclusions on contact conditions can be accurately investigated. Obviously, stresses observed around small inclusions are limited because only few nodes are describing local gradients. Considering the local stress of the steady state, when the coupling between contact and non-homogeneities converged, full stress fields can be obtained using a simple code acting like a close-up (See Fig. 1.21)

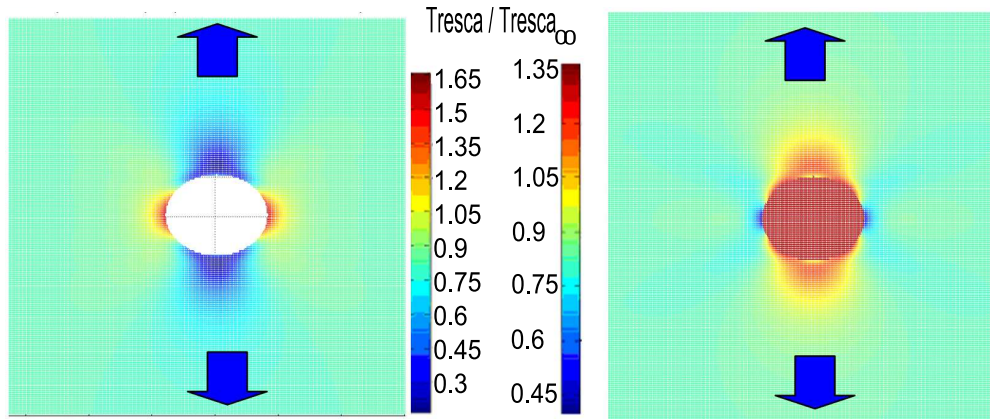


Figure 1.21: Dimensionless Tresca's stress around a spherical cavity (left) and a particle of alumina (right) in an aluminium media in simple traction

- Cubical inclusions are then used, allowing a discretization of the domain in many subdomains of various shapes. Spherical, elliptical, polyhedral or even cylindrical subdomains are discretized in many cubes, giving a good approximation of the original shape if the mesh size is small. However, this method is limited and clusters of hundreds of spherical inclusions can not be investigated. This technique will be compared to analytical solutions of spherical and elliptical inclusions and then applied to coating problems. Numerical results found in the literature will be used, and various frictional problems and coating thicknesses are then investigated. Finally, problem of coatings of non-uniform thickness will be treated.

Numerical methods have been updated (3D-FFT) and the convergence of the conjugate gradient method has been improved. In consequence, semi-analytical methods will remain a fast-computing option for contact related three-dimensional analyses, even when considering partially sliding contacts, worn coatings, clusters of inclusions and elastic-plastic properties.

Chapter 2

The elastic-plastic contact

The resolution of problems in contact mechanics consists in finding the real contact area, the contact pressure, shears and slips distribution. The origin of all the theory is the famous paper of Heinrich Hertz, which gave the solution of the elastic contact between two ellipsoidal bodies without friction. Even today, this is the basics for industries in conception of dry, non conforming and elastic contacts, as it exists in gears and rolling bearings for instance. Since 1882, this topic has been extensively developed, and one can observe two main types of studies. Mathematically, some work has been done for extending the Hertz analysis to other geometries, for studying other material behaviors, and for developing existence and solution unicity theorems. For engineers, some work has been done for some specific cases, in order to better understand phenomena that occur in real systems, using numerical methods, and more recently, semi-analytical methods.

Contents

2.1	The elastic contact	31
2.1.1	Contact kinematic	31
2.1.2	Loadings transmitted into the contact	33

*Semi-analytical modeling of complex mechanical contacts:
Application to inclusions and wear of coated surfaces*

29

2.1.3	The half-space	34
2.1.4	Discretization of surface loadings	41
2.1.5	Normal problem	43
2.1.6	Tangential problem	46
2.1.7	Coupling between the normal and tangential problem	49
2.2	The elastic-plastic half-space	51
2.2.1	Elastic-plastic algorithm	51
2.2.2	Plasticity model	52
2.2.3	Residual stress calculation	53
2.2.4	Maxwell-Betti's reciprocal theorem	56
2.2.5	Normal residual displacements [JAC 01]	57
2.2.6	Tangential residual displacements [FUL 09]	59
2.2.7	Validations using a Finite Element model	61
2.2.8	Comparison between the FEA and analytical results	62
2.2.9	Validation using a finite element model without friction	65
2.3	Numerical methods and improvements	66
2.3.1	Weak formulation	66
2.3.2	Conjugate Gradient Method (CGM)	67
2.3.3	Convergence of the tangential contact solver	68
2.3.4	Discrete Continuous Fast Fourier Transforms (DC-FFT)	70
2.3.5	2D-FFT Algorithm	74
2.3.6	3D-FFT Algorithm	74
2.3.7	2.5D-FFT Algorithm	76
2.3.8	Instability on plastic strains	77
2.3.9	Conclusion	79
2.4	Fretting considering the elastic-plastic regime	80
2.4.1	Fretting modes and material properties	80
2.4.2	Fretting mode II: Indentation	81
2.4.3	Fretting mode I: Sliding	92
2.4.4	Conclusion	96
2.5	Conclusion	98

2.1 The elastic contact

Note This section is dedicated to the elastic contact solver. The problem is briefly exposed, the contact solver is detailed and numerical methods used in the algorithm are explained. The core of the elastic solver has been developed by L.Gallego and further explanation can be found in [GAL 07a].

2.1.1 Contact kinematic

Let's consider two elastic bodies 1 and 2 defined by their undeformed surfaces in the orthonormal basis $Oxyz$. The plane $x - y$ is actually separating both surfaces. When both surfaces considered are non-conforming, the plane $x - y$ is tangent to the point/line of contact. Surfaces are then defined by:

$$\begin{aligned} z_1 &= f_1(x, y), \\ z_2 &= f_2(x, y). \end{aligned} \quad (2.1)$$

At a point of coordinate (x, y) , the separation is:

$$h(x, y) = f_1(x, y) - f_2(x, y). \quad (2.2)$$

Surfaces f_1 and f_2 have small gradients so it can be approximate to the plane $x - y$. Rigid body displacements are defined by δ_{z1} (respectively δ_{z2}) along the normal direction, and by δ_{x1} and δ_{y1} (respectively δ_{x2} and δ_{y2}) in slips' directions. Angular rotations ϕ_{x1} and ϕ_{y1} (respectively ϕ_{x2} and ϕ_{y2}) are rolling angles while ϕ_{z1} (respectively ϕ_{z2}) is the twisting angle. All movements of the body 1 (respectively the body 2) can be described using such parameters. (See Figure 2.1) It must be noticed that all displacements and angles are expressed at the point O , center of the contact. Rolling angles do not initiate a rolling movement when angles are kept small, but this angle will create a misalignment that significantly modifies the normal problem.

Finally, the distance between both surfaces $g(x, y)$ ('g' meaning 'gap') is defined by the initial separation of both bodies, the rigid body displacement $\delta_z = \delta_{z1} + \delta_{z2}$, rolling angles $\phi_x = \phi_{x1} + \phi_{x2}$ and $\phi_y = \phi_{y1} + \phi_{y2}$ and elastic deflections $\bar{u}_z = \bar{u}_{z1} + \bar{u}_{z2}$:

$$g(x, y) = h(x, y) + \bar{u}_z - \delta_z - y \cdot \phi_x + x \cdot \phi_y. \quad (2.3)$$

Using displacements, contact condition is expressed by:

$$g(x, y) = 0, \text{ into the contact,} \quad (2.4)$$

$$g(x, y) > 0, \text{ out of the contact.} \quad (2.5)$$

Slipping conditions have to be defined. Slips in the interface will be noted \mathbf{s} . \mathbf{s} is a vector of component s_x and s_y . This slip \mathbf{s}^t is defined between the current time increment t and the previous time increment t' . Finally, \mathbf{s}^t is expressed as follows:

$$\mathbf{s}^t = \begin{pmatrix} \Delta \bar{u}_x^t - \Delta \delta_x^t + y \cdot \Delta \phi_z^t \\ \Delta \bar{u}_y^t - \Delta \delta_y^t - x \cdot \Delta \phi_z^t \end{pmatrix}. \quad (2.6)$$

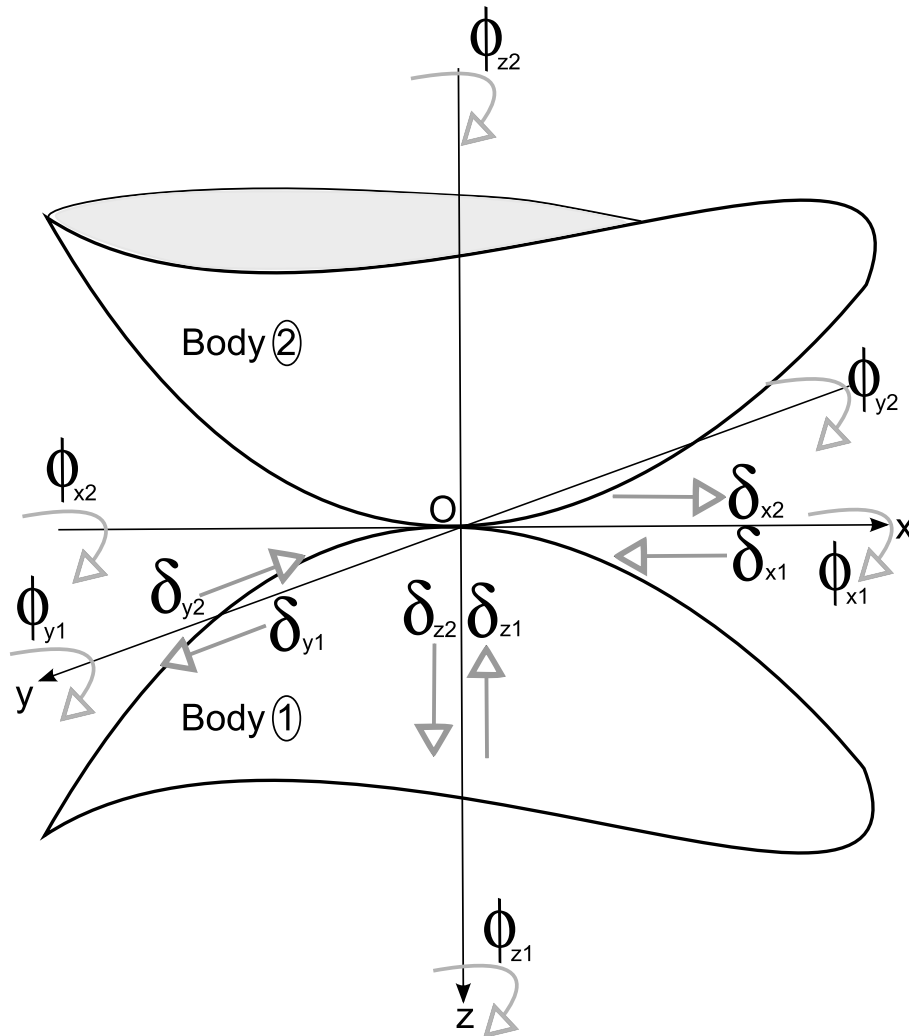


Figure 2.1: Rigid body displacements

2.1.2 Loadings transmitted into the contact

Loadings transmitted into the contact are defined by the normal force P , the tangential force \mathbf{Q} of components Q_x and Q_y , and the moment \mathbf{M} transmitted at the point O and of components M_x , M_y and M_z . M_x and M_y are the bending moments while M_z is the moment of torsion. Those forces are transmitted through the contact zone Γ_C thanks to stresses into the surface. Normal stresses or contact pressure will be noted p while shear stresses or shears of components q_x and q_y will be noted \mathbf{q}_τ . Those stress fields must verify equilibrium equations expressed hereafter:

$$P = \int_{\Gamma_C} p \, dS, \quad (2.7)$$

$$Q_x = \int_{\Gamma_C} q_x \, dS, \quad (2.8)$$

$$Q_y = \int_{\Gamma_C} q_y \, dS, \quad (2.9)$$

$$M_x = \int_{\Gamma_C} p \cdot y \, dS, \quad (2.10)$$

$$M_y = - \int_{\Gamma_C} p \cdot x \, dS, \quad (2.11)$$

$$M_z = \int_{\Gamma_C} (x \cdot q_y - y \cdot q_x) \, dS. \quad (2.12)$$

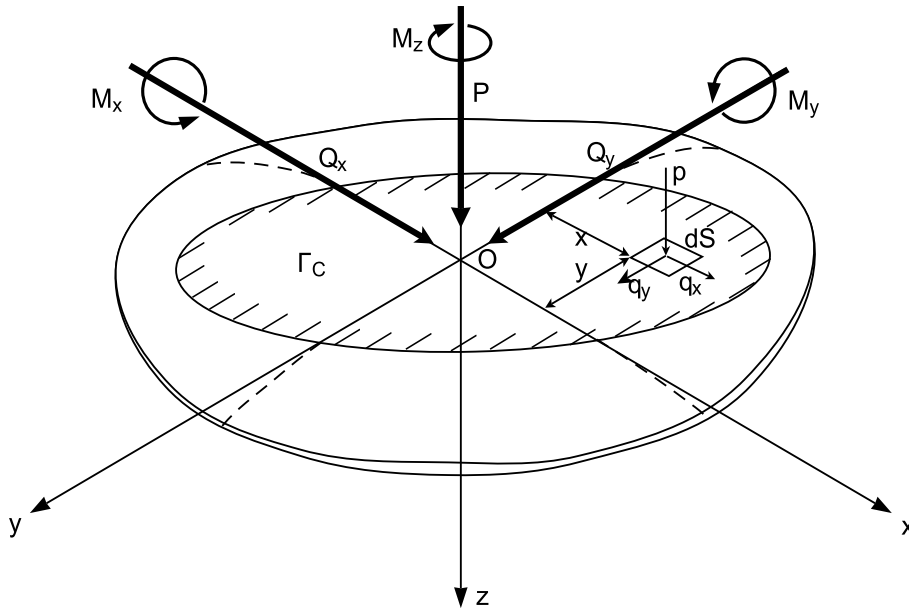


Figure 2.2: Forces and moments transmitted into the contact

2.1.3 The half-space

The elastic contact can be described using semi-analytical methods using some analytical solutions. Those solutions are given in this section, and express the influence of a pressure or a shear field on the surface deflections and volume stresses, considering an homogeneous and isotropic elastic half-space defined by $z \leq 0$. Elastic deflection far away are nil because of the boundary conditions. Normal tractions $p(x, y)$ and tangential tractions $q_x(x, y)$ and $q_y(x, y)$ are applied to a closed surface S close to the origin. Neumann's problem consists in finding the elastic deflections u_x , u_y and u_z and stresses σ of components σ_x , σ_y , σ_z , τ_{xy} , τ_{yz} and τ_{zx} . The theory of potentials has been used by Boussinesq [BOU 85] and Cerruti [CER 82] in order to solve this problem when considering a punctual force. This work has been extended by Love [LOV 52] to a rectangular surface $\Delta x \times \Delta y$ of center O and normally loaded using a constant pressure p , and by Vergne [VER 85] to a constant shear q_x or q_y . All those solutions are expressed in [JOH 85], more typically for deflections of a surface point $M(x, y)$ and stresses of a point $M(x, y, z)$ of the volume when considering a load applied at the origin. The distance between O and M will be noted ρ and expressed by $\rho = \sqrt{x^2 + y^2 + z^2}$.

When volumic forces are neglected, Navier equations are expressed as follows:

$$\nabla^2 \mathbf{u} = 0. \quad (2.13)$$

Displacements can be expressed using bi-harmonic functions because they verify a Laplace's equation. Moreover, displacements must respect boundary conditions and loadings. Let's consider the distance between the loaded point $O(\xi, \eta)$ of the surface and another point $M(x, y, z)$ of the half-space

$$OM \equiv \rho = \{(\xi - x)^2 + (\eta - y)^2 + z^2\}^{1/2}. \quad (2.14)$$

Three potential functions can be defined, respecting Laplace's equation

$$\begin{aligned} F_1 &= \int \int_S q_x(\xi, \eta) \Omega \, d\xi \, d\eta, \\ G_1 &= \int \int_S q_y(\xi, \eta) \Omega \, d\xi \, d\eta, \\ H_1 &= \int \int_S p(\xi, \eta) \Omega \, d\xi \, d\eta, \end{aligned} \quad (2.15)$$

where

$$\Omega = z \ln(\rho + z) - \rho. \quad (2.16)$$

Derivate functions are also defined

$$\begin{aligned} F &= \frac{\partial F_1}{\partial x} = \int \int_S q_x(\xi, \eta) \ln(\rho + z) \, d\xi \, d\eta, \\ G &= \frac{\partial G_1}{\partial x} = \int \int_S q_y(\xi, \eta) \ln(\rho + z) \, d\xi \, d\eta, \\ H &= \frac{\partial H_1}{\partial x} = \int \int_S p(\xi, \eta) \ln(\rho + z) \, d\xi \, d\eta. \end{aligned} \quad (2.17)$$

Defining functions ψ_1 and ψ by:

$$\psi_1 = \frac{\partial F_1}{\partial x} + \frac{\partial G_1}{\partial y} + \frac{\partial H_1}{\partial z} \quad (2.18)$$

$$\psi = \frac{\partial \psi_1}{\partial z} = \frac{\partial F}{\partial x} + \frac{\partial G}{\partial y} + \frac{\partial H}{\partial z}. \quad (2.19)$$

Love [LOV 52] proved that elastic deflections u_x , u_y and u_z at the point $M(x, y, z)$ can be expressed as follows:

$$u_x = \frac{1}{4\pi G} \left\{ 2 \frac{\partial F}{\partial z} - \frac{\partial H}{\partial x} + 2\nu \frac{\partial \psi_1}{\partial x} - z \frac{\partial \psi}{\partial x} \right\}, \quad (2.20)$$

$$u_y = \frac{1}{4\pi G} \left\{ 2 \frac{\partial G}{\partial z} - \frac{\partial H}{\partial y} + 2\nu \frac{\partial \psi_1}{\partial y} - z \frac{\partial \psi}{\partial y} \right\}, \quad (2.21)$$

$$u_z = \frac{1}{4\pi G} \left\{ \frac{\partial F}{\partial z} - (1 - 2\nu)\psi - z \frac{\partial \psi}{\partial z} \right\}. \quad (2.22)$$

Then, stresses can be obtained using the Hooke's law,

$$\sigma_x = \frac{2\nu G}{1 - 2\nu} \left(\frac{\partial u_x}{\partial x} + \frac{\partial u_y}{\partial y} + \frac{\partial u_z}{\partial z} \right) + 2G \frac{\partial u_x}{\partial x}, \quad (2.23)$$

$$\sigma_y = \frac{2\nu G}{1 - 2\nu} \left(\frac{\partial u_x}{\partial x} + \frac{\partial u_y}{\partial y} + \frac{\partial u_z}{\partial z} \right) + 2G \frac{\partial u_y}{\partial y}, \quad (2.24)$$

$$\sigma_z = \frac{2\nu G}{1 - 2\nu} \left(\frac{\partial u_x}{\partial x} + \frac{\partial u_y}{\partial y} + \frac{\partial u_z}{\partial z} \right) + 2G \frac{\partial u_z}{\partial z}, \quad (2.25)$$

$$\tau_{xy} = G \left(\frac{\partial u_x}{\partial y} + \frac{\partial u_y}{\partial x} \right), \quad (2.26)$$

$$\tau_{yz} = G \left(\frac{\partial u_y}{\partial z} + \frac{\partial u_z}{\partial y} \right), \quad (2.27)$$

$$\tau_{zx} = G \left(\frac{\partial u_z}{\partial x} + \frac{\partial u_x}{\partial z} \right). \quad (2.28)$$

Finally, solutions (2.20) to (2.22) are used to determine elastic deflection for both normal and tangential loadings. It must be noticed that double integrals found in (2.15) and (2.17) is not easy to find. This is a problem encountered in later sections when looking for analytical solutions for elastic-plastic and non-homogeneous problems. In following equations, subscripts I and J may describe either x , y or z .

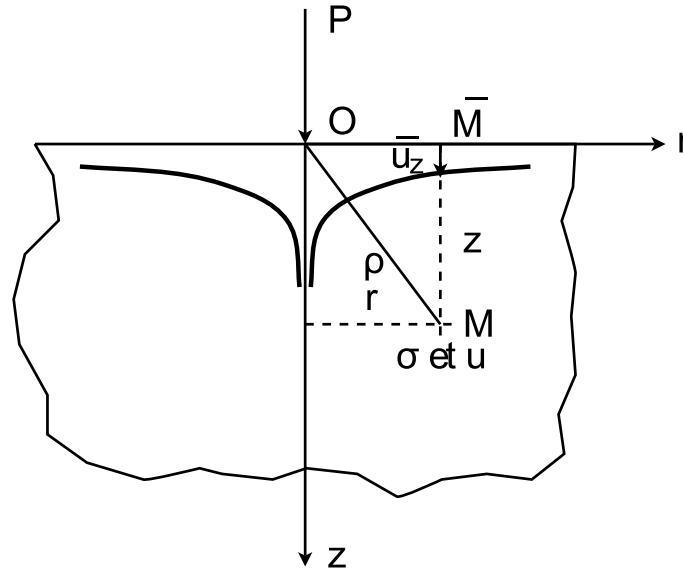


Figure 2.3: Elastic deflections induced by a normal loading

Contribution of pressure field p on half-space stresses is given by:

$$\frac{\sigma_{IJ}}{p} = C_{IJ}^p(x, y, z, E, \nu) = S_{IJ}^p\left(x + \frac{\Delta_x}{2}, y + \frac{\Delta_y}{2}, z, E, \nu\right) + S_{IJ}^p\left(x - \frac{\Delta_x}{2}, y - \frac{\Delta_y}{2}, z, E, \nu\right) - S_{IJ}^p\left(x + \frac{\Delta_x}{2}, y - \frac{\Delta_y}{2}, z, E, \nu\right) - S_{IJ}^p\left(x - \frac{\Delta_x}{2}, y + \frac{\Delta_y}{2}, z, E, \nu\right), \quad (2.29)$$

with

$$S_{xx}^p(x, y, z, E, \nu) = \frac{\nu}{\pi} \arctan\left(\frac{z^2 + y^2 - y\rho}{zx}\right) + \frac{1-2\nu}{\pi} \arctan\left(\frac{\rho - y + z}{x}\right) + \frac{z}{2\pi} \frac{xy}{(x^2 + z^2)\rho}, \quad (2.30)$$

$$S_{yy}^p(x, y, z, E, \nu) = \frac{\nu}{\pi} \arctan\left(\frac{z^2 + y^2 - y\rho}{zx}\right) + \frac{1-2\nu}{\pi} \arctan\left(\frac{\rho - x + z}{y}\right) + \frac{z}{2\pi} \frac{xy}{(y^2 + z^2)\rho}, \quad (2.31)$$

$$S_{zz}^p(x, y, z, E, \nu) = \frac{1}{2\pi} \arctan\left(\frac{z^2 + y^2 - y\rho}{zx}\right) - \frac{z}{2\pi} \frac{xy}{\rho} \left(\frac{1}{x^2 + z^2} + \frac{1}{y^2 + z^2}\right), \quad (2.32)$$

$$S_{xy}^p(x, y, z, E, \nu) = -\frac{z}{2\pi} \frac{1}{\rho} - \frac{1-2\nu}{2\pi} \ln(\rho + z), \quad (2.33)$$

$$S_{yz}^p(x, y, z, E, \nu) = \frac{z^2}{2\pi} \frac{x}{(y^2 + z^2)\rho}, \quad (2.34)$$

$$S_{xz}^p(x, y, z, E, \nu) = \frac{z^2}{2\pi} \frac{y}{(x^2 + z^2)\rho}. \quad (2.35)$$

In the same manner, elastic deflections of the surface can be defined. $\bar{\rho} = \sqrt{x^2 + y^2}$ and the contribution of the pressure field p on the elastic deflection of the surface is given by:

$$\begin{aligned} \frac{\bar{u}_J}{p} = K_J^p(x, y, E, \nu) = & U_J^p\left(x + \frac{\Delta_x}{2}, y + \frac{\Delta_y}{2}, E, \nu\right) + U_J^p\left(x - \frac{\Delta_x}{2}, y - \frac{\Delta_y}{2}, E, \nu\right) \\ & - U_J^p\left(x + \frac{\Delta_x}{2}, y - \frac{\Delta_y}{2}, E, \nu\right) - U_J^p\left(x - \frac{\Delta_x}{2}, y + \frac{\Delta_y}{2}, E, \nu\right), \end{aligned} \quad (2.36)$$

with

$$U_x^p(x, y, E, \nu) = -\frac{(1+\nu)(1-2\nu)}{2\pi E} \left(2x \arctan\left(\frac{\bar{\rho}-y}{x}\right) - y \ln \bar{\rho} \right), \quad (2.37)$$

$$U_y^p(x, y, E, \nu) = -\frac{(1+\nu)(1-2\nu)}{2\pi E} \left(2y \arctan\left(\frac{\bar{\rho}-x}{y}\right) - x \ln \bar{\rho} \right), \quad (2.38)$$

$$U_z^p(x, y, E, \nu) = -\frac{(1-\nu^2)}{\pi E} (y \ln(\bar{\rho}-x) + x \ln(\bar{\rho}-y)). \quad (2.39)$$

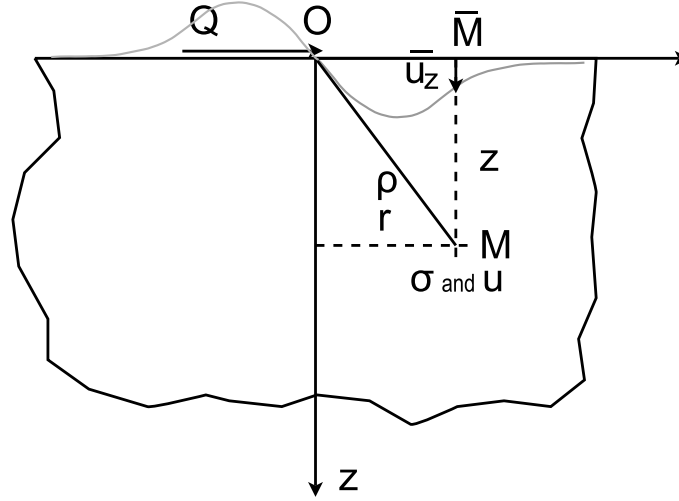


Figure 2.4: Elastic deflections induced by a tangential loading

Contribution of pressure field q_x on half-space stresses is given by:

$$\begin{aligned} \frac{\sigma_{IJ}}{q_x} = C_{IJ}^{q_x}(x, y, z, E, \nu) = & S_{IJ}^{q_x}\left(x + \frac{\Delta_x}{2}, y + \frac{\Delta_y}{2}, z, E, \nu\right) + S_{IJ}^{q_x}\left(x - \frac{\Delta_x}{2}, y - \frac{\Delta_y}{2}, z, E, \nu\right) \\ & - S_{IJ}^{q_x}\left(x + \frac{\Delta_x}{2}, y - \frac{\Delta_y}{2}, z, E, \nu\right) - S_{IJ}^{q_x}\left(x - \frac{\Delta_x}{2}, y + \frac{\Delta_y}{2}, z, E, \nu\right), \end{aligned} \quad (2.40)$$

with

$$S_{xx}^{q_x}(x, y, z, E, \nu) = -\frac{z}{2\pi\rho} \frac{1}{\rho} \left(1 + \frac{-x^2 + zy}{(\rho+z)(\rho-y)}\right) + \frac{\nu}{\pi} \frac{y}{\rho+z} - \frac{1}{\pi} \ln(\rho-y), \quad (2.41)$$

$$S_{yy}^{q_x}(x, y, z, E, \nu) = -\frac{z}{2\pi\rho} \frac{y}{\rho(\rho+z)} - \frac{\nu}{\pi} \left(\frac{y}{\rho+z} + \ln(\rho-y)\right), \quad (2.42)$$

$$S_{zz}^{q_x}(x, y, z, E, \nu) = \frac{z^2}{2\pi\rho} \frac{y}{(x^2+z^2)}, \quad (2.43)$$

$$S_{xy}^{q_x}(x, y, z, E, \nu) = -\frac{z}{2\pi\rho} \frac{x}{\rho(\rho+z)} - \frac{\nu}{\pi} \frac{x}{\rho+z} - \frac{1}{2\pi} \ln(\rho-x), \quad (2.44)$$

$$S_{yz}^{q_x}(x, y, z, E, \nu) = -\frac{z}{2\pi\rho} \frac{1}{\rho}, \quad (2.45)$$

$$S_{xz}^{q_x}(x, y, z, E, \nu) = \frac{z}{2\pi \rho} \frac{xy}{(x^2 + z^2)} + \frac{1}{2\pi} \arctan \left(\frac{z^2 + y^2 - y\rho}{zx} \right). \quad (2.46)$$

Contribution of pressure field q_y on half-space stresses is given by:

$$\begin{aligned} \frac{\sigma_{IJ}}{q_y} = C_{IJ}^{q_y}(x, y, z, E, \nu) = & S_{IJ}^{q_y} \left(x + \frac{\Delta_x}{2}, y + \frac{\Delta_y}{2}, z, E, \nu \right) + S_{IJ}^{q_y} \left(x - \frac{\Delta_x}{2}, y - \frac{\Delta_y}{2}, z, E, \nu \right) \\ & - S_{IJ}^{q_y} \left(x + \frac{\Delta_x}{2}, y - \frac{\Delta_y}{2}, z, E, \nu \right) - S_{IJ}^{q_y} \left(x - \frac{\Delta_x}{2}, y + \frac{\Delta_y}{2}, z, E, \nu \right), \end{aligned} \quad (2.47)$$

with

$$S_{xx}^{q_y}(x, y, z, E, \nu) = -\frac{z}{2\pi \rho(\rho + z)} \frac{x}{\rho + z} - \frac{\nu}{\pi} \left(\frac{x}{\rho + z} + \ln(\rho - x) \right), \quad (2.48)$$

$$S_{yy}^{q_y}(x, y, z, E, \nu) = \frac{z}{2\pi \rho} \left(1 + \frac{-y^2 + zx}{(\rho + z)(\rho - x)} \right) + \frac{\nu}{\pi} \frac{x}{\rho + z} - \frac{1}{\pi} \ln(\rho - x), \quad (2.49)$$

$$S_{zz}^{q_y}(x, y, z, E, \nu) = \frac{z^2}{2\pi \rho} \frac{x}{(y^2 + z^2)}, \quad (2.50)$$

$$S_{xy}^{q_y}(x, y, z, E, \nu) = -\frac{z}{2\pi \rho(\rho + z)} \frac{y}{\rho + z} - \frac{\nu}{\pi} \frac{y}{\rho + z} - \frac{1}{2\pi} \ln(\rho - y), \quad (2.51)$$

$$S_{yz}^{q_y}(x, y, z, E, \nu) = \frac{z}{2\pi \rho} \frac{yx}{(y^2 + z^2)} + \frac{1}{2\pi} \arctan \left(\frac{z^2 + x^2 - x\rho}{zy} \right), \quad (2.52)$$

$$S_{xz}^{q_y}(x, y, z, E, \nu) = -\frac{z}{2\pi} \frac{1}{\rho}. \quad (2.53)$$

In the same manner, elastic deflections of the surface can be defined. $\bar{\rho} = \sqrt{x^2 + y^2}$ and the contribution of the pressure field q_x on the elastic deflection of the surface is given by:

$$\begin{aligned} \frac{\bar{u}_J}{q_x} = K_J^{q_x}(x, y, E, \nu) = & U_J^{q_x} \left(x + \frac{\Delta_x}{2}, y + \frac{\Delta_y}{2}, E, \nu \right) + U_J^{q_x} \left(x - \frac{\Delta_x}{2}, y - \frac{\Delta_y}{2}, E, \nu \right) \\ & - U_J^{q_x} \left(x + \frac{\Delta_x}{2}, y - \frac{\Delta_y}{2}, E, \nu \right) - U_J^{q_x} \left(x - \frac{\Delta_x}{2}, y + \frac{\Delta_y}{2}, E, \nu \right), \end{aligned} \quad (2.54)$$

with

$$U_x^{q_x}(x, y, E, \nu) = -\frac{1-\nu^2}{\pi E} x \ln(\bar{\rho}-y) - \frac{1+\nu}{\pi E} \ln(\bar{\rho}-x), \quad (2.55)$$

$$U_y^{q_x}(x, y, E, \nu) = -\frac{\nu(1+\nu)}{\pi E} \bar{\rho}, \quad (2.56)$$

$$U_z^{q_x}(x, y, E, \nu) = \frac{(1+\nu)(1-2\nu)}{2\pi E} \left(-2x \arctan\left(\frac{\bar{\rho}-y}{x}\right) + y \ln \bar{\rho} \right). \quad (2.57)$$

the contribution of the pressure field q_y on the elastic deflection of the surface is given by:

$$\begin{aligned} \frac{\bar{u}_J}{q_y} = K_J^{q_y}(x, y, E, \nu) = & U_J^{q_y}\left(x + \frac{\Delta_x}{2}, y + \frac{\Delta_y}{2}, E, \nu\right) + U_J^{q_y}\left(x - \frac{\Delta_x}{2}, y - \frac{\Delta_y}{2}, E, \nu\right) \\ & - U_J^{q_y}\left(x + \frac{\Delta_x}{2}, y - \frac{\Delta_y}{2}, E, \nu\right) - U_J^{q_y}\left(x - \frac{\Delta_x}{2}, y + \frac{\Delta_y}{2}, E, \nu\right), \end{aligned} \quad (2.58)$$

with

$$U_x^{q_y}(x, y, E, \nu) = -\frac{\nu(1+\nu)}{\pi E} \bar{\rho}, \quad (2.59)$$

$$U_y^{q_y}(x, y, E, \nu) = -\frac{1-\nu^2}{\pi E} y \ln(\bar{\rho}-x) - \frac{1+\nu}{\pi E} \ln(\bar{\rho}-y), \quad (2.60)$$

$$U_z^{q_y}(x, y, E, \nu) = \frac{(1+\nu)(1-2\nu)}{2\pi E} \left(-2y \arctan\left(\frac{\bar{\rho}-x}{y}\right) + x \ln \bar{\rho} \right). \quad (2.61)$$

2.1.4 Discretization of surface loadings

Each half-space surfaces may now be discretized in N_p rectangles uniformly loaded (See Figure 2.5). Pressure field p and shear fields q_x and q_y are constant over a rectangle and are defined by their coordinates x_i and y_j . There is N_x rectangles along the x-axis and N_y rectangles along the y-axis. Distance between each points – centers of rectangles – along the x-direction is Δ_x and distance between each points along the y-direction is Δ_y .

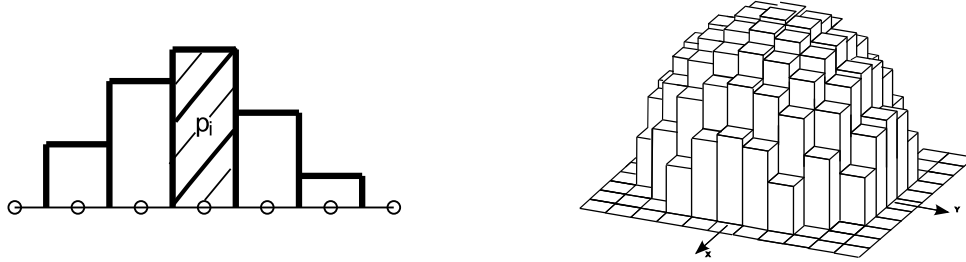


Figure 2.5: Normal load discretized in rectangles of uniform pressure

The volume is then discretized in many cubes – or parallelepipeds – and can be defined by x_i , y_j and z_k . In the same manner, stresses are considered uniform in each element. Because a 3D-FFT will be used later, the pace Δ_z along the z-direction must be constant, as well as Δ_x in the x-direction and Δ_y in the y-direction.

Stresses can be found while superimposing contributions of each element of the surface. Coefficient of influence used have been expressed in equations (2.29), (2.40) and (2.47)). Stresses in $M(x_i, y_j, z_k)$ are:

$$\begin{aligned}
 \sigma_{IJ}(x_i, y_j, z_k) = & \sum_{l=1, N_x} \sum_{m=1, N_y} p(x_l, y_m) (C_{IJ}^p(x_l - x_i, y_m - y_j, z_k, E_1, \nu_1)) \\
 & + \sum_{l=1, N_x} \sum_{m=1, N_y} q_x(x_l, y_m) (C_{IJ}^{q_x}(x_l - x_i, y_m - y_j, z_k, E_1, \nu_1)) \\
 & + \sum_{l=1, N_x} \sum_{m=1, N_y} q_y(x_l, y_m) (C_{IJ}^{q_y}(x_l - x_i, y_m - y_j, z_k, E_1, \nu_1)).
 \end{aligned} \tag{2.62}$$

In the same manner, elastic deflections are found while superimposing contributions of each element of the surface, using coefficient of influence expressed in (2.36), (2.54) and (2.58). However, elastic deflections found in the contact depend on elastic deflections of both elastic half-spaces. It must be noticed that $p = p_1 = p_2$, $q_x = q_{x1} = -q_{x2}$ and $q_y = q_{y1} = -q_{y2}$. Finally normal displacements are

$$\begin{aligned}
 \bar{u}_z(x_i, y_j) &= \sum_{l=1, N_x} \sum_{m=1, N_y} p(x_k, y_l) (K_z^P(x_l - x_i, y_m - y_j, E_1, \nu_1) + K_z^P(x_l - x_i, y_m - y_j, E_2, \nu_2)) \\
 &+ \sum_{l=1, N_x} \sum_{m=1, N_y} q_x(x_k, y_l) (K_z^{q_x}(x_l - x_i, y_m - y_j, E_1, \nu_1) - K_z^{q_x}(x_l - x_i, y_m - y_j, E_2, \nu_2)) \\
 &+ \sum_{l=1, N_x} \sum_{m=1, N_y} q_y(x_k, y_l) (K_z^{q_y}(x_l - x_i, y_m - y_j, E_1, \nu_1) - K_z^{q_y}(x_l - x_i, y_m - y_j, E_2, \nu_2)),
 \end{aligned} \tag{2.63}$$

and tangential displacement are ($J = x$ or y)

$$\begin{aligned}
 \bar{u}_J(x_i, y_j) &= \sum_{l=1, N_x} \sum_{m=1, N_y} p(x_k, y_l) (K_J^P(x_l - x_i, y_m - y_j, E_1, \nu_1) - K_J^P(x_l - x_i, y_m - y_j, E_2, \nu_2)) \\
 &+ \sum_{l=1, N_x} \sum_{m=1, N_y} q_x(x_k, y_l) (K_J^{q_x}(x_l - x_i, y_m - y_j, E_1, \nu_1) + K_J^{q_x}(x_l - x_i, y_m - y_j, E_2, \nu_2)) \\
 &+ \sum_{l=1, N_x} \sum_{m=1, N_y} q_y(x_k, y_l) (K_J^{q_y}(x_l - x_i, y_m - y_j, E_1, \nu_1) + K_J^{q_y}(x_l - x_i, y_m - y_j, E_2, \nu_2)).
 \end{aligned} \tag{2.64}$$

More typically, subscripts are used to indicate locations of the source and the image. Coefficients of influence are still tensors C and K ,

$$\sigma_{IJijk} = \sum_{N_x} \sum_{N_y} p_{lm} C_{IJijk}^p + \sum_{N_x} \sum_{N_y} q_x{}_{lm} C_{IJijk}^{q_x} + \sum_{N_x} \sum_{N_y} q_y{}_{lm} C_{IJijk}^{q_y}, \tag{2.65}$$

$$\begin{aligned}
 u_{Jij} &= \bar{u}_{Jij}^p + \bar{u}_{Jij}^{q_x} + \bar{u}_{Jij}^{q_y} \\
 &= \sum_{N_x} \sum_{N_y} p_{lm} K_{Jijlm}^p + \sum_{N_x} \sum_{N_y} q_x{}_{lm} K_{Jijlm}^{q_x} + \sum_{N_x} \sum_{N_y} q_y{}_{lm} K_{Jijlm}^{q_y}.
 \end{aligned} \tag{2.66}$$

Elastic deflections induced by a pressure field p and a shear field q_x and q_y are sufficient to solve the normal and tangential problem when bodies are elastic. Stresses below the contact are useful when non-homogeneous – inclusions and/or coatings – and/or plastic bodies are considered.

2.1.5 Normal problem

The normal problem consists in finding the unique solution of simultaneous equations and inequations defining the contact conditions. In this problem, the normal load P is known, the domain considered must be larger than the true contact area – unknown at this time – and finally, the tangential loading is not considered yet. Typically, the normal problem must determine five variables:

- contact pressure p_{ij} ;
- elastic deflections $\vec{u}_{z,ij}^p$;
- contact area Γ_c ;
- rigid body displacement δ_z ;
- gap between both bodies g_{ij} .

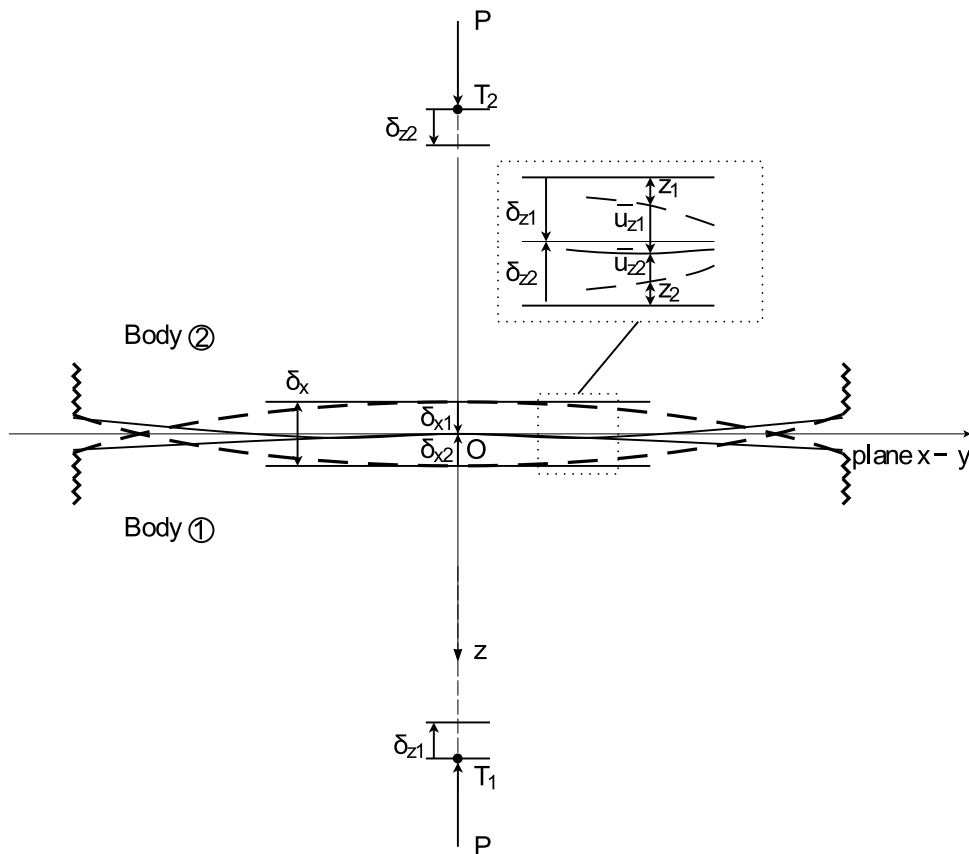


Figure 2.6: The elastic normal problem

The normal problem is presented in Figure FIG.2.6. The unique solution must verify the following equations and inequations:

- bodies do not interpenetrate

$$g_{ij} = 0 \quad (i, j) \in \Gamma_c, \quad (2.67a)$$

$$g_{ij} > 0 \quad (i, j) \notin \Gamma_c, \quad (2.67b)$$

where g_{ij} is the gap between both bodies

$$g_{ij} = \bar{u}_{zij}^p + h_{ij} - \delta_z; \quad (2.68)$$

- pressure are higher or equal to zero

$$p_{ij} > 0 \quad (i, j) \in \Gamma_c, \quad (2.69a)$$

$$p_{ij} = 0 \quad (i, j) \notin \Gamma_c; \quad (2.69b)$$

- this problem will be based on the normal loading conservation

$$\sum_{(i,j) \in \Gamma_p} p_{ij} S = P. \quad (2.70)$$

The problem is solved on a grid $N_p = N_x \times N_y$. If N_c points are into the contact area Γ_c , then the pressure must be equal to zero for $N_p - N_c$ elements. This problem has $3N_p + 1$ equations as seen in TAB.2.1 and can be solved.

Variables	N_{inc}	Equations	N_{eq}
p_{ij}	N_p	(2.69b)	$N_p - N_c$
		(2.67a)	N_c
g_{ij}	N_p	(2.68)	N_p
\bar{u}_{zij}^p	N_p	(2.66)	N_p
δ_z	1	(2.1.5)	1
Variables	$3N_p+1$	Equations	$3N_p+1$

Table 2.1: Variables of the normal problem

However, the contact area Γ_c is not known initially, and must be determined. It must be noticed that normal load P can be replaced by a rigid body displacement δ_z , the normal load is then unknown, but the contact problem remain complete because one variable has been replaced by another one. Rigid body displacement can be imposed in the shot peening algorithm developed by T.Chaise, or during tribological experiments.

When bending moments M_x and M_y are taken into account – the center of pressure is no longer in $O(0,0)$ – two additional variables must be considered.

$$M_x = \sum_{N_x} \sum_{N_y} p_{ij} y_j S, \quad (2.71a)$$

$$M_y = - \sum_{N_x} \sum_{N_y} p_{ij} x_i S. \quad (2.71b)$$

Two angles $\phi_x = \phi_{x1} + \phi_{x2}$ and $\phi_y = \phi_{y1} + \phi_{y2}$ are then introduced and correspond to the misalignments. The equation 2.68 becomes

$$g_{ij} = \bar{u}_{z ij}^p + h_{ij} - \phi_{xy} + \phi_{yx} - \delta_z = 0 (i, j) \in \Gamma_c, \quad (2.72a)$$

$$g_{ij} = \bar{u}_{z ij}^p + h_{ij} - \phi_{xy} + \phi_{yx} - \delta_z > 0 (i, j) \notin \Gamma_c. \quad (2.72b)$$

When the tangential problem is no longer neglected, the tangential problem may have an influence on the normal problem – i.e. two materials of different material properties pressed together – and equation 2.68 becomes

$$g_{ij} = \bar{u}_{z ij}^p + h_{ij} - \phi_{xy} + \phi_{yx} - \delta_z + \bar{u}_{z ij}^{qx} + \bar{u}_{z ij}^{qy} \quad (2.73)$$

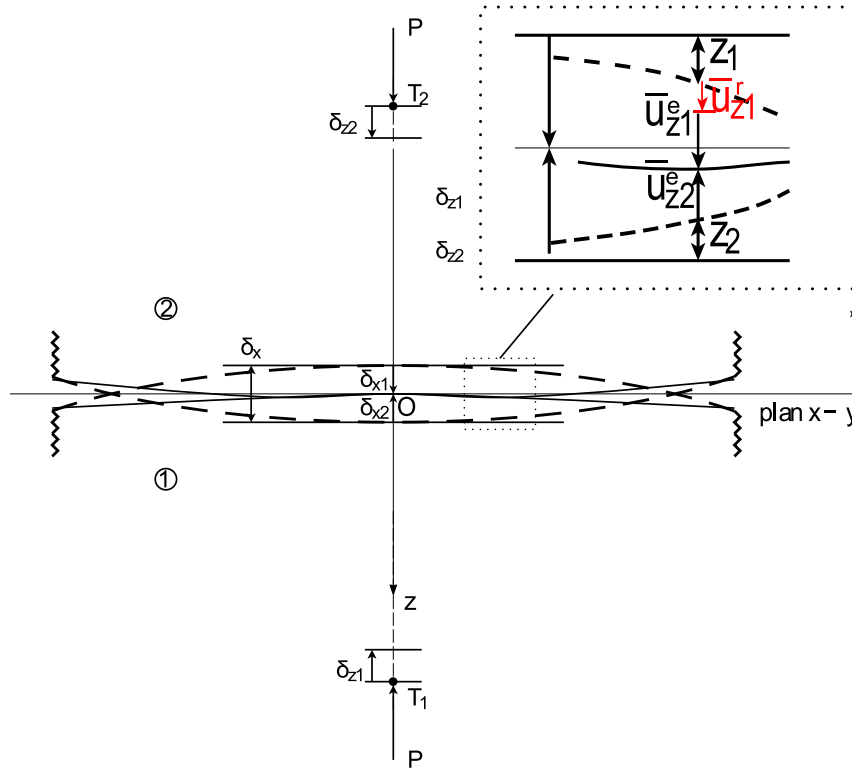


Figure 2.7: Residual displacements used in the normal problem

When plastic behaviors are considered, normal residual displacements of a surface point due to cuboids of uniform plastic strain should be carefully considered. The normal displacements were given in an integral form by Chiu [CHI 78], analytically integrated in [JAC 02]. They were also given in term of Galerkin vectors in [LIU 05a]. The knowledge of residual normal displacements is sufficient for frictionless contact problems, as seen in Figure 2.7. Finally, equation 2.68 becomes

$$g_{ij} = \bar{u}_{zij}^p + h_{ij} - \phi_{xy} + \phi_{yx} - \delta_z + \bar{u}_{zij}^{qx} + \bar{u}_{zij}^{qy} + \bar{u}_{zij}^r \quad (2.74)$$

More globally, misfit displacements \bar{u}_{zij}^m will be considered in non-homogeneous cases and can be compared to the residual displacement \bar{u}_{zij}^r . \bar{u}_{zij}^r and \bar{u}_{zij}^m will be expressed later.

2.1.6 Tangential problem

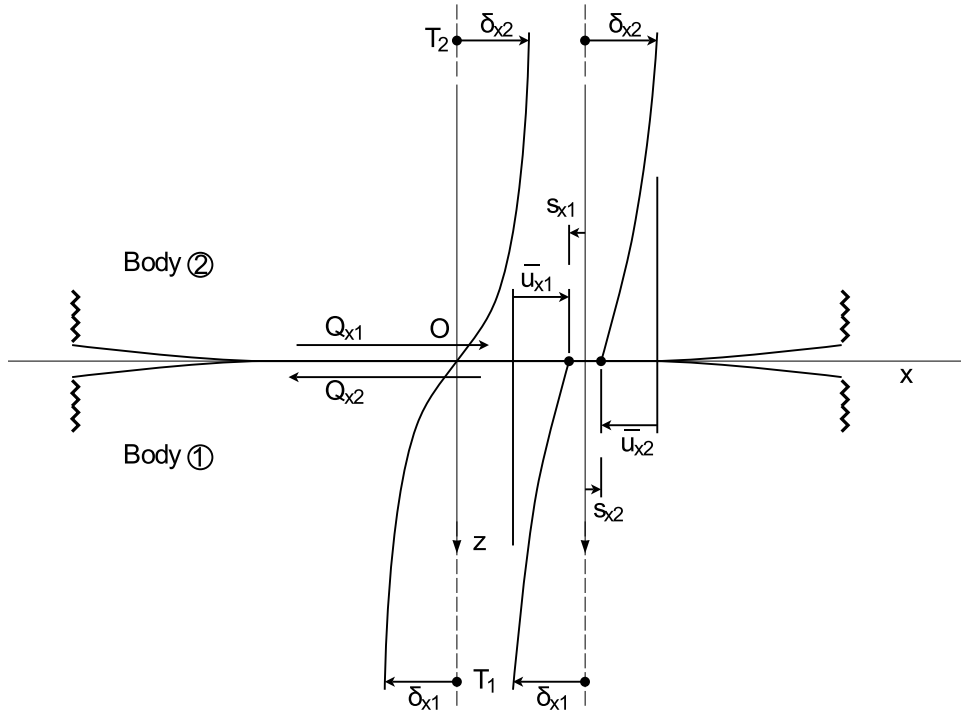


Figure 2.8: The elastic tangential problem

When tangential displacements \bar{u}_τ are not equal to zero – one or both components \bar{u}_x and \bar{u}_y are not equal to zero – the tangential problem must be solved. Tangential displacements are not equal to zero under tangential loadings, for instance. When bodies have dissimilar properties – dissimilar elastic, elastic-plastic and/or non-homogeneous properties – the influence coefficients K_x^p and K_y^p are not equal to zero, and a normal loading will induce some tangential displacements. The normal and tangential problem

are then coupled (2.1.7).

The tangential problem is very similar to the normal problem, and consists in finding the unique solution of simultaneous equations and inequations defining the stick-slip conditions. The tangential load Q_x and Q_y is known and the domain Γ_c considered is known thanks to the normal problem algorithm.

Variables of the tangential problem are then:

- shear fields q_{xij} and q_{yij} ;
- relative elastic displacements $\bar{u}_{xij}^{q_x}$ et $\bar{u}_{yij}^{q_y}$;
- the slipping area Γ_{sl} ;
- the sticking area Γ_{st} so that $\Gamma_c \equiv \Gamma_{sl} \cup \Gamma_{st}$;
- tangential rigid body displacements δ_x and δ_y ;
- slipping amplitudes and directions \mathbf{s} (components s_x and s_y)

The tangential problem is presented in FIG.2.8. Slips are still defined between time step t and t' according to the equation (2.6). The unique solution must verify the following equations and inequations:

- slips in the slipping and sticking area,

$$\bar{\mathbf{u}}_{\tau ij}^{\tau t} + \bar{\mathbf{u}}_{\tau ij}^{p t} - \bar{\mathbf{u}}_{\tau ij}^{\tau t'} - \bar{\mathbf{u}}_{\tau ij}^{p t'} - \Delta \delta_{\tau}^t = \mathbf{s}_{ij}^t = 0 \quad (i, j) \in \Gamma_{st}, \quad (2.75a)$$

$$\bar{\mathbf{u}}_{\tau ij}^t - \bar{\mathbf{u}}_{\tau ij}^{t'} - \Delta \delta_{\tau}^t = \mathbf{s}_{ij}^t \neq 0 \quad (i, j) \in \Gamma_{sl}; \quad (2.75b)$$

- The Coulomb's law of friction is respected,

$$\|\mathbf{q}_{ij}^t\| < \mu p_{ij}^t \quad (i, j) \in \Gamma_{st}, \quad (2.76a)$$

$$\mathbf{q}_{ij} = -\mu p_{ij}^t \frac{\mathbf{s}_{ij}^t}{\|\mathbf{s}_{ij}^t\|} \quad (i, j) \in \Gamma_{sl}; \quad (2.76b)$$

- this problem will be based on the tangential loading conservation

$$\sum_{(i,j) \in \Gamma_p} \mathbf{q}_{ij}^t S = \mathbf{Q}^t. \quad (2.77)$$

Variables	N_{inc}	Equations	N_{eq}
\mathbf{q}_{ij}^t	$2N_c$	(2.76b)	$2N_{sl}$
		(3.27a)	$2N_{st}$
$\bar{\mathbf{u}}_{\tau ij}^t$	$2N_c$	(2.66)	$2N_c$
\mathbf{s}_{ij}^t	$2N_{sl}$	(3.27b)	$2N_{sl}$
δ_{τ}^t	2	(2.1.6)	2
Variables	$4N_c+2N_{sl}+2$	Equations	$4N_c+2N_{sl}+2$

Table 2.2: Variables of the tangential problem

The problem is solved over the N_c points of the contact area, but the number of points in the slipping area N_{sl} and the number of points in the sticking area N_{st} remains unknown at this time. However, this problem has $4N_c + 2N_{sl} + 2$ variables and can be solved as shown in TAB.2.2.

When twisting moment M_z is taken into account an additional variable must be considered (2.12)

$$M_z = \sum_{N_x} \sum_{N_y} (q_{y ij} x_i - q_{x ij} y_j) S. \quad (2.78)$$

The angle ϕ_z is then introduced and corresponds to twisting angle, which is typically creating circumferential slips. The equation (3.27a) and (3.27b) become:

$$\bar{\mathbf{u}}_{\tau ij}^{\tau t} + \bar{\mathbf{u}}_{\tau ij}^{p t} - \Delta \delta_{\tau}^t - \begin{pmatrix} -y \cdot \Delta \phi_z^t \\ +x \cdot \Delta \phi_z^t \end{pmatrix} = \Delta \mathbf{s}_{ij}^t = 0 \quad (i, j) \in \Gamma_{st}, \quad (2.79a)$$

$$\bar{\mathbf{u}}_{\tau ij}^{\tau t} + \bar{\mathbf{u}}_{\tau ij}^{p t} - \Delta \delta_{\tau}^t - \begin{pmatrix} -y \cdot \Delta \phi_z^t \\ +x \cdot \Delta \phi_z^t \end{pmatrix} = \Delta \mathbf{s}_{ij}^t \neq 0 \quad (i, j) \in \Gamma_{sl}. \quad (2.79b)$$

When plast behaviors are considered, tangential residual displacements of a surface point due to cuboids of uniform plastic strain should be carefully considered. The tangential displacements were given in an integral form by Chiu [CHI 78] but analytical forms are not available. A part of this work was about expressing those tangential residual displacement analytically. The knowledge of residual normal displacements is sufficient as seen in Figure 2.9. Finally equations 3.27a and 3.27b become

$$\Delta \bar{\mathbf{u}}_{\tau ij}^{\tau t} + \Delta \bar{\mathbf{u}}^{p t} + \Delta \bar{\mathbf{u}}^{r t} - \Delta \delta_{\tau}^t - \begin{pmatrix} -y \cdot \Delta \phi_z^t \\ +x \cdot \Delta \phi_z^t \end{pmatrix} = \Delta \mathbf{s}_{ij}^t = 0 \quad (i, j) \in \Gamma_{st}, \quad (2.80a)$$

$$\Delta \bar{\mathbf{u}}_{\tau ij}^{\tau t} + \Delta \bar{\mathbf{u}}^{p t} + \Delta \bar{\mathbf{u}}^{r t} - \Delta \delta_{\tau}^t - \begin{pmatrix} -y \cdot \Delta \phi_z^t \\ +x \cdot \Delta \phi_z^t \end{pmatrix} = \Delta \mathbf{s}_{ij}^t \neq 0 \quad (i, j) \in \Gamma_{sl}. \quad (2.80b)$$

More globally, misfit displacements $\Delta \bar{\mathbf{u}}^{m t}$ will be considered in non-homogeneous cases and can be compared to the residual displacement $\Delta \bar{\mathbf{u}}^{r t}$. $\Delta \bar{\mathbf{u}}^{r t}$ and $\Delta \bar{\mathbf{u}}^{m t}$ will be expressed later.

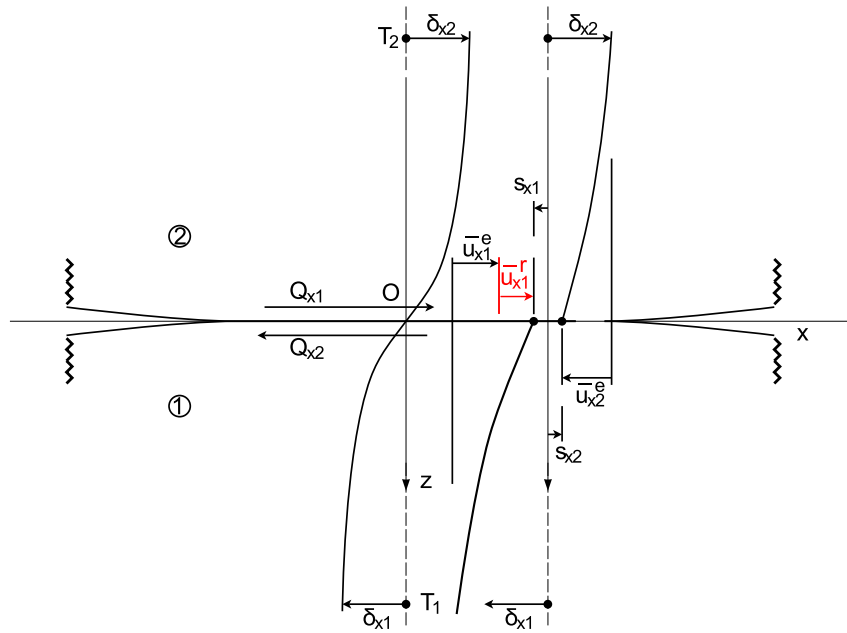


Figure 2.9: Residual displacements used in the tangential problem

2.1.7 Coupling between the normal and tangential problem

Note It is noteworthy that contact pressure is assumed to be parallel everywhere, thus the present model may have difficulty simulating the contact of bodies with large slopes, such as sharp conical tips. The contact problems studied in this work will comply above assumptions since they are spherical contacts. But many geometries (pin, ellipsoidal,...) can be used by the present model without any difficulty.

An iterative approach is used to solve the contact problem, normal and tangential problems are solved one after the other. (i) The normal problem is solved assuming no shear tractions, the contact area Γ_c and the pressure field p_{ij} are found. (ii) The tangential problem is solved considering the pressure field p_{ij} . Shears \mathbf{q}_{ij} , slips \mathbf{s}_{ij} and sticking area Γ_{st} are found. (iii) If shears are not equal to zero, the normal problem must be solved considering the pressure field \mathbf{q}_{ij} . This loop must be repeated until the contact problem converged, this process was first used by Panagiotopoulos in [PAN 75].

This process is required since coefficients of influence expressed in section 2.1.3 prove that normal and tangential problems are cross linked. To recap:

$$\begin{aligned} u_{Jij}^- &= \bar{u}_{Jij}^p + \bar{u}_{Jij}^{qx} + \bar{u}_{Jij}^{qy} \\ &= \sum_{N_x} \sum_{N_y} p_{lm} K_{Jijlm}^p + \sum_{N_x} \sum_{N_y} q_{xlm} K_{Jijlm}^{qx} + \sum_{N_x} \sum_{N_y} q_{ylm} K_{Jijlm}^{qy} \end{aligned} \quad (2.81)$$

The problem is 'fully coupled' (coupling level: 2) and solutions found are physically consistent. For instance, the second mode of fretting (spherical indentation) typically requires a fully coupled analysis since normal tractions induce radial shears. Analytical solutions are found in [SPE 75] but must be discussed in 2.4.2.

$$\begin{aligned}
 \bar{u}_{xij} &= \bar{u}_{xij}^p + \bar{u}_{xij}^{qx} + \bar{u}_{xij}^{qy} \\
 \bar{u}_{yij} &= \bar{u}_{yij}^p + \bar{u}_{yij}^{qx} + \bar{u}_{yij}^{qy} \\
 \bar{u}_{zij} &= \bar{u}_{zij}^p + \bar{u}_{zij}^{qx} + \bar{u}_{zij}^{qy}
 \end{aligned}
 \tag{2.82}$$

Initial code experienced many convergence issues which have been discussed in Section 2.3.3. In order to reduce both the computing time and the convergence issues when a fully coupled analysis is not required, L.Gallego defined a 'partially coupled' or 'uncoupled' problem.

The problem is 'partially coupled' (coupling level: 1) when normal and tangential problems are no longer coupled, but solutions in one tangential direction still depend on the other. For instance, the third mode of fretting (sphere twisted over a flat) may be simplified using a partially coupled analysis. Normal tractions will have no influence on tangential shears, which are then circumferential. This assumption is very common and analytical results are expressed in [JOH 85] and [DIN 05]. The Panagiotopoulos process is not used, reducing the computing time.

$$\begin{aligned}
 \bar{u}_{xij} &= \bar{u}_{xij}^{qx} + \bar{u}_{xij}^{qy} \\
 \bar{u}_{yij} &= \bar{u}_{yij}^{qx} + \bar{u}_{yij}^{qy} \\
 \bar{u}_{zij} &= \bar{u}_{zij}^p
 \end{aligned}
 \tag{2.83}$$

The problem is 'uncoupled' (coupling level: 0) when all problems are uncoupled. Solutions in each direction (x,y or z) do not depend on the solution in another direction. For instance, the first mode of fretting (sphere moved in the x-direction) may be simplified considering that shears along the x-direction only depend on the tangential force/displacement along the x-direction. This assumption is very common and found in the Cattaneo-Mindlin [CAT 38] [MIN 49] Concept [JOH 85]. The Panagiotopoulos process is not used and the slipping direction is known initially, greatly reducing the computing time.

$$\begin{aligned}
 \bar{u}_{xij} &= \bar{u}_{xij}^{qx} \\
 \bar{u}_{yij} &= \bar{u}_{yij}^{qy} \\
 \bar{u}_{zij} &= \bar{u}_{zij}^p
 \end{aligned}
 \tag{2.84}$$

An efficient technique has been introduced in the contact algorithm in Section 2.3.3 so the numerical burden has been reduced for 'fully coupled' approaches. But many analytical solutions neglect the normal/tangential coupling, and lower coupling levels are still required to validate this code.

2.2 The elastic-plastic half-space

For soft metallic materials, metals at high temperature, rough surfaces or dry contacts with high friction coefficient the yield stress within the material could be easily exceeded even at low normal load. The plastic behavior has to be considered in further analysis.

The elastic-plastic algorithm is first presented, the plasticity model is described and elementary solutions are then detailed. The effect of a cuboid of uniform plastic strain in a half-space on residual stresses, normal and tangential displacements are exposed and validations are made using a Finite Element (FE) model. Solutions for tangential displacements were not available until now. It is found that the influence coefficients for tangential displacements are of the same order of magnitude as the ones describing the normal displacement. This result is of great importance for frictional contact problems when coupling the normal and tangential problem in the elastic-plastic regime, such as stick-slip problems, and also for metals and alloys with low or moderate yield stress.

2.2.1 Elastic-plastic algorithm

The algorithm developed to solve the incremental elastic-plastic contact with friction problem is presented in Figure 2.11. This algorithm is similar to the one proposed by Jacq et al. [JAC 02]. But the normal contact is now coupled to the tangential contact and solved using the CG [POL 99] and DC-FFT [LIU 00] methods as proposed by L.Gallego et al. [GAL 06].

- The 'initial state' defined by L.Gallego may now include residual displacements, so the geometry used to solve the contact problem is modified to account for the permanent deformation of the surface due to plastic strains, as described in Figure 2.7 and 2.9.
- The stress field is computed considering the contribution of the residual strains, the contact pressure and shears distributions.
- The plasticity model is then used to calculate the plastic strain increment using a return mapping algorithm [FOT 96], enabling the calculation of the residual stresses using a new 3D-FFT method.
- The residual displacements are then calculated in all directions [JAC 02] [FUL 10] using a 2D-FFT algorithm.
- The residual displacements are then compared to the ones found during the previous step. Until the residual displacements increments converge, the initial state will be updated using residual stresses, tangential and normal residual displacements.
- If residual displacements converged, plastic strains, normal and tangential residual displacements, pressure, shears and slips and hardening parameters are then increased by their increment to define a new initial condition for the next loading step.

Note It is of a great importance to remind that current shears, slips and plastic strains will be expressly used in the following loading steps, making the code fully coupled and also sensitive to the loading path and contact history, making this work different from others.

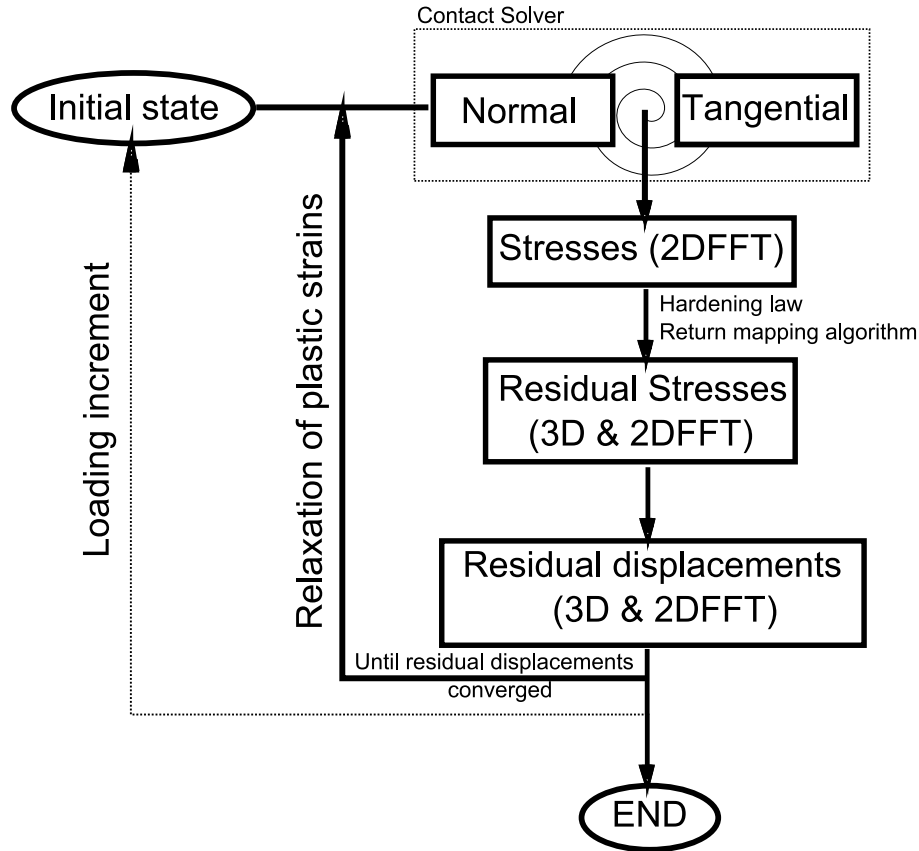


Figure 2.10: Flow chart of the actual fully coupled elastic-plastic contact code

2.2.2 Plasticity model

Plasticity is an irreversible phenomenon that requires an incremental description. In a general incremental formulation of plasticity, a plastic strain increment depends upon the stress, the stress increment and upon the hardening parameters:

$$\delta\epsilon^P = f(\sigma, \delta\sigma, \text{Hardening parameters}) \quad (2.85)$$

Tresca and Von Mises criteria are very close to each other and both give a correct representation of the yield surface. For numerical reasons, a simple model of isotropic hardening based on a Von Mises criterion is used. The model chosen is that of Prandtl-Reuss. The hardening law can be described by a Swift's law, a bilinear law or interpolated.

2.2.3 Residual stress calculation

Plastic strains are related to stresses. Therefore, the stress field must be evaluated from elastic-plastic contact conditions. Considering the reciprocal theorem applied to a half-space, the stress at every point can be divided in four parts:

$$\sigma = \sigma^p + \sigma^{qx} + \sigma^{qy} + \sigma^r \quad (2.86)$$

The first three terms are related to the contact pressure and shear. The third one was currently neglected [ANT 04] because the tangential problem was not solved and only fully-sliding contacts in one direction were considered. But in this study σ^{qy} is also taken into account in order to deal with fully-coupled problems. The influence coefficients that give the stresses induced by a rectangular cell on the boundary surface of a half-space submitted to a uniform pressure or shear can be found for example in [VER 85].

$$\sigma_{ij}^p(A) = \sum C_{ij}^p(A, C) \cdot p(C) \quad (2.87)$$

$$\sigma_{ij}^t(A) = \sum C_{ij}^t(A, C) \cdot p(C) \quad (2.88)$$

The fourth term is related to plastic strains, and can be calculated following the method proposed by Chiu [CHI 77] [CHI 78], considering a cuboidal zone with uniform initial strains or eigenstrains and surrounded by an infinite elastic half-space [CHI 78].

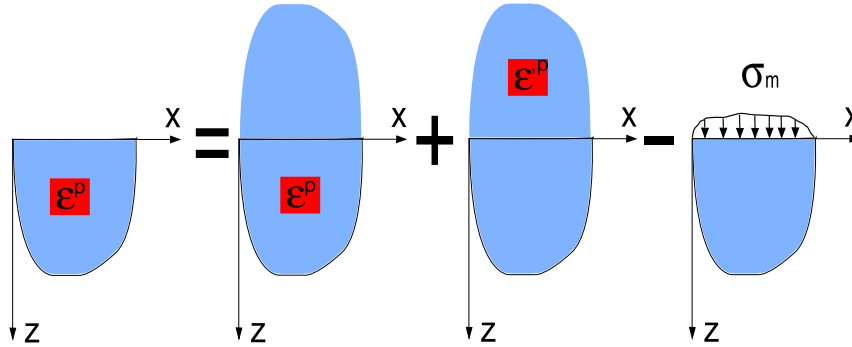


Figure 2.11: A problem considering a cuboidal zone in which plastic strains are uniform in a half-space can be decomposed in three elementary problems

The solution is calculated from the superimposition of three solutions which leads to:

$$\sigma_{ij}^r(M) = \sum A_{ijkl}(M, C) \cdot \epsilon_{kl}^p(C) \quad (2.89)$$

An infinite space is considered. Consider a point $M(\vec{\xi}_1^m, \vec{\xi}_2^m, \vec{\xi}_3^m)$ and a mark $(C, \xi_1^m, \xi_2^m, \xi_3^m)$, bound to the center of the cuboid of size $2\Delta x_1 \cdot 2\Delta x_2 \cdot 2\Delta x_3$. The coordinates of the vectors linking the corners of the element to this point are noted $\vec{C}_m = (\xi_1^m, \xi_2^m, \xi_3^m)$

$$\vec{C}_1 = (\xi_1^m - \Delta x_1, \xi_2^m - \Delta x_2, \xi_3^m - \Delta x_3) \quad (2.90a)$$

$$\vec{C}_2 = (\xi_1^m + \Delta x_1, \xi_2^m - \Delta x_2, \xi_3^m - \Delta x_3) \quad (2.90b)$$

$$\vec{C}_3 = (\xi_1^m + \Delta x_1, \xi_2^m + \Delta x_2, \xi_3^m - \Delta x_3) \quad (2.90c)$$

$$\vec{C}_4 = (\xi_1^m - \Delta x_1, \xi_2^m + \Delta x_2, \xi_3^m - \Delta x_3) \quad (2.90d)$$

$$\vec{C}_5 = (\xi_1^m - \Delta x_1, \xi_2^m + \Delta x_2, \xi_3^m + \Delta x_3) \quad (2.90e)$$

$$\vec{C}_6 = (\xi_1^m - \Delta x_1, \xi_2^m - \Delta x_2, \xi_3^m + \Delta x_3) \quad (2.90f)$$

$$\vec{C}_7 = (\xi_1^m + \Delta x_1, \xi_2^m - \Delta x_2, \xi_3^m + \Delta x_3) \quad (2.90g)$$

$$\vec{C}_8 = (\xi_1^m + \Delta x_1, \xi_2^m + \Delta x_2, \xi_3^m + \Delta x_3) \quad (2.90h)$$

Elastic strains at point M generated by a cuboid of constant and unity plastic strain ε_{11}^p are given by:

$$\varepsilon_{1111} = \frac{1}{8\pi^3} \sum_{m=1}^8 \left[D_{,1111}^m + \frac{2-\nu}{1-\nu} \cdot (D_{,1122}^m + D_{,1133}^m) \right] - H(M) \quad (2.91a)$$

$$\varepsilon_{2211} = -\frac{1}{8\pi^3} \sum_{m=1}^8 \left[-D_{,1122}^m + \frac{\nu}{1-\nu} \cdot (D_{,2222}^m + D_{,2233}^m) \right] \quad (2.91b)$$

$$\varepsilon_{3311} = -\frac{1}{8\pi^3} \sum_{m=1}^8 \left[-D_{,1133}^m + \frac{\nu}{1-\nu} \cdot (D_{,2233}^m + D_{,3333}^m) \right] \quad (2.91c)$$

$$\varepsilon_{1211} = \frac{1}{8\pi^3} \sum_{m=1}^8 \left[\frac{\nu}{1-\nu} D_{,1112}^m + \frac{1+\nu}{1-\nu} \cdot (D_{,2221}^m + D_{,3312}^m) \right] \quad (2.91d)$$

$$\varepsilon_{1311} = \frac{1}{8\pi^3} \sum_{m=1}^8 \left[\frac{\nu}{1-\nu} D_{,1113}^m + \frac{1+\nu}{1-\nu} \cdot (D_{,3331}^m + D_{,2213}^m) \right] \quad (2.91e)$$

$$\varepsilon_{2311} = \frac{1}{8\pi^3} \sum_{m=1}^8 \left[\frac{\nu}{1-\nu} (D_{,2223}^m + D_{,3332}^m) \right] \quad (2.91f)$$

In the presence of unity shear strain ($\varepsilon_{12}^p + \varepsilon_{21}^p$) = 2, elastic deformations at point M are given by:

$$\varepsilon_{1112} = \frac{1}{8\pi^3} \cdot \sum_{m=1}^8 \left[\frac{-2\nu}{1-\nu} D_{,1112}^m + 2(D_{,2221}^m + D_{,3312}^m) \right] \quad (2.92a)$$

$$\varepsilon_{2212} = \frac{1}{8\pi^3} \cdot \sum_{m=1}^8 \left[\frac{-2\nu}{1-\nu} D_{,1222}^m + 2(D_{,1112}^m + D_{,3312}^m) \right] \quad (2.92b)$$

$$\varepsilon_{3312} = \frac{1}{8\pi^3} \cdot \sum_{m=1}^8 \left[\frac{-2\nu}{1-\nu} D_{,3312}^m \right] \quad (2.92c)$$

$$\varepsilon_{1212} = \frac{1}{8\pi^3} \cdot \sum_{m=1}^8 \left[\frac{-2\nu}{1-\nu} D_{,1122}^m + D_{,1111}^m + D_{,2222}^m + D_{,1133}^m + D_{,2233}^m \right] - H(M) \quad (2.92d)$$

$$\varepsilon_{1312} = \frac{1}{8\pi^3} \cdot \sum_{m=1}^8 \left[-\frac{1+\nu}{1-\nu} D_{,1123}^m + D_{,2223}^m + D_{,3332}^m \right] \quad (2.92e)$$

$$\varepsilon_{2312} = \frac{1}{8\pi^3} \cdot \sum_{m=1}^8 \left[-\frac{1+\nu}{1-\nu} D_{,2213}^m + D_{,1113}^m + D_{,3331}^m \right] \quad (2.92f)$$

with $H(M)=1$ if M is inside the cuboid and $H(M)=0$ otherwise.

The functions D are defined by:

$$D_{,1111}^m = 2\pi^2 \left[\arctan \left[\frac{(\gamma_2^m)(\gamma_3^m)}{(\gamma_1^m)R} \right] - \frac{(\gamma_1^m)(\gamma_2^m)(\gamma_3^m)}{2R} \left(\frac{1}{(\gamma_1^m)^2 + (\gamma_2^m)^2} + \frac{1}{(\gamma_1^m)^2 + (\gamma_3^m)^2} \right) \right] \quad (2.93a)$$

$$D_{,1112}^m = -\pi^2 \left[\text{sign}(\gamma_3^m) \cdot \ln \left(\frac{R + |\gamma_3^m|}{\sqrt{(\gamma_1^m)^2 + (\gamma_2^m)^2}} \right) - \frac{(\gamma_1^m)^2 \gamma_3^m}{((\gamma_1^m)^2 + (\gamma_2^m)^2)R} \right] \quad (2.93b)$$

$$D_{,1122}^m = \frac{\pi^2 (\gamma_1^m)(\gamma_2^m)(\gamma_3^m)}{R((\gamma_1^m)^2 + (\gamma_2^m)^2)} \quad (2.93c)$$

$$D_{,1123}^m = -\frac{\pi^2 \gamma_1^m}{R} \quad (2.93d)$$

with $R = \sqrt{(\gamma_1^m)^2 + (\gamma_2^m)^2 + (\gamma_3^m)^2}$

The rest of derivatives are obtained by circular permutation of the subscripts. From Hooke's law, it is then possible to find out stresses and to determine the components of the tensor A for every point M . Solutions expressed hereinbefore are related to an infinite space. However, numerical techniques used in this work – such as the 3D-FFT (See Section 2.3.6) – will superimpose the three solutions in order to emulate a half-space. This technique will be detailed later and is used when considering plastic cuboids, spherical and cubical non-homogeneities, using various coefficients of influence.

Note Solutions expressed directly in a half-space are much more complicated and can be found in [JAC 02]. The 2D-FFT algorithm required when using those solutions was numerically demanding and is no longer used (See Section 2.3.5), except in Section 2.3.7 where advantages are discussed, and in some frictional applications of elastic-plastic contacts (See Section 2.4).

2.2.4 Maxwell-Betti's reciprocal theorem

Let's consider two independent loads applied to an elastic body of volume Ω and of boundary Γ . The first state $(u, \varepsilon, \sigma, f_i)$ exists with initial strains ε^∞ . The second state is undefined for the moment and will be noted $(u^*, \varepsilon^*, \sigma^*, f_i^*)$. The reciprocal theorem, also known as Maxwell-Betti's theorem, expresses an equilibrium of works between both states. It has been shown that the theorem with initial strains can be written as [Jac 02]:

$$-\int_{\Gamma} u_i^* \cdot \sigma_{ij} \cdot n_j \cdot d\Gamma + \int_{\Omega} f_i \cdot u_i^* \cdot d\Omega = -\int_{\Gamma} u_i \cdot \sigma_{ij}^* \cdot n_j \cdot d\Gamma + \int_{\Omega} f_i^* \cdot u_i \cdot d\Omega - \int_{\Gamma} \varepsilon_{ij}^0 \cdot \sigma_{ij}^* \cdot d\Gamma \quad (2.94)$$

The reciprocal theorem is now applied to both bodies in contact, where each of them is considered as a half-space Ω whose boundary Γ is loaded on a part $\Gamma_c(A)$, and initial strains occupy a volume $\Omega_p(C)$. Body forces are neglected in both states ($f^*=0$ and $f=0$), and it will be considered that $Tr(\varepsilon^p) = 0$ which is a classical assumption in plasticity. Since $\sigma_{ij} \cdot n_j = -p_i$, then (2.94) becomes:

$$\int_{\Gamma_c} u_i^* \cdot p_i \cdot d\Gamma = \int_{\Gamma} u_i \cdot p_i^* \cdot d\Gamma - 2 \cdot \mu \cdot \int_{\Omega_p} \varepsilon_{ij}^p \cdot \varepsilon_{ij}^* \cdot d\Omega \quad (2.95)$$

Plastic strains ε^∞ and pressure distribution p of the real state are known. So, the unknown displacement U can be expressed by:

$$U_i(A) = \int_{\Gamma_c} u_i^*(M, p^*(A)) \cdot p_i(M) \cdot d\Gamma + 2 \cdot \mu \cdot \int_{\Omega_p} \varepsilon_{ij}^p(M) \cdot \varepsilon_{ij}^*(M, p_i^*(A)) \cdot d\Omega \quad (2.96)$$

with M a point of the surface or volume integration. The first part of (2.96) is known as Love and Cerruti's term.

The surface displacement of each body can then be expressed as a function of contact loads and of plastic strains existing in the considered body. The authors will now consider only one body in contact with an elastic-plastic behavior, the other one being purely elastic. The formulation could be extended to the case of two elastic-plastic bodies without major difficulties. It is then necessary to express the virtual strains as a function of the virtual contact loads. Note that in what follows both (x_1, x_2, x_3) and (x, y, z) will be used indifferently as coordinate system. The method and the analytical functions F_{3ij} that describe the normal displacement of a surface point due to a cuboid of uniform plastic strain are recalled to gather all important analytical solutions. The next section focuses on the tangential displacement of a surface point due to a cuboid of uniform plastic strain.

2.2.5 Normal residual displacements [JAC 01]

Let's consider a virtual state corresponding to the application of a unit force along the x-axis applied on the elementary surface area centered at point A.

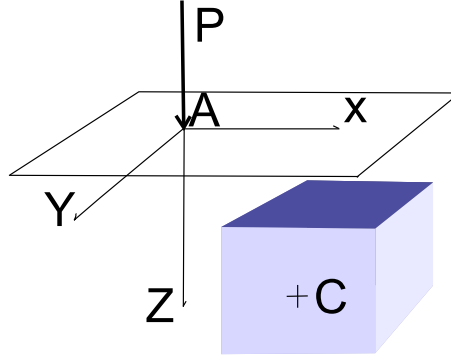


Figure 2.12: Cuboid of uniform plastic strain

The displacements generated are expressed by Boussinesq, see Johnson [JOH 85].

$$U_x^* = \frac{P}{4.\pi.G} \cdot \left[\frac{x.z}{R^3} - (1 - 2.\nu) \cdot \frac{x}{R.(R+z)} \right] \quad (2.97)$$

$$U_y^* = \frac{P}{4.\pi.G} \cdot \left[\frac{y.z}{R^3} - (1 - 2.\nu) \cdot \frac{y}{R.(R+z)} \right] \quad (2.98)$$

$$U_z^* = \frac{P}{4.\pi.G} \cdot \left[\frac{z^2}{R^3} + \frac{2.(1 - \nu)}{R} \right] \quad (2.99)$$

The reciprocal theorem is used to express the surface displacements as a function of contact forces and plastic strains within the body under the assumption that the plastic volume is incompressible, i.e. $Tr(\epsilon^p) = 0$:

$$U_3^r(A) = 2.\mu. \sum_{n=1}^N \epsilon_{ij}^p(C_n) \cdot \int_{\Omega_p} \epsilon_{3ij}^*(A, M) d\Omega = \sum_{n=1}^N \epsilon_{ij}^p \cdot D_{3ij}(A, C_n) \quad (2.100)$$

Consequently the residual displacements are functions of plastic strain ϵ_{ij}^p , Poisson's ratio ν , and location $(c1, c2, c3)$ and size of the cuboid of uniform plastic strain $(2\Delta x, 2\Delta y, 2\Delta z)$:

$$\begin{aligned} D_{3ij} = & F_{3ij}(c1 + \Delta x, c2 + \Delta y, c3 + \Delta z) - F_{3ij}(c1 + \Delta x, c2 + \Delta y, c3 - \Delta z) \\ & - F_{3ij}(c1 + \Delta x, c2 - \Delta y, c3 + \Delta z) - F_{3ij}(c1 - \Delta x, c2 + \Delta y, c3 + \Delta z) \\ & + F_{3ij}(c1 + \Delta x, c2 - \Delta y, c3 - \Delta z) + F_{3ij}(c1 - \Delta x, c2 - \Delta y, c3 + \Delta z) \\ & + F_{3ij}(c1 - \Delta x, c2 + \Delta y, c3 - \Delta z) - F_{3ij}(c1 - \Delta x, c2 - \Delta y, c3 - \Delta z) \end{aligned} \quad (2.101)$$

The D_{3ij} functions may be derived from previous equations in an integral form:

$$D_{311} = \frac{1}{2\pi} \cdot \iint \left[\frac{x \cdot z}{\rho^3} - (1 - 2\nu) \cdot \frac{x}{\rho \cdot (\rho + z)} \right] dydz \quad (2.102)$$

$$D_{322} = \frac{1}{2\pi} \cdot \iint \left[\frac{y \cdot z}{\rho^3} - (1 - 2\nu) \cdot \frac{y}{\rho \cdot (\rho + z)} \right] dx dz \quad (2.103)$$

$$D_{333} = \frac{1}{2\pi} \cdot \iint \left[\frac{z^2}{\rho^3} + \frac{2 \cdot (1 - \nu)}{\rho} \right] \quad (2.104)$$

$$D_{312} = \frac{1}{4\pi} \cdot \left[\iint \left[\frac{x \cdot z}{\rho^3} - (1 - 2\nu) \cdot \frac{x}{\rho \cdot (\rho + z)} \right] dx dz + \iint \left[\frac{z^2}{\rho^3} + \frac{2 \cdot (1 - \nu)}{\rho} \right] dy dz \right] \quad (2.105)$$

$$D_{313} = \frac{1}{4\pi} \cdot \left[\iint \left[\frac{x \cdot z}{\rho^3} - (1 - 2\nu) \cdot \frac{x}{\rho \cdot (\rho + z)} \right] dx dy + \iint \left[\frac{y \cdot z}{\rho^3} - (1 - 2\nu) \cdot \frac{y}{\rho \cdot (\rho + z)} \right] dy dz \right] \quad (2.106)$$

$$D_{323} = \frac{1}{4\pi} \cdot \left[\iint \left[\frac{z^2}{\rho^3} + \frac{2 \cdot (1 - \nu)}{\rho} \right] dx dy + \iint \left[\frac{y \cdot z}{\rho^3} - (1 - 2\nu) \cdot \frac{y}{\rho \cdot (\rho + z)} \right] dx dz \right] \quad (2.107)$$

The F_{3ij} functions have been analytically integrated by Jacq et al.:

$$F_{311} = \frac{1}{\pi} \cdot \left[-\nu \cdot x \cdot \ln(y + R) - (1 - 2\nu) \cdot z \cdot \operatorname{atan} \left(\frac{y + z + R}{x} \right) \right], \quad (2.108)$$

$$F_{322} = \frac{1}{\pi} \cdot \left[-\nu \cdot y \cdot \ln(x + R) - (1 - 2\nu) \cdot z \cdot \operatorname{atan} \left(\frac{x + z + R}{y} \right) \right] \quad (2.109)$$

$$F_{333} = \frac{1}{\pi} \cdot \left[(1 - 2\nu) \cdot \left[2 \cdot z \cdot \operatorname{atan} \left(\frac{R + y + x}{z} \right) + x \cdot \ln(R + y) + y \cdot \ln(R + x) \right] + \frac{z}{2} \cdot \operatorname{atan} \left(\frac{x \cdot y}{z \cdot R} \right) \right] \quad (2.110)$$

$$F_{312} = \frac{1}{\pi} \cdot [-2 \cdot \nu \cdot R - (1 - 2\nu) \cdot z \cdot \ln(z + R)] \quad (2.111)$$

$$F_{313} = \frac{1}{\pi} \cdot \left[2 \cdot x \cdot \operatorname{atan} \left(\frac{y + z + R}{x} \right) + y \cdot \ln(z + R) \right] \quad (2.112)$$

$$F_{323} = \frac{1}{\pi} \cdot \left[2 \cdot y \cdot \operatorname{atan} \left(\frac{x + z + R}{y} \right) + x \cdot \ln(z + R) \right], \quad (2.113)$$

with $R = \sqrt{x^2 + y^2 + z^2}$

Normal residual displacements of the surface due to plastic strains existing in the half-space can now be computed, using the relations described above.

2.2.6 Tangential residual displacements [FUL 09]

Let's consider a virtual state corresponding to the application of a unit force Q_x along the x-axis applied on the elementary surface area centered at point A, as shown hereafter.

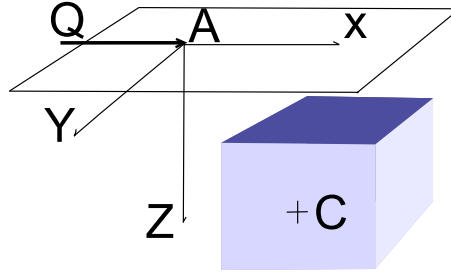


Figure 2.13: Cuboid of uniform plastic strain

The displacements generated are expressed by Cerruti [CER 82]:

$$U_x^* = \frac{Q_x}{4.\pi.G} \cdot \left[\frac{1}{R} + \frac{x^2}{R^3} + (1-2.\nu) \cdot \frac{x^2}{R.(R+z)^2} \right] \quad (2.114)$$

$$U_y^* = \frac{Q_x}{4.\pi.G} \cdot \left[\frac{x.y}{R^3} - (1-2.\nu) \cdot \frac{x.y}{R.(R+z)^2} \right] \quad (2.115)$$

$$U_z^* = \frac{Q_x}{4.\pi.G} \cdot \left[\frac{x.z}{R^3} + (1-2.\nu) \cdot \frac{x}{R.(R+z)} \right] \quad (2.116)$$

The reciprocal theorem is used to express the surface displacements as a function of contact forces and plastic strains within the body under the assumption that $Tr(\epsilon^p) = 0$:

$$U_i^r(A) = 2.\mu \cdot \sum_{n=1}^N \epsilon_{ij}^p(C_n) \cdot \int_{\Omega_p} \epsilon_{ij}^*(A, M) d\Omega = \sum_{n=1}^p \epsilon_{ij}^p \cdot D_{lij}(A, C_n) \quad (2.117)$$

with U^* defined above and $\epsilon_{ij}^* = \frac{1}{2} \cdot (U_{i,j}^* + U_{j,i}^*)$

The residual displacements are functions of plastic strain ϵ_{ij} , Poisson's ratio ν , and cuboid location $(c1, c2, c3)$ and size $(\Delta x, \Delta y, \Delta z)$:

$$\begin{aligned} D_{lij} = & F_{lij}(c1 + \Delta x, c2 + \Delta y, c3 + \Delta z) - F_{lij}(c1 + \Delta x, c2 + \Delta y, c3 - \Delta z) \\ & - F_{lij}(c1 + \Delta x, c2 - \Delta y, c3 + \Delta z) - F_{lij}(c1 - \Delta x, c2 + \Delta y, c3 + \Delta z) \\ & + F_{lij}(c1 + \Delta x, c2 - \Delta y, c3 - \Delta z) + F_{lij}(c1 - \Delta x, c2 - \Delta y, c3 + \Delta z) \\ & + F_{lij}(c1 - \Delta x, c2 + \Delta y, c3 - \Delta z) - F_{lij}(c1 - \Delta x, c2 - \Delta y, c3 - \Delta z) \end{aligned} \quad (2.118)$$

The D_{lij} functions may be derived from previous equations in an integral form:

$$D_{111} = \frac{1}{2.\pi} \cdot \iint \left[\frac{1}{\rho} + \frac{x^2}{\rho^3} + (1-2.\nu) \cdot \left(\frac{1}{\rho+z} - \frac{x^2}{\rho.(\rho+z)^2} \right) \right] dydz \quad (2.119)$$

$$D_{122} = \frac{1}{2.\pi} \cdot \iint \left[\frac{x.y}{\rho^3} - (1-2.\nu) \cdot \frac{x.y}{\rho.(\rho+z)^2} \right] dx dz \quad (2.120)$$

$$D_{133} = \frac{1}{2.\pi} \cdot \iint \left[\frac{x.z}{\rho^3} + (1-2.\nu) \cdot \frac{x}{\rho.(\rho+z)} \right] dx dy \quad (2.121)$$

$$D_{112} = \frac{1}{4.\pi} \cdot \left[\iint \left[\frac{1}{\rho} + \frac{x^2}{\rho^3} + (1-2.\nu) \cdot \left(\frac{1}{\rho+z} - \frac{x^2}{\rho.(\rho+z)^2} \right) \right] dx dz + \iint \left[\frac{x.y}{\rho^3} - (1-2.\nu) \cdot \frac{x.y}{\rho.(\rho+z)^2} \right] dy dz \right] \quad (2.122)$$

$$D_{113} = \frac{1}{4.\pi} \cdot \left[\iint \left[\frac{1}{\rho} + \frac{x^2}{\rho^3} + (1-2.\nu) \cdot \left(\frac{1}{\rho+z} - \frac{x^2}{\rho.(\rho+z)^2} \right) \right] dx dy + \iint \left[\frac{x.z}{\rho^3} + (1-2.\nu) \cdot \frac{x}{\rho.(\rho+z)} \right] dy dz \right] \quad (2.123)$$

$$D_{123} = \frac{1}{4.\pi} \cdot \left[\iint \left[\frac{x.y}{\rho^3} - (1-2.\nu) \cdot \frac{x.y}{\rho.(\rho+z)^2} \right] dx dy + \iint \left[\frac{x.z}{\rho^3} + (1-2.\nu) \cdot \left(\frac{x}{\rho.(\rho+z)} \right) \right] dx dz \right] \quad (2.124)$$

The analytical expressions for functions F_{1jk} below have been obtained by analytical integration as done by Jacq et al. for functions F_{3jk} .

$$F_{111} = \frac{1}{2.\pi} \cdot \left[z.\ln(R+y) + y.\ln(R+z) + 2.x.\operatorname{atan} \left(\frac{y+z+R}{x} \right) + x.\operatorname{atan} \left(\frac{y.z}{x.R} \right) + (1-2.\nu) \cdot \left(2.x.\operatorname{atan} \left(\frac{y+z+R}{x} \right) + z.\ln(R+y) + \frac{1}{2}.y.\ln(R+z) - \frac{z.y}{2(R+z)} \right) \right], \quad (2.125)$$

$$F_{122} = \frac{1}{2.\pi} \cdot \left[-y.\ln(R+z) + (1-2.\nu) \cdot y \cdot \left(\frac{z}{2.(R+z)} + \frac{1}{2}.\ln(R+z) \right) \right] \quad (2.126)$$

$$F_{133} = \frac{1}{2.\pi} \cdot \left[-2.\nu.z.\ln(R+y) + (1-2.\nu) \cdot \left[2.x.\operatorname{atan} \left(\frac{R+y+z}{x} \right) + y.\ln(R+z) \right] \right] \quad (2.127)$$

$$F_{112} = \frac{1}{\pi} \cdot \left[z.\ln(R+x) + 2.y.\operatorname{atan} \left(\frac{x+z+R}{y} \right) + \frac{1-2.\nu}{2} \cdot \left(x.\ln(R+z) + \frac{z.x}{R+z} \right) \right] \quad (2.128)$$

$$F_{113} = \frac{1}{\pi} \cdot \left[y.\ln(R+x) + 2.z.\operatorname{atan} \left(\frac{x+y+R}{z} \right) \right] \quad (2.129)$$

$$F_{123} = \frac{-R}{\pi}, \quad (2.130)$$

with $R = \sqrt{x^2 + y^2 + z^2}$

Actually, D_{1jk} is a coefficient of influence defining the tangential displacement along the X-direction of a cuboid located at $(c1,c2,c3)$ and of size $(2\Delta x, 2\Delta y, 2\Delta z)$ in which a unique strain ϵ_{ij} is considered equal to one.

F_{2jk} functions can be easily found by circular permutation of indices. The tangential residual displacements of the surface due to plastic strains existing in the half-space can now be computed, using the relations described above. This is actually a breakthrough, since equations described above are now permitting a coupling of plastic and frictional effects. Frictional problems are now possible in the elastic-plastic regime.

2.2.7 Validations using a Finite Element model

A comparison with a finite element (FE) analysis performed with the commercial FE package Abaqus V6.7, will be performed to validate the analytical solutions and check the analytical methods' accuracy for both F_{1jk} and F_{3jk} solutions. The equivalent problem solved by the FE method is presented below. The use of symmetrical and anti-symmetrical boundaries permits to limit the FE model to one quarter of a parallelepiped. One quarter of a cuboid of uniform plastic strain is set below the surface in such a manner that its axis of symmetry coincides with the vertical axis Z. Symmetrical or anti-symmetrical boundary conditions (BC) are used for X=0 and Y=0 planes, but depending on plastic strains imposed, those boundaries will change as shown in Table 2.3. The upper face is naturally free. On the three other external faces that are far away from the plastic cuboid, free and fully constrained boundaries have been used alternatively. No difference has been observed on the results, so the meshed body could be considered as a quarter of a half-space. Using those symmetries, the problem is 60 units wide by 60 units high. The volume near the plastic cuboid and above the surface has been refined with 0.5-sized elements. Therefore one quarter of the half-space is meshed with only 30,000 C3D8 elements. While the 'plastic zone' is supposed of unit-size in the full problem, two refined cuboids of total dimension 0.5x0.5x1 are used in this quarter problem. The center of the equivalent cuboid is here located at a point 5 units below the surface. The same elastic properties are used for both the elastic and 'plastic' zones. Young's modulus choice doesn't matter while it has no influence on strain and displacement in a dimensionless form. Thus it is arbitrary taken equal to 1 MPa. On the other hand, the Poisson's ratio is important and taken equal to 0.3 since it is considered as a non-specific case.

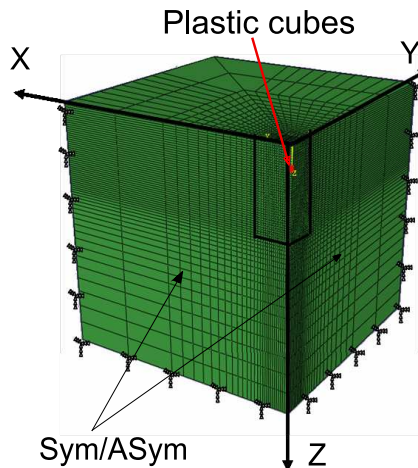


Figure 2.14: Finite Element Model

The model is based on an equivalent approach using thermo-elastic properties for this 'plastic zone' to create a thermal expansion similar to the plastic strain required. For this reason, anisotropic thermal expansion properties are defined for the 2 'plastic elements'. During Step-1 a predefined thermal field $T=1^{\circ}\text{C}$ creates the additional elastic strain desired:

$$\varepsilon_{ij}^T = \alpha_{ij}^T \cdot T \quad (2.131)$$

Case #	Strains	Symmetries
1	$\epsilon_{11}^p = -\epsilon_{22}^p = 1$	XSym / YSym
2	$\epsilon_{11}^p = -\epsilon_{33}^p = 1$	XSym / YSym
3	ϵ_{12}^p	XASym / YASym
4	ϵ_{13}^p	XASym / YSym
5	ϵ_{23}^p	XSym / YASym

Table 2.3: Boundary conditions of the FE Model

FE analyses have been performed under the assumption of linear elasticity ('perturbation' option for Abaqus), assumption that is also made in the analytical modeling. The assumption of incompressibility ($\text{Tr}(\epsilon_p)=0$) of the plastic volume used in the analysis, see Eq. 2.117, to derivate the analytical expressions should be also verified when imposing the equivalent anisotropic thermal expansions in the FE model. For this reason the diagonal components of the strain tensor should not be imposed individually. However since the problem is linear the effect of each tensor component could be superimposed resulting *in fine* in the validation of each term individually. The 5 equivalent thermal loadings finally used to validate the analytical solutions are given in Table 2.3.

2.2.8 Comparison between the FEA and analytical results

Let's consider a cuboid of uniform strain of dimension $2b \times 2b \times 2b$ ($b \times b \times 2b$ for the quarter FE model) with its center located at a distance $C_3 = \frac{Z_0}{2b}$ below the surface. The surface displacements reduce to Eq. 2.132 and can be easily plotted knowing the analytical solutions expressed in Eq.2.108- 2.113 and Eq.2.125- 2.130 .

$$u_k^r(A) = \epsilon_{ij}^p \cdot D_{kij}(A, C_n) \quad (2.132)$$

As previously stated all FE simulations will be performed for a cuboid of uniform strain located at depth $C_3 = \frac{Z_0}{2b} = 5$ in a dimensionless form. A comparison of the numerical results obtained by FEA and those derived from the analytical expressions is presented in 2.15. Results are given for a surface profile first along the X or Y-axis, and then for the first bisectrice in the plane (O,X,Y). This third plot was necessary due to the (anti)-symmetrical properties imposing some F_{ijk} equal to zero along the X or Y-axis. Finally it is found a remarkably good agreement between the numerical (FEA) and the analytical solutions proposed by the authors. The only noticeable difference is found in Figure 2.16 for the in-plane displacement due to the strain component ϵ_{12}^p . This difference is due to the failure of the boundary conditions in reproducing the half-space assumption for a thermal distortion of the cuboid in the plane parallel to the surface, which appears far away from the origin when moving closer to the domain boundaries.

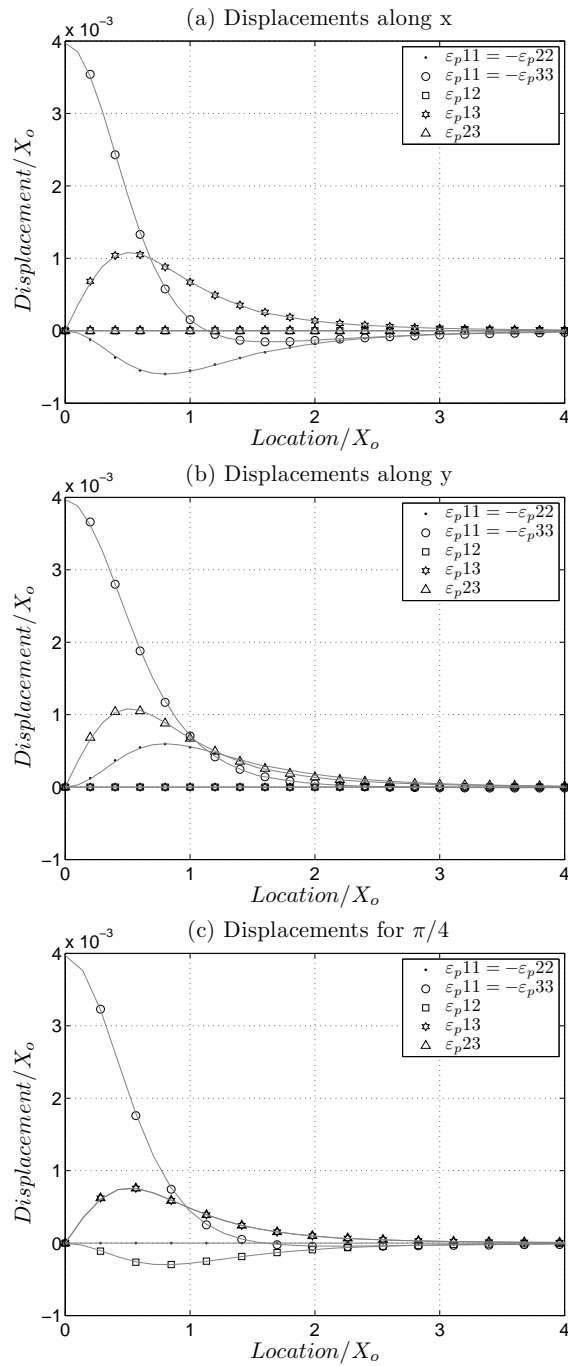


Figure 2.15: Normal displacements induced by a unique plastic cube so that $Z_0/2b=5$, where solid lines are FEM results and symbols are found analytically

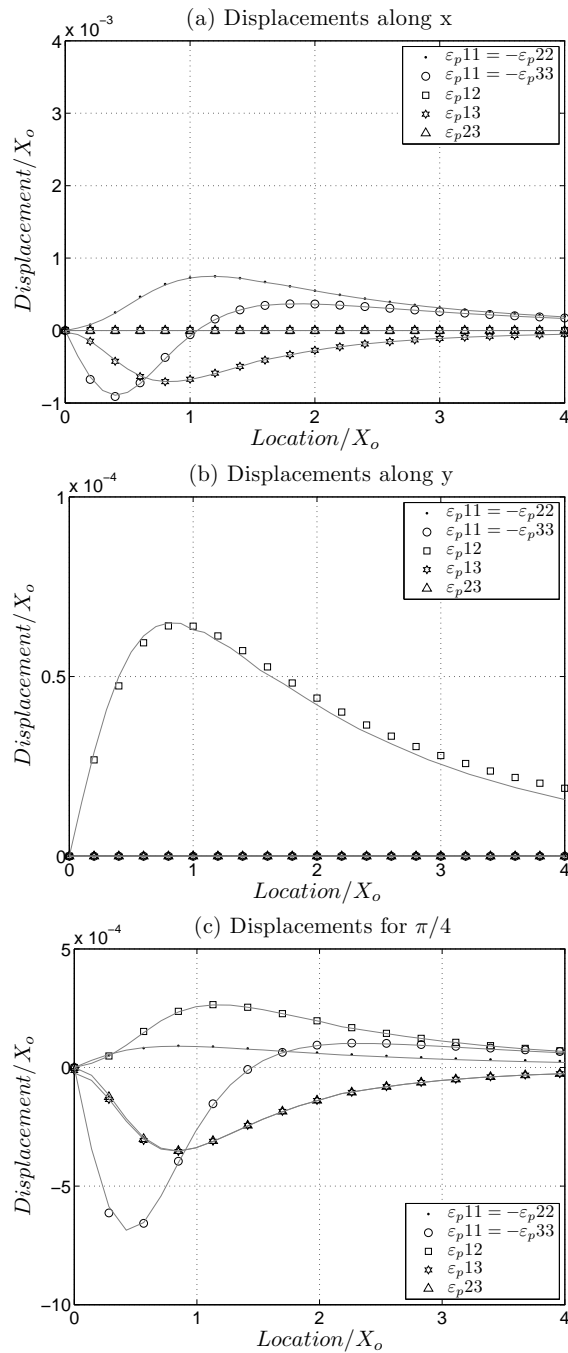


Figure 2.16: Tangential displacements induced by a unique plastic cube so that $Zo/2b=5$, where solid line are FEM results and symbols are found analytically

2.2.9 Validation using a finite element model without friction

A first validation is needed in order to be sure that modifications do not change results for frictionless contacts. A rigid sphere of radius $r=105\mu\text{m}$ and an elastic plastic flat are pressed together. Flat is a ball-bearing steel of elastic properties $E=210\text{ GPa}$ and $\nu=0.3$. A Swift's law is used to define the hardening $\sigma=B.(C+p^n)$ and parameters used are $B=1240$, $C=30$, $n=0.085$. This problem has been solved and validated in C.Jacq's thesis using a FE model. Data will be used to validate the actual code.

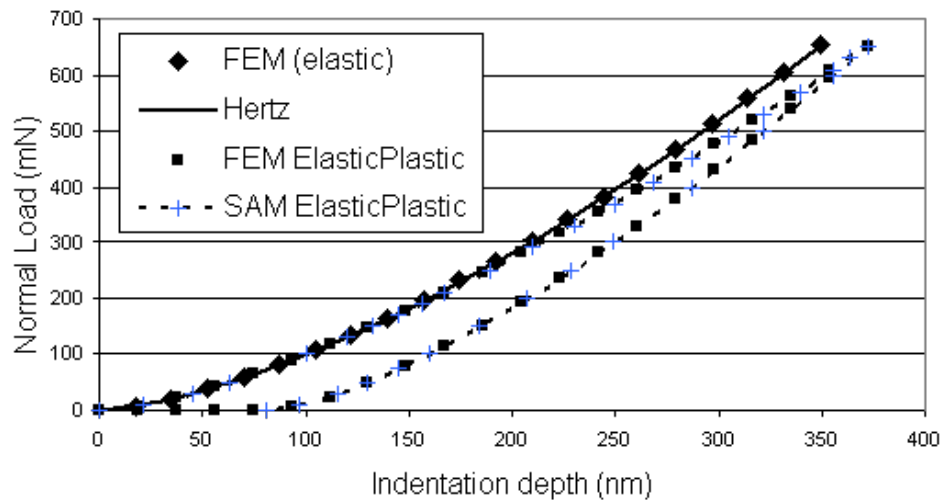


Figure 2.17: Indentation curves found using both a FEM and a SAM

First computations revealed a poor agreement between the real ($372\mu\text{m}$) and estimated ($430\mu\text{m}$) maximum depth for this problem, while frictionless elastic tests succeeded. Plasticity was overestimated in this problem. A relaxation of one was considered since this date in Jacq's code (meaning no relaxation) in order to reduce the computing time, but results were considerably altered. For lower relaxation a much better agreement is found. For instance, a relaxation δ_{relax} equals to 0.3 leads to an over-estimation of less than 0.4%. Error becomes almost nil for $\delta_{relax}=0.2$, as seen in Fig.2.17, and such value will be used for further studies.

Results obtained for the frictional contacts in the elastic regime are compared to the results found by Gallego in parts 2.4.3, 2.4.2 and ???. Those results are then extended to the elastic-plastic regime.

2.3 Numerical methods and improvements

2.3.1 Weak formulation

Weak formulations are used in mechanical equations in order to describe a complete problem [DUV 72]. The unique solution of the contact problem can be found by minimizing the strain energy and considering that one body can not interpenetrate the other one (2.67a). Kalker gives the solutions for two elastic half-spaces in contact. The contact pressures p are positive and the contact shears \mathbf{q} are bounded by the Coulomb's law.

$$\min \int_{\Gamma_c} \left(h^* + \frac{1}{2} \bar{u}_z \right) p dS + \int_{\Gamma_c} \left(\mathbf{W}_\tau^* + \frac{1}{2} \bar{\mathbf{u}}_\tau - \bar{\mathbf{u}}_\tau^{-1} \right) \mathbf{q} dS, \quad (2.133a)$$

$$p \geq 0, \quad (2.133b)$$

$$\|\mathbf{q}\| \leq \mu p. \quad (2.133c)$$

h^* is the distance between undeformed geometries. It includes the initial separation and the rigid body displacements induced by translations and rotations. In the same manner, \mathbf{W}_τ^* is the tangential displacements tensor induced by rigid body displacements.

It comes for the normal and tangential problem:

$$\min \left(\frac{1}{2} \mathbf{p}^T \mathbf{A}_z^p \mathbf{p} + \mathbf{h}^{*T} \mathbf{p} + c_\tau \right), \quad (2.134a)$$

$$p_{ij} \geq 0. \quad (2.134b)$$

$$\min \left(\frac{1}{2} \mathbf{q}^T \mathbf{A}_\tau^q \mathbf{q} + \mathbf{W}^{*T} \mathbf{q} + c_p \right), \quad (2.134c)$$

$$\|\mathbf{q}_{ij}\| \leq \mu p_{ij}. \quad (2.134d)$$

The tangential problem may also create some normal displacements (when coupling is considered), \mathbf{h}^* will include those displacements. In the same manner, the normal problem may also create some tangential displacements, \mathbf{W}^* will include those displacements and tangential displacements found for the previous time-step. It comes:

$$\mathbf{h}^* = \mathbf{h} + \mathbf{A}_z^q \mathbf{q} - \delta_z - \mathbf{y} \cdot \phi_x + \mathbf{x} \cdot \phi_y \quad (2.135a)$$

$$\mathbf{W}^* = -\Delta \delta_\tau^t + \begin{pmatrix} \vdots \\ -y_{ij} \cdot \Delta \phi_z^t \\ \vdots \\ x_{ij} \cdot \Delta \phi_z^t \\ \vdots \end{pmatrix} + \mathbf{A}_\tau^p \mathbf{p} - \bar{\mathbf{u}}_\tau^{t-1} \quad (2.135b)$$

$c_p = \frac{1}{2} \mathbf{p}^T \mathbf{A}_z^p \mathbf{p} + (\mathbf{h} - \delta_z)^T \mathbf{p}$, respectively $c_\tau = \frac{1}{2} \mathbf{q}^T \mathbf{A}_\tau^q \mathbf{q} + (-\Delta \delta_\tau^t - \bar{\mathbf{u}}_\tau^{t-1}) \mathbf{q}$ is the complementary energy of the normal problem, respectively the tangential problem.

In the normal problem, the constraint is linear and the problem is known as a quadratic optimization problem, where λ_{ij} is the gap g_{ij} between the two surfaces. Equations become similar to equations found in section 2.1.5 page 43 (2.134a) (See [GAL 10]):

$$\mathbf{A}_z^p \mathbf{p} + \mathbf{h}^{*T} - \lambda_{ij} = 0, \quad (2.136a)$$

$$p_{ij} > 0, \quad \lambda_{ij} = 0, \quad (2.136b)$$

$$p_{ij} = 0, \quad \lambda_{ij} \geq 0. \quad (2.136c)$$

For the tangential contact problem, λ_{ij} is the slip amplitude, and equations become similar to equations found in section 2.1.6 page 46. The constraint is not linear, therefore applying the Lagrangian method leads to (See [GAL 10]):

$$\mathbf{A}_\tau^q \mathbf{q} + \mathbf{W}^{*T} + \begin{pmatrix} \vdots \\ \lambda_{ij} \frac{q_{xij}}{\mu p_{ij}} \\ \vdots \\ \lambda_{ij} \frac{q_{yij}}{\mu p_{ij}} \\ \vdots \end{pmatrix} = 0 \quad (2.137a)$$

$$\|\mathbf{q}_{ij}\| < \mu p_{ij}, \quad \lambda_{ij} = 0, \quad (2.137b)$$

$$\|\mathbf{q}_{ij}\| = \mu p_{ij}, \quad \lambda_{ij} \geq 0. \quad (2.137c)$$

Finally, several methods can be used to minimize the quadratic form. Polonsky and Keer [POL 99] used a contact algorithm based on the conjugate gradient method (CGM).

2.3.2 Conjugate Gradient Method (CGM)

The Conjugate Gradient is an iterative method which generates a sequence of approximations of the solution starting from an arbitrary initial approximation. This scheme is detailed by Polonsky and Keer in [POL 99] and is based on three main formulae, exposed hereafter for the normal problem:

$$p_{ite+1} = p_{ite} - \frac{r_{ite}^T \cdot r_{ite}}{d_{ite}^T \cdot K \cdot d_{ite}} \cdot d_{ite} \quad (2.138a)$$

$$r_{ite+1} = r_{ite} - \frac{r_{ite}^T \cdot r_{ite}}{d_{ite}^T \cdot K \cdot d_{ite}} \cdot K \cdot d_{ite} \quad (2.138b)$$

$$d_{ite+1} = -r_{ite} + \frac{r_{ite+1}^T \cdot r_{ite+1}}{r_{ite}^T \cdot r_{ite}} \cdot d_{ite} \quad (2.138c)$$

$$K = A_z^p + A_z^q \cdot q \quad (2.138d)$$

where ite is the iteration inside the loop algorithm, r_{ite} is the residue, d_{ite} is the direction and K is called the Kernel, defined for each point of the contact.

A uniform pressure field is often considered for the initial approximation of p_o , while $d_0 = r_0 = h^* - h - \delta_z - K \cdot p_0$ (See Equation ??). Three variables are also used, δ , G and G_{old} and then initialized $\delta = 0$ and $G_{old} = 1$.

- Considering the pressure field p_{ite} (and the pressure field q), the normal displacements U_z^p and U_z^q are found using a DC-FFT algorithm.
- The gap r_{ite} between both geometries $r_{ite} = g_{ite} = u_z^p + u_z^q + h^*$ is found for each point of the contact zone (See equation 2.138b), it is the residue r_{ite} of the system and tends to zero while the problem converges. G becomes the sum of all squared gaps: $G = \text{Sum}(g^2)$.
- The direction d_{ite+1} is then found using equation 2.138c, and G is then stored in G_{old} .
- The residue $\mathbf{r}_{ite+1}^p = \mathbf{A}_z^p \cdot \mathbf{d}$ is found using a DC-FFT algorithm. The increment along this direction is defined by: $\alpha = \frac{\sum \mathbf{g} \cdot \mathbf{d}}{\sum \mathbf{r} \cdot \mathbf{d}}$.
- The pressure field is then equal to $\mathbf{p}_{ite+1} = \mathbf{p}_{ite} + \alpha \cdot \mathbf{d}$
- According to equation 2.138b and equation 2.138c, the contact zone may evolve. If the pressure p_{ite+1} is locally lower than zero, then the pressure is set equal to zero and the point is no longer in the contact zone. If the gap $r_{ite} = g_{ite}$ is lower than zero, then the point is in the contact zone and the pressure $\mathbf{p}_{ite+1} = \alpha \cdot \mathbf{d}$.
- This process continues until the pressure converges.

A very similar algorithm as been used by Gallego for the tangential problem [GAL 07a].

The multiplication operations between the influence coefficient tensor \mathbf{A}_z^p by the surface traction fields and the direction vector d are time consuming, and require N^2 operations considering a surface of N elements. To reduce the computing time, the Fast Fourier Transform is used within each iteration of the CGM, so that previous equations only require $N \cdot \log(N)$ operations (See section 2.3.4).

2.3.3 Convergence of the tangential contact solver

Most of hazardous points have been investigated and solutions have been proposed for frictionless contacts. A coupled approach, considering friction and hardening is now possible. Because the normal problem requires the determination of the contact area and pressure field only, it is much simpler than finding the sticking zone, slips/shears amplitudes and directions. For this reason, tangential problem appears to be less robust than the normal problem. Three types of lack of robustness can be noticed:

- (i) The solution is oscillating around a non-stable position.
- (ii) The solution is converging too slowly.
- (iii) Everything else is mainly due to a strong difference between the previous state and the actual state because of a poor discretization of the loading.

(ii) and (iii) are rare and can be avoided by refining the loading which helps the convergence. A normal loading may contain hundred steps, requiring ten plasticity loops by step, up to ten contact loops for the convergence of the Panagiotopoulos process for each plasticity loop. A classic computation may then solve the tangential problem around ten thousands times. Because of this, (i) is frequent and becomes critical when dealing with both hardening and friction and it is of a great importance to reduce such errors.

In first versions, convergence was forced after thousand increments in the tangential problem, regardless of the error at this time, in order to avoid computation failures. Alerts were consciously bypassed. However, effect on the global response was not perceptible during tests, but this issue has to be investigated. A rigid sphere of radius $r=1\text{mm}$ and an elastic-plastic fat are pressed together. Elastic-plastic properties of the fat are $E=200\text{GPa}$, $\nu=0.3$, $S_y=1000\text{MPa}$, $E_t=0.5x E$. Four computations with different friction coefficients will be considered ($\mu=0, 0.1, 0.2, 0.3$). A total of 41 alerts are detected in those computations with errors up to 38%, as seen in figure 2.18a. One of the solutions consists in adding a relaxation in the tangential algorithm, while implementing the new direction during incremental update. Using such improvement, oscillations around a stable position can be avoided (cf. figure 2.19). With a relaxation of 0.8, number of errors can be reduced from 41 to 9 as seen in Figure 2.19b.

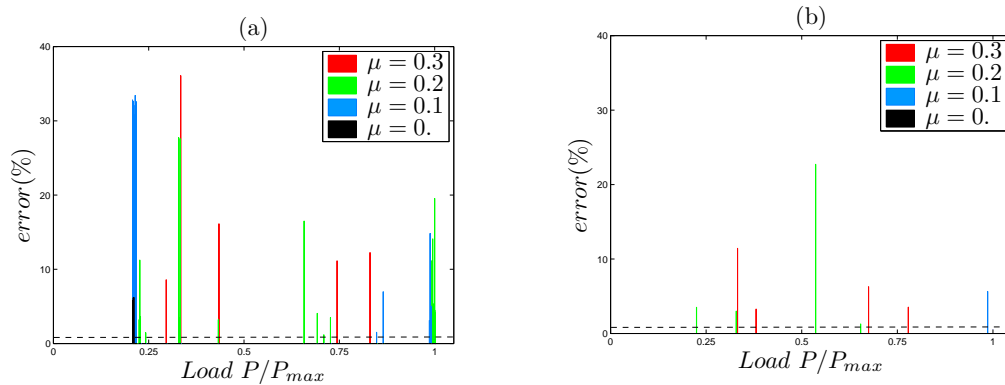


Figure 2.18: Errors encountered in four different simulations, considering no relaxation (a) or a relaxation of 0.8 (b) in the tangential algorithm

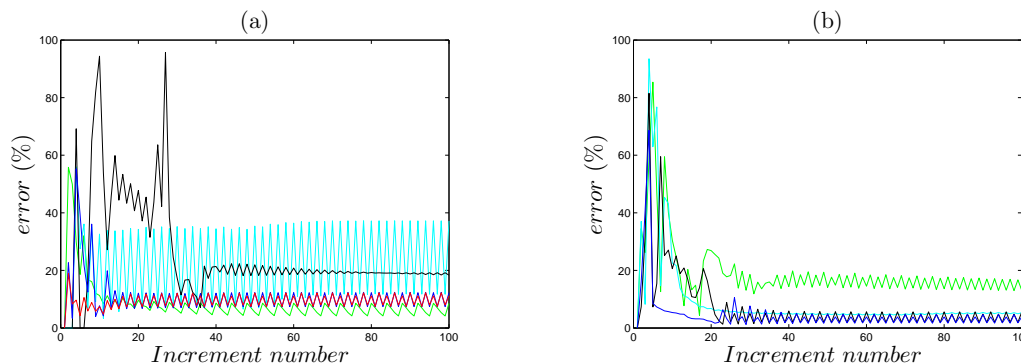


Figure 2.19: Convergence anomalies encountered for $\mu=0.3$, considering no relaxation (a) or a relaxation of 0.8 (b) in the tangential algorithm

An adaptative relaxation has been implemented in the tangential algorithm, on the increment α along the direction d . If the number of increments is noted $n_{increment}$ then for:

- $1 < n_{increment} < 300$ then $\delta_{relax} = 1$
- $301 < n_{increment} < 600$ then $\delta_{relax} = 0.8$
- $601 < n_{increment} < 999$ then $\delta_{relax} = 0.6$

Because most of tangential problems converge in about 20 increments, this adaptative relaxation optimizes the computing time. Moreover, the relaxation changes when convergences are too long, which helps to reduce the number of alerts down to 5 with acceptable percentage of errors as seen in (cf. figure 2.20a). Oscillations around a stable position become very rare and remaining alerts may be avoided using a finer loading discretization.

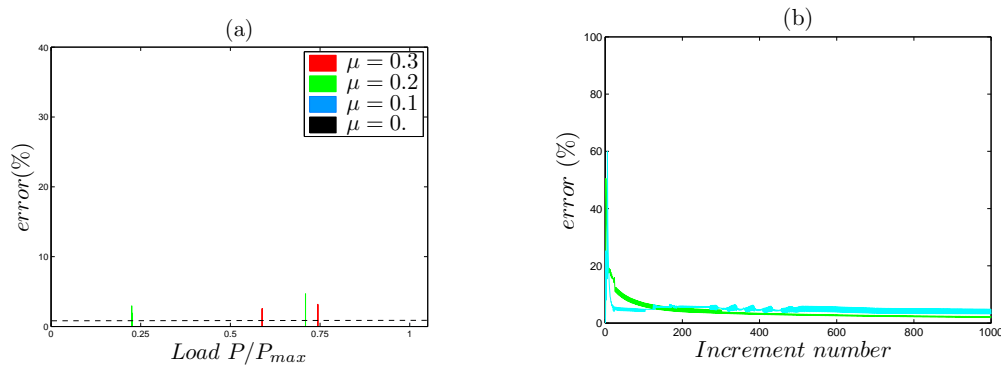


Figure 2.20: Errors encountered in four different simulations considering an adaptative relaxation (a) and corresponding convergence anomalies for $\mu=0.3$ (b)

2.3.4 Discrete Continuous Fast Fourier Transforms (DC-FFT)

Introduction As seen in the Conjugate Gradient method, displacements, but also stresses, are calculated from influence coefficients that actually correspond to the Green functions in their discretized form (See equations 2.65 and 2.66).

It is classically a double summation for the stress and elastic deflections induced by a contact loading. The number of operations depends on the size of the domain considered; if the calculation zone is (N_x, N_y) then the number of operations for one double summation is $N_x \cdot N_y$, often simplified by N^2 when sizes are similar in both directions.

The Discrete-Convolution and Fast Fourier Transform, noted DC-FFT or FFT, have been proposed in order to accelerate this calculation. This enable reduction of the number of operations [JU 96, POL 99], but the contact zone has to be at least equal to two times the contact zone to obtain accurate results [LIU 00].

The one-dimensional FFT Let us introduce a one-dimensional convolution product between the functions $x(t)$ and $h(t)$:

$$y(t) = \int_{-\infty}^{+\infty} x(t)h(t - \tau)d\tau \equiv x(t) * h(t). \quad (2.139)$$

Denoting $\tilde{h}(\omega)$ the Fourier transform of the function $h(t)$:

$$\tilde{h}(\omega) = \int_{-\infty}^{+\infty} h(t)e^{-i\omega t} dt. \quad (2.140)$$

The convolution theorem is obtained by applying the Fourier transform to the convolution product in equation 2.139:

$$\tilde{y}(\omega) = \tilde{x}(\omega)\tilde{h}(\omega). \quad (2.141)$$

Then a simple multiplication is made in the frequency domain. Afterwards, the inverse Fourier transform yields to the result in the spatial domain:

$$y(t) = 1/2\pi \int_{-\infty}^{+\infty} \tilde{y}(\omega)e^{i\omega t} dt. \quad (2.142)$$

The contact problem being solved as a discrete domain, the discrete Fourier transform and its inverse are then introduced, considering a discrete form of h and x , respectively h_r and x_r , of N points. It comes:

$$\hat{h}_s = \sum_{r=0}^{N-1} h_r e^{-2\pi i r s / N}, \quad s = 0, \dots, N-1. \quad (2.143)$$

$$h_j = (1/\text{sqrt}(N)) \sum_{r=0}^{N-1} \hat{h}_r e^{2\pi i r j / N}, \quad j = 0, \dots, N-1. \quad (2.144)$$

The discrete convolution is then:

$$y_j = \sum_{r=0}^{N-1} x_r h_{j-r}, \quad j = 0, \dots, N-1. \quad (2.145)$$

and is expressed from a set of data of length L_0 . Implicitly, the discrete convolution is realized over an infinite length, introducing a periodicity equals to L_0 of both samples to be convoluted. This is called the circular convolution, and can be expressed as:

$$y_j = \mathbf{x} \otimes \mathbf{h} = \sum_{r=0}^{N-1} x_r h_{j-r+NH(r-j)}, \quad j = 0, \dots, N-1. \quad (2.146)$$

with the Heaviside function:

$$H(x) \begin{cases} = 0 & \text{if } x < 0, \\ = 1 & \text{if } x \geq 0. \end{cases} \quad (2.147)$$

The number of terms of \mathbf{K} and p is the same, $j \in [0, N-1]$. The Heaviside function is active when $j - r < 0$ which avoids negative indices for \mathbf{K} and means to replace the index by $j - r + N$. There is then a circular summation, and it induces a periodicity in the sample. It is then possible to introduce the convolution product in the discretized form, which is related to the circular convolution product:

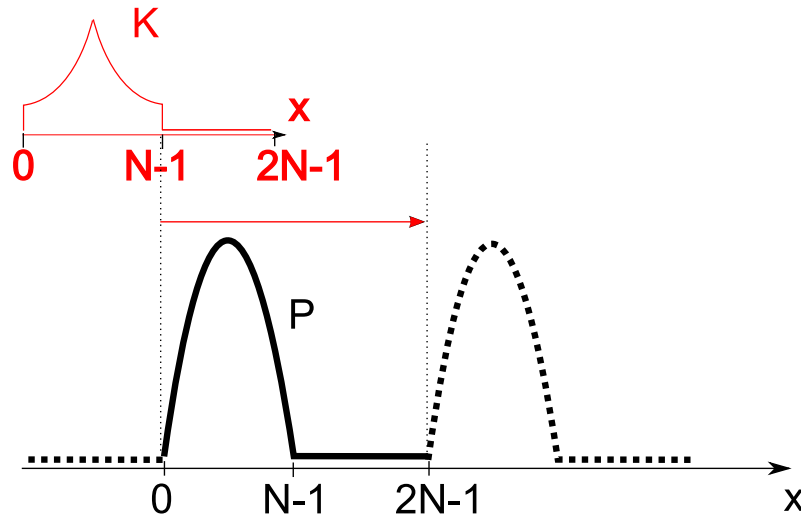


Figure 2.21: Convolution of the pressure field P and the coefficient of influence K_z^p in the frequency domain

$$\hat{y}_s = \hat{x}_s \hat{h}_s, \quad s = 0, \dots, N-1. \quad (2.148)$$

The Fast Fourier Transform (FFT) is a Fourier transform algorithm reducing the number of iterations from N^2 to $N \cdot \log(N)$ [SIN 69]. This algorithm is also used for the Inverse Fourier Transform and the number of iterations is also $N \cdot \log(N)$. The convolution in the frequency domain also requires N iterations. Finally, the double summation requires $N + 3N \log N$ iterations when using the frequency domain, instead of $O(N^2)$ in the spatial domain. This becomes particularly advantageous for large number of N .

Zero-padding The target domain $[0, N-1]$ is doubled in each direction and becomes $[0, 2N-1]$, while pressures are set equal to zero in the extra part of the domain. Zero-padding is applied to the target domain only (a pressure field for instance).

Wrap-around order For the influence coefficients, the domain size $[0, N-1]$ is also doubled (See figure 2.22). According to the parity properties of the coefficients of influence, the domain $[N, 2N-1]$ is fulfilled with the coefficients of influence of the domain $[0, N-1]$. For $[N]$, the value is set equal to zero in order to avoid the overlapping both domains.

The DC-FFT method The technique of zero padding and wrap-around order are the necessary treatments for properly converting the linear convolution into the cyclic convolution. The target domain is doubled in each direction (See Figure 2.22). Finally, the DC-FFT (Discrete Convolution and Fast Fourier Transform) detailed by Liu is:

1. Find the influence coefficients, $\{K_j\}_N$,
2. Expand $\{K_j\}_N$ into $\{K_j\}_{2N}$ with zero-padding and wrap-around order,
3. Apply FFT to $\{K_j\}_{2N}$ and obtain $\{\hat{K}_s\}_{2N}$;

4. Input the pressure, $\{p_j\}_N$;
5. Expand the pressure $\{p_j\}_N$ into $\{p_j\}_{2N}$ with zero-padding and wrap-around order, $p_j = p_j, j \in [0, N-1], p_j = 0, j \in [N, 2N-1]$;
6. Apply FFT to $\{p_j\}_{2N}$ and obtain $\{\hat{p}_s\}_{2N}$;
7. Make the element-by-element production of the complex numbers, and obtain the frequency response $\{\hat{v}_s\}_{2N}$;
8. Apply the IFFT to $\{\hat{v}_s\}_{2N}$ and obtain $\{u_j\}_{2N}$;
9. Discard the spoiled terms and keep $\{u_j\}_{2N}, j \in [0, N-1]$.

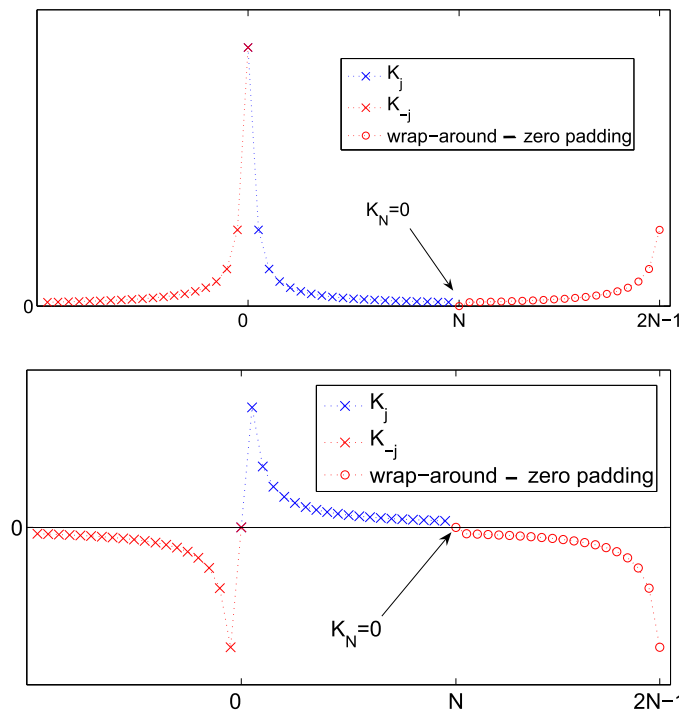


Figure 2.22: wrap-around and zero-padding for pair coefficients such as K_z^P (top) and impair coefficients such as K_z^{qX} (bottom)

2.3.5 2D-FFT Algorithm

The 2-dimensional Fourier transform and its inverse exposed in equations 2.143 and 2.144 become:

$$\hat{h}_{sx, sy} = \sum_{r_x=0}^{N_x-1} \sum_{r_y=0}^{N_y-1} h_{r_x, r_y} e^{-2\pi i r_x s_x / N} e^{-2\pi i r_y s_y / N}, \quad s = 0, \dots, N-1. \quad (2.149)$$

$$h_{j_x, j_y} = (1/N_x N_y) \sum_{r_x=0}^{N_x-1} \sum_{r_y=0}^{N_y-1} \hat{h}_{r_x, r_y} e^{2\pi i r_x j_x / N_x} e^{2\pi i r_y j_y / N_y}, \quad j = 0, \dots, N-1. \quad (2.150)$$

In consequence, the 2-dimensional Fourier transform is obtained using the 1D-FFT along the first direction and then on the second direction. The order retained for the application of the 1D-FFT does not have any importance. The 2D-FFT will be used in many cases where a surface source has an influence on a surface image. But it can also be extended to three dimensional problems when proceeding slice by slice. All those cases are described hereafter (See figure 2.23):

- Surface source vs. surface image: Elastic deflections induced by the contact pressure or shears.
- Surface source vs. volume image: Stresses located at a certain depth caused by the contact pressure and shears. In order to define the stresses in the volume image, the 2D-FFT algorithm will be used N_z times, where N_z is the number of elements along the normal direction.
- Volume source vs. surface image: Residual displacements observed on the surface and induced by plastic deformations located at a certain depth. Coefficients of influence needed exist and have been defined in a half-space in [CHI 78]. Once again, the 2D-FFT algorithm will be used for each depth N_z of the volume source. It must be noticed that the 2D-FFT is not used for misfit displacements caused by non-homogeneities contained in the half-space since solutions do not exist in a half-space; in this case, the 3D-FFT is not an option.
- Volume source vs. volume image: Residual stresses and misfit stresses induced by plastic or misfit strains of the volume source. The source domain is browsed, for each depth $N_{z,source}$ the 2D-FFT is used for each image depth $N_{z,image}$. This technique becomes very cumbersome since (assuming that $N_{xy,source}$ and $N_{xy,image}$ are similar) the domain is browsed $N_{z,source} \cdot N_{z,image}$ times. Moreover, the influence coefficients are heavy to manipulate and drastically increase the computing time because of an high access to the hard-drive. Hopefully, the volume source vs. volume image problem has been greatly improved by the 3D-FFT algorithm exposed hereafter.

The two dimensional fast Fourier transform (2D-FFT) reduces the number of iterations from N^4 to $2N \cdot \log(2N)$. The convolution in the frequency domain still requires $2N$ iterations. Including the IFFT, the double summation requires $2N + 6N \log(2N)$.

2.3.6 3D-FFT Algorithm

The 3-dimensional Fourier transform and its inverse exposed in equations 2.143 and 2.144 can be expressed in three dimensions. The 3D-FFT is obtained using the 1D-FFT along three directions.

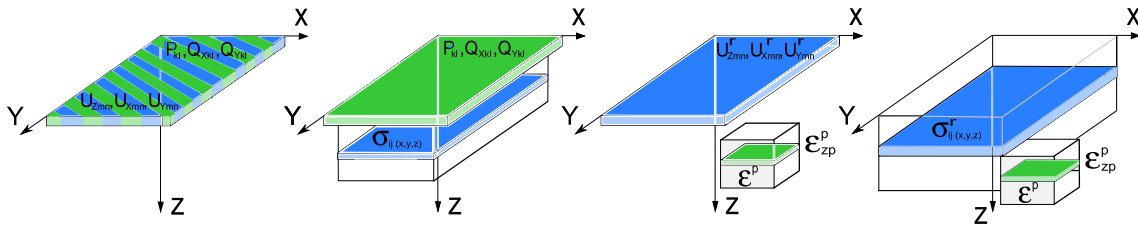


Figure 2.23: Use of the 2D-FFT in the actual code. Sources are shown in green, while images are shown in blue

It is commonly used for volume source vs. volume image calculations. Moreover, this is of a great importance in the non-homogeneous solver since the solutions in an half-space are not available, making the 2D-FFT inappropriate.

Common method is to decompose an isotropic half-space problem into three sub-problems, as seen in Figure 2.24. The first sub-problem considers the same cuboid but in an infinite space, $\epsilon^* = (\epsilon_{11}^*, \epsilon_{22}^*, \epsilon_{33}^*, \epsilon_{12}^*, \epsilon_{13}^*, \epsilon_{23}^*)$. The second one considers an image counterpart – an inclusion as seen in a mirror – in the same infinite space. Its eigenstrains ϵ_m^p is modified in order to respect symmetric conditions: $\epsilon_m^* = (\epsilon_{11}^*, \epsilon_{22}^*, \epsilon_{33}^*, \epsilon_{12}^*, -\epsilon_{13}^*, -\epsilon_{23}^*)$

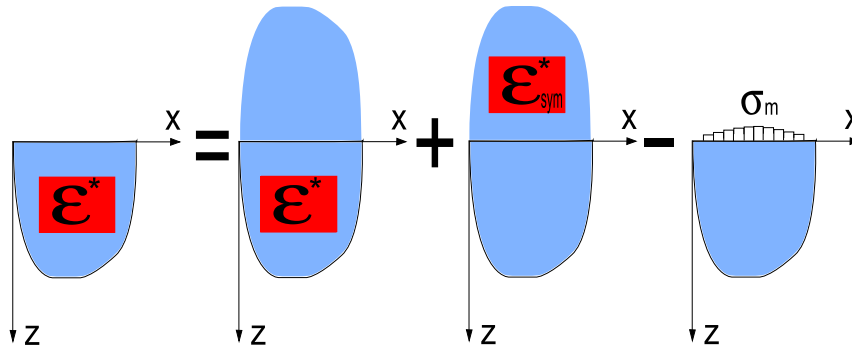


Figure 2.24: Decomposition of the problem about a cuboidal inclusion containing constant eigenstrains ϵ^* in an isotropic half-space bounded by the plane $z=0$ into three sub-problems

It must be noticed that the eigenstrain ϵ^* can be a plastic strain ϵ^p in the plastic solver or a misfit strain β in the non-homogeneous solver. Sub-problems defined hereinbefore are used in the 3-dimensional Fast Fourier Transform algorithm or 3D-FFT. It actually includes two 3D-FFT and a 2D-FFT algorithm, as seen in figure 2.25.

Note The 2D-FFT algorithm uses influence coefficients found in an infinite half space. The difference resides in the form used for the σ_m . In the 2D-FFT coefficients, the field σ_m has a continuous form, expressed as a function of the first and second problem, so the stress fields induced by the free surface is found analytically. Those analytical solutions become very complex and it must be assumed that the eigenstrain is incompressible, which works great in the plastic case but incompatible with the non-homogeneous case. The 3D-FFT use a discrete form of the pressure

field σ_m , and is computed numerically. Then the pressure field is applied and the stress field is found.

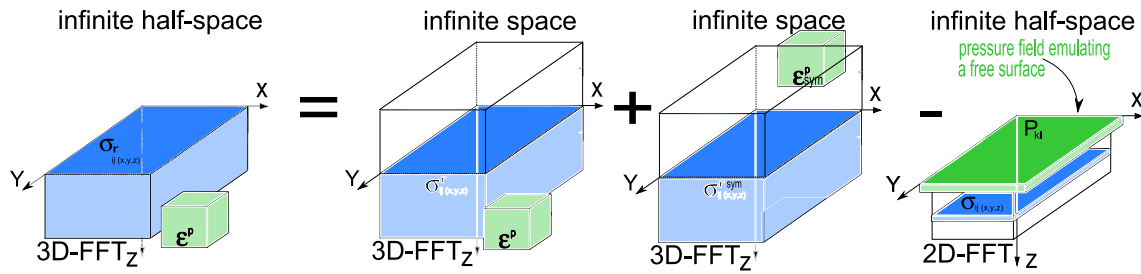


Figure 2.25: Use of the 3D-FFT

The great advantage of this method is that the 3D-FFT naturally reduces the computing time compared to a 2D-FFT. But the main advantage of the method is the reduced size of the influence coefficients tensors. In the 2D-FFT, a $N_{x,image}, N_{y,image}, N_{z,image}$ tensor is defined for each depth of the source $N_{x,source}, N_{y,source}, N_{z,source}$, which leads to a $N_{x,image} \cdot N_{y,image} \cdot N_{z,image} \cdot N_{x,source} \cdot N_{y,source} \cdot N_{z,source}$ tensor (or N^6). In the 3D-FFT algorithm, coefficients of influence used are related to a cuboid in an infinite space. Since the free surface is not explicitly considered at this stage, and because of the algorithm scheme, the influence coefficient tensor is of the size of $2(N)^3$. The computing time is drastically reduced because of the lower access to the hard drive.

2.3.7 2.5D-FFT Algorithm

Time consumption has been drastically reduced thanks to the use of the 3D-FFT. When elements considered are not close to the surface, this method works great. Considering a $2b$ -sized element located at a depth Z_0 below the surface, no difference has been observed for a depth $Z_0 \geq 5/2b$ because strain fields – misfit or residual strain field – are defined analytically in both infinite half spaces and pressure field which emulates an infinite half space is properly discretized as shown below.

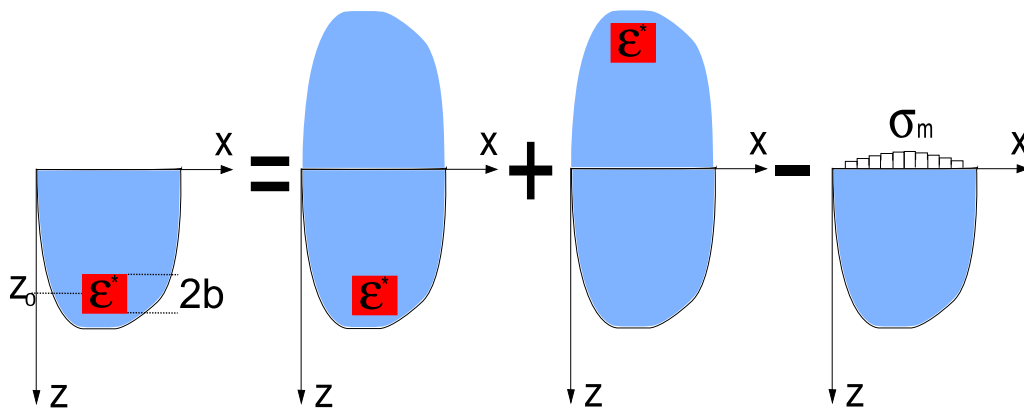


Figure 2.26: 3D-FFT techniques for inclusions far from the surface

However, this method becomes obsolete considering 'eigenstrains' – including hardening and non-homogeneous aspects – arising into the contact. Discretization of the pressure field σ_m becomes critical and leads to an over-estimation of normal and tangential displacements into the contact. For this reason, over-shooting of the real solution may be observed and non-physical solutions can be found. This become critical when considering elastic-plastic contact with friction, since the maximum Von Mises stress may appear into the contact. But also when considering layers and spherical inclusions arising into the contact.

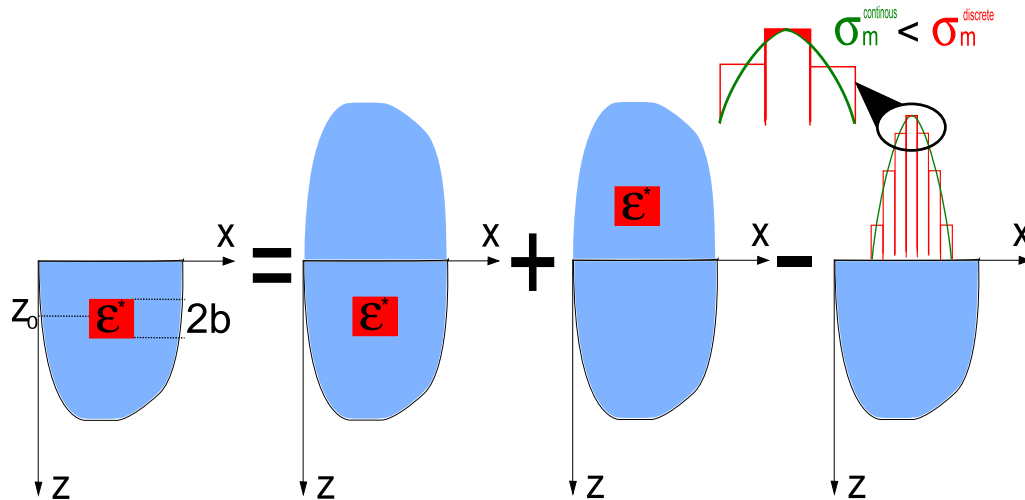


Figure 2.27: 3D-FFT techniques for inclusions close to the surface and related problems

No solution has been found for the non-homogeneous solver since the analytical solutions are limited because of their complexity (the eigenstrain β is not necessarily incompressible). In the elastic-plastic solver, the solution consists in dividing the problem in two sub-problems. The 3D-FFT can be used for plastic strains located at a depth $Z_0 \geq 5/2b$ while the 2D-FFT is used for $Z_0 > 5/2b$. This method uses both the 2D-FFT algorithm and the 3D-FFT depending on the domain considered and will unofficially refer as 2.5D-FFT.

2.3.8 Instability on plastic strains

A second problem was encountered in plastic solver when estimating plastic strains, even at low load. After a certain level, plastic strain profiles became irreversibly rough and were getting even worse after few cycles. In spite of this numerical noise, profiles stayed globally unchanged as seen in (cf. figure 2.28). This problem has been encountered for various simulations, even when using initial codes, and identifying it was tough. Reason of this is still unclear today, but an efficient method has been established avoiding it.

This problem was particularly frequent in shot-penning simulations (T.Chaise thesis) where a heavy load has to be applied. Because the domain size is limited – about $55 \times 55 \times 80$ elements – the discretization was chosen so that the mesh size is the same in all directions ($\Delta y/\Delta x=1$, $\Delta z/\Delta x=1$). Mesh was not fine enough at lower load while plasticity arised and many small singularities occurred locally and start growing after each step loading. Location of numerical noise was often located close to the surface where gradients along z are much higher than in any other direction.

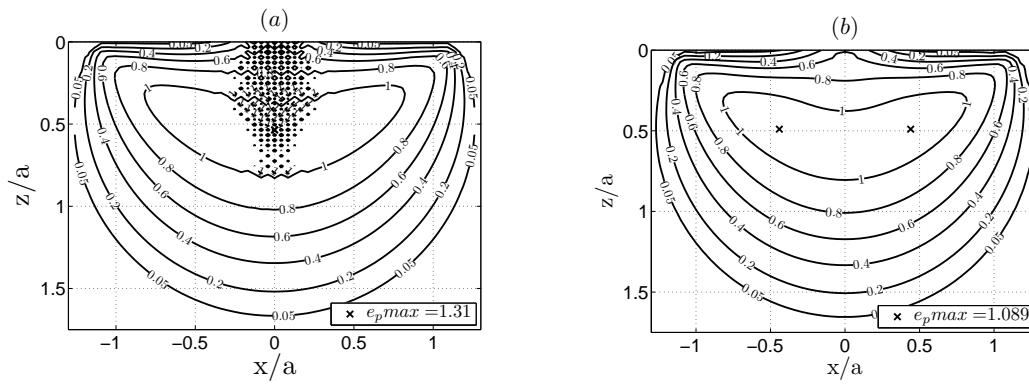


Figure 2.28: Stresses instability typically found with a poor (a) and finer discretization (b) along z

Gradients are neglected since each cube is supposed uniformly deformed. It has been proposed to reduce gradients along z from a cube to another by considering a refined mesh along z ($\Delta y/\Delta x=1$, $\Delta z/\Delta x=0.5$). Using such refinement, no numerical noise has been observed in any computation of any kind and constitutes an interesting solution with a limited computing time.

Similar problem was frequently observed in wear simulations. The domain size is still limited to about $70 \times 70 \times 70$ elements. The discretization was chosen so the mesh size is the same in all directions ($\Delta y/\Delta x=1$, $\Delta z/\Delta x=1$). Because of wear, the contact area may evolve significantly and finally approaches the domain boundaries. In this case, part of the solution is neglected because out of the domain, and numerical instabilities are then observed on the extremities of the surface. If the simulation continues, numerical instabilities are transmitted from an element to the element next to it until it reaches the center of the contact. It is obvious that the only solution is to optimize the domain size so the worn geometry never approaches the domain boundaries.

2.3.9 Conclusion

Contact solvers based on the semi-analytical method need elementary analytical solutions to compute. Love [LOV 52] and Cerruti [CER 82] solutions used in elastic contact solver are elementary solutions relating the surface pressure and shear distributions to the subsurface stress state and surface displacements. New elementary solutions are required when plasticity is involved. While Chiu [CHI 78] described the effect of a unique plastic zone on the residual stress and strain states, Jacq et al. [JAC 02, JAC 01] related analytically the subsurface plastic strains to the normal surface displacements. All these elementary solutions have been used in a three-dimensional semi-analytical elastic-plastic contact code [Jac 02]. A special attention to the tangential effects involved by plasticity has been paid since it has not been properly considered until now. This chapter gave the analytical expressions that relate the components of the strain tensor of an incompressible cuboid of uniform strain on the tangential displacements of any point of the free surface of a half-space. Both normal and tangential solutions have been compared to a finite element analysis and a very good agreement was found, which validates the analytical solutions. Those analytical solutions were implemented into an elastic-plastic contact solver to investigate frictional contact problems. Numerical methods have been improved using a 3D-FFT algorithm. The actual code has been validated using an existing FE model, considering an indentation process without friction. Instabilities during the estimation of plastic strains and anomalies in the convergence of the tangential problem were studied and few solutions were applied to get a better robustness.

2.4 Fretting considering the elastic-plastic regime

2.4.1 Fretting modes and material properties

This code can perform different kind of stick-slip contacts, among which are the three modes of fretting, as seen in figure 2.29. Those modes will be investigated in this paper, with an elastic-plastic f at, since fully sliding contacts have already been largely investigated [GAL 07a]. No repeated loadings will be treated although it constitutes fretting definition unless it is mentioned.

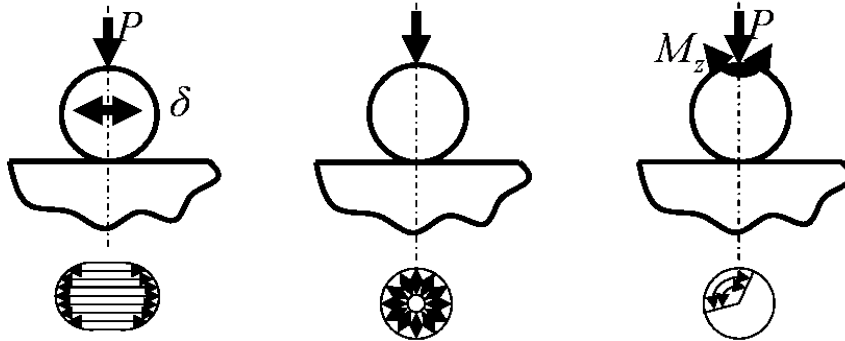


Figure 2.29: Three modes of fretting defined by Mohrbacher [MOH 95]

Computations shown will consist of a rigid ball of radius 1mm on an elastic plastic f at. The hardening law will be considered bilinear, but several hardening laws can also be considered. The elastic plastic properties of the f at are arbitrary chosen and are presented in table 2.4. The coefficient of friction will vary from 0. to 0.4 in simulations, highlighting the influence of the fully coupled approach.

Geometries	Sphere of radius 1mm	Flat
Young's modulus	$E = \infty$	$E = 210GPa$
Poisson coefficient	$\nu = 0.3$	$\nu = 0.3$
Tangent modulus	\emptyset	$Et = 0GPa$
Yield stress	\emptyset	$Sy = 7344MPa$

Table 2.4: Material properties used in elastic-plastic simulations

2.4.2 Fretting mode II: Indentation

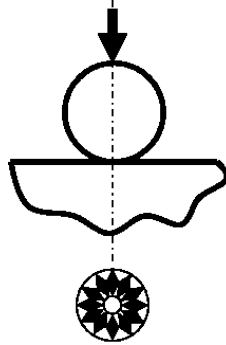


Figure 2.30: Second mode of fretting creates radial slips

Indentation tests are perhaps the most commonly applied means of testing the mechanical properties of materials. An indenter with a geometry known to high precision is the Berkovich tip (three-sided pyramid geometry). But 3D simulations using Finite Element Method (FEM) are cumbersome which makes them most of the time unaffordable or inaccurate (for example for stick-slip contact problems). Indentation simulations treated here are academic and limited to spherical indenters, but pyramidal shaped indenters can also be treated without any difficulty.

In the academic case of a rigid sphere loaded with a normal force P on an elastic-plastic fat, radial displacements may occur. A sticking zone appears for $0 < r < c$ and a slipping zone for $c < r < a$ where 'c' defines the sticking radius and 'a' defines the slipping radius. The fully coupled approach can determine the stick/slip regime in the contact, estimating the sticking and slipping radii. Then, elastic stress fields below the surface can be easily determined. Spence defines 'c' and 'a' as follow [SPE 75].

$$\frac{a}{2c} \cdot \ln \left(\frac{a+c}{a-c} \right) = \frac{\beta}{\mu} \cdot K'(c/a) = \frac{\beta}{\mu} \cdot K(\sqrt{1-(c/a)^2}) \quad (2.151)$$

With K the complete elliptic integral of the first kind and β the Dundurs' constant:

$$\beta = \frac{1}{2} \cdot \left[\frac{(1-2\nu_1)/G_1 - (1-2\nu_2)/G_2}{(1-\nu_1)/G_1 + (1-\nu_2)/G_2} \right] \quad (2.152)$$

Note However, Spence considers the influence of the normal loading on the tangential problem, but neglects the coupling between both problems.

For higher coefficient of friction, influence of tangential problem on normal problem can't be neglected and some differences may be expected. Considering elastic properties defined in table 2.4, $\beta=0.2856$ and the influence of the coefficient of friction on the radii is shown in figure 2.30.

For low coefficients of friction, the Spence's solution fails to predict the vanishment of the sticking area. Another problem encountered by L.Gallego was a persistent sticking area. In actual code, region around zero is still accurate, but criteria have to be refined in order to get an acceptable precision. To recap, the actual elastic-plastic method accurately predicts the second mode of fretting

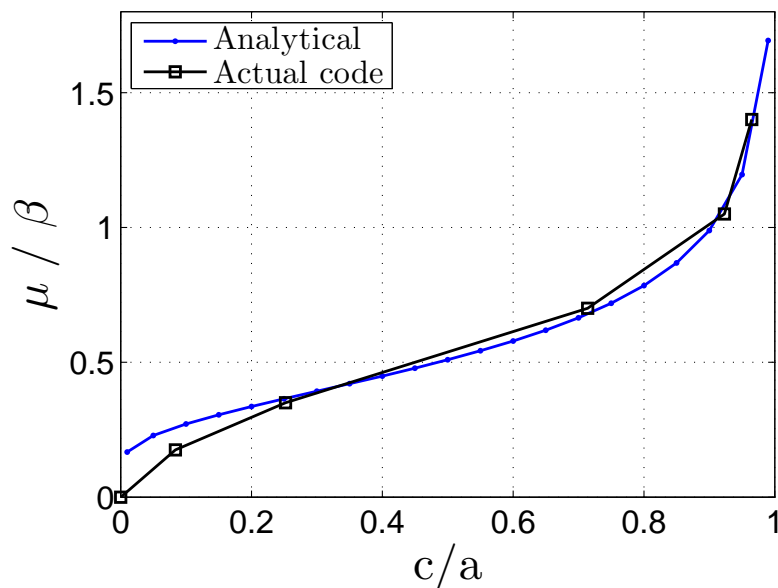


Figure 2.31: Comparison with the sticking radii given by Spence [SPE 75] ($\mu = 0, 0.05, 0.1, 0.2, 0.3, 0.4$)

in elastic regime, with an acceptable precision, and is based on Gallego's work. Considering this validation, computations can now be used considering plasticity.

Because the sticking zone rapidly evolves during the loading process for $\mu/\beta > 0.9$, requiring a finer load discretization to avoid a poor solution as the code depends on the load-history; and because plasticity is an iterative process when relaxation is not set to one; the highest coefficient of friction considered in later studies will then be 0.5 (See table 2.5)

Friction coefficient	0.0	0.05	0.1	0.2	0.3	0.5
Normal load P (N)	up to 12.3 N					
PHertz (MPa)	up to 14690Mpa					

Table 2.5: Normal loading simulations considering a plastic behavior

Coefficient of friction, related to material properties, is very well known for influencing the critical load in fully sliding contact. While coefficient of friction increases, critical load decreases. Previous SA contact codes neglected the coupling between both normal and tangential problems, assuming no friction or a fully slipping contact only as the tangential problem was not solved. Those assumptions are obviously not accurate in a case of indentation. Using the actual code influence of the coefficient of friction can already be highlighted in the partial slip regime of the rigid sphere loaded on a steel-fat, as shown in figure 2.32. In this case, the critical load decreases and has a horizontal asymptote for a value different of zero. This result can be theoretically explained, and depends on material properties.

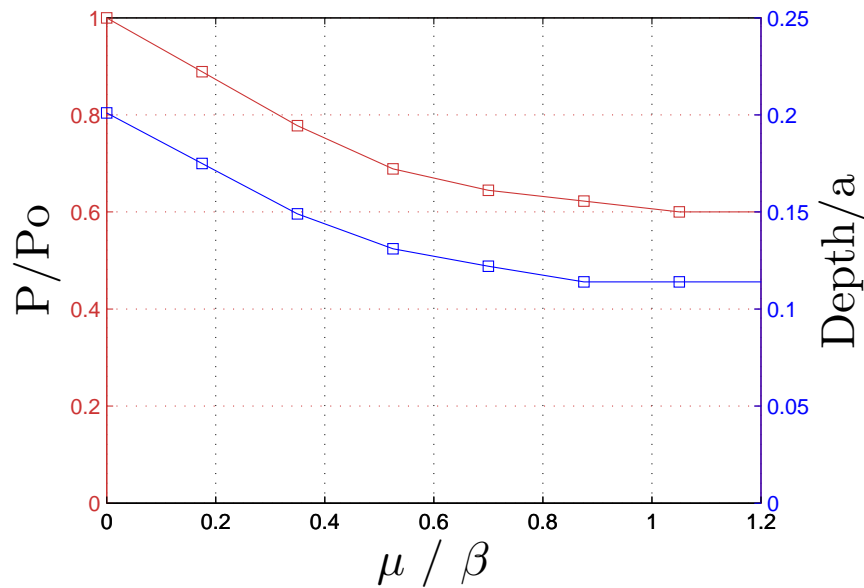


Figure 2.32: Influence of the friction coefficient on the critical load (left) and depth (right) at the onset of yielding normalized by the values for frictionless contact and stick-slip contacts

On the first hand shears are bounded by the pressure times the coefficient of friction in the slipping zone. On the other hand, as the coefficient of friction increases, the slipping annulus vanishes. This observation itself permits to explain the shape of the critical load vs. friction coefficient curve. Coefficients of friction so that μ/β is greater than 0.9 lead to a small slipping zone where the influence of the coefficient of friction is reduced. Considering a perfectly plastic material (See table 2.4), and indentation properties defined in table 2.5, we are about to investigate the influence of plasticity on the stick-slip regime in normally loaded contacts. It has been shown in recent experiments [OVC 09], that very high plastic rates lead to a sticking regime, while normal and/or tangential tractions are applied.

The ratio between the Hertzian pressure and the yield stress will be considered in order to give dimensionless results, P_0 / S_y . Isotropic hardening is considered and a von Mises criterion is used.

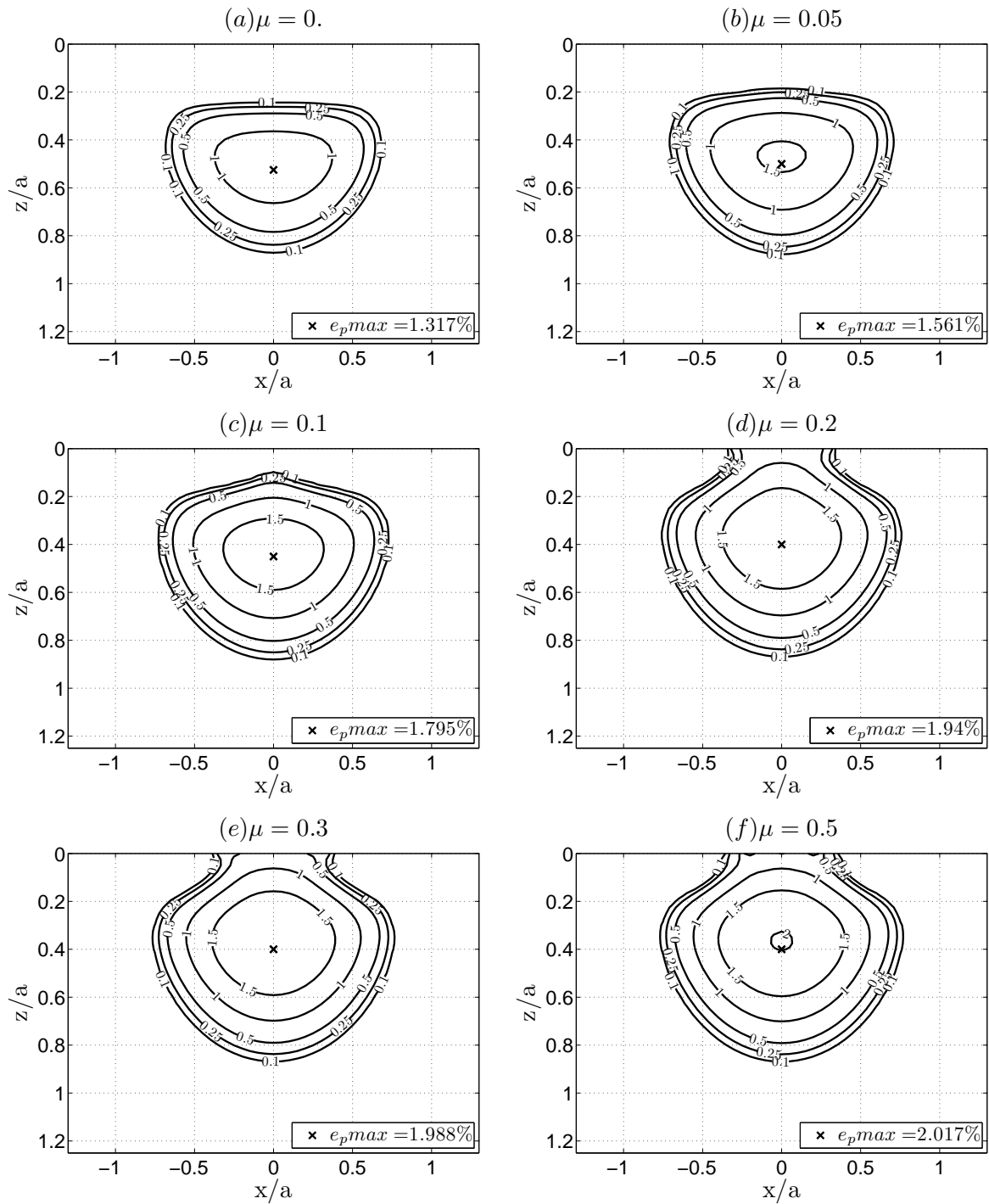


Figure 2.33: Equivalent plastic strain for an indentation test ($P_0/S_y=2$) and various coefficients of friction

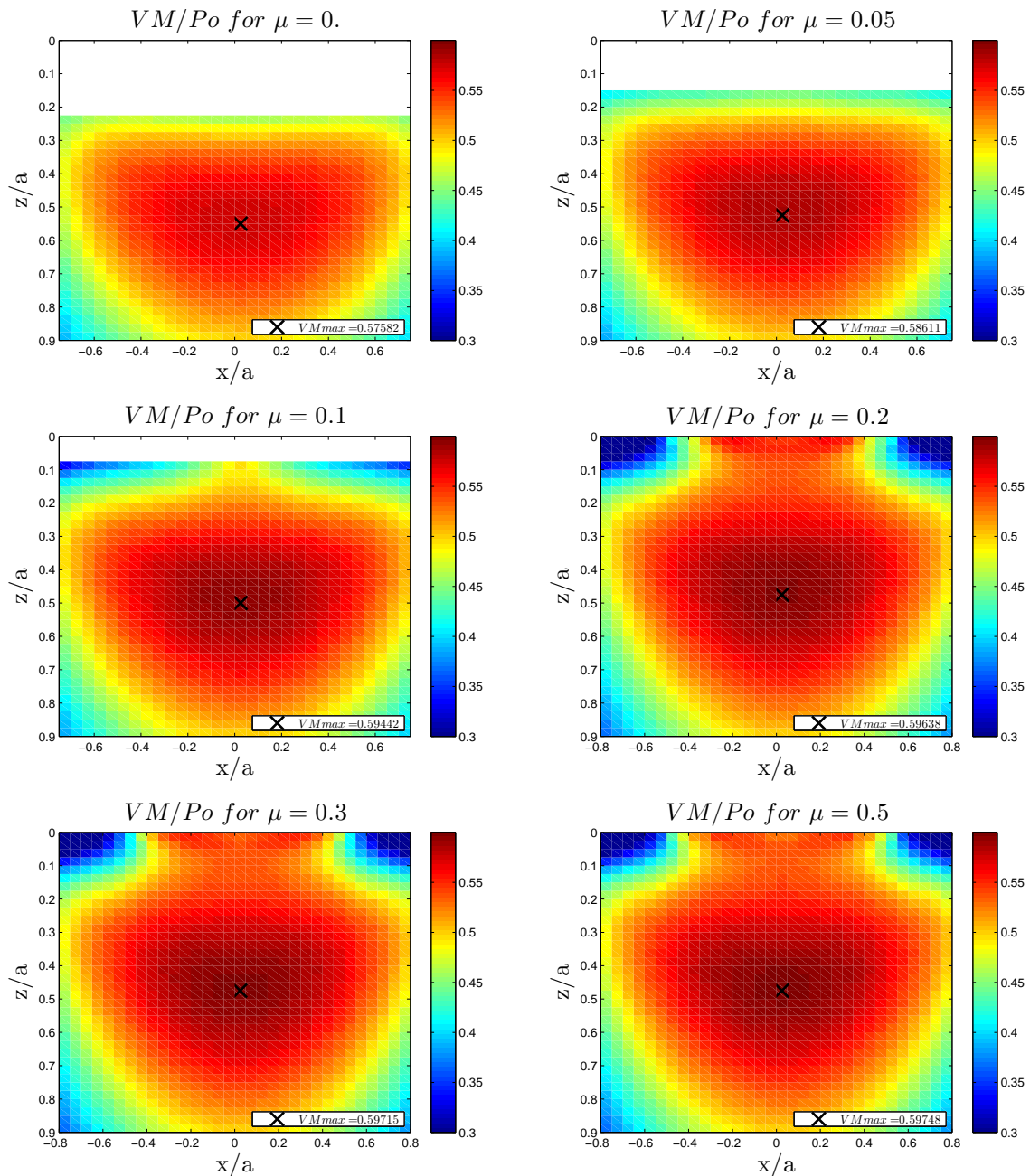


Figure 2.34: Von Mises stress for an indentation test when loaded ($Po/Sy=2$) and various coefficients of friction

Po/Sy is kept small and $Po/Sy=2$. Because of additional surface tractions caused by friction, the critical load decreases, and additional plastic strains are finally observed for P_{max} . Moreover, it can be observed that for $\mu = 0.2$ ($\beta = 0.2856$ and $\mu/\beta = 0.7$) plastic strains arise into the contact as seen in figure 2.33. The influence of friction on the maximum plastic strain is also presented in

figure 2.35.

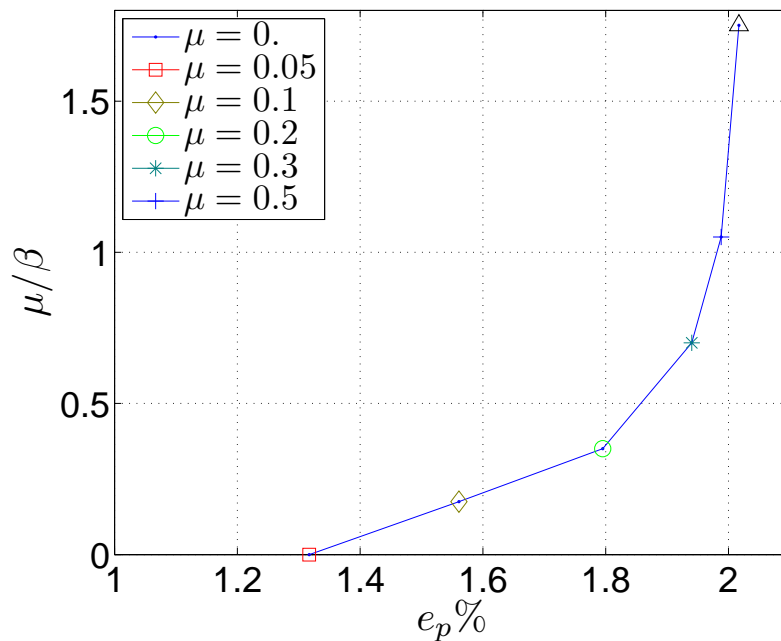


Figure 2.35: Influence of friction on the maximum plastic strain for $Po/Sy=2$

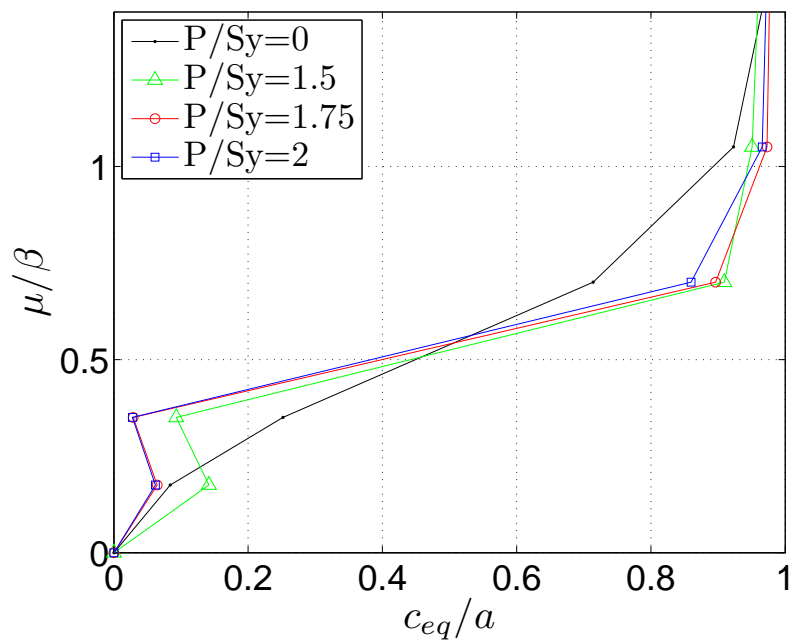


Figure 2.36: Evolution of sticking radii with the coefficient of friction

For $\mu/\beta < 0.5$, the sticking radius c is reduced by plastic strains. On the other hand, for $\mu/\beta \geq 0.5$, plastic strains arise into the contact and increases the sticking radius (See Figure 2.36). For $\mu = 0.2$ ($\mu/\beta = 7$) some differences may be observed in the order of data and is due to a second annulus of slip, making the definition of c_{eq} and c different. This problem will be discussed later.

On the meantime, plastic strain profiles presented in figure 2.33 are modifying the contact geometry, creating radial and vertical displacements, as shown in figure 2.37. Those residual displacements modify the contact conditions, pressure, shears and slip profiles and are of a great importance.

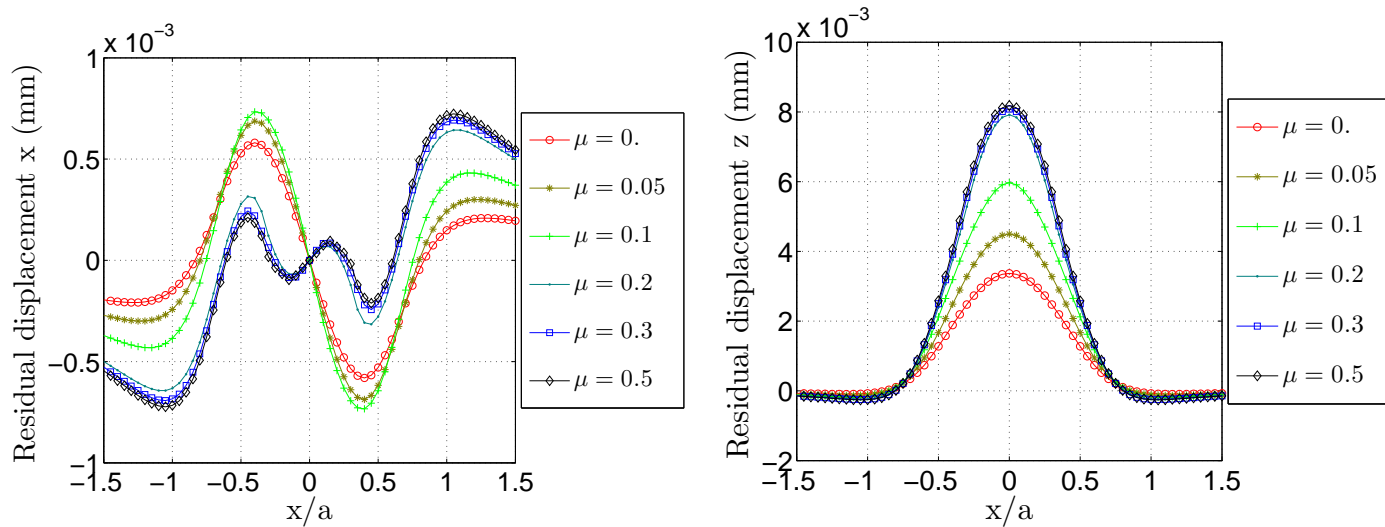


Figure 2.37: Residual print along x (left) and z (right) for an indentation test ($P_o/S_y=2$) and various coefficients of friction

The shape of the normal residual displacement fields are quite similar, regardless of the friction coefficient, but amplitudes are more than doubled. Classically, a pile-up effect is observed outside of the contact and a sink-in effect is observed in the middle of the contact for all cases. However, the shape of the tangential residual displacement fields are strongly modified when considering high coefficients of friction, and a wave-effect is observed in the middle of the contact for $\mu/\beta = 0.7$ or higher. As a matter of fact, this wave actually appears when plasticity arises into the contact. Two cases are then considered:

- for $\mu/\beta < 0.7$: The plastic zone is located below the surface. Any point of the surface which is outside of the contact zone, or close to the edges of the contact, is moving away because of the pile-up effect. Other points, in the middle of the contact, are moving in the opposite direction because of the sink-in effect.
- for $\mu/\beta > 0.7$ The plastic zone can be divided in two regions, (i) a region located below the surface which produces similar surface displacements as for lower friction coefficient and (ii) the plastic zone found at the surface in the center of the contact. This region (ii) creates an additional tangential residual displacement. The actual profile can be found by summing both effect (i) and (ii) as shown in figure 2.38.

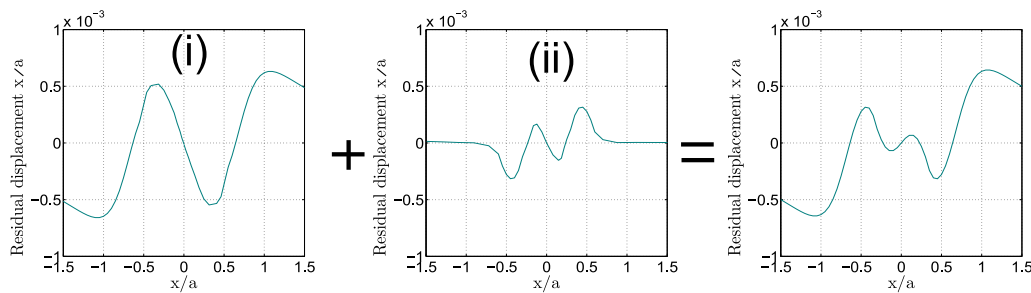


Figure 2.38: The shape of the tangential residual displacements when considering (i) the influence of deep plastic strains and (ii) the influence of plastic strains close to the surface. Results have been modified to be illustrative, should not be used for reference and are presented in order to help the lecturer only.

Normal residual displacements are classically taken into account in the literature. However, tangential residual displacements were not considered, and were neglecting the influence of friction in stick/slip contacts such as indentation processes. In consequence, figure 2.37 proves the importance of a fully-coupled approach and the importance of tangential residual displacements.

In figure 2.36, the equivalent sticking radius c_{eq}/a was calculated using the slipping and sticking contact areas, with N_{stick} and N_{slip} the number of points in the sticking and slipping zone, and assuming a unique annulus of slips.

$$c_{eq}/a = \sqrt{\frac{N_{stick}}{N_{stick} + N_{slip}}} \quad (2.153)$$

Oddly, this assumption is not true in some cases and two annuli of slips may exist in the same contact as shown in figure 2.39d. This phenomenon has not yet been verified experimentally or numerically, but is discussed below.

Frictionless elastic-plastic indentation is classical (See Figure 2.39a). The maximum contact pressure drops at the center of the contact and the contact area slowly evolves. The contact pressure is progressively fattened. The maximum contact pressure may eventually move away from the center, and forms an annulus of maximum pressure, for highest plastic strains.

For lowest coefficients of friction ($\mu/\beta < 0.7$) and $Po/Sy=2$, the maximum contact pressure drops at the center of the contact, and the sticking radius decreases (See Figure 2.39b and 2.39c). A slight peak of pressure may be observed in the middle of the contact zone because of the coupling between the normal and tangential problem and the small sticking area.

For ($\mu/\beta = 0.7$) and $Po/Sy=2$, plastic strains reach the surface. Then the sticking radius slowly increases (See Figure 2.39d). In the meantime, an annulus of maximum shear is formed for $Po/Sy=1.75$ at the edge of the hardened area of the contact. This annulus of maximum shear finally creates a second annulus of slips. An annulus of pressure is also observed.

For highest coefficients of friction ($\mu/\beta < 0.7$) and $Po/Sy=2$, conclusions are very similar (See Figure 2.39e and 2.39f). However, the annulus of maximum shear observed at the edge of the hardened area of the contact is not sufficient to form an annulus of slip. It could be forecast that, for higher loads or higher levels of plasticity i.e. $Po/Sy > 2$, a second annulus of slip may appear.

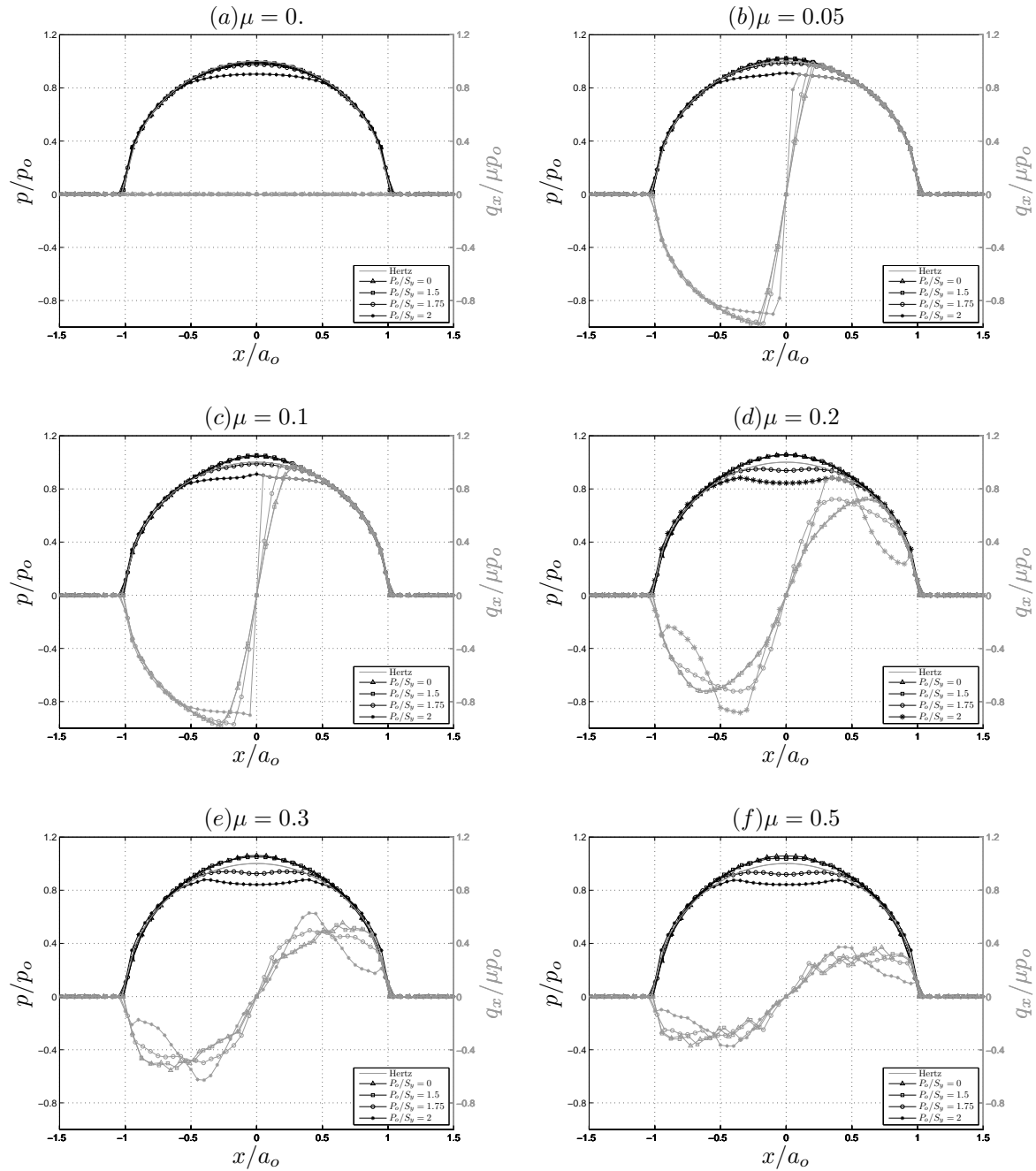


Figure 2.39: Pressure and shears normalized by the hertzian pressure for various plastic rates ($P_0/S_y=0$, $P_0/S_y=1.5$, $P_0/S_y=1.75$ and $P_0/S_y=2$) and for various friction coefficients

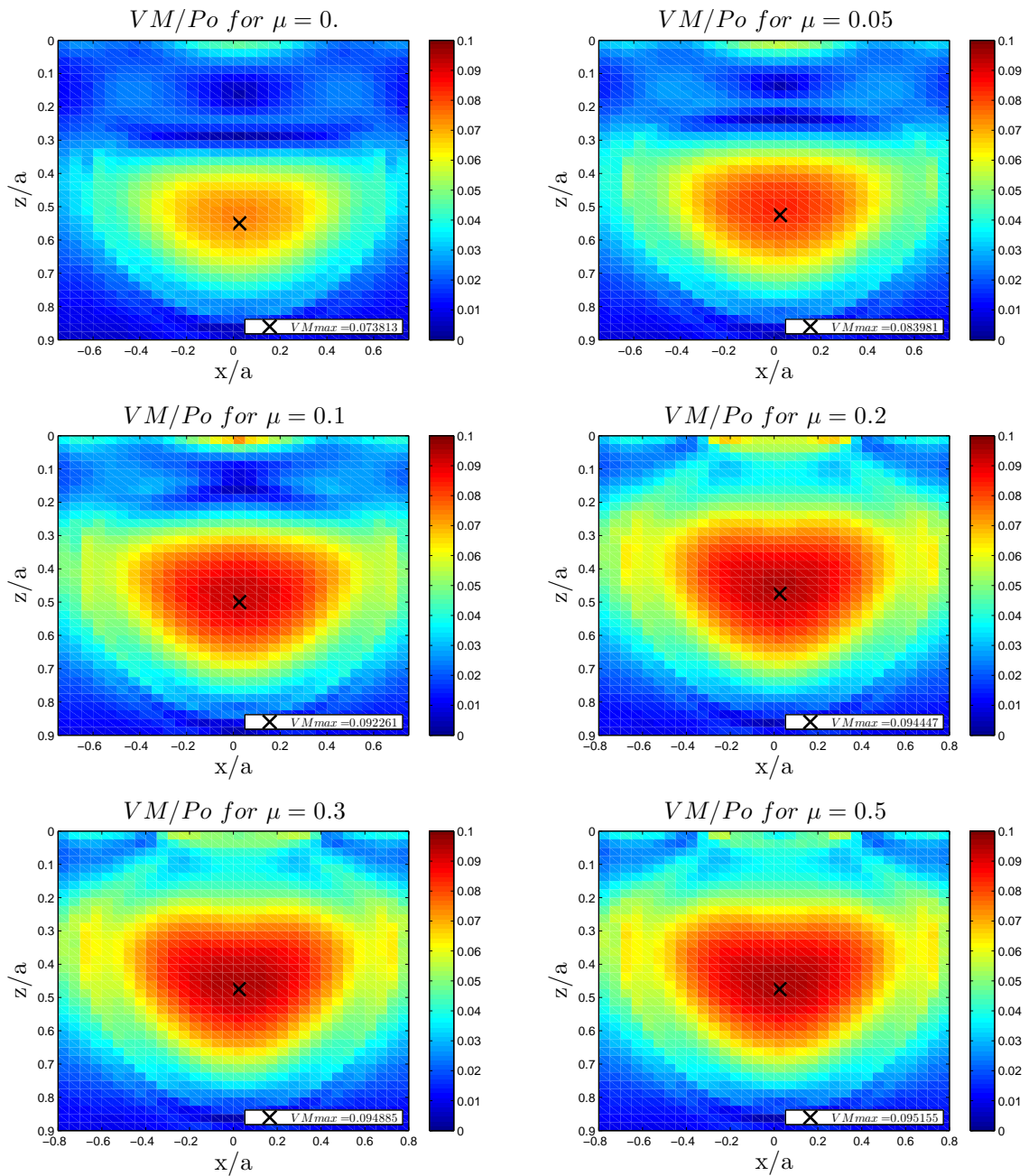


Figure 2.40: Von Mises residual stress for an indentation test when unloaded ($Po/Sy=2$) and various coefficients of friction

Finally, the von Mises residual stresses and hydrostatic residual stress normalized by the hertzian pressure are shown in figures 2.40 and 2.41. Figure 2.41 is of a great importance, highlighting the influence of plasticity on traction and compressive zones.

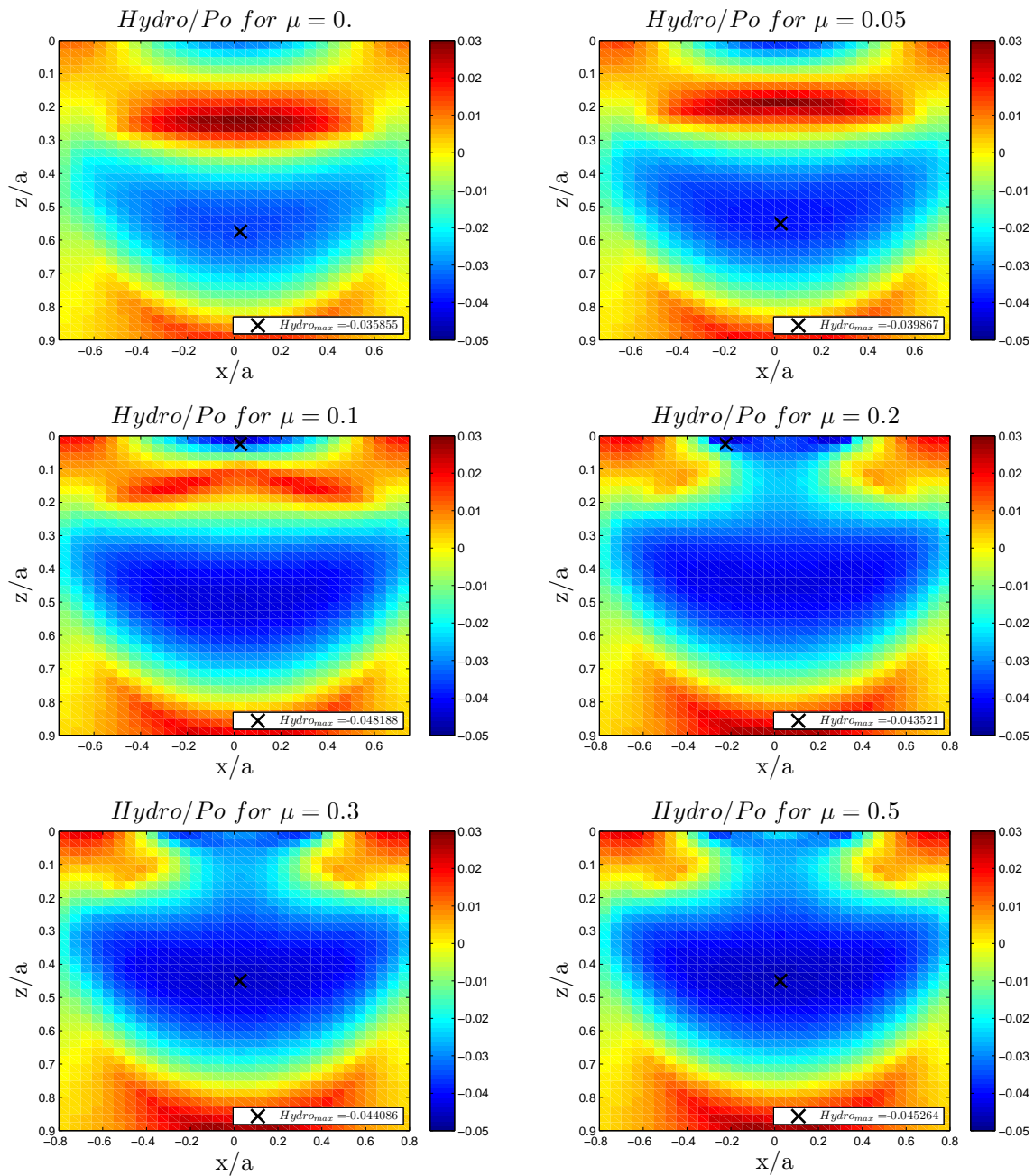


Figure 2.41: Hydrostatic residual stress for an indentation test when unloaded (Po/Sy=2) and various coefficients of friction

2.4.3 Fretting mode I: Sliding

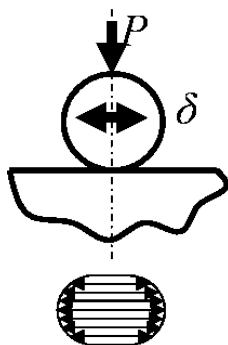


Figure 2.42: First mode of fretting creates slips along one direction

Fretting tests are commonly applied for testing the tribological properties of materials, but scratch tests are also used for testing the mechanical properties of materials. The given indenter is initially normally loaded (See section 2.4.2). A tangential loading (force or displacement) is then applied, and can be linear for scratch-characterization tests or oscillating for fretting tests.

The academic case of a rigid sphere loaded with a normal force P and a tangential force Q on an elastic f at have been intensively studied and analytical solutions are known as the Cattaneo-Mindling Concept [CAT 38, MIN 49, MIN 53]. However, this problem becomes much more complicated while considering an elastic-plastic f at and a complete coupling between the normal, tangential and plastic problems.

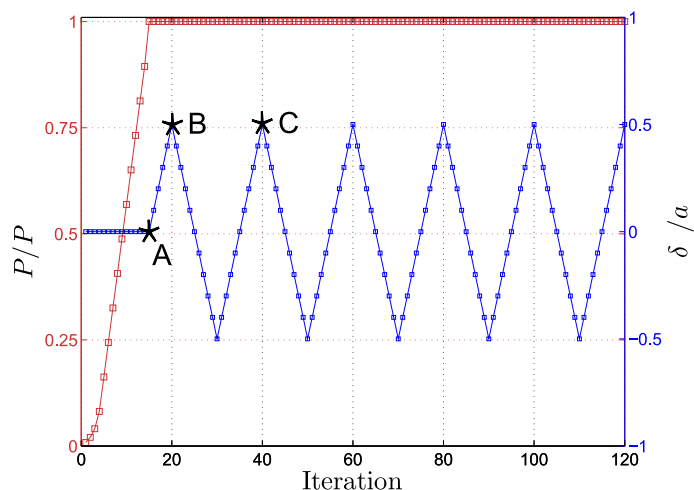


Figure 2.43: Normal and tangential loadings for a sphere moving over an elastic-plastic surface, in the stick-slip regime

Few results will be presented considering a tangential load $Q = 0.5\mu P$ and various coefficients of friction ($\mu = 0.05$, $\mu = 0.1$, $\mu = 0.2$, $\mu = 0.3$, $\mu = 0.5$). Those results are highlighting some of the possibilities permitted by such method and can not account for all possible phenomena. Two cases will be considered for the tangential force Q :

- (I) A tangential force Q is applied up to $Q = 0.5\mu P$, and the system response is studied from point A to point B (See Figure 2.43)
- (II) The tangential force is now oscillating between $Q = 0.5\mu P$ and $Q = -0.5\mu P$, and the system response is studied from point B to point C.

(I) Considering an increasing tangential force: On the first hand, considering the normal loading P and plastic properties, plastic strains are not visibly changed for coefficients of friction $\mu < 0.3$ and the influence of a given plastic strain field on the stick-slip regime will be clearly visible.

On the other hand, for $\mu \geq 0.3$, the tangential loading is sufficient to change the plastic strain profiles and a mutual interaction will be observed. Plastic strain fields for $\mu = 0.3$ and $\mu = 0.5$ are presented in figure 2.44.

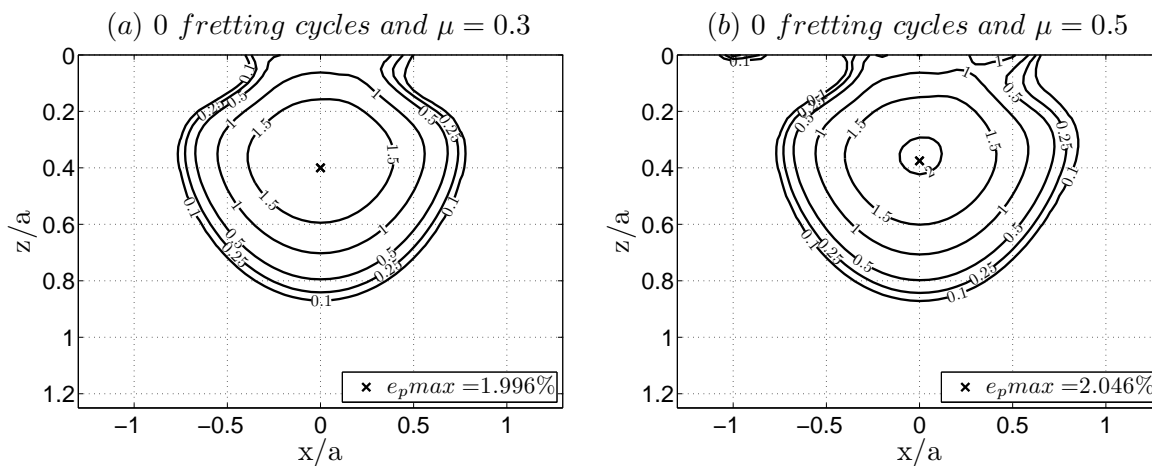


Figure 2.44: Equivalent plastic strains in the stick-slip regime ($Q = 0.5\mu P$) for $\mu = 0.3$ and $\mu = 0.5$ at point B in figure 2.43

As a matter of fact, residual displacements are not modified for $\mu < 0.3$ as seen in figure 2.46 when compared to figure 2.37.

On the other hand, for $\mu \geq 0.3$, a slight dissymmetry is visible for normal residual displacements which remain globally unchanged. On the opposite, tangential residual displacements are drastically modified on the sliding direction side and is due to additional plastic strains at the interface as seen in figure 2.46. It must be noticed that the maximum equivalent plastic strain is slightly increased only, and is still located below the surface for $Q = 0.5\mu P$.

Contact conditions are presented in figure 2.45. For $Q/\mu P = 0$ shears are axisymmetric, while shears should all be along the sliding direction for $Q = \mu P$. In consequence, slipping region in which $qx/\mu po = -1$ evolves and progressively becomes sticking until the contact reaches the gross-slip regime and $qx/\mu po = 1$ in the contact area for $Q = \mu P$. Same evolutions are observed in the Cattaneo-Mindlin Concept. In this study Q is not greater than $0.5\mu P$.

However, it must be noticed that a second slipping region may appear (See Figure 2.45e) or exist (See Figure 2.45d) when considering high coefficients of friction ($\mu \geq 2$) and hardening

occurring at the interface. This is not observed in the elastic regime, and is due to the tangential residual displacements presented in figure 2.46.

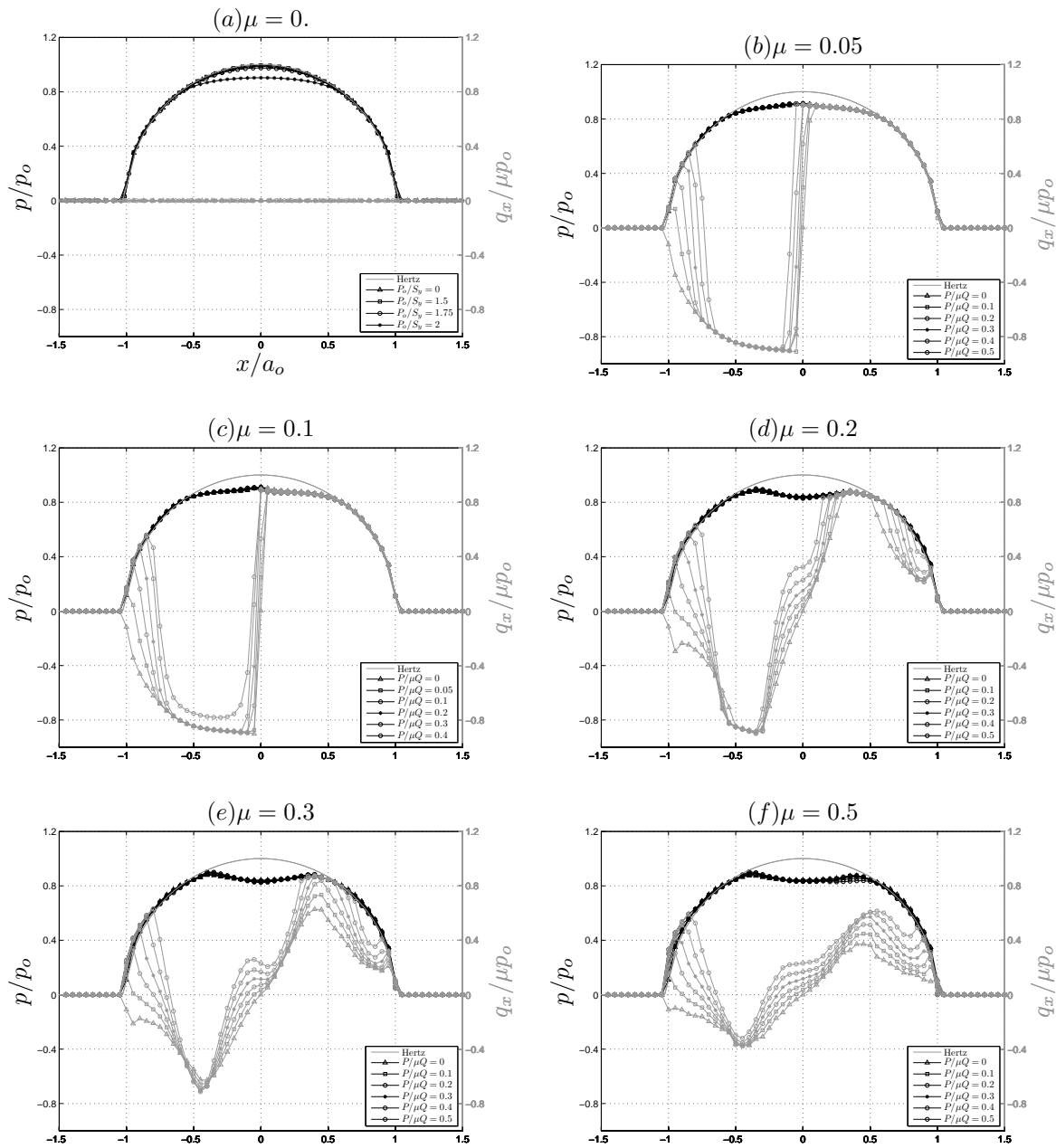


Figure 2.45: Pressure and shears normalized by the hertzian pressure for $P_0/S_y=2$, an increasing tangential load and for various friction coefficients

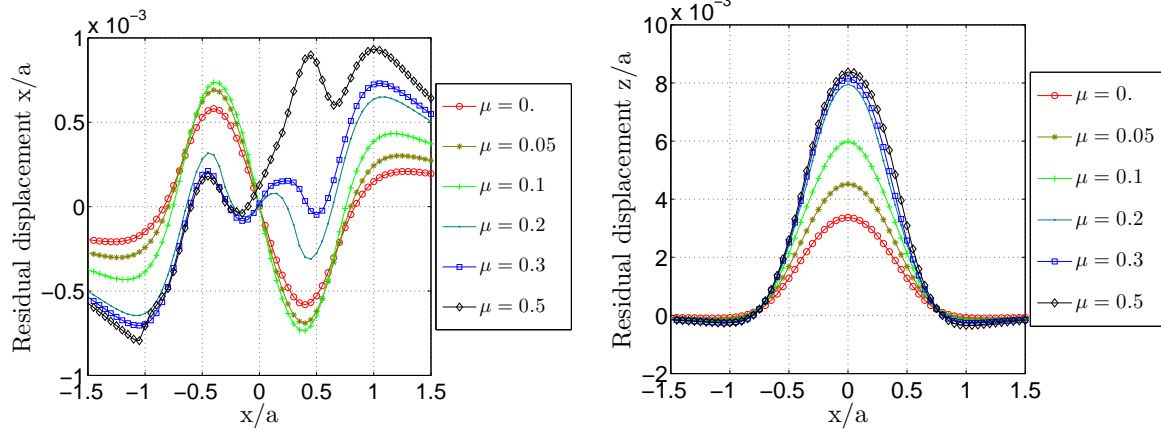


Figure 2.46: Residual print along x (left) and z (right) in the stick-slip regime ($Q = 0.5\mu P$) considering an elastic-plastic media (point B in figure 2.43) so that $Po/Sy=2$ and various coefficients of friction

(II) Considering an oscillating tangential force: The tangential load Q will now describe a complete fretting cycle from point B to point C (See Figure 2.43). Considering the normal loading P and plastic properties, plastic strains are not visibly changed for coefficients of friction $\mu < 0.3$ and plastic strain fields are not presented for such coefficient of friction. However, for $\mu \geq 0.3$ plastic deformations are produced at the interface making plastic strain profiles quasi-symmetric (See Figure 2.47). It must be noticed that the maximum plastic strain, located deeper below the surface is not modified.

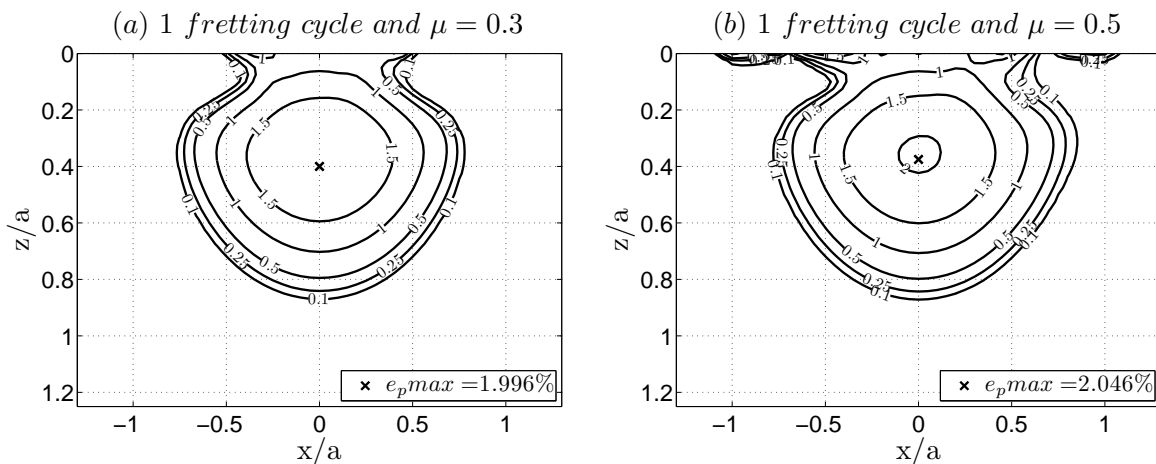


Figure 2.47: Equivalent plastic strains in the stick-slip regime ($Q = 0.5\mu P$) for $\mu = 0.3$ and $\mu = 0.5$ at point C in figure 2.43

As a matter of fact, residual displacements are not modified for $\mu < 0.3$ as seen in figure 2.48 when compared to figure 2.37. Tangential residual displacements are drastically modified for $x/a < 0$ and $\mu \geq 0.3$ because of the spherical indenter going back and forth, and new plastic strains produced for $x/a < 0$.

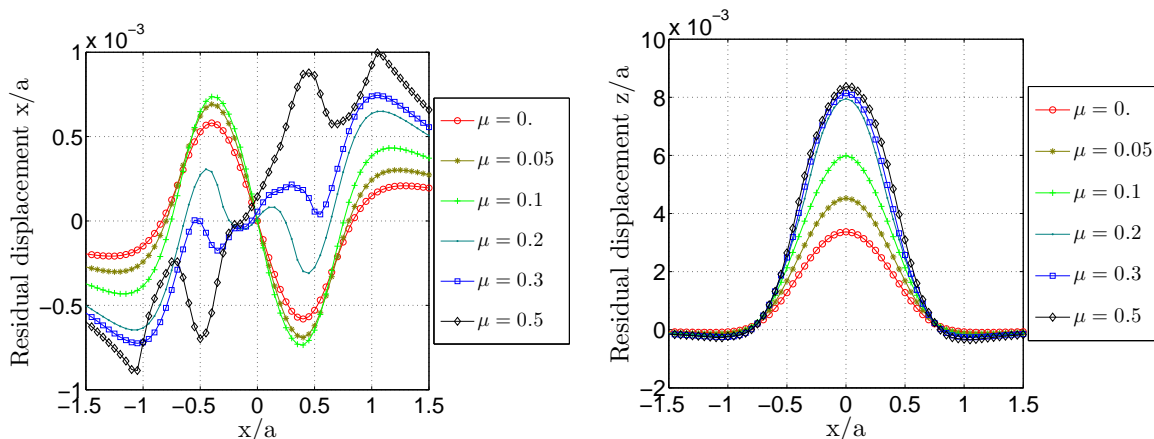


Figure 2.48: Residual print along x (left) and z (right) in the stick-slip regime ($Q = 0.5\mu P$) considering an elastic-plastic media so that $Po/Sy=2$, after 1 fretting cycle (point C in figure 2.43), and various coefficients of friction

Contact conditions are presented in figure 2.49 and become complicated for a non practiced eye. In figures 2.49e and 2.49f, plastic strains created at the interface in the stick-slip regime make shear profiles particularly rough, and each curve of both figures should be watched carefully and are not as rough as it seems...

2.4.4 Conclusion

Two modes of fretting were briefly studied in this section. The second mode of fretting (indentation) and the first mode of fretting (sliding).

The second mode was first investigated and is very academic. But many key-parameters had to be chosen and results presented could be very different when considering another set of parameters. A perfectly plastic hardening law was considered and the yield stress Sy was set equal to $Sy = 0.5Po$, where Po is the Hertzian pressure in the elastic case. Using another hardening law could drastically change the results. It was observed that for $\mu/\beta \geq 0.7$, additional plastic strains were produced in the middle of the contact making tangential residual displacement profiles characteristic. Shear profiles were modified accordingly, and a second annulus of slip was observed and located approximately at the edge of the disc of plastic strains at the interface. This result is typical and was not observed yet, but an explanation was given. Von Mises stresses, von Mises and hydrostatic residual stresses were also presented and highlighted a strong influence of friction in the contact regime even during indentation processes. It must be noticed that friction has a great influence on the residual print and mechanical properties could be underestimated when considering a frictionless contact.

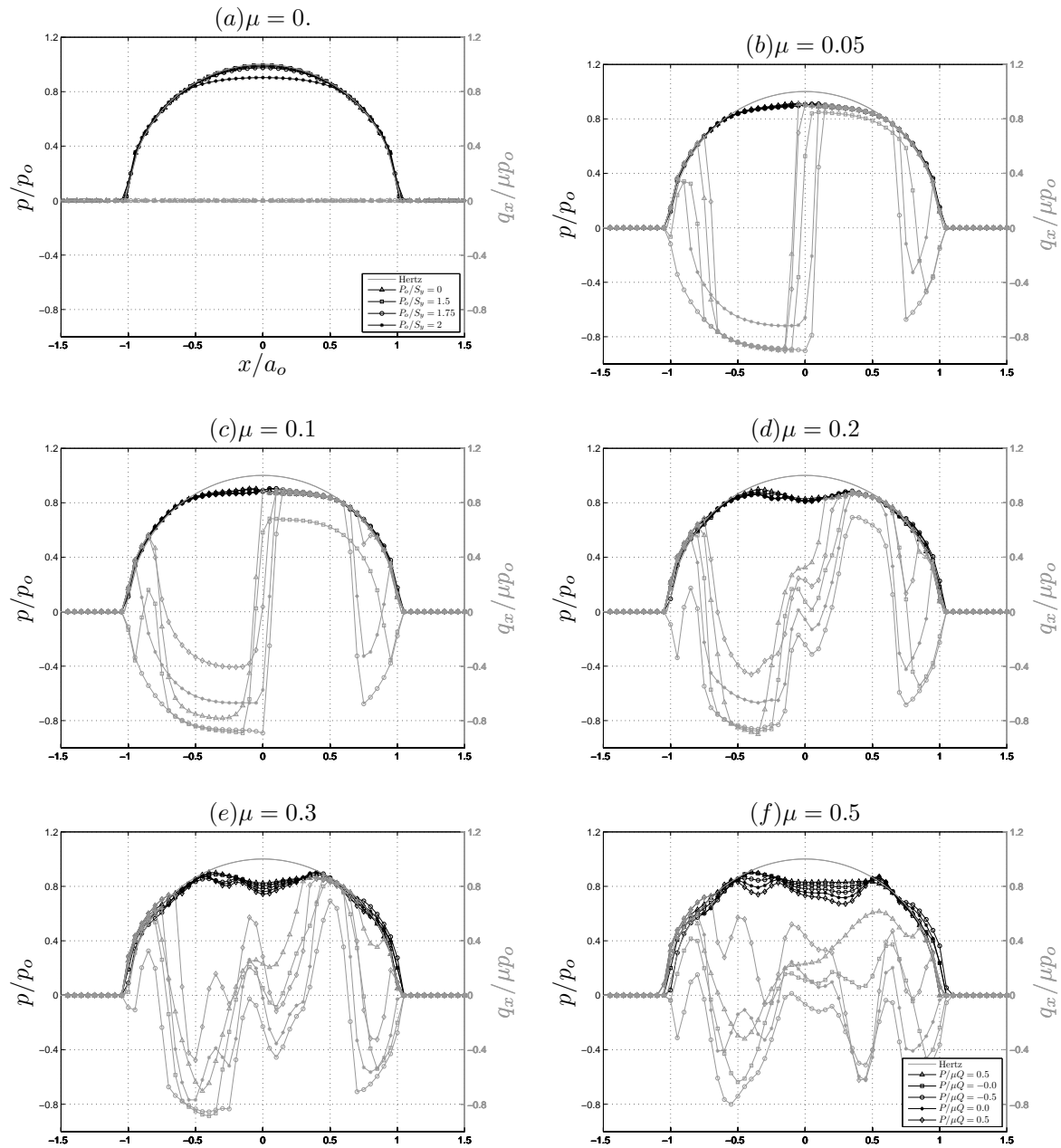


Figure 2.49: Pressure and shears normalized by the hertzian pressure for $P_0/S_y=2$, an oscillating tangential load (from point B to C) and for various friction coefficients

The first mode was then investigated and it appeared that the normal load P had a great influence on results. In addition, the maximum tangential force Q was also of a great importance. This problem is more complicated and can not account for all cases, even when presenting dimensionless results, so it was decided to present two cases among all others. Additional plastic strains were observed at the interface for $\mu/\beta \geq 1.05$ when increasing the tangential load Q up to $Q = 0.5\mu P$. Normal residual displacements remained almost unchanged, but tangential residual displacements were clearly modified for $\mu/\beta \geq 1.05$. Finally, contact pressure and shear profiles were presented after an initial tangential loading and after the first fretting cycle. It was shown that plastic strain and residual displacement profiles became globally symmetric after a complete fretting cycle.

2.5 Conclusion

Chiu's formulae used to define the influence of a cuboid of plastic strain on the normal residual displacements have been used and extended to the tangential residual displacements problem. Analytical solutions were found and validated using a FE model. It has been shown that normal and tangential residual displacements are of the same order of magnitude.

Using Gallego's [GAL 07a, GAL 06] and Jacq's [JAC 01, JAC 02] works and recent developments, a fast-computing method was developed and the stability of various internal algorithms was improved. The actual method is able to deal with friction and plasticity at the same time, even in the partial-slip regime, by coupling the normal, tangential and plastic effects. Using such method, two modes of fretting were briefly investigated and highlighted the influence of hardening on the contact conditions. Results relative to this study are discussed in conclusion 2.4.4. A particular phenomenon was observed and should be verified using a three-dimensional FEA considering both friction and hardening.

Chapter 3

Inclusions

Materials used in construction are often considered flawless, which is sufficient at a macro-scale. However, aeronautics and many other fields require a finer approach in order to reduce risks and increase lifetime of parts. High stresses may be found locally under contact conditions. Considering soft or hard inclusions, stresses can be locally much higher, and crack nucleation and growth may occur, reducing drastically the lifetime predictions.

Inclusions can be made of metal (Tungsten, Copper, etc), oxides (Alumina, etc) and non metallic (Carbon, Gaz, etc) of different shapes (Spherical, elliptical, etc). It is of a great importance to consider those inclusions and their elastic-plastic properties in some applications. In this chapter, the Eshelby's theory and recent improvements will be exposed considering spherical and cubical inclusions. Influence of a soft and hard inclusion on the contact will be exposed, and a cluster of inclusions will then be considered.

Contents

3.1 The Equivalent Inclusions Method (EIM) of Eshelby and developments	101
3.1.1 The Equivalent Inclusions Method (EIM) of Eshelby	101
3.1.2 Determination of ϵ^* and ϵ	103
3.1.3 Potentials ϕ and ψ for a sphere	104
3.1.4 Eshelby's tensor of a spherical inclusion	105

3.1.5	Eshelby's tensor for a cubical inclusions	106
3.1.6	Infinite half space using a 3D-FFT algorithm	107
3.1.7	The non-homogeneous solver	109
3.1.8	Non-homogeneous problems considering frictional aspects	110
3.1.9	Non-homogeneous problems with plastic behaviors	112
3.2	Validation of elementary solutions	114
3.2.1	Misfit stresses caused by a spherical inclusion	114
3.2.2	Misfit displacements caused by a spherical inclusion	117
3.2.3	Misfit stresses around a parallelepipedic inclusion	120
3.2.4	Misfit displacements caused by a cuboidal inclusion	120
3.3	Influence of non-homogeneities on contact conditions considering no gradient	123
3.3.1	Influence of the Young's modulus using a cluster of inclusions	124
3.3.2	Influence of the inclusion's radius using a unique inclusion	126
3.3.3	Influence of the Poisson's ratio using a cluster of inclusions	129
3.3.4	Influence of the inclusion's depth using a unique inclusion	131
3.3.5	Mutual interactions	131
3.3.6	Summary	135
3.4	Inclusions considering gradients	137
3.4.1	Enrichment of a complete half-space	137
3.4.2	Inclusions discretized in many cubes	139
3.4.3	Inclusions when considering gradients	142
3.5	Conclusion	143

3.1 The Equivalent Inclusions Method (EIM) of Eshelby and developments

3.1.1 The Equivalent Inclusions Method (EIM) of Eshelby

J.D. Eshelby considers two kind of heterogeneities in a matrix with given material properties. Non-homogeneities which have different mechanical properties, while inclusions which have the same mechanical properties but additional strains, mainly due to cooling processes after thermal treatments. This convention will be used later in this manuscript. However, the formalism used by Eshelby is not convenient, and rarely used in papers. For this reason, the formalism used hereafter is the same as the one used by T.Mura and Moschovidis [MOS 75a]. Let's consider an infinite volume V containing an ellipsoidal domain Ω . The Hooke's tensors are C_m for the matrix and C_i for the ellipsoidal heterogeneity. The matrix is then strained by ϵ^∞ , uniform far away. The problem is about defining fields in and out of the heterogeneity.

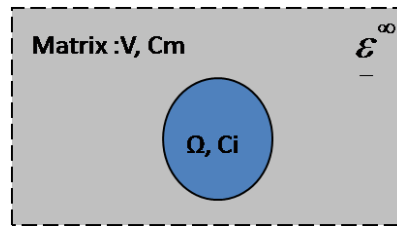


Figure 3.1: Ellipsoidal heterogeneity surrounded by an infinite volume

An 'eigenstrain' will be considered, ϵ^p , and can be hydrostatic due to cooling processes for instance. Furthermore, ϵ will be the elastic strain in and outside the INCLUSIONS and created by its presence, as seen in FIG.3.2.

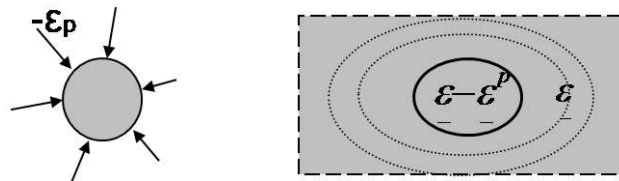


Figure 3.2: Strains defined herebefore, for an ellipsoidal inclusion

Considering the inclusion described herebefore in an infinite matrix, and applying an uniform strain field far away, no difference can be observed for the additional strain field ϵ . If a NON-HOMOGENEITY is then considered, with a Hooke's tensor C_i , and the body is free of stresses far away ϵ^∞ is applied far away, no difference can be observed for the additional strain field ϵ . However, if ϵ^∞ is not nil, the additional strain field ϵ will be modified, as seen in FIG.3.3. It must be noticed that the expressions used to define the additional strain field ϵ are different in and outside the ellipsoid.

According to conventions used in plasticity, the eigenstrain will be noted ϵ^* . This eigenstrain is of a great importance in order to consider an INCLUSION problem instead of a NON-

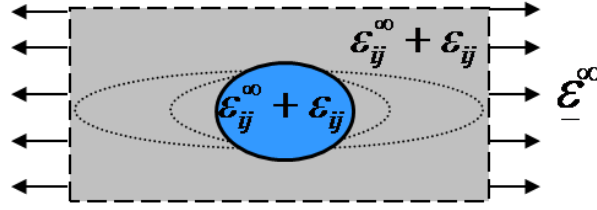


Figure 3.3: Strains defined herebefore, for an ellipsoidal non-homogeneity in a strain field

HOMOGENEITY problem. The problem described in FIG.3.3 is then equivalent to an inclusion problem as defined herebelow.

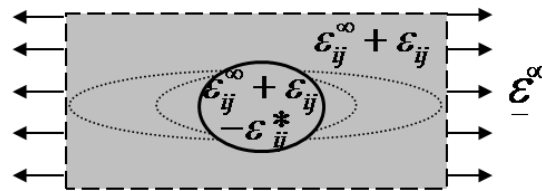


Figure 3.4: Strains for an inclusion equivalent to non-homogeneity in a strain field

Using the equivalence of problems defined in FIG.3.3 and FIG.3.4, and an initial hydrostatic eigenstrain as defined in FIG.3.2, stresses can be expressed by:

$$\sigma = C^I(\epsilon^{\infty} + \epsilon^p - \epsilon) = C^M(\epsilon^{\infty} + \epsilon - \epsilon^* - \epsilon^p) \quad (3.1)$$

A relationship between the strains ϵ , ϵ^* and ϵ^p exists, introducing the Eshelby's tensor noted 'S'. 'S' is defined as a function of harmonic potentials ϕ and ψ .

$$\epsilon = S.\beta = S.(\epsilon^* + \epsilon^p) \quad (3.2)$$

This set of two equations with the two unknown variables ϵ^* and ϵ permits the determination of the eigenstrain ϵ^* . ϵ will then be determined in and out of the heterogeneity. An analogy could be drawn between additional strain field induced by a non-homogeneity and the residual strain field induced by plasticity. However, misfit strains ϵ depend on the uniform strain applied far away, residual strains do not. Later, the eigenstrain considered will be noted $\beta = \epsilon^* + \epsilon^p$, according to notations used in the literature. Misfit strains can also be expressed using Green's functions, as seen in Moschovidis' thesis.

$$\epsilon_{ij} = \frac{1}{8.\pi.(1-\nu)} \cdot (\psi_{,ijkl}.\beta_{kl} - 2.\nu.\phi_{,ij}.\beta_{kk} - 2.(1-\nu).(\phi_{,kj}.\beta_{ik} + \phi_{,ki}.\beta_{jk})) \quad (3.3)$$

where ϕ and ψ are bi-harmonic potentials defined by:

$$\phi = \iiint_{\Omega} \frac{1}{|x-x'|} dx' \quad \psi = \iiint_{\Omega} |x-x'| dx' \quad (3.4)$$

Gradients can be taken into account, strain fields are then developed using Taylor series, where D_{ijkl} , D_{ijklq} , D_{ijklqr} are complex functions of ϕ and ψ . [MOS 75b]

$$\begin{aligned}\varepsilon_{ij}^{\infty} &= E_{ij} + E_{ijk}.x_k + E_{ijkl}.x_k.x_l + \dots \\ \varepsilon_{ij}^* &= E_{ij}^* + E_{ijk}^*.x_k + E_{ijkl}^*.x_k.x_l + \dots \\ \varepsilon_{ij} &= B_{ij} + B_{ijk}.x_k + B_{ijkl}.x_k.x_l + \dots \\ \beta_{ij} &= D_{ij} + D_{ijk}.x_k + D_{ijkl}.x_k.x_l + \dots\end{aligned}\quad (3.5)$$

It is commonly admitted that a development of the second order is good enough. This approach becomes roughly numerical and generates a 60 unknown variables system. (6 E_{ij}^* , 18 E_{ijk}^* and 36 E_{ijkl}^*). However, considering that mesh size is small enough to ensure constant strain in each mesh discretization, and the small error occurring [COU 03], no gradient will be considered farther.

Finally, the approach defined above considers many simplifications such as:

- Infinite matrix with elastic properties
- Unique ellipsoidal inclusion/non-homogeneity.
- Dimensionless problem (cohesion is not accounted for)
- Displacements at the interface are continuous (sticked)

3.1.2 Determination of ε^* and ε

Since the Eshelby's tensor is not necessarily invertible, the definition of the Eshelby's tensor $\varepsilon = S.\beta = S.(\varepsilon^* + \varepsilon_p)$ is used in the continuum equation of stresses for the non-homogeneity and inclusion problem:

$$C^I.(\varepsilon^{\infty} + \varepsilon - \varepsilon^p) = C^M.(\varepsilon^{\infty} + \varepsilon - \varepsilon^* - \varepsilon^p) \quad (3.6)$$

The eigenstrain ε^* is then:

$$\varepsilon^* = (\Delta C.S - C^M)^{-1}.\Delta C.(-\varepsilon^{\infty} - S.\varepsilon^p + \varepsilon^p) \quad (3.7)$$

Where ΔC is the difference of material properties so that: $\Delta C = C^M - C^I$

The eigenstrain ε^* will be estimated for each non-homogeneity and each time it is needed; for instance when strains applied far away change. This approach is purely analytical, using matrix computations, except for the inversion of the first term which is made numerically. Once ε^* is estimated, strains and stresses inside and outside of the non-homogeneity can be found.

When many inclusions – or non-homogeneities – are considered, computations can be time consuming. However, it must be noticed that misfit strains are linearly dependent of each component of eigenstrains. So, if only few sizes – or later, few shapes – are considered, influence coefficients K^{β} for each component of each kind of inclusion centered in (x_0, y_0, z_0) can be calculated once for all.

$$\sigma_{ij(x,y,z)} = \sum_{inclusions} \beta_{kl}.K_{ijkl(x-x_0,y-y_0,z-z_0)}^{\beta} \quad \text{or} \quad \sigma_{(x,y,z)} = K_{(x-x_0,y-y_0,z-z_0)}^{\beta}.\beta$$

Numerical methods, such as the DC-FFT, used thereafter are exposed in [LIU 00] and will be extended considering 3D-FFT instead of 2D-FFT, which considerably reduce the memory size and computing time [ZHO 06].

3.1.3 Potentials ϕ and ψ for a sphere

The misfit strain ϵ depends on the eigenstrain β and harmonic potentials ϕ and ψ . Those potentials are different for every geometry and can be expressed for ellipsoids as follow:

$$\frac{\partial \psi}{\partial x} = x \cdot \pi \cdot a \cdot b \cdot c \cdot \int_{\Omega}^{\infty} \frac{U \cdot u \cdot du}{(a^2 + u) \cdot \Delta} \quad \phi = \pi \cdot a \cdot b \cdot c \cdot \int_{\Omega}^{\infty} \frac{U \cdot du}{\Delta} \quad (3.8)$$

With Δ equal to:

$$\Delta = (a^2 + u)^{1/2} \cdot (b^2 + u)^{1/2} \cdot (c^2 + u)^{1/2} \quad (3.9)$$

And U defined by:

$$U(u) = 1 - \frac{x^2}{a^2 + u} - \frac{y^2}{b^2 + u} - \frac{z^2}{c^2 + u} \quad (3.10)$$

The lower bound of integrals, λ , is the highest positive root of the equation $U(u)=0$ for a point out of the inclusion. If the point considered is inside, λ is set equal to zero ($\lambda=0$).

Until now, numerical solvings have been avoid considering no gradient. However, fields created by any ellipsoidal inclusion – including prolate and oblate ellipsoids, but excluding spherical inclusions – is expressed using incomplete elliptic integrals of the first and second kind, F and E respectively, requiring a numerical solving. More generally, four kinds of inclusions are highly interesting (FIG.3.5), but require a numerical computation of both potentials. Those inclusions will be investigated in a coming study.

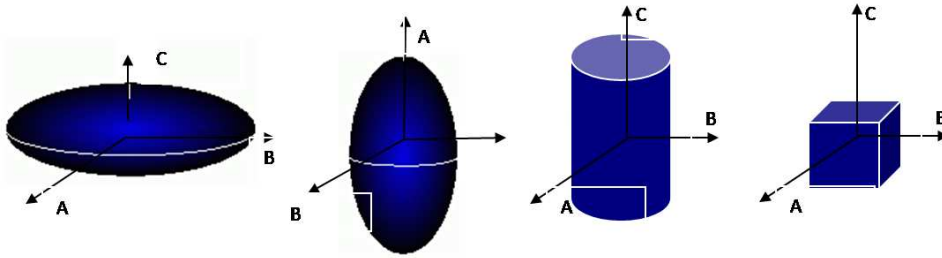


Figure 3.5: Oblate (left) and prolate (right) ellipsoids, finite cylinder, cube

In this chapter, spherical inclusions will be considered and implemented in the elastic-plastic contact code. Further development will only consist of defining potentials for different geometries, without major modification of the existing routines.

The lower bound of integrals defined previously, when considering a point outside of the spherical inclusion, is the highest positive root of $U(u)=0$. With $a=b=c$, it comes:

$$U(u) = 1 - \frac{x^2}{a^2 + u} - \frac{y^2}{b^2 + u} - \frac{z^2}{c^2 + u} = 0, \text{ then } u = -a^2 + x^2 + y^2 + z^2 \quad (3.11)$$

Potentials become:

$$\frac{\partial \psi}{\partial x} = x \cdot \pi \cdot a \cdot b \cdot c \cdot \int_{\lambda}^{\infty} \left(\frac{u}{(a^2 + u)^{5/2}} - \frac{u \cdot (x^2 + y^2 + z^2)}{(a^2 + u)^{7/2}} \right) \cdot du \quad (3.12)$$

$$\phi = \pi \cdot a \cdot b \cdot c \cdot \int_{\lambda}^{\infty} \left(\frac{1}{(a^2 + u)^{3/2}} - \frac{x^2 + y^2 + z^2}{(a^2 + u)^{5/2}} \right) \cdot du \quad (3.13)$$

We can use this method to give a simple expression of potentials ϕ and ψ out of the sphere. So, for $r > a$:

$$\begin{aligned} \phi &= \frac{4}{3} \cdot \pi \cdot a^2 \cdot \frac{a}{r} \\ \psi &= \frac{4}{3} \cdot \pi \cdot a^4 \cdot \left(-\frac{1}{5} \cdot \frac{a \cdot x}{r^3} + \frac{x}{r \cdot a} \right) \end{aligned} \quad (3.14)$$

Derivates can be easily found but are cumbersome and won't be exposed in this chapter. Most of derivates are expressed and can be found in section 3.2.1. Influence of an eigenstrain on all points outside of the inclusion can now be found using the equation of misfit strains expressed by Moschovidis:

$$\varepsilon_{ij}^m = \frac{1}{8 \cdot \pi \cdot (1 - \nu)} \cdot (\psi_{,ijkl} \cdot \beta_{kl} - 2 \cdot \nu \cdot \phi_{,ij} \cdot \beta_{kk} - 2 \cdot (1 - \nu) \cdot (\phi_{,kj} \cdot \beta_{ik} + \phi_{,ki} \cdot \beta_{jk})) \quad (3.15)$$

When β equal to unity ($\beta=1$), misfit strains are the coefficient of influence computed once for all at the beginning of the computations for each ratio between the mesh and inclusion size.

3.1.4 Eshelby's tensor of a spherical inclusion

If the lower bound λ of integrals defined previously is set equal to zero, potentials can be defined inside of the spherical inclusion. Using the equation relating misfit strains and eigenstrains expressed by Moschovidis, the misfit strains inside the inclusion can be expressed as a function of eigenstrains using a tensor known as the Eshelby's tensor, so that $\varepsilon = S \cdot \beta$. After simplifications, it comes:

$$\begin{aligned} S_{1111} = S_{2222} = S_{3333} &= \frac{7 - 5 \cdot \nu}{15 \cdot (1 - \nu)} \\ S_{1122} = S_{2211} = S_{2233} = S_{3322} = S_{3311} = S_{1133} &= \frac{5 \cdot \nu - 1}{15 \cdot (1 - \nu)} \\ S_{1212} = S_{2323} = S_{3131} &= \frac{4 - 5 \cdot \nu}{15 \cdot (1 - \nu)} \end{aligned} \quad (3.16)$$

The tensor 'S' is then a second-order symmetric tensor. It must be noticed that this tensor does not depend on the size of the inclusion 'a'.

$$S = \begin{bmatrix} \frac{7-5\nu}{15 \cdot (1-\nu)} & \frac{5\nu-1}{15 \cdot (1-\nu)} & \frac{5\nu-1}{15 \cdot (1-\nu)} & 0 & 0 & 0 \\ \frac{5\nu-1}{15 \cdot (1-\nu)} & \frac{7-5\nu}{15 \cdot (1-\nu)} & \frac{5\nu-1}{15 \cdot (1-\nu)} & 0 & 0 & 0 \\ \frac{5\nu-1}{15 \cdot (1-\nu)} & \frac{5\nu-1}{15 \cdot (1-\nu)} & \frac{7-5\nu}{15 \cdot (1-\nu)} & 0 & 0 & 0 \\ 0 & 0 & 0 & \frac{4-5\nu}{15 \cdot (1-\nu)} & 0 & 0 \\ 0 & 0 & 0 & 0 & \frac{4-5\nu}{15 \cdot (1-\nu)} & 0 \\ 0 & 0 & 0 & 0 & 0 & \frac{4-5\nu}{15 \cdot (1-\nu)} \end{bmatrix} \quad (3.17)$$

This method differs from the method exposed by Eshelby in his collected work, using various coefficients ($I_a, I_b, I_c, I_{aa}, I_{bb}, I_{cc}, I_{ab}, I_{ac}, I_{bc}$) which are also a reduction of surface integrals into simple integrals [ROU 81]. However, those coefficients are based on the same theoretical background, and similar results can be found. Eshelby's tensor for a sphere and considering a Poisson's ratio $\nu = 0.3$ for the matrix finally gives:

$$S = \begin{bmatrix} 0.5238 & 0.0476 & 0.0476 & 0 & 0 & 0 \\ 0.0476 & 0.5238 & 0.0476 & 0 & 0 & 0 \\ 0.0476 & 0.0476 & 0.5238 & 0 & 0 & 0 \\ 0 & 0 & 0 & 0.2381 & 0 & 0 \\ 0 & 0 & 0 & 0 & 0.2381 & 0 \\ 0 & 0 & 0 & 0 & 0 & 0.2381 \end{bmatrix} \quad (3.18)$$

3.1.5 Eshelby's tensor for a cubical inclusions

Considering cubical elements rapidly appeared necessary for the enrichment of the media. The misfit strain β is considered uniform in cubical inclusions. Many solutions exist for cubical elements, when dealing with plasticity for instance, and could be used hereafter. Some solutions still have to be found.

	Plastic cube ($\nu=0.5$)	Cubical non-homogeneity ($\nu \neq 0.5$)
ϵ^*	ϵ^p	Eshelby's tensor for a cube
Influence of ϵ^* on σ	[Chiu]	[Chiu] when using a 3D-FFT
Influence of ϵ^* on δ_z	[Chiu, Jacq]	Using σ^m in the 3D-FFT
Influence of ϵ^* on δ_x and δ_y	[Chiu, Fulleringer]	New technique required

Table 3.1: Elementary solutions required when dealing with cubical inclusions

It must be noticed that the Eshelby's tensor of a sphere is uniform and used to describe the strain level inside the inclusions. However, the Eshelby's tensor of a cube is not uniform and must be defined by expanding in Taylor's series around the origin [MOS 75b] using the element's coordinates. At this time, gradients inside the cubical inclusions will be neglected. However, they will be considered in Leroux' thesis.

Eshelby's tensor of a cube can be found analytically and is used to express the misfit strain ϵ to the eigenstrain ϵ^* as follow: $\epsilon = S \cdot \beta = S \cdot (\epsilon^* + \epsilon^p)$. Equation 3.15 is still valid and is necessary for the determination of the Eshelby's tensor.

$$\epsilon_{ij}^m = \frac{1}{8 \cdot \pi \cdot (1 - \nu)} \cdot (\psi_{ijkl} \cdot \beta_{kl} - 2 \cdot \nu \cdot \phi_{ij} \cdot \beta_{kk} - 2 \cdot (1 - \nu) \cdot (\phi_{kj} \cdot \beta_{ik} + \phi_{ki} \cdot \beta_{jk})) \quad (3.19)$$

MacMillan has obtained the potential functions of a homogeneous rectangular parallelepiped with the edge values: $(2 \cdot a_1, 2 \cdot a_2, 2 \cdot a_3)$. The coordinate system has its origin at the center of the parallelepiped and axes are parallel to the edges. Equations become very similar to the equations found in section 2.2.3 for the calculation of the residual stresses, since Chiu's work is an extension of the MacMillan potentials. It comes for potentials:

$$\psi(x) = \sum_{n=1}^8 (-1)^n H(c_n) \quad \phi(x) = \sum_{n=1}^8 (-1)^n E(c_n) \quad (3.20)$$

where H and E are defined by:

$$H(c) = \frac{1}{4} c_1 c_2 c_3 R + \frac{1}{6} \left\{ (R^2 - c_1^2) c_2 c_3 \log(R + c_1) + (R^2 - c_2^2) c_3 c_1 \log(R + c_2) + (R^2 - c_3^2) c_1 c_2 \log(R + c_3) \right\} \\ - \frac{1}{12} \left\{ c_1^4 \arctan\left(\frac{c_2 c_3}{c_1 R}\right) + c_2^4 \arctan\left(\frac{c_3 c_1}{c_2 R}\right) + c_3^4 \arctan\left(\frac{c_1 c_2}{c_3 R}\right) \right\} \quad (3.21)$$

$$E(c) = c_1 c_2 \log(R + c_3) + c_2 c_3 \log(R + c_1) + c_3 c_1 \log(R + c_2) \\ - \frac{1}{2} \left\{ c_1^2 \arctan\left(\frac{c_2 c_3}{c_1 R}\right) + c_2^2 \arctan\left(\frac{c_3 c_1}{c_2 R}\right) + c_3^2 \arctan\left(\frac{c_1 c_2}{c_3 R}\right) \right\} \quad (3.22)$$

and $c = (c_1, c_2, c_3)$, $R = (c_1^2 + c_2^2 + c_3^2)^{1/2}$ and c_n are the coordinates of corners in the coordinate system. Eshelby's tensor for a cube is found and, considering a Poisson's ratio $\nu = 0.3$ for the matrix, finally gives:

$$S = \begin{bmatrix} 0.5959 & 0.0116 & 0.0116 & 0 & 0 & 0 \\ 0.0116 & 0.5959 & 0.0116 & 0 & 0 & 0 \\ 0.0116 & 0.0116 & 0.5959 & 0 & 0 & 0 \\ 0 & 0 & 0 & 0.2021 & 0 & 0 \\ 0 & 0 & 0 & 0 & 0.2021 & 0 \\ 0 & 0 & 0 & 0 & 0 & 0.2021 \end{bmatrix} \quad (3.23)$$

Similar tensors can be found for parallelepipedic inclusions, depending on the ratios $\Delta Y / \Delta X$ and $\Delta Z / \Delta X$. It must be noticed that this tensor is different from the Eshelby's tensor of a sphere.

3.1.6 Infinite half space using a 3D-FFT algorithm

High stresses may be found locally under contact conditions considering soft or hard inclusions, and crack nucleation and growth may occur. For this reason, inclusions are very important in contact problems where lifetime predictions are an issue. In order to run such computations, it is necessary to extend previous solutions – valid for infinite spaces – to half-spaces.

T.Mura worked on such application [MUR 77] and [MUR 79], trying to extend the equation given by Muskhelishvili – relating misfit strains and eigenstrains – to infinite half-spaces. In spite of its complexity, those solutions consider an inclusion with hydrostatic eigenstrains. It is obvious that hydrostatic eigenstrains are not necessarily encountered in inclusions under contact conditions. Even if those solutions are not fruitful here, the method will be exposed and assumptions will be removed using semi-analytical methods.

Common method is to decompose an isotropic half-space problem into three sub-problems, as seen in Fig. 3.6. The first sub-problem considers the same inclusion but in an infinite space, $\beta = (\beta_{11}, \beta_{22}, \beta_{33}, \beta_{12}, \beta_{13}, \beta_{23})$. The second one considers an image counterpart inclusion as

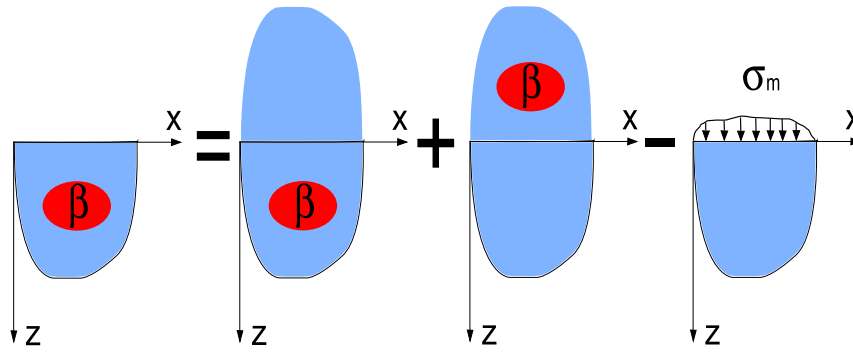


Figure 3.6: Decomposition of the problem about a cuboidal inclusion containing constant eigenstrains ϵ^* in an isotropic half-space bounded by the plane $z=0$ into three subproblems

seen in a mirror in the same infinite space. Its eigenstrains β_m is modified in order to respect symmetric conditions: $\beta_m = (\beta_{11}, \beta_{22}, \beta_{33}, \beta_{12}, -\beta_{13}, -\beta_{23})$

Solution for one inclusion in an infinite space has been exposed previously and is fully analytical, while the determination of β for non-homogeneities is partially numerical. Solution for two inclusions in an infinite half space is the sum of solutions for both inclusions. It is then possible to determine stresses all over the infinite space for two inclusions (A)+(B). Normal tractions σ_{33} are nil at the free surface of an half-space, for this reason a pressure field is then applied (C) in order to transfer the infinite space problem into a half-space. This pressure field comes from the solution of σ_{33} induced by both inclusions.

$$\sigma_{33}^m(x,y,0) = -\beta_{kl} \cdot K_{33kl}^\beta(x-x_o, y-y_o, -z_o) - \beta_{kl}^m \cdot K_{33kl}^\beta(x-x_o, y-y_o, z_o) \quad (3.24)$$

Finally stresses for each point of the infinite half – now equivalent to a half-space – is the sum of stresses created by the first inclusion (A), the image counterpart (B) and the pressure field emulating a free surface (C).

$$\sigma_{ij}^m(x,y,z) = \beta_{kl} \cdot K_{ijkl}^\beta(x-x_o, y-y_o, z-z_o) + \beta_{kl}^m \cdot K_{ijkl}^\beta(x-x_o, y-y_o, z+z_o) - \int_{-\infty}^{\infty} \int_{-\infty}^{\infty} K_{ij}^p \cdot \sigma_{33}^m dx dy \quad (3.25)$$

One of the problem encountered by T.Mura is the integration of this third term, while σ_{33}^m is a complex function related to the influence of both inclusion on the stress σ_{33} at the interface. For this reason, it was easier to solve this integral with a hydrostatic eigenstrains β . [MUR 79]

The pressure field σ^m can be first estimated numerically, and its influence is then quantified using the influence coefficients of pressures on stresses and the 2D-FFT algorithm. This semi-analytical approach refers to the 3D-FFT algorithm developed in section 2.3.6 and removes the restrictions on the eigenstrains β .

Of course, the solution depends on the numerical estimation of the pressure field σ_{33}^m . This estimation depends on the mesh refinement considered (See section 2.3.7) and is most likely accurate on the domain considered. However, the pressure is implicitly equal to zero out of the domain. Accuracy is then dependent of the surface considered for σ_{33}^m . It has been decided to extend the surface for the stress calculation in order to get a better accuracy when looking at the stresses in the volume (See figure 3.7). Since coefficients of influence may vary from an inclusion to another

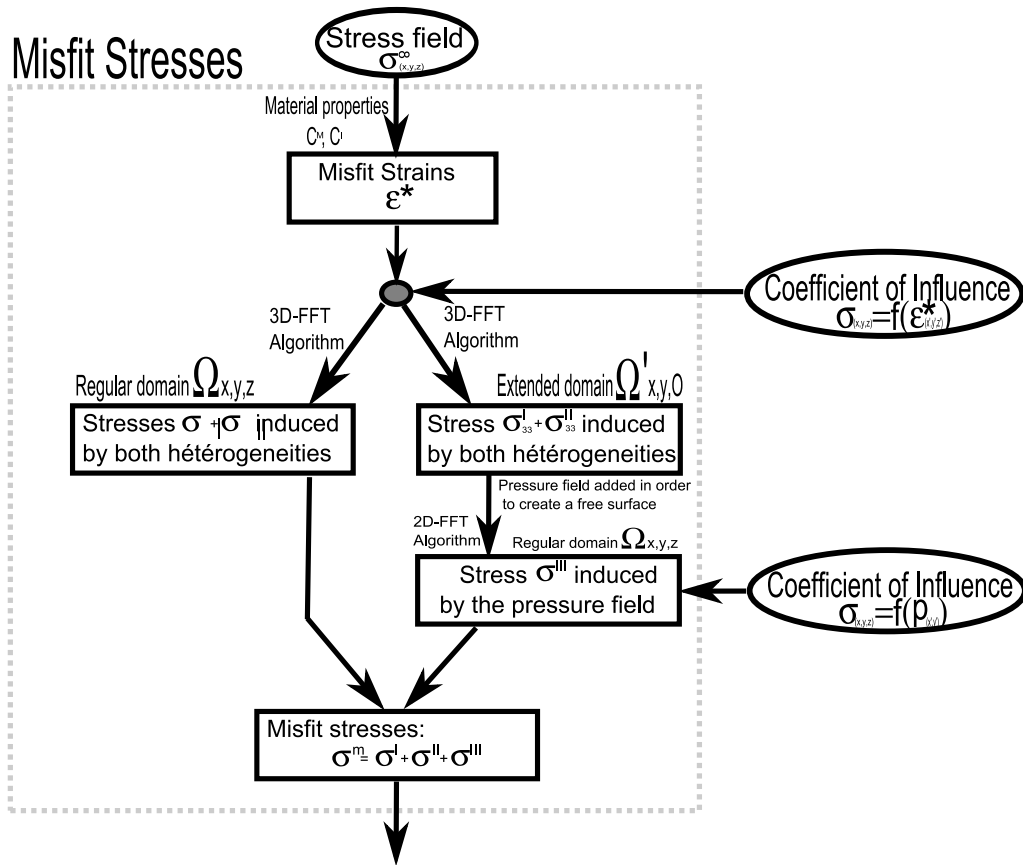


Figure 3.7: Flow chart of the misfit stresses algorithm

– considering the relative size and shapes of inclusions considered – the misfit stress algorithm can be used many times in a row, and solutions are finally summed.

It is worth noting that this problem has been treated in plasticity using a combination of the 2D-FFT and the 3D-FFT, requiring elementary solutions for a cuboidal zone in which plastic strains (incompressible) are uniform in both an infinite space and a half-space (See Table 3.2). But solutions for a cuboidal zone – or spherical zone – in which misfit strains (compressible) are uniform in a half-space do not exist, and the 2D-FFT can not be used. The 3D-FFT seems to be the only way to run computations considering non-homogeneous aspects and the user will have to deal with it carefully.

* T.Mura worked on spherical inclusions in a half-space, however eigenstrains were supposed to be hydrostatic and does not fit the general case. Additional work can be found but no one is generic.

3.1.7 The non-homogeneous solver

The misfit stress algorithm can be used separately. It works like a micro-scale tool, where the local stress $\sigma_{x,y,z}^\infty$, the eigenstrain ϵ^* and ϵ^p are defined for a spherical inclusion. Run independently, a

	Solutions for an ∞ space	Solutions for an ∞ half space
Cubical inclusion ($\nu=0.5$)	Y.P. Chiu	Y.P.Chiu / C.Jacq / B.Fulleringer
Spherical inclusion ($\nu = 0.5$)	J.D. Eshelby	*
Cubical inclusion ($\nu \neq 0.5$)	Y.P. Chiu	\emptyset
Spherical inclusion ($\nu \neq 0.5$)	J.D. Eshelby	*

Table 3.2: Existing analytical solutions of infinite and semi-infinite spaces, when considering spherical or cubical inclusions with various Poisson's ratios

finer mesh can be defined so the local stress created are more accurately described. It becomes particularly important for small inclusions when looking at 45° .

This algorithm is now implemented in the contact solver. The stress field $\sigma_{x,y,z}$ observed in the elastic-plastic case below the surface will be considered locally as the stress $\sigma_{x,y,z}^\infty$. The eigenstrains β are defined for each inclusions considering their material properties and the local stress by solving each time equation 3.7. The misfit stresses σ^m obtained are then added to the existing contact and residual stress fields σ and σ^r .

Since the non-homogeneous inclusion will have an impact on the contact conditions, the contact surface must be updated. The misfit displacements U_x^m , U_y^m and U_z^m are then introduced. Those displacements will update the surface geometry, and the problem will be solved until they converged (See figure 3.8). For comparison, the process was used with residual displacements in the elastic-plastic contact code. Once the solver has converged, the solution for an elastic and homogeneous problem is found, and equivalent to the non-homogeneous required.

3.1.8 Non-homogeneous problems considering frictional aspects

Contact problem is actually composed of a normal and a tangential contact problem. The normal problem determines, among other things, the pressure field and the contact area. The surface separation equation has been explained in previous chapters and is:

$$g_{ij} = \bar{u}_{z\ ij}^p + \bar{u}_{z\ ij}^{qx} + \bar{u}_{z\ ij}^{qy} + \bar{u}_{z\ ij}^r + \bar{u}_{z\ ij}^m + h_{ij} - \phi_{xy} + \phi_y x - \delta_z = 0 (i, j) \in \Gamma_c, \quad (3.26a)$$

$$g_{ij} = \bar{u}_{z\ ij}^p + \bar{u}_{z\ ij}^{qx} + \bar{u}_{z\ ij}^{qy} + \bar{u}_{z\ ij}^r + \bar{u}_{z\ ij}^m + h_{ij} - \phi_{xy} + \phi_y x - \delta_z > 0 (i, j) \notin \Gamma_c. \quad (3.26b)$$

where $h(x,y)$ is the initial distance between the bodies and $\delta_{z(x,y)}$ the rigid body displacements. $U_{z(x,y)}^p$ is the normal displacement created by the pressure field which must be estimated. $U_{z(x,y)}^q$, $U_{z(x,y)}^q \cdot x$ and $U_{z(x,y)}^q \cdot y$ and $U_{z(x,y)}^r$ are the normal displacements created by the shear fields and plastic strains, which are supposed constant during the determination of the pressure field. When dealing with inhomogeneities, another displacement has to be taken into account. This displacement is created by misfit strains and will be noted $U_{z(x,y)}^m$. It will be supposed constant during the determination of the pressure field, and updated later in the computation. The tangential problem determines the shear and slip fields and the sticking area. It has been studied in elastic problems and in elastic

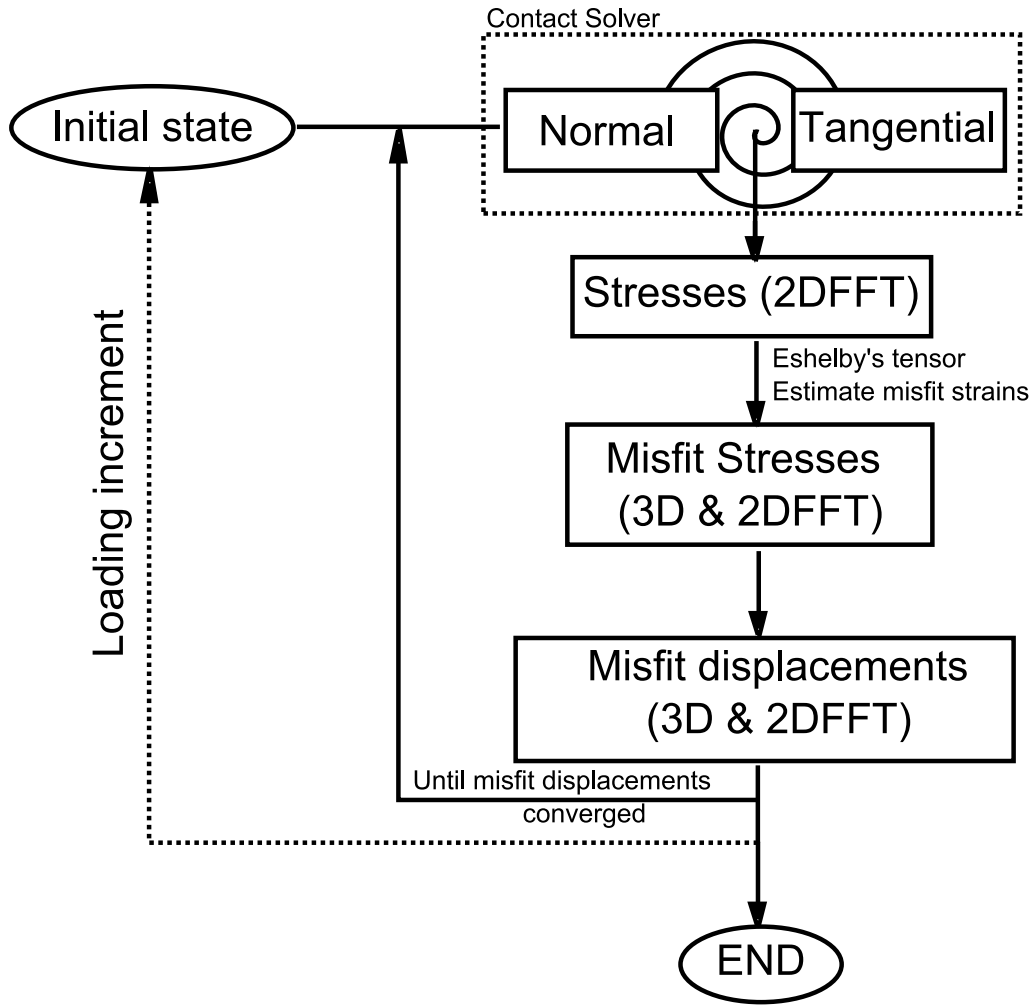


Figure 3.8: Flow chart of the actual heterogeneous-elastic contact solver

plastic contacts in this thesis. Then the expression of sticking and slipping zones are expressed as follow:

$$\left[\bar{\mathbf{u}}_{\tau ij}^p + \bar{\mathbf{u}}_{\tau ij}^{qx} + \bar{\mathbf{u}}_{\tau ij}^{qy} + \bar{\mathbf{u}}_{\tau ij}^r + \bar{\mathbf{u}}_{\tau ij}^m \right]_{t'}^t - \Delta \delta_{\tau}^t = \mathbf{s}_{ij}^t = 0 \quad (i, j) \in \Gamma_{st}, \quad (3.27a)$$

$$\left[\bar{\mathbf{u}}_{\tau ij}^p + \bar{\mathbf{u}}_{\tau ij}^{qx} + \bar{\mathbf{u}}_{\tau ij}^{qy} + \bar{\mathbf{u}}_{\tau ij}^r + \bar{\mathbf{u}}_{\tau ij}^m \right]_{t'}^t - \Delta \delta_{\tau}^t = \mathbf{s}_{ij}^t \neq 0 \quad (i, j) \in \Gamma_{sl}; \quad (3.27b)$$

where δ_{τ}^t is the rigid body displacement. While slips are defined between two consecutive steps, the slips depend on tangential displacements at the moment 't' and 't-1' and are historic-sensitive. In other words, it also means that the loading history is taken into account. $\bar{\mathbf{u}}_{\tau ij}^{qx}$ and $\bar{\mathbf{u}}_{\tau ij}^{qy}$ are the tangential displacements created by the shear fields which must be estimated. $\bar{\mathbf{u}}_{\tau ij}^p$ and $\bar{\mathbf{u}}_{\tau ij}^r$ are the tangential displacements created by the pressure field and plastic strains, which are supposed constant during the determination of the shear fields. When dealing with non-homogeneities, two additional displacements have to be taken into account. Those displacements are created by misfit strains and will be noted $\bar{\mathbf{u}}_{\tau ij}^m$.

Finally, $\bar{\mathbf{u}}_{z,ij}^m$ and $\bar{\mathbf{u}}_{\tau,ij}^m$ are displacements induced by misfit strains and defined in previous subsections.

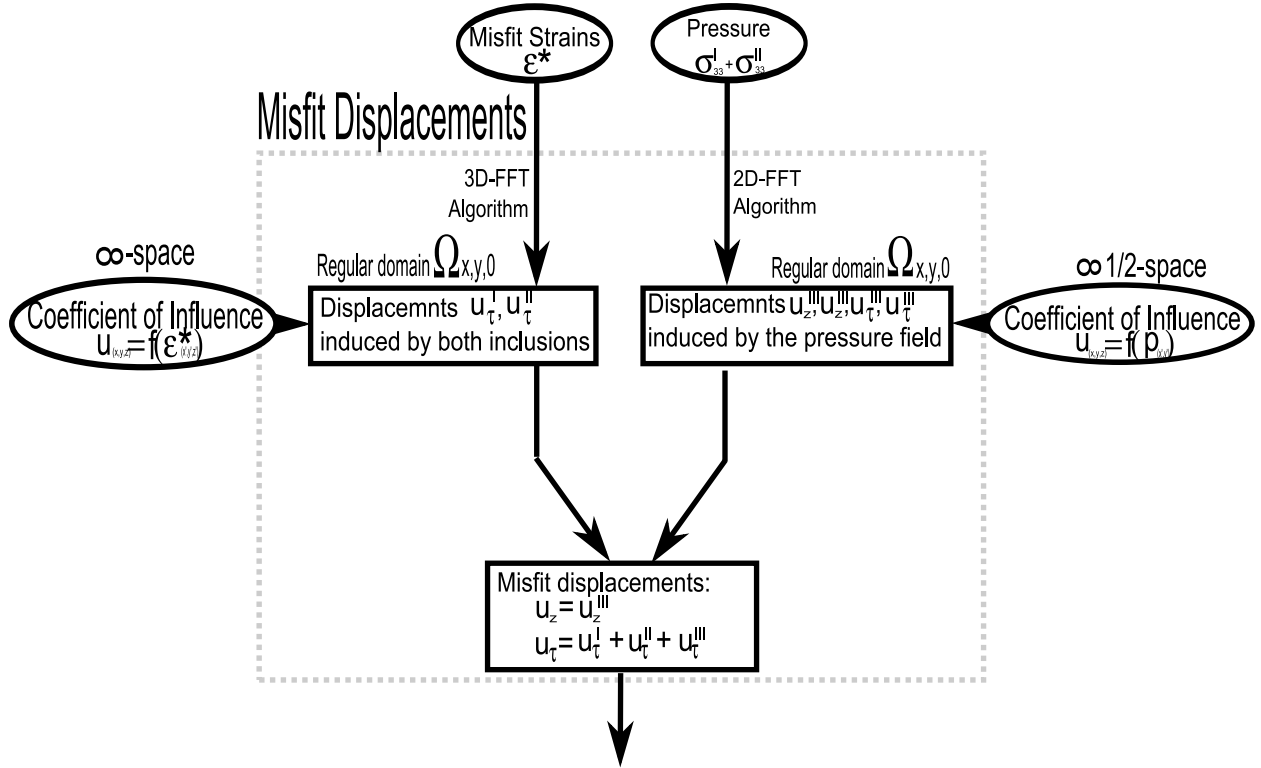


Figure 3.9: Flow chart of the misfit displacement algorithm

3.1.9 Non-homogeneous problems with plastic behaviors

Inclusions can be made of metal (Tungsten, Copper,...), oxides (Alumina,...) and non metallic (Carbon, Gaz,...) of different shapes (Spherical, elliptical,...). It is of a great importance to consider those inclusions and their elastic-plastic properties in some applications, such as for rolling contact. Because all effects can superimposed in linear elastic-plastic problems (such as pressures and shears, contact stresses and residual stresses) misfit stresses can be added in actual elastic-plastic contact code. However, misfit stresses are explicitly expressed for heterogeneity in an elastic media, and has to be extended to take residual stresses into account. This extension is not an issue and the continuum equation of stresses for the non-homogeneity and inclusion becomes:

$$C^I (\epsilon_{contact}^{\infty} + \epsilon_{residual}^{\infty} + \epsilon - \epsilon^P) = C^M (\epsilon_{contact}^{\infty} + \epsilon_{residual}^{\infty} + \epsilon - \epsilon^* - \epsilon^P) \quad (3.28)$$

Where $\epsilon_{contact}^{\infty}$ is the strain field created by contact conditions at the center of the inclusion when no inclusion is considered, $\epsilon_{residual}^{\infty}$ is the strain field created by plastic strains at the center of the inclusion when no inclusion is considered. This extension effectively relates true stresses – contact and residual stresses – to the response of non-homogeneities in the media.

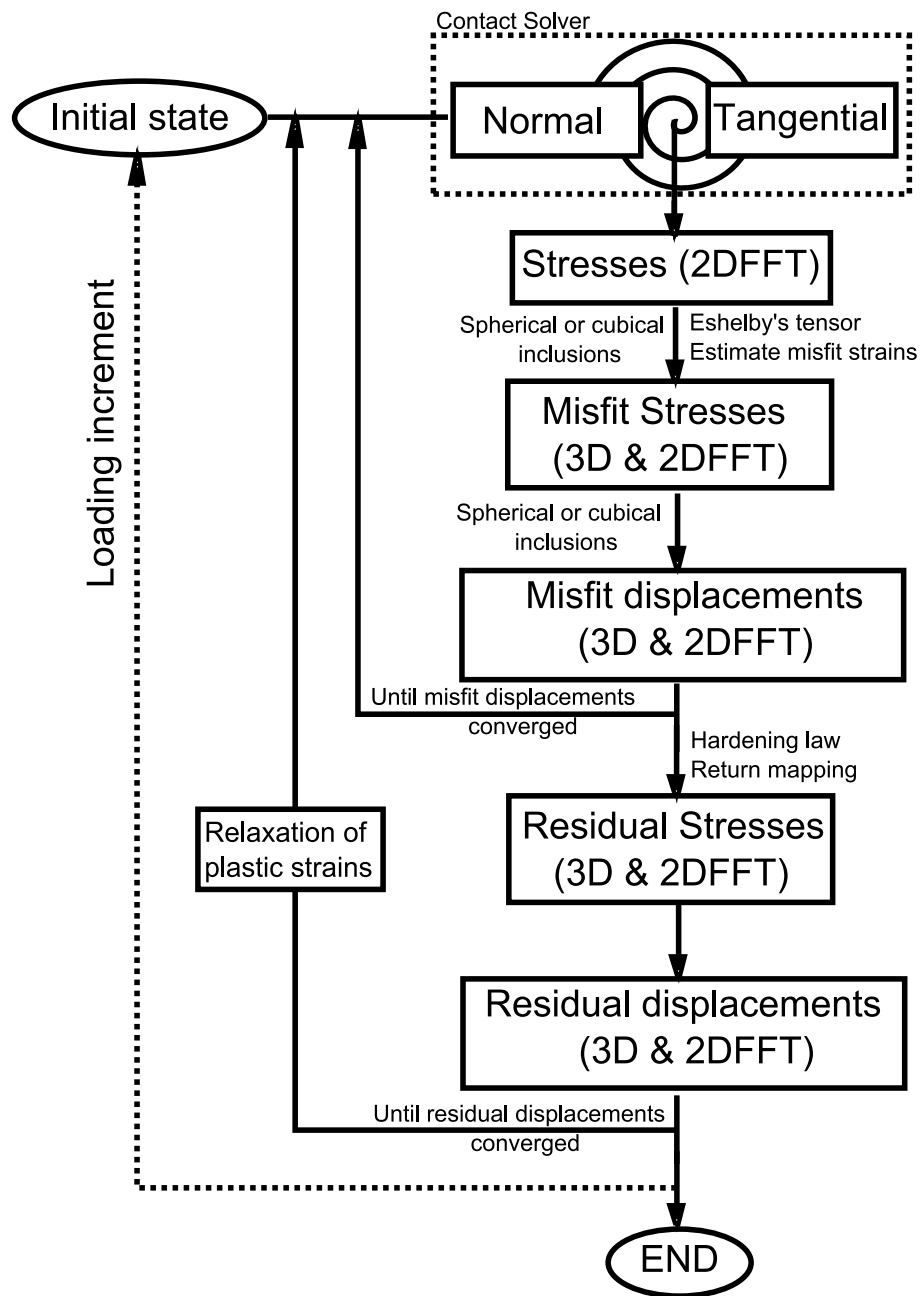


Figure 3.10: Flow chart of the actual heterogeneous-elastic-plastic contact solver

3.2 Validation of elementary solutions

3.2.1 Misfit stresses caused by a spherical inclusion

As seen in section 3.1.3, the misfit strain field is defined by:

$$\varepsilon_{ij} = \frac{1}{8\pi \cdot (i - \nu)} \cdot (\Psi_{,ijkl} \cdot \beta_{kl} - 2 \cdot \nu \cdot \phi_{,ij} \cdot \beta_{kk} - 2 \cdot (1 - \nu) \cdot (\phi_{,kj} \cdot \beta_{ik} + \phi_{,ki} \cdot \beta_{jk})) \quad (3.29)$$

where harmonic and biharmonic potentials ϕ and Ψ are defined by:

$$\begin{aligned} \phi &= \frac{4}{3} \cdot \pi \cdot a^2 \cdot \frac{a}{r} \\ \Psi &= \frac{4}{3} \cdot \pi \cdot a^4 \cdot \left(-\frac{1}{5} \cdot \frac{a \cdot x}{r^3} + \frac{x}{r \cdot a} \right) \end{aligned} \quad (3.30)$$

a is the radius of the inclusion. Later, the coordinates x , y and z are normalized by the inclusion radius. Derivates of potentials are dimensionless inside the inclusion and expressed hereafter, while other potentials can be found using circular permutation techniques.

Inside the inclusion:

$$\begin{aligned} \phi_{,11} &= -\frac{4\pi}{3} & \phi_{,12} &= 0 & \phi_{,23} &= 0 \\ \Psi_{,1111} &= -\frac{8\pi}{5} & \Psi_{,1122} &= -\frac{8\pi}{15} & \Psi_{,1112} &= 0 & \Psi_{,1123} &= 0 \end{aligned} \quad (3.31)$$

Outside the inclusion:

$$\begin{aligned} \phi_{,11} &= \frac{4\pi \cdot x^2}{r^5} - \frac{4\pi}{3 \cdot r^3} & \phi_{,12} &= \frac{4\pi \cdot x \cdot y}{r^5} & \phi_{,23} &= \frac{4\pi \cdot y \cdot z}{r^5} \\ \Psi_{,1111} &= \frac{4\pi}{3} \cdot \left(\frac{21 \cdot x^4}{r^9} - \frac{18 \cdot x^2}{r^7} + \frac{9}{5 \cdot r^5} - \frac{15 \cdot x^4}{r^7} + \frac{18 \cdot x^2}{r^5} - \frac{3}{r^3} \right) \\ \Psi_{,1122} &= \frac{4\pi}{3} \cdot \left(\frac{21 \cdot y^2 \cdot x^2}{r^9} - \frac{3 \cdot y^2}{r^7} - \frac{3 \cdot x^2}{r^7} + \frac{3}{5 \cdot r^5} - \frac{15 \cdot y^2 \cdot x^2}{r^7} + \frac{3 \cdot y^2}{r^5} + \frac{3 \cdot x^2}{r^5} - \frac{1}{r^3} \right) \\ \Psi_{,1112} &= \frac{4\pi}{3} \cdot \left(\frac{21 \cdot y \cdot x^3}{r^9} - \frac{9 \cdot x \cdot y}{r^7} - \frac{15 \cdot y \cdot x^3}{r^7} + \frac{9 \cdot x \cdot y}{r^5} \right) \\ \Psi_{,1123} &= \frac{4\pi}{3} \cdot \left(\frac{21 \cdot z \cdot y \cdot x^2}{r^9} - \frac{3 \cdot z \cdot y}{r^7} - \frac{15 \cdot z \cdot y \cdot x^2}{r^7} + \frac{3 \cdot z \cdot y}{r^5} \right) \end{aligned} \quad (3.32)$$

Misfit strains ε are then used to find the misfit stresses, using the Hooke's law:

$$\sigma = \lambda \cdot tr(\varepsilon) \cdot \mathbf{I} + 2\mu \cdot \varepsilon \quad (3.33)$$

The coefficients of influence used in the code are then directly expressing the misfit stress σ_{ij} induced by an eigenstrain β_{kl} . The 3D-FFT is then used for solving the problem in an isotropic half-space, since solutions are available in an infinite space only.

The elastic field in a half-space due to a spherical inclusion with uniform eigenstrains are then compared to the available results found in the literature. Seo and Mura [MUR 79] investigated the elastic stress field caused by an ellipsoidal inclusion and for various ellipticity ratios. However, a strong assumption was made and eigenstrain is supposed to be pure dilatation ($\beta_{ii} = 1$).

Numerical results are available for a spherical inclusion tangent to the surface, and located at a depth Z_0 so that $Z_0 = 2 \cdot a_3$, where a_3 is the sphere radius:

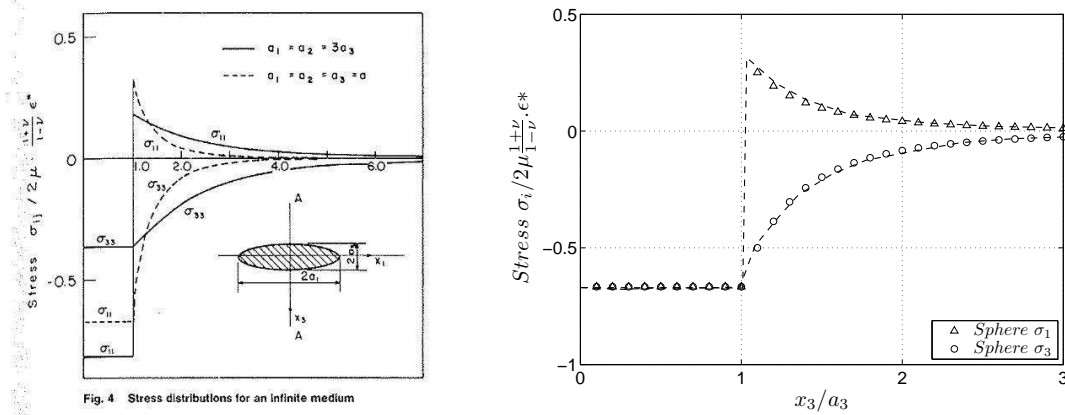


Figure 3.11: Stress distribution along the x_3 -direction ($x_1=x_2=0$) for an inclusion in an infinite space [MUR 79]

- In order to see the effect of the free boundary surface, the stress distributions for an infinite medium are shown in figure 3.11. Principal stresses σ_{11} and σ_{33} are compared to the numerical results. Solid lines are results found analytically and symbols are semi-analytical results. This reveals a very good agreement between the numerical integration and the analytical integration. The stress inside the inclusion is uniform.

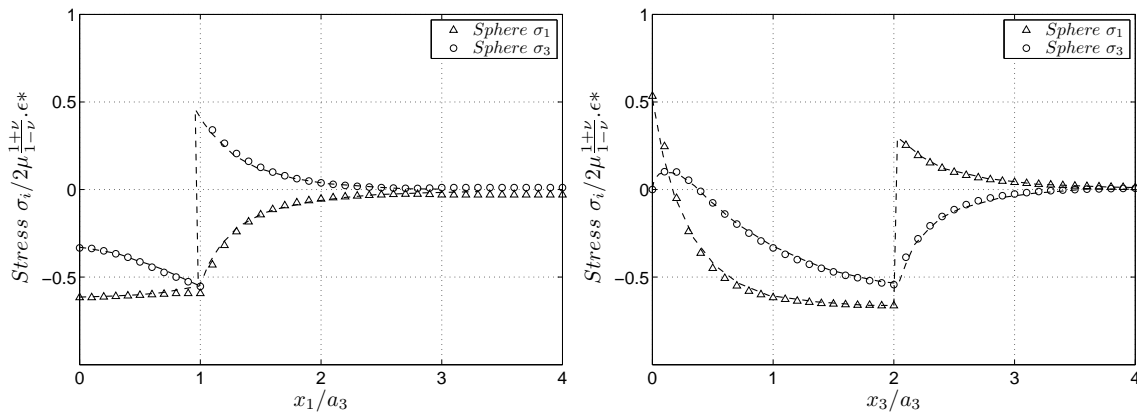


Figure 3.12: Stress distribution along the x_1 -direction on the left ($x_2=0$ and $x_3=a_3$) and x_3 -direction on the right ($x_1=x_2=0$) for $c=a_3$.

- A spherical inclusion of radius $2a_3$ located at a depth $z_0 = a_3$ is now considered (the inclusion is tangent to the free surface). The stress distribution in the transversal direction for $Z_0 = 2a_3$ is shown in figure 3.12a, and in the normal direction for $x = y = 0$ in figure 3.12b. First of all, it must be noticed that the stress inside the inclusion is no longer uniform because of the free surface influence. The spherical inclusion creates some tension in the interior points near the free surface. σ_{11} is discontinuous at the interface in the normal direction, while σ_{33} is continuous. On the opposite, σ_{33} is discontinuous at the interface in

the transversal direction, while σ_{11} becomes continuous according to Mura. Solid lines are results found analytically and symbols are semi-analytical results.

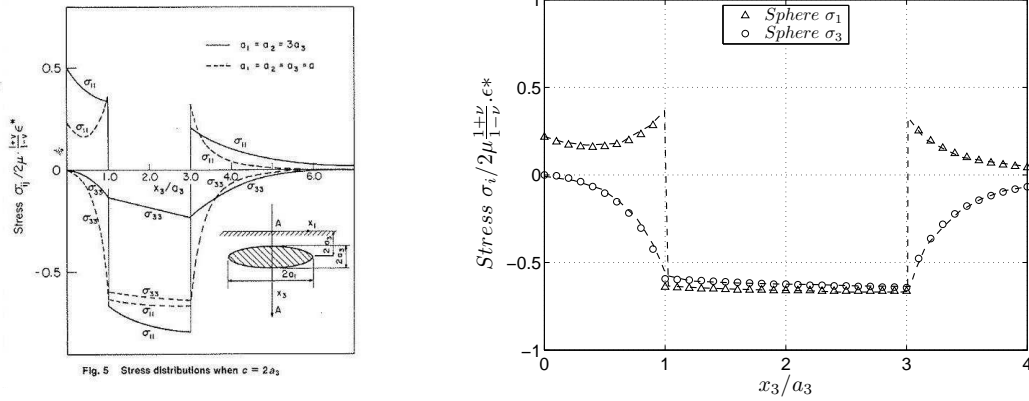


Figure 3.13: σ_{11} and σ_{33} at $x_1=x_2=0$ for a spherical inclusion of radius a_3 located at a depth $z_0 = 2a_3$ [MUR 79].

- The stress distribution in the normal direction for $x = y = 0$ is now investigated for a spherical inclusion of radius $2a_3$ located at a depth $z_0 = 2a_3$. Similar results are shown in figure 3.42.

The analytical integration and the numerical computation, using the 3D-FFT algorithm, has been compared to numerical results obtained by Seo and Mura. However, the numerical method was limited to purely dilatational eigenstrains $\beta_{11} = \beta_{22} = \beta_{33}$ while the actual semi-analytical method is not limited to this specific case. It is of a great importance in a contact solver since the contact stresses are not pure dilatations.

3.2.2 Misfit displacements caused by a spherical inclusion

The spatial displacements are used to determine the tangential deflections of the surface in the 3D-FFT algorithm. Another set of influence coefficients is then defined and derives from the previous equations. Since $\epsilon_{ij} = 1/2 \cdot (U_{i,j} + U_{j,i})$, it is found that displacements U_i derive from ϵ_{ii} :

$$U_i = \frac{1}{8 \cdot \pi \cdot (i - \nu)} \cdot (\Psi_{,ikl} \cdot \beta_{kl} - 2 \cdot \nu \cdot \phi_{,i} \cdot \beta_{kk} - 2 \cdot (1 - \nu) \cdot (\phi_{,k} \cdot \beta_{ik} + \phi_{,ki} \cdot \beta_k)) \quad (3.34)$$

The coordinates x , y and z are normalized by the inclusion radius a . Derivates of potentials are homogeneous to a and expressed hereafter, while other potentials can be found using circular permutation techniques.

$$\begin{aligned} \phi_{,1} &= -\frac{4 \cdot \pi}{3} \cdot \frac{xa^3}{r^3} \\ \Psi_{,111} &= \frac{4 \cdot \pi}{3} \cdot a^4 \cdot \left(-\frac{3 \cdot a \cdot x^3}{r^7} + \frac{3 \cdot x^3}{a \cdot r^5} + \frac{9 \cdot a \cdot x}{5 \cdot r^5} - \frac{3 \cdot x}{a \cdot r^3} \right) \\ \Psi_{,122} &= \frac{4 \cdot \pi}{3} \cdot a^4 \cdot \left(-\frac{3 \cdot a \cdot x \cdot y^2}{r^7} + \frac{3 \cdot x \cdot y^2}{a \cdot r^5} + \frac{3 \cdot a \cdot x}{5 \cdot r^5} - \frac{x}{a \cdot r^3} \right) \\ \Psi_{,112} &= \frac{4 \cdot \pi}{3} \cdot a^4 \cdot \left(-\frac{3 \cdot a \cdot y \cdot x^2}{r^7} + \frac{3 \cdot y \cdot x^2}{a \cdot r^5} + \frac{3 \cdot a \cdot y}{5 \cdot r^5} - \frac{y}{a \cdot r^3} \right) \\ \Psi_{,123} &= \frac{4 \cdot \pi}{3} \cdot a^4 \cdot \left(-\frac{3 \cdot a \cdot x \cdot y \cdot z}{r^7} + \frac{3 \cdot x \cdot y \cdot z}{a \cdot r^5} \right) \end{aligned} \quad (3.35)$$

The FEM defined in section 2.2.7 has been used, but the eigenstrain is no longer incompressible (it is no longer a plastic cuboid, but a cubical inclusion). The spherical inclusion must have the same volume than the cube of size $2b$. The cube is located at a depth z_0 so that $z_0/2b = 5$. It comes that the spherical inclusion of radius a is located at a depth z_0 so that $a = \sqrt[3]{3/(20 \cdot \pi)} \cdot z_0$.

Various cases are now considered: $\beta_{11} = 1$, $\beta_{22} = 1$, $\beta_{33} = 1$, $\beta_{12} = 1$, $\beta_{13} = 1$ and $\beta_{23} = 1$. Both the normal (See figure 3.14) and tangential displacements (See figure 3.15) are presented along the x-axis, y-axis and over an angle of 45° for the six cases.

Finally, the analytical integration and the numerical computation, using the 3D-FFT algorithm, has been validated assuming that misfit displacements created by a spherical inclusion are similar to the misfit displacements created by a cubical inclusion if located far from the inclusion.

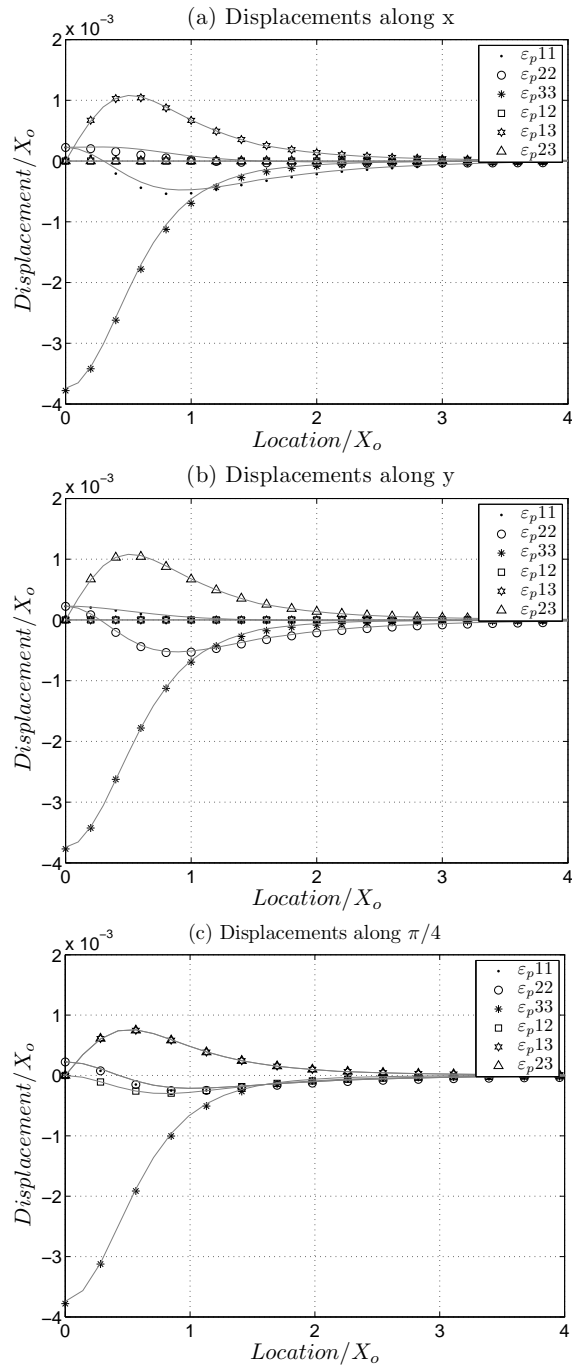


Figure 3.14: Normal displacements for a plastic cube (FEM) and a spherical inclusion of equivalent volume (symbols) at a certain depth Z_o so that $Z_o/2b=5$. Note that the trace is no longer equal to zero

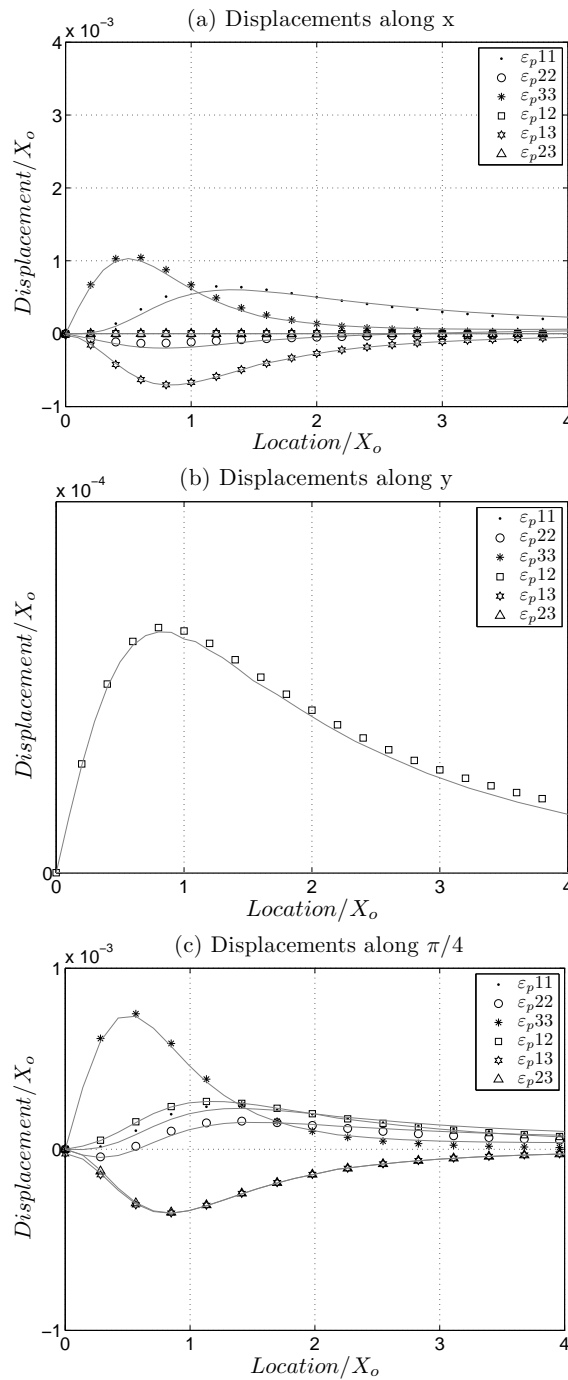


Figure 3.15: Tangential displacements for a plastic cube (FEM) and a spherical inclusion of equivalent volume (symbols) at a certain depth Z_0 so that $Z_0/2b=5$. Note that the trace is no longer equal to zero

3.2.3 Misfit stresses around a parallelepipedic inclusion

Potentials have been defined in section 2.2.3, and are similar to the potentials defined by Chiu for the elastic-plastic problem. They will not be detailed here.

3.2.4 Misfit displacements caused by a cuboidal inclusion

The spatial displacements are used to determine the tangential deflections of the surface in the 3D-FFT algorithm. Another set of influence is then defined and derives from the previous equations. Based on Chiu's work [CHI 78], it is found that displacements U_i can be expressed as follow:

$$U_i = \frac{1}{16.\pi^3.v} \cdot \sum_{n=1,8} (-1)^n \left(\frac{1-2\nu}{1-\nu} \lambda \beta_{kk} D_{,imm} + 4\mu \beta_{ij} D_{,jmm} - \frac{2\mu}{1-\nu} \cdot \beta_{mj} D_{,imj} \right) \quad (3.36)$$

Where D are defined at each corner of the cuboid by their coordinates \vec{C}_n

$$\vec{C}_1 = (x - \Delta x, y - \Delta y, z - \Delta z) \quad (3.37a)$$

$$\vec{C}_2 = (x + \Delta x, y - \Delta y, z - \Delta z) \quad (3.37b)$$

$$\vec{C}_3 = (x + \Delta x, y + \Delta y, z - \Delta z) \quad (3.37c)$$

$$\vec{C}_4 = (x - \Delta x, y + \Delta y, z - \Delta z) \quad (3.37d)$$

$$\vec{C}_5 = (x - \Delta x, y + \Delta y, z + \Delta z) \quad (3.37e)$$

$$\vec{C}_6 = (x - \Delta x, y - \Delta y, z + \Delta z) \quad (3.37f)$$

$$\vec{C}_7 = (x + \Delta x, y - \Delta y, z + \Delta z) \quad (3.37g)$$

$$\vec{C}_8 = (x + \Delta x, y + \Delta y, z + \Delta z) \quad (3.37h)$$

While considering that misfit strains β are homogeneous inside the cuboid of size $(\Delta x, \Delta y, \Delta z)$, derivatives of potentials are expressed hereafter and other potentials can be found using circular permutation techniques:

$$\begin{aligned} D_{,111} &= -\pi^2 \cdot y \cdot \ln \left(\frac{R+z}{\sqrt{x^2+y^2}} \right) - \pi^2 \cdot z \cdot \ln \left(\frac{R+y}{\sqrt{x^2+y^2}} \right) \\ D_{,112} &= -\pi^2 \cdot x \cdot \ln \left(\frac{R+z}{\sqrt{x^2+y^2}} \right) \\ D_{,123} &= -\pi^2 \cdot R \end{aligned} \quad (3.38)$$

Various cases are now considered: $\beta_{11} = 1$, $\beta_{22} = 1$, $\beta_{33} = 1$, $\beta_{12} = 1$, $\beta_{13} = 1$ and $\beta_{23} = 1$. Both the normal (See figure 3.16) and tangential displacements (See figure 3.17) are presented along the x-axis, y-axis and over an angle of 45° for the six cases. Similar results are found.

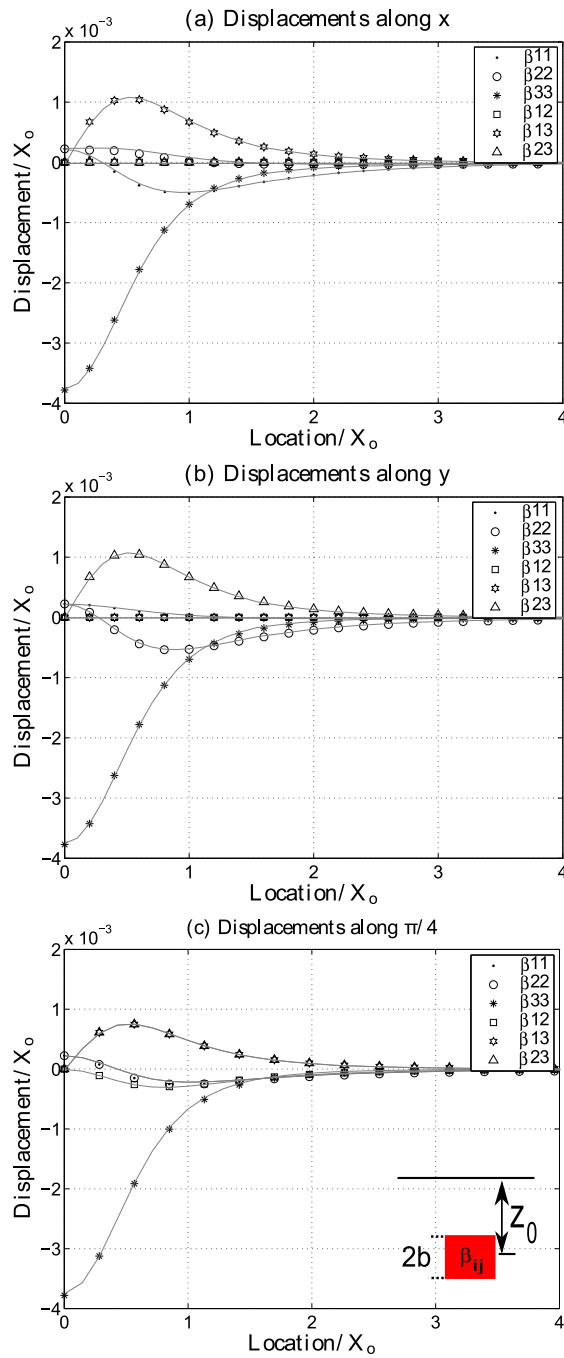


Figure 3.16: Normal displacements for a plastic cube (FEM) and a cubical inclusion (symbols) at a certain depth Z_0 so that $Z_0/2b=5$. Note that the trace is no longer equal to zero

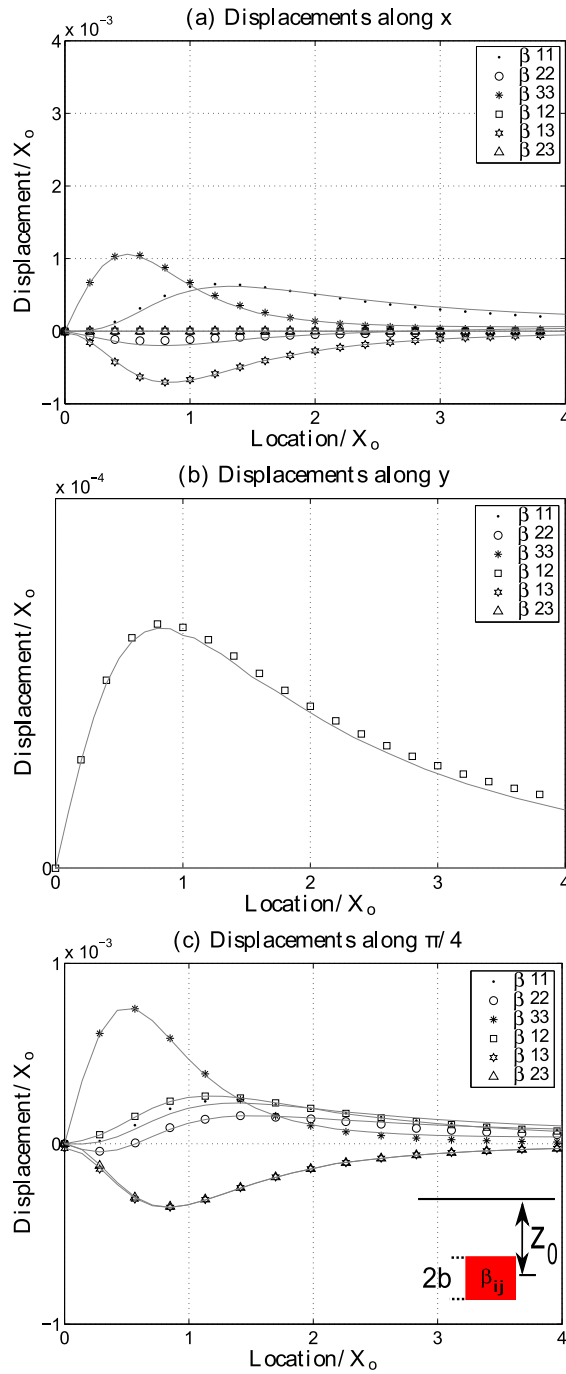


Figure 3.17: Tangential displacements for a plastic cube (FEM) and a cubical inclusion (symbols) at a certain depth Z_0 so that $Z_0/2b=5$. Note that the trace is no longer equal to zero

3.3 Influence of non-homogeneities on contact conditions considering no gradient

The method may be applied to nano-indentation, as schematically shown in Figure 3.18. In this section, the Young's modulus and Poisson's ratio of the matrix are chosen as $E_m=210\text{GPa}$ and $\nu_m=0.3$, respectively. The indenter is rigid with a radius $R=105\mu\text{m}$. The maximum load P is 650mN . For the homogeneous half-space, this load leads to a contact radius $a=6.05\mu\text{m}$ and a maximum contact pressure $P_0=8469\text{MPa}$.

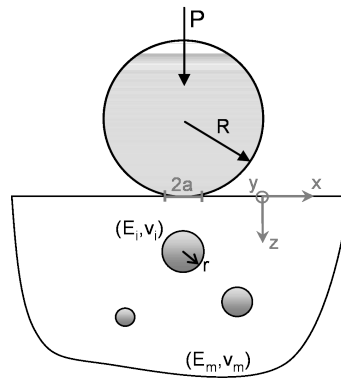


Figure 3.18: Normal loading of a half-space containing multiple inclusions

To the author knowledge this type of contact problem has not been solved explicitly in the published literature. The pressure distribution is usually assumed Hertzian; see for example Kabo and Ekberg [KAB 04], or Courbon et al. [COU 03]. Such an assumption could be made if the inclusion is located far from the surface. However, it will be shown here that the contact pressure distribution may be significantly modified by the presence of inhomogeneities close to the surface, which subsequently affect the subsurface stress distribution. The effect of different parameters of the inhomogeneities was first investigated: their Young's modulus, Poisson's ratio, and radius. The grid test Table 3.3 shows different arrangements to study the influence of each inclusion parameter.

N^o	Inclusion parameter	Discretization mesh (Cuboids)	Young's Modulus ratio	Poisson's ratio	Radius r	Arrangement
1	Young's modulus	84x84x31	Variable $0 \leq \gamma \leq 2$	$\nu = 0.3$	$r=0.1a$	3D Uniform Distribution (484 Inclusions)
2	Inclusions radius	84x84x31	$\gamma = 2$	$\nu = 0.3$	variable $0.03 \leq r/a \leq 1.33$	One inclusion in two depth configurations
3	Poisson's ratio	84x84x31	$\gamma = 0.5$ and $\gamma = 2$	Variable $0 \leq \nu \leq 0.45$	$r=0.1a$	3D Uniform Distribution (484 Inclusions)
4	Depth	84x84x31	$\gamma = 2$	$\nu = 0.3$	$r=0.13a$	2D Uniform Distribution (49 inclusions)

Table 3.3: Different configurations to study the influence of each inclusion parameters

3.3.1 Influence of the Young's modulus using a cluster of inclusions

A cluster of spherical inhomogeneities is considered in a first example. The inhomogeneities are equally spaced into a domain constituted of $84 \times 84 \times 31$ cuboids such as the space between the inclusion centers is $\Delta x = \Delta y = \Delta z = 0.27a$ as shown in Figure 3.19. This configuration includes 484 inclusions and the edge of a cuboid (mesh) is $0.2 \mu m$. The radius of the inclusions is $r = 0.6 \mu m = 0.1a$. Thus the total volume of inhomogeneities takes up 22% of the domain. The ratio of the inclusion Young's modulus to the matrix one is defined by the dimensionless parameter $\gamma = E_i / E_m$ whereas the Poisson's ratio is set constant $\nu_I = 0.3$.

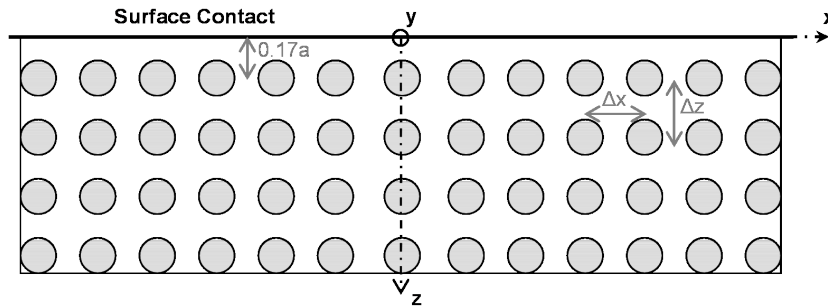


Figure 3.19: Representation of the inclusion pattern in the (Oxz) plane

Figure 3.20 presents the dimensionless contact pressure distribution for various Young's modulus ratios γ ranging from 0 to 2. The contact pressure and x and y -coordinates are normalized by the Hertz pressure P_0 and contact radius a , respectively, which is the solution in the absence of inhomogeneity. It can be verified that the contact pressure distribution for a cluster of homogeneous inclusions (i.e. inhomogeneities with $\gamma=1$) is equivalent to that of the homogeneous half-space (without inhomogeneity) which is the Hertz solution.

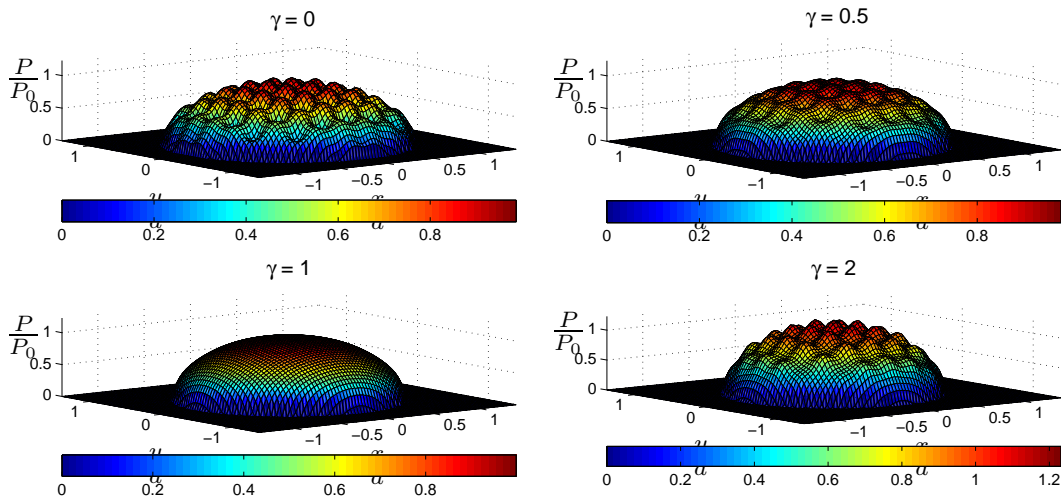


Figure 3.20: Contact pressure distribution for inhomogeneities of various stiffnesses ($\gamma=0, 0.5, 1, 2$)

Figure 3.21 shows the dimensionless pressure profile in the plane $y=0$ for the various ratios γ . It can be observed that, when the inclusion is softer than the half-space, i.e. $\gamma < 1$, the substrate material surrounding the inclusions becomes more compliant and the contact pressure gets smaller than the Hertzian pressure whereas the contact area increases. When the inclusions are stiffer than the matrix, the contact pressure exhibits peaks of magnitude higher than the solution without inclusion, and the contact area slightly decreases.

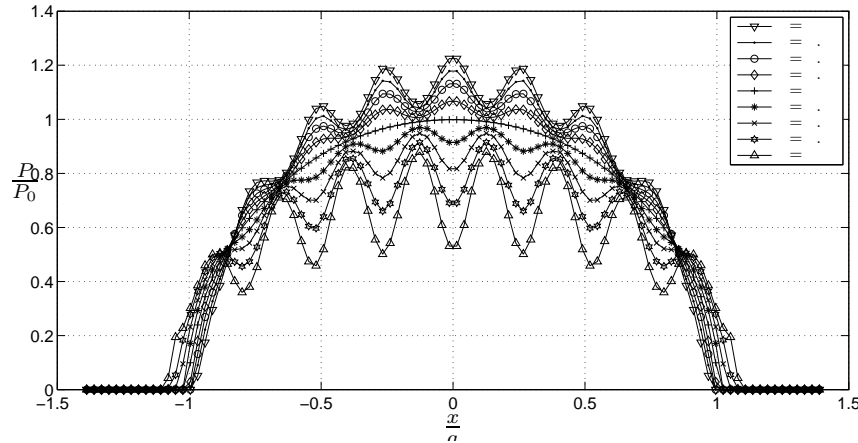


Figure 3.21: Contact pressure profile for inhomogeneities of various stiffnesses ($\gamma=0$ to 2)

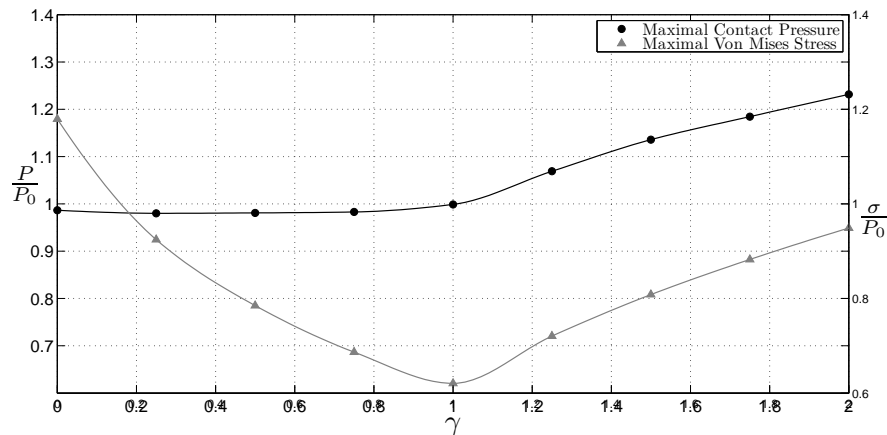


Figure 3.22: Maximum dimensionless contact pressure and von Mises stress vs. the ratio $\gamma = E_i/E_m$

The maximum of the dimensionless contact pressure and von Mises stress are shown in Figure 3.22 as function of the γ ratio. It can be seen that, when both Poisson's ratios equal 0.3, the maximum of the dimensionless contact pressure increases with the inclusion stiffness when the inclusions are stiffer than the matrix ($\gamma > 1$), whereas it remains almost constant and slightly

lower than the homogeneous solution when inclusions are softer ($\gamma < 1$). An increase of more than 22% in maximum contact pressure is found in this example when the Young's modulus of inhomogeneities is twice that of the matrix. Conversely the minimum of the dimensionless contact pressure decreases when decreasing the γ ratio for inclusions softer than the matrix, whereas it remains almost constant and slightly higher than the homogeneous solution for stiffer inclusions (see Figure 3.21). Regarding the maximum von Mises stress, it is observed in Figure 3.22 that either decreasing or increasing the inhomogeneity stiffness from the homogeneous solution increases the stress magnitude. The dimensionless von Mises stress reaches 0.94 for $\gamma=2$ (i.e. stiff inclusion) and 1.18 when $\gamma=0$ (void). Note that the maximum of the dimensionless von Mises stress is found minimum for $\gamma=1$, i.e. $\sigma/P_0=0.61$, which corresponds to the Hertzian or homogeneous solution.

3.3.2 Influence of the inclusion's radius using a unique inclusion

The effect of a single spherical inhomogeneity located near the surface and with its center lying along the axis of symmetry as shown in Figure 3.23 is now investigated. As shown schematically two situations can be encountered. In Figure 3.23(a) one point of the inhomogeneity surface is always tangent to the contact surface and the center of the inhomogeneity is located at $(0,0,r)$. In Figure 3.23(b) the center of the inhomogeneity is kept fixed and located at $(0,0,h=0.5a)$ which is close for a circular contact with homogeneous material to the point where the von Mises stress is found maximum. Note that in the current example the Poisson's ratios and the Young's modulus ratio are $\nu = 0.3$ and $\gamma = 2$, respectively.

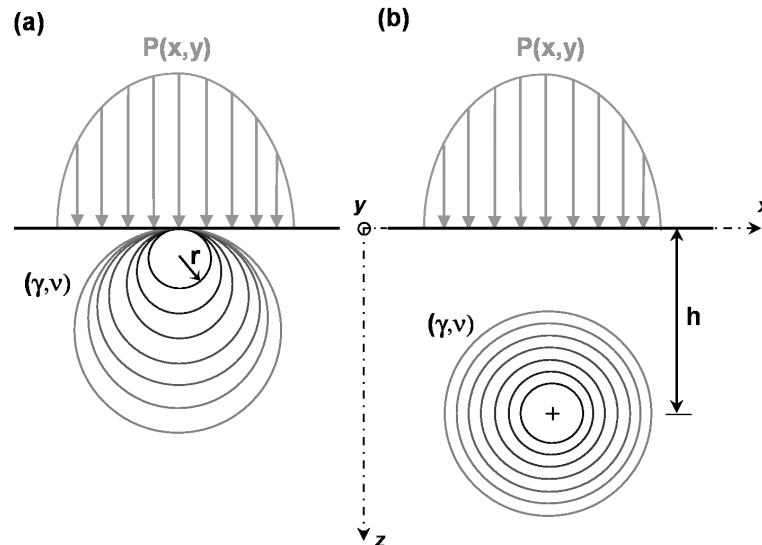


Figure 3.23: Schematic representation of two configurations to study the influence of the inhomogeneity of various radius r . a) The inhomogeneity is always tangent to the surface, b) the center of the inhomogeneity is fixed at depth $h=0.5a$

Figure 3.24 presents the profile of the dimensionless contact pressure in the plane $y=0$ for

different inclusion radii when they are tangential to the surface, see Figure 3.23(a). The same profile is shown in Figure 3.27 when the inclusion center remains fixed, see Figure 3.23(b). It is obvious that the presence of an inhomogeneity in the vicinity of the contact strongly affects the contact pressure distribution. For inclusions tangent to the contact surface effects are significant even for small radius; $r=0.03a$ implies an increase in contact pressure of nearly 25%. For inhomogeneities located at the Hertzian depth the effect on the contact pressure becomes significant for $r=0.17a$ and larger radius. Figure 3.26 shows the maximum dimensionless contact pressure and von Mises stress for different values of radius r for configurations (a) and (b) in Figure 3.23. For configuration (a), the maximum contact pressure is found maximum and equal to $P_{max}=1.75P_0$ for $r=0.17a$, whereas the maximum von Mises stress is found for $0.33a < r < 0.67a$. For configuration (b) i.e. when the inclusion center is maintained fixed, one observes a monotonic increase of the contact pressure and von Mises stress with the radius of the inhomogeneity. A soft inclusion will lead to a reduction of the contact pressure in a similar manner.

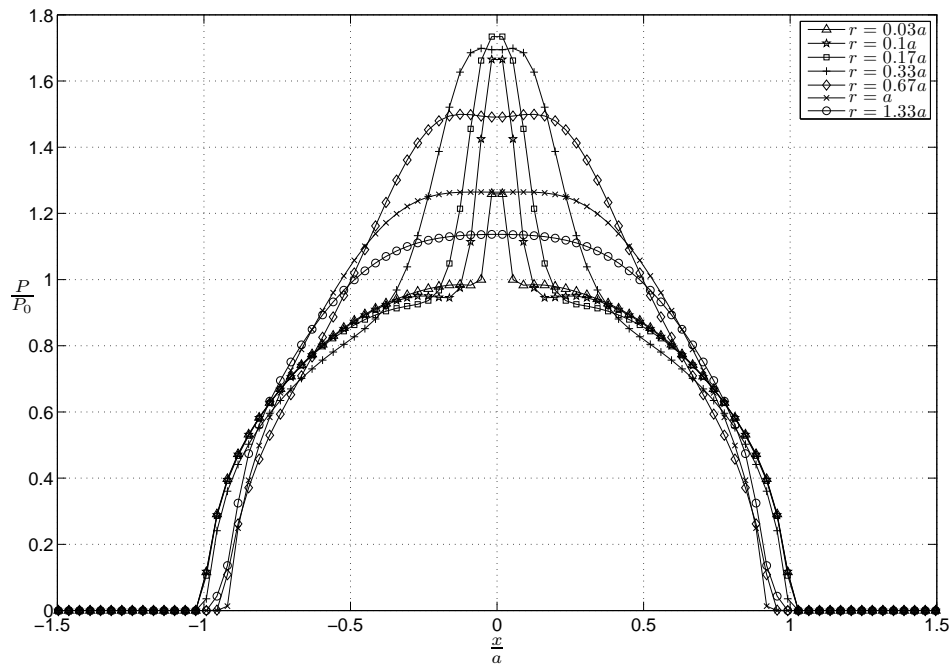


Figure 3.24: Contact pressure profile in the plane $y=0$ for an inhomogeneity ($\nu=0.3$ and $\gamma=2$) of different radii and tangential to the surface, cf. figure 3.23(a)

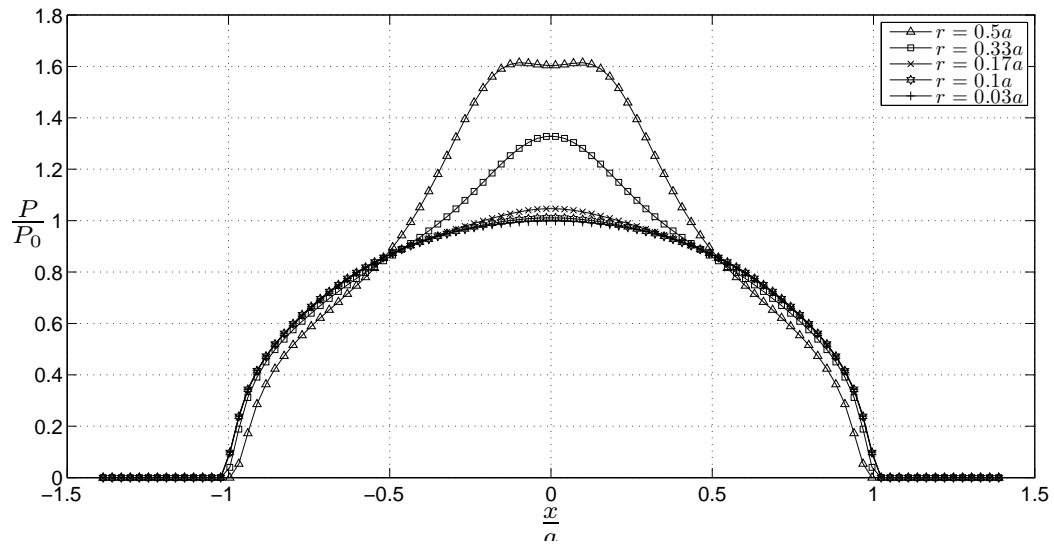


Figure 3.25: Contact pressure profile in the plane $y=0$ for an inhomogeneity ($\nu=0.3$ and $\gamma=2$) of different radii at depth $h=0.5a$, cf. Figure 3.23(b)

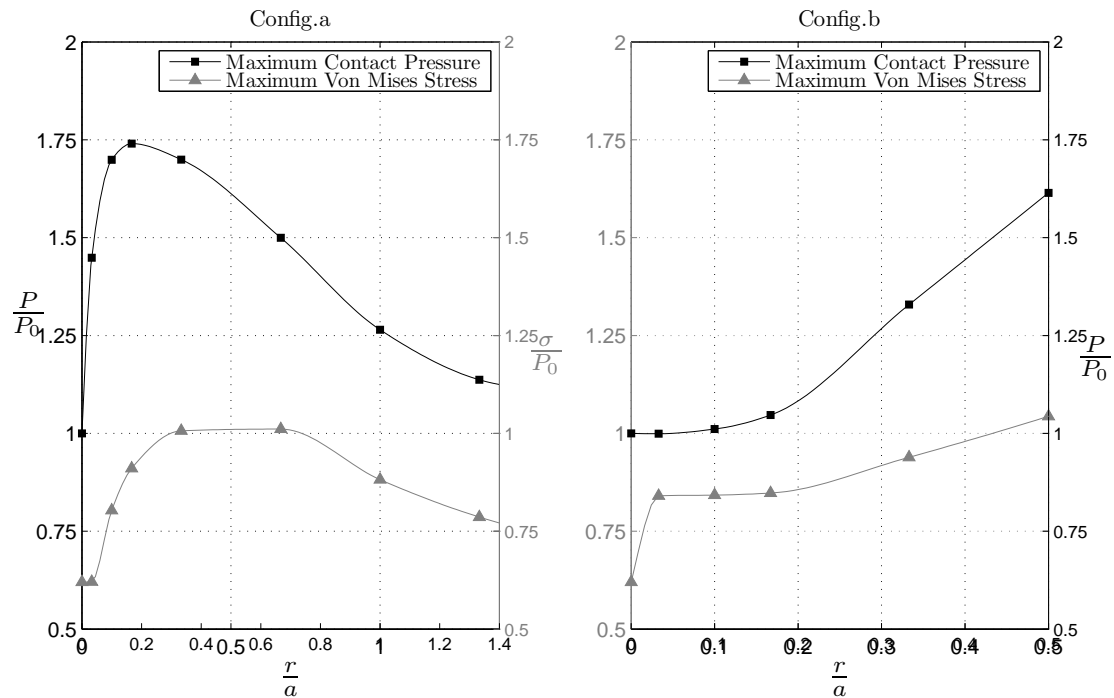


Figure 3.26: Maximum contact pressure and von Mises stress vs. the inclusion radius

3.3.3 Influence of the Poisson's ratio using a cluster of inclusions

When several inhomogeneities are present the solution may be affected by the interactions between them. Figure 3.27 shows the distribution of the contact pressure for a cluster of spherical inhomogeneities. Here all neighboring inclusions of same radius $r=0.17a$ are tangent to the contact surface. It is observed that the maximum of the contact pressure ($P_{\max}=1.65P_0$) becomes slightly lower compared to the case of a single inhomogeneity ($P_{\max}=1.75P_0$) whereas the maximum of the von Mises stress slightly increases from $\sigma_{\max}=0.92P_0$ to $\sigma_{\max}=0.99P_0$.

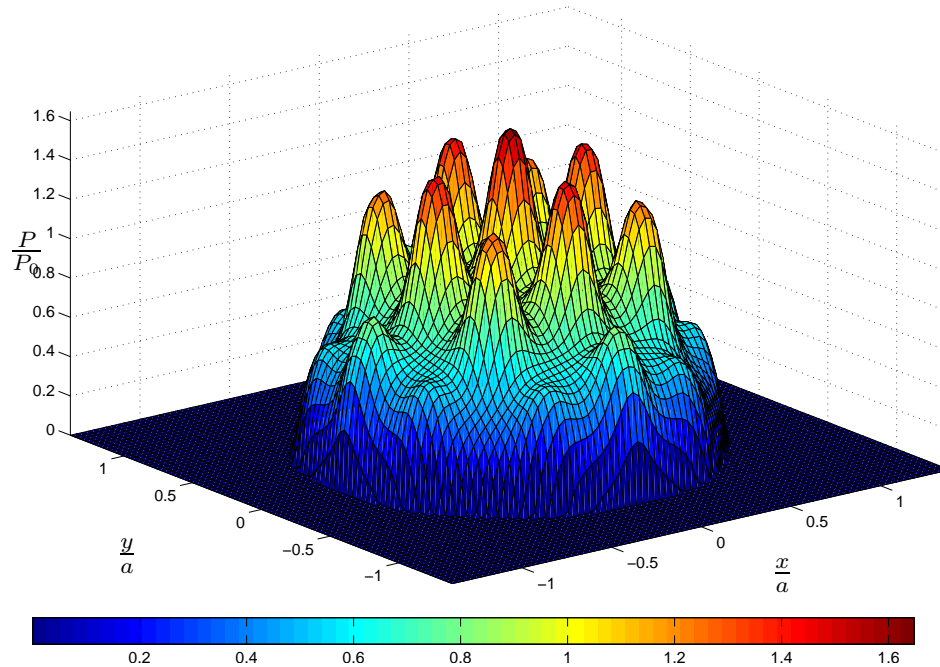


Figure 3.27: Distribution of the contact pressure for a cluster of spherical inhomogeneities tangent to the contact surface

The effect of the Poisson's ratio is now analyzed. A cluster of spherical inhomogeneities equally spaced within a domain composed of $84 \times 84 \times 31$ cuboids such that the inclusion center is $\Delta x = \Delta y = \Delta z = 0.27a$ is considered, giving 484 inclusions. The size (edge) of each cuboid is $0.2 \mu\text{m}$. The radius of the inclusions is $r = 0.6 \mu\text{m} = 0.1a$. Thus the inhomogeneities take up 22% of the volume within the domain of interest (no inclusion is considered far away from the contact). Figure 3.28 shows the dimensionless maximum of the contact pressure and von Mises stress with different Poisson's ratios for relatively compliant ($\gamma=0.5$) and stiff inhomogeneities ($\gamma=2$). For stiff inclusions ($\gamma=2$), the maximum of the contact pressure is not too much influenced by the variation of the Poisson's ratio except for nearly incompressible ones ($\nu=0.45$) that produces an increase of the contact pressure of nearly 28% on the top of each of them.

Meantime the maximum von Mises stress decreases continuously when the Poisson's ratio increases. For relatively soft inclusions ($\gamma=0.5$) the maximum contact pressure is independent of the Poisson's ratio – in fact only the minimum of the pressure distribution is influenced – see

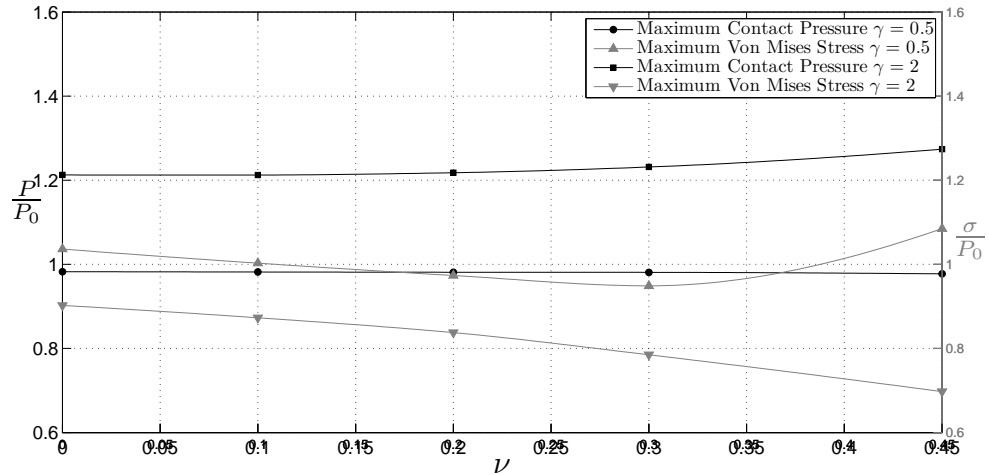


Figure 3.28: Maximum contact pressure and von Mises stress vs. the inclusion Poisson's ratio

Figure 3.29. More surprisingly, it can be observed that, in term of von Mises stress, the worst situation for a soft inclusion is when they are nearly incompressible ($\sigma/P_0=1.09$ for $\nu=0.45$).

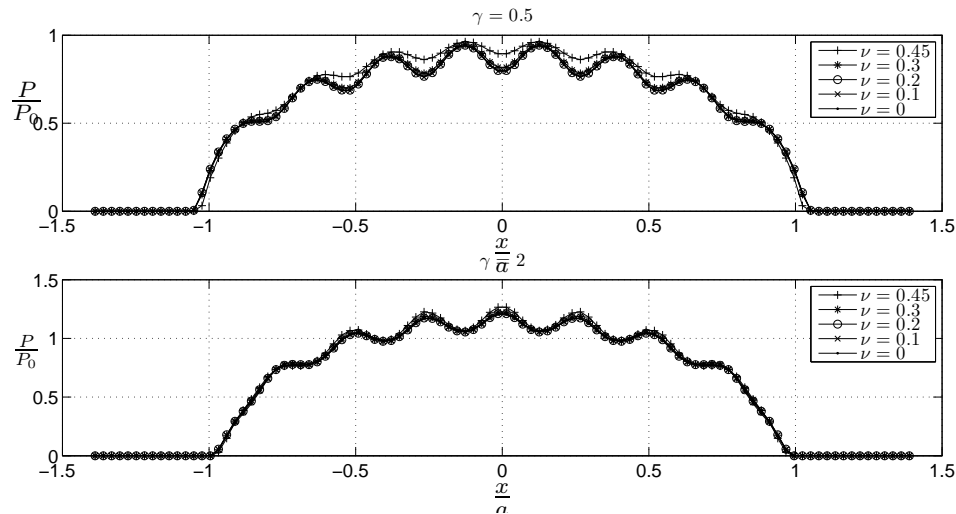


Figure 3.29: Profile of the contact pressure in the plane $y=0$ for soft or stiff inhomogeneities for various inclusion Poisson's ratio ($\nu_m=0.3$)

3.3.4 Influence of the inclusion's depth using a unique inclusion

The effect of the depth h of a horizontal plane of inhomogeneities is now investigated. A set of 49 inclusions equally spaced in a zone composed of cuboids is considered such as the distance between inclusion centers is $\Delta x = \Delta y = 0.37a$. The edge of a cuboid is $0.2\mu\text{m}$. The inhomogeneities with Young's modulus ratio $\gamma=2$ and Poisson's ratio $\nu=0.3$ have a radius $r=0.8\mu\text{m}=0.13a$. Figure 3.30 shows the effects of the plane depth on the contact pressure profile in the plane $y=0$. The pressure fluctuation becomes significant when the inclusions are located at a depth lower than $0.3a$, and reaches a maximum when they are tangent to the contact surface (i.e. for $h=0.87a$). Figure 3.31 shows the influence of the depth h where inhomogeneities are located on the maximum contact pressure and von Mises stress. Obviously the influence of inhomogeneities on the contact pressure diminishes as the inhomogeneities move away from the contact surface. When $h/a > 0.4$, the effect of the inhomogeneities on contact pressure becomes insignificant and the distribution of contact pressure converges to the solution of homogeneous half-space. The pressure peak reaches $1.75P_0$ when the inclusions are tangent to the surface ($\gamma=2$, $\nu=0.3$). Note that the maximum von Mises stress is found for $h/a \simeq 0.5$ which is coherent with the Hertz solution. To look more closely on how nearby inclusions interact only two of them will be now considered.

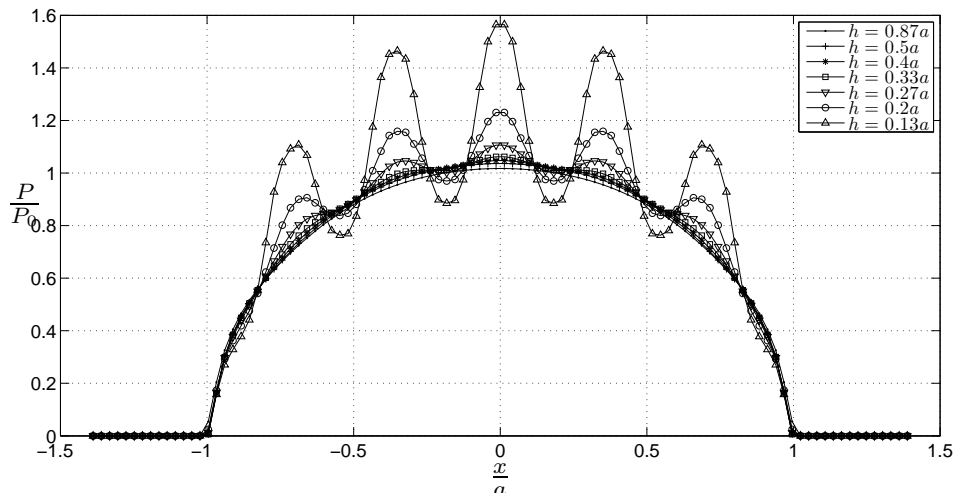


Figure 3.30: Profile of the contact pressure in the plane $y=0$ for a set of 49 inhomogeneities equally spaced in a horizontal plane at depth h

3.3.5 Mutual interactions

The interaction between inhomogeneities is another factor that significantly affects the location and magnitude of the maximum von Mises stress. It can be noted that the interaction can be neglected when the spacing between the center of two close inclusions becomes larger than four times their radius. The influence of neighboring inclusions is studied here by considering two spherical inclusions in the elastic half-space as shown in Figure 3.32, one of them (inclusion numbered 1) being lying along the z -axis which is the axis of symmetry normal to the circular contact area. The inhomogeneities have the same Poisson's ratio $\nu = 0.3$ and the same radius

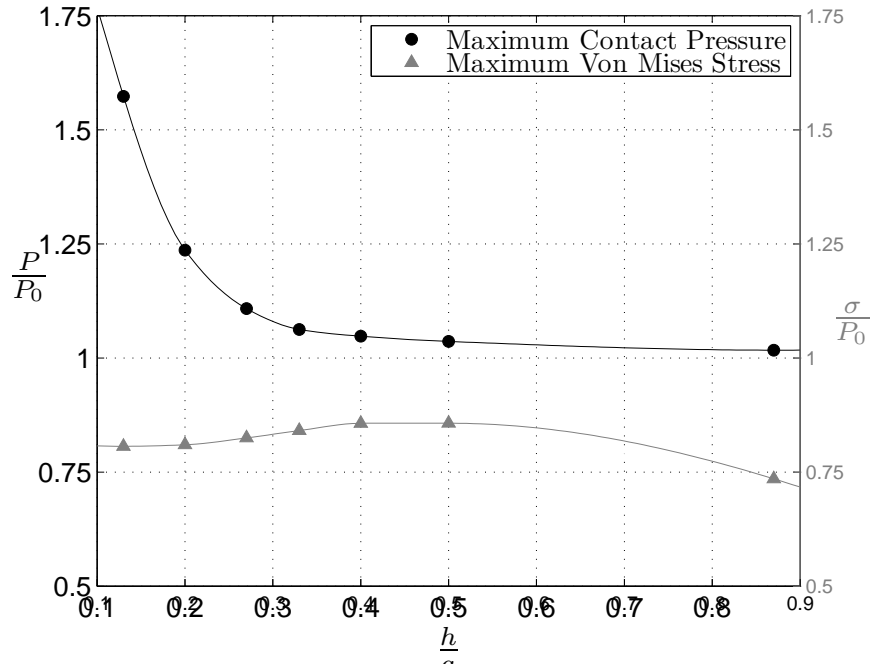


Figure 3.31: Maximum contact pressure and von Mises stress as a function of the depth where inclusions are located

$r=0.13a$. The centers of two inhomogeneities are separated by a distance d . The variable d is formulated through the dimensionless distance β such as $\beta = (d - 2.r)/r$. $\beta=0$ means that the 2 inclusions are in contact ($\beta \in [0, \infty[$).

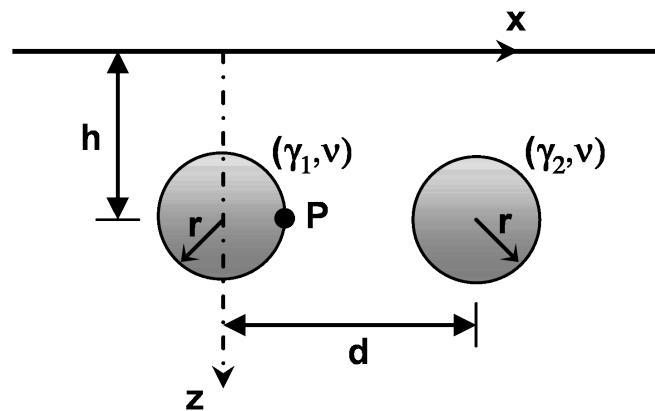


Figure 3.32: Representation of two inhomogeneities in the elastic half-space

Figure 3.33 shows the contact pressure profile for different combinations of Young's modulus relatively to the matrix, i.e. $\gamma_1 = 0.5$ and 2 and $\gamma_2 = 0, 0.5$, and 2. Here the inclusions are separated by the distance $\beta=0.25$ at the depth $h=0.23a$. For reference, the Hertzian solution is also plotted.

It is shown that, independently of the stiffness of the first inhomogeneity, the peak or dip of the contact pressure on the top of this first inhomogeneity is hardly affected by the presence of a second one when located in the same horizontal plane, including when inclusions are relatively close (here $\beta=0.25$). It could be concluded that the effect of neighboring inclusions on the contact pressure above a first one is quite limited, when they are located at the same depth. Conversely, an alignment of inclusions along the vertical direction will affect the pressure distribution on the top of the stringer.

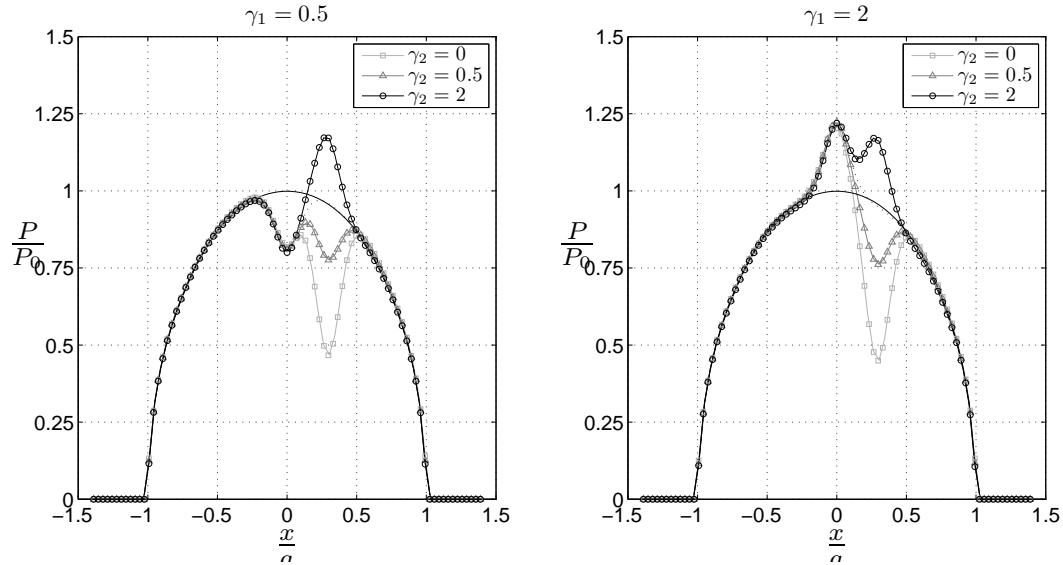


Figure 3.33: Profile of the contact pressure on the top of two inclusions of various stiffnesses γ_1 and γ_2

The mismatch of material properties could induce sliding failures at the interface between the inclusions and the matrix. The region where the maximum shear stress is located could also give birth to fatigue cracks. Figure 3.34 shows the influence of the spacing between the two inclusions located at depth $h=0.23a$ for different ratios of their Young's modulus normalized by the matrix value (γ_1, γ_2) on the maximum shear stress evaluated at point P located at coordinates $(x, 0, 0.23a)$. For comparison, the maximum shear stress for a single inclusion is also included in the form of a dash line. It is shown that the maximum shear stress starts to be significantly affected when the dimensionless spacing β is lower than 3. Note that, when both a soft and a stiff inclusions are present, the shear stress decreases and increases near the soft and stiff inclusion, respectively. It can be also noticed that the maximum shear stress tends to increase at point P when two inclusions softer than the matrix become closer. Conversely the maximum stress is relaxed near the inclusion interface when both interacting inclusions are stiffer than the matrix. Finally the worst situation is found in presence of voids or cavities ($\gamma=0$), particularly when they are located near stiff inhomogeneities ($\sigma_m/P_0=0.54$ for $\beta=0.25$, $\gamma_1=2$ and $\gamma_2=0$, see right plot in Figure 3.34).

It should be recalled that for a circular point contact the maximum shear stress is located at depth $h=0.5a$ (0.48a accurately), whereas the two interacting inclusions have been previously located at depth $h=0.23a$ only in order to strongly affect the contact pressure distribution which is no

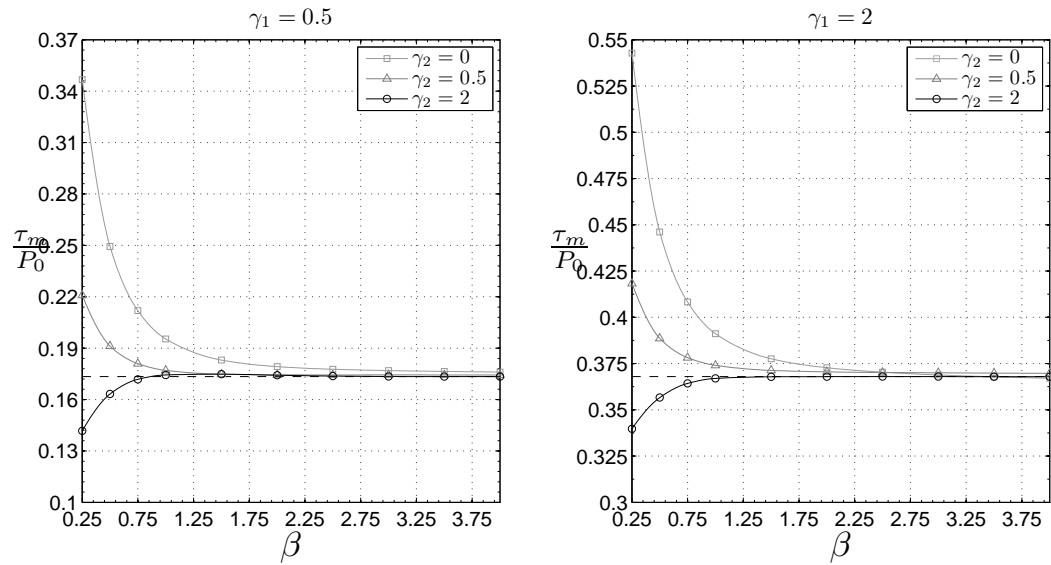


Figure 3.34: Maximum shear stress at point P of coordinate $(r,0,0.23a)$ as a function of the spacing between the two inclusions located at depth $h=0.23a$

more Hertzian. Figure 3.35 shows similar results as in Figure 3.34 except that the two inclusions are now located at depth $h=0.5a$ and the stress given at point P' located at the coordinates $(r,0,0.5a)$. It is found that, when $3 < d/r < 5$ and for two inclusions softer than the matrix, the magnitude of the maximum shear stress increases slightly compared to the case of a single inclusion. When $d/r < 3$ (i.e. $\beta < 1$), the soft inclusion relaxes the surrounding material and reduces the magnitude of maximum shear stress. On the other hand, the effect of stiff inclusion could cause the maximum shear stress to increase as the distance between the inclusions decreases. The very different behaviors of the interactions between two close inhomogeneities as plotted in Figures 3.34 and 3.35 could be explained first by the contact pressure distribution on the top of inclusions.

However the interaction effects near the interface inclusion/matrix are not entirely considered due to the approximate solution of the equivalent inclusion method. The compatibility strain is concentrated around a low zone close to the interface, and generates high strain gradient. In this section, the strain distributions around the interacting inclusions are computed by using Eshelby's equivalent inclusion method with constant eigenstrains and uniform applied strains. Benedikt [BEN 06] presented three-dimensional stress analysis around interacting spherical inclusions. A Taylor series expansion is employed to find the approximate solution of equivalent method equations with constant, linear, or quadratic eigenstrains. The accuracy of this analytical method is performed to compare results to finite element computations. The quadratic expansion order of the constrained strain and eigenstrains allows to reduce the error between the equivalent inclusion method and finite element solution for two close inhomogeneities. Furthermore the choice of the location of the point around which the Taylor expansion is carried out has an influence on the accuracy of the solution.

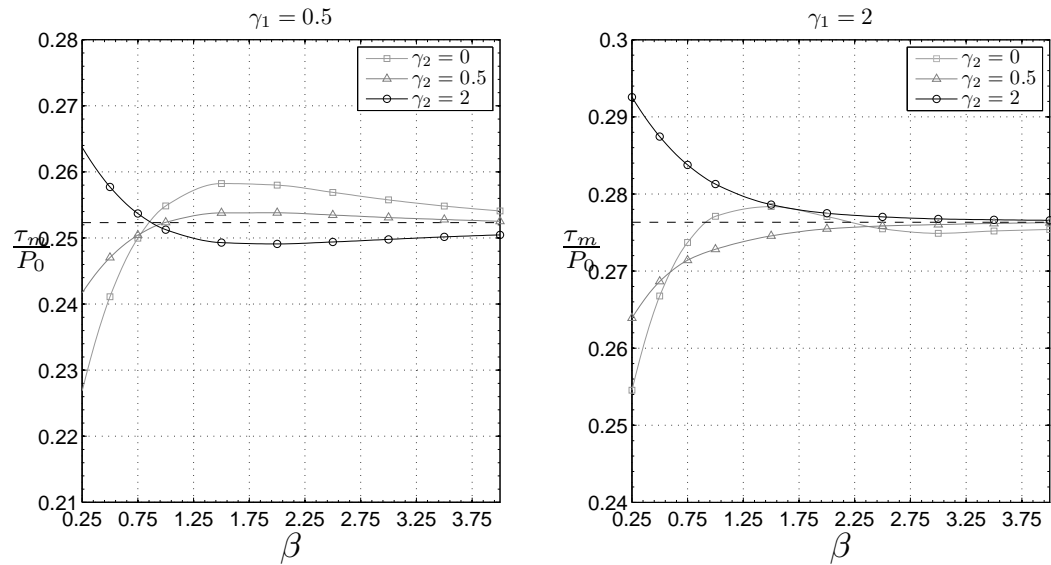


Figure 3.35: Maximum shear stress at point P' of coordinate $(r,0,0.5a)$ as a function of the spacing between the two inclusions located at depth $h=0.5a$

3.3.6 Summary

A list of the most important results is given below:

- The pressure fluctuation becomes significant when the inclusions are located at a depth h lower than $0.3a$, a being the Hertz contact radius, and reaches a maximum when they are tangent to the contact surface. When $h/a > 0.4$, the effect of the inhomogeneities on the contact pressure becomes insignificant and the distribution of contact pressure converges to the solution of homogeneous half-space.
- For stiff inhomogeneities of Young's modulus two times the matrix one ($\gamma=2$), and Poisson's ratio of 0.3 also identical to those of the matrix, the peak of pressure may reach up to $1.75 \times P_0$, P_0 being the Hertz contact pressure, when the inclusions are tangent to the surface.
- The contact pressure on the top of an inhomogeneity is hardly affected by neighbours ones when they are located in the same plane parallel to the contact surface, including when they are very close.
- The Poisson's ratio of the inhomogeneities has a strong influence on the pressure distribution when it tends to the incompressible case ($\gamma=0.5$).
- The presence of a soft inclusion close to a stiff one significantly increases the local stress nearby the hard inclusion. A concentration factor of nearly 2 ($\sigma_m/P_0=0.54$ for $\beta=0.25$, $\gamma_1=2$ and $\gamma_2=0$) can be found when a void is located nearby a stiff one ($\gamma=2$) at mid-way ($z=0.23a$) between the Hertzian depth ($z=0.48a$) and the surface, compared to the homogeneous Hertz solution ($\sigma_m/P_0=0.3$ at $z=0.48a$).

Acknowledgments Thanks go to Mr. J. Leroux for his helpful discussions and applications highlighting the influence of a cluster of spherical inclusions onto the surface during his Master's degree [LER 10].

3.4 Inclusions considering gradients

3.4.1 Enrichment of a complete half-space

Considering an arrangement of cuboidal inclusions (similar results are found when enriched with an arrangement of spherical inclusions), the whole domain will be enriched so it becomes an homogeneous half-space with a different Young's modulus. This assumption becomes true if the stress levels below the surface are correctly described by the mesh discretization. Because the 3D-FFT is considering a numerical integration of the pressure field sub-problem, a tiny error could be induced due to a poor discretization made locally for elements close to the surface.

In order to prove the accuracy of the method for a simple case of indentation, a rigid spherical tip will indent an elastic fat. Three different cases will then be considered, (i) a homogeneous media with (E, ν) describing its elastic properties, (ii) a homogeneous media for which the Young's modulus is equal to 80% of E , and the Poisson's ratio is kept equal to $\nu = 0.3$. Both problems can be easily solved using an elastic contact solver or the Hertz's solution. (iii) The third case will then consider an elastic media (E, ν) but a damage rate of 20% will then be considered all over the media. In other words, for each mesh discretization of the media, a cubical inclusion will be considered and its mechanical properties are $(0.8 \times E, \nu)$. To recap, those three cases are shown hereafter (See Figure 3.36)

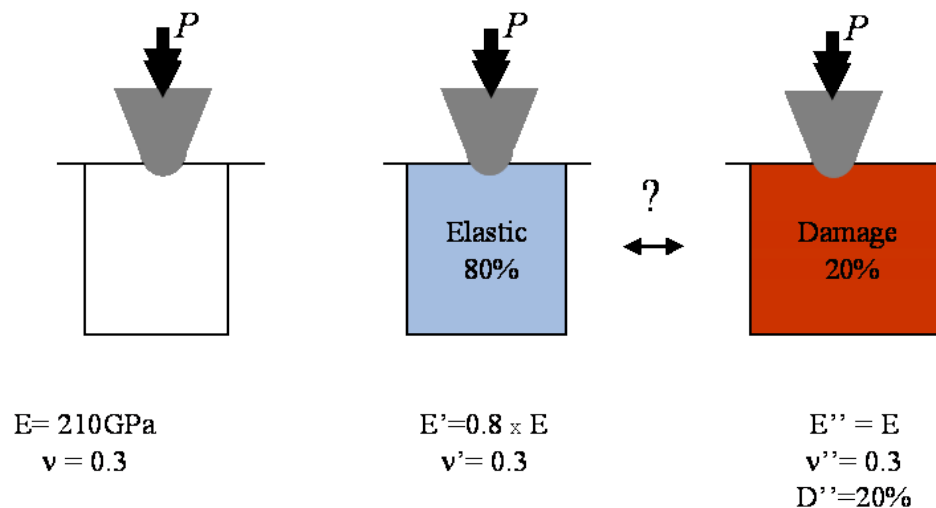


Figure 3.36: Three cases are considered; case (ii) and (iii) are theoretically equivalent

Elastic problems (i) and (ii) are implicitly semi-infinite, while the damage problem (iii) is defined in the domain considered and is explicitly finite because elastic properties (E, ν) will be considered out of the domain for the third problem. In order to get a better agreement, the damaged domain is extended and must contain all stressed regions. Misfit displacements are calculated using the 3D-FFT algorithm and used to update the geometry, which leads to a different pressure field. Pressure fields are then compared below, and show a good agreement, validating this approach.

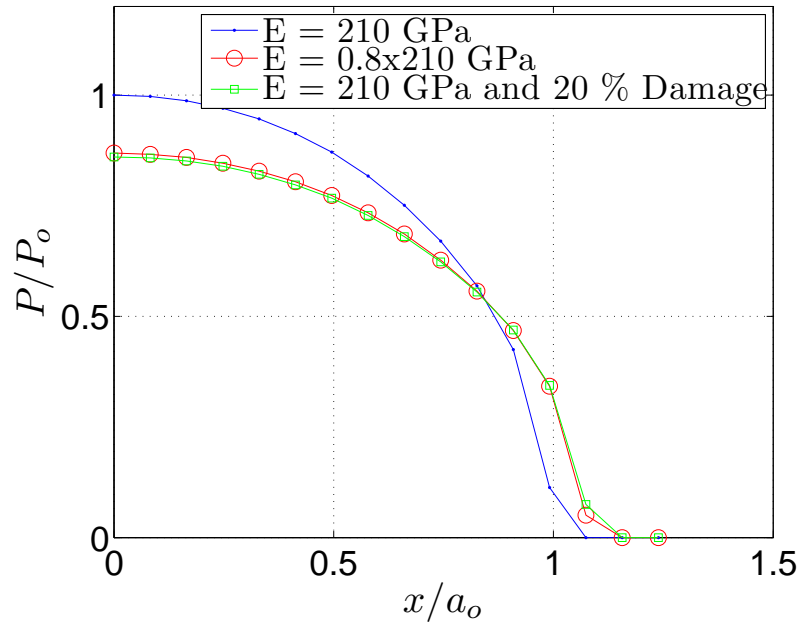


Figure 3.37: Pressure fields for all cases considered. Case (ii) and (iii) are equivalent

This is a very simple analysis, but it shows the feasibility of non-homogeneous analyses using cubical inclusion as a local enrichment in order to describe any kind of geometry. Considering previous developments, spherical, ellipsoidal, cuboidal or even polyhedral inclusions can be discretized in many cubical inclusions and studied using such method.

3.4.2 Inclusions discretized in many cubes

First, consider an ellipsoidal inclusion ($a_1=a_2=3.a_3$) or a spherical inclusion ($a_1=a_2=a_3$) in an infinite media. Numerical calculations were carried out with $\nu=0.3$. The dimensionless stress distributions are shown hereafter. Solid curves are analytical results [MUR 79] and symbols are semi-analytical results. A good agreement is found even when inclusions are poorly discretized, considering only 10 cubes for a_3 .

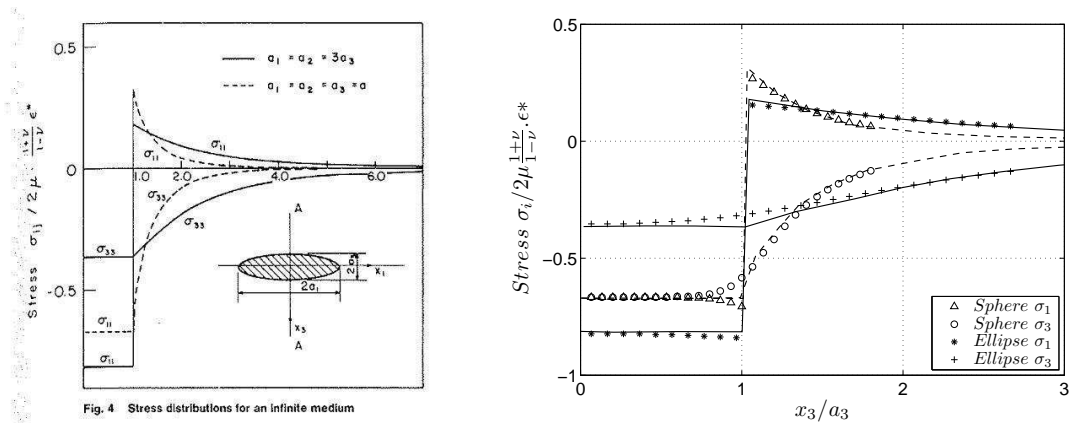


Figure 3.38: Stress distribution along the x_3 -direction ($x_1=x_2=0$) for an inclusion in an infinite space. Solid lines are analytical solutions [MUR 79] and symbols are semi-analytical results

It is noticed that stresses are uniform in ellipsoidal inclusions according to Eshelby's work. Small differences can be observed in regions surrounding inclusions due to the discretization in many cubical elements. This error tends to be nil when inclusions get much more discretized, but computing time becomes rapidly unaffordable. Component σ_{zz} is compressive everywhere, in and out of the inclusion, while component σ_{xx} is compressive inside and tensile outside. This observation can be made, regardless of the ratio of ellipticity.

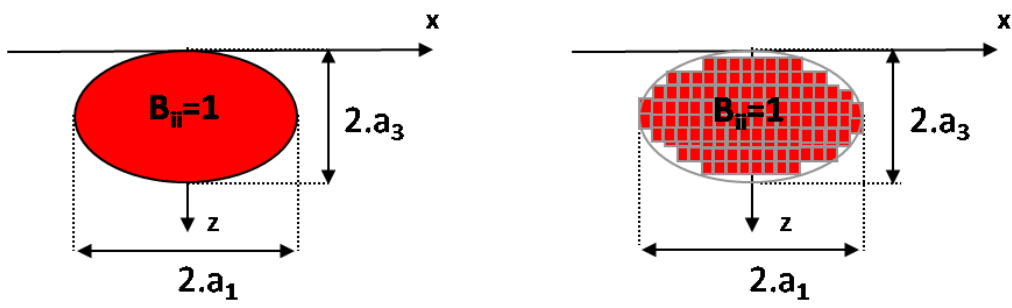


Figure 3.39: Spherical ($a_1=a_2=a_3$) and ellipsoidal ($a_1=a_2=3.a_3$) inclusions tangent to the free surface

Now, let's consider an ellipsoidal inclusion ($a_1=a_2=3.a_3$) or a spherical inclusion ($a_1=a_2=a_3$) in a semi-infinite space. Those inclusions will be located at a depth $c=a_3$, meaning that the upper

side of inclusions are tangent to the surface. Dimensionless stresses will be shown along directions x_1 and x_3 , and including the center of the inclusion ($x_1=x_2=0$ and $x_3=a_3$). Once again, results found analytically are shown using solid curves while semi-analytical results are shown using various symbols.

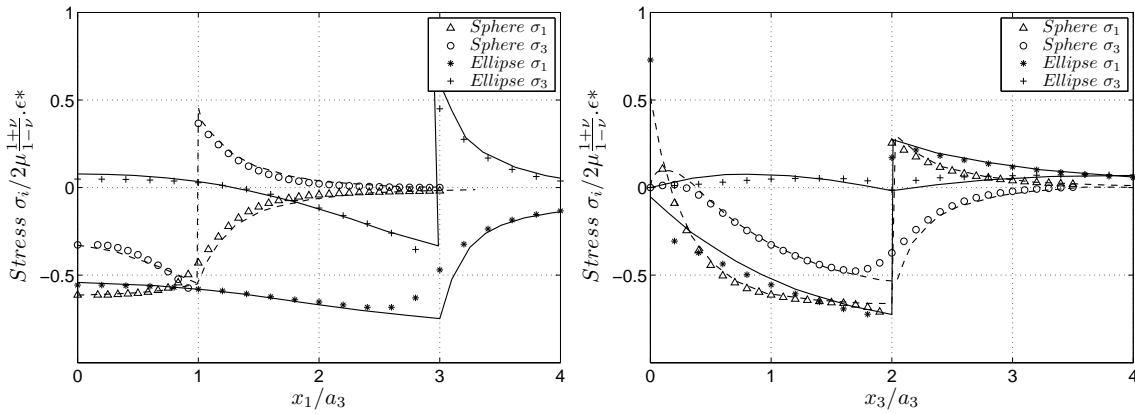


Figure 3.40: Stress distribution along the x_1 -direction on the left ($x_2=0$ and $x_3=a_3$) and x_3 -direction on the right ($x_1=x_2=0$) for $c=a_3$. Solid lines are results found analytically [MUR 79] and symbols are semi-analytical results

A good agreement is found despite some problems already encountered in previous studies when enriched elements are located close to the surface. Due to the discretization and geometries considered, only few elements are located just below the surface, their effect become negligible compared to the others' effect. Agreement is not as good as when considering the component σ_{xx} near the free surface, induced by an ellipsoid. Semi-analytical results highlight a tensile region in the free surface while Mura predicts a compressive region. Mura's result is not consistent with further results found in the same paper, while those results confirm the value of s_{11} found here ($x_1=x_2=x_3=0$). Along the x_1 -axis, the stress uniformity inside the inclusion for the infinite medium is diminished by the existence of the free surface and some regions near the free surface become under tension from compression. Along the x_3 -axis, the stress component σ_{zz} is continuous and takes a maximum tension at an interior point and a maximum compression at the interface ($x_1=x_2=0$ and $x_3=2.a_3$). The maximum compression appears at the interface point. Its magnitude is quite different for the two cases and the compression region is broader in the ellipsoidal case than in the spherical case. It must be noticed that σ_{zz} is now a tensile stress in some regions while it was exclusively a compression stress when considering an infinite half space. The stress component σ_{xx} is tensile close to the surface and becomes rapidly compressive at interior points and increases with x_3 . It changes discontinuously to tension for exterior points and decays to zero at infinity. Same variations of s_{11} are observed for both geometries.

Accuracy of the method has to be checked when considering inclusion at various depths. An ellipsoidal inclusion ($a_1=a_2=3.a_3$) or a spherical inclusion ($a_1=a_2=a_3$) are then considered at a depth $c=2.a_3$. Stress components σ_{xx} and σ_{zz} along the x_3 -direction are shown hereafter and highlight the same agreement.

As proposed by Mura, and in order to check the accuracy of the method, the stress component σ_{xx} at $x_1=x_2=x_3=0$ is shown for various depths and aspect ratios of ellipsoid ($a_1=a_2=a_3$; $a_1=a_2=3.a_3$ and $a_1=a_2=7.a_3$). For the spherical inclusion σ_{xx} shows large tension at the surface

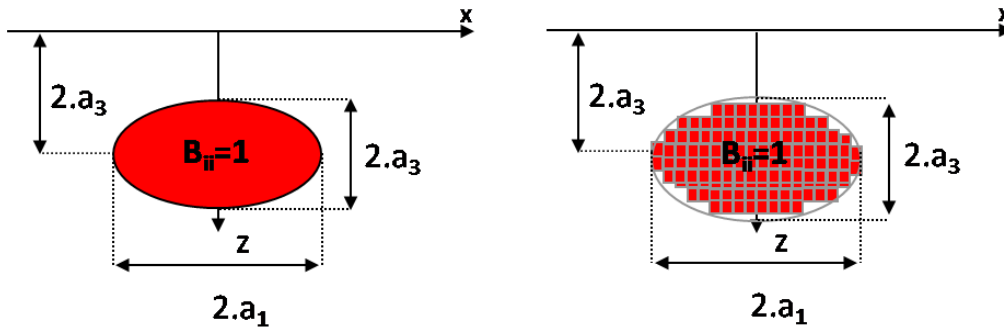


Figure 3.41: Spherical ($a_1=a_2=a_3$) and ellipsoidal ($a_1=a_2=3.a_3$) inclusions located at depth $c=2.a_3$

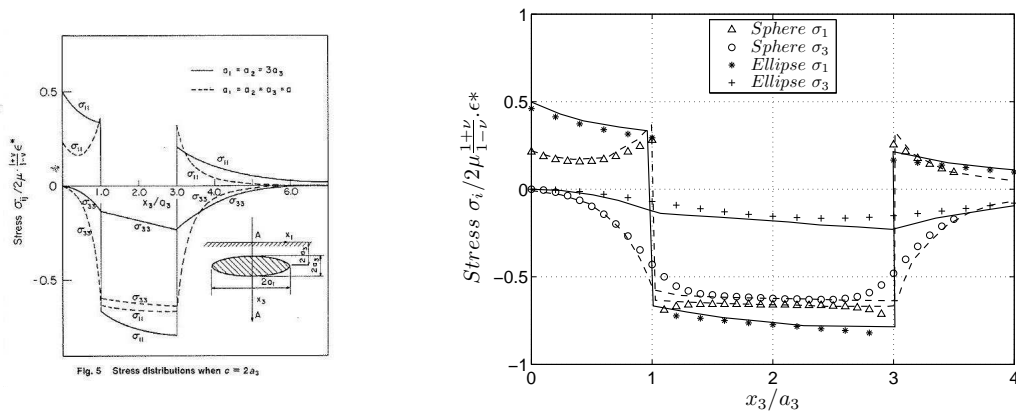


Figure 3.42: σ_{11} at $x_1=x_2=x_3=0$ showing the effects of c and shapes of the inclusion, solid lines are analytical solutions and symbols are semi-analytical results [MUR 79]

and it decreases with c . It becomes almost zero when $c > 3.a$. σ_{xx} at the surface decreases when the ellipsoid becomes flatter. However, the effect of the depth c is less prevalent in the flatter inclusion. Depending on the depth of the inclusion, a spherical inclusion can be more critical than an ellipsoidal inclusion or not.

To recap, analytical solutions for ellipsoidal inclusions in half-space do exist when considering some assumptions such as purely dilatational eigenstrains. Thermal expansion can be treated with such assumption, but it is not sufficient when misfit strains have to be taken into account. A semi-analytical method has been developed so that ellipsoidal inclusion can be considered without any assumptions on misfit strains. Those ellipsoidal inclusions can be treated using two different methods:

- Influence coefficients of an ellipsoid in an infinite media and a 3D-FFT algorithm are used. The method is very powerful when dealing with small inclusions so gradients of stresses that will generate misfit strains can be neglected. This method has been largely studied in previous chapters.
- Influence coefficients of many small cubes that will define an elliptical domain can be used. In this method, ellipsoidal inclusions have been discretized in many cubical elements and

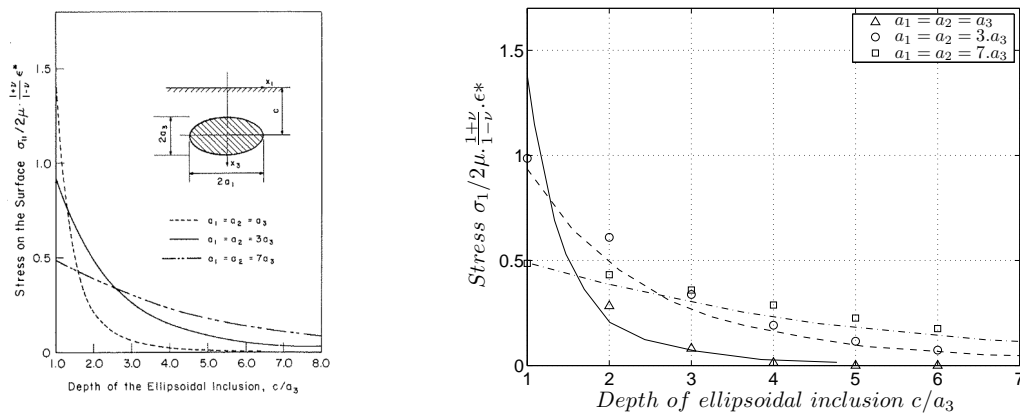


Figure 3.43: σ_{11} at $x_1=x_2=x_3=0$ showing the effects of c and shapes of the inclusion, solid lines are analytical solutions and symbols are semi-analytical results [MUR 79]

stress field induced by such refinement has been successfully compared to analytical results. This method has many advantages. Any geometry can be investigated, such as ellipsoidal, cubical or polyhedral inclusions. Moreover, misfit strains can be defined using local stresses of the homogeneous problem, so that gradients are explicitly taken into account. Inclusion's effect can now be studied, regardless of its size or location below the contact.

Considering this, the following chapter will try to highlight the interest of this method when considering ellipsoidal inclusions of large size below a spherical indenter. Gradients will be taken into account or not, and differences will be discussed. A study carried on by J.Leroux will permit to integrate gradients analytically in a cubical inclusion so that refinements won't be necessary explicitly.

3.4.3 Inclusions when considering gradients

Considering previous validations, further analysis will only show semi-analytical results. Inclusion's domain is now defined by many cubical inclusions, so that effect of gradients of contact or residual stresses can be taken into account. Local stress will be used to find misfit strains instead of considering the central stress and considering it uniform through the inclusion which is basically the Eshelby's theory used in all papers. Even if elliptical inclusions are considered hereafter, it must be noticed that any geometry could be treated, such as elliptical, cubical or polyhedral inclusions.

A rigid indenter with a spherical tip will be considered ($R=2\text{mm}$). Flat is made of steel and considered elastic ($E=210\text{ GPa}$, $\nu=0.3$). A normal load is then applied ($P=12.307\text{N}$) so that contact radius 'a' fits requirements ($a=20\mu\text{m}$). Contact is supposed frictionless, but misfit displacements are calculated in all three directions on the surface so frictional contacts can now be considered. Dimensions of elementary elements are the same in all directions and are $1\mu\text{m}$. An ellipsoidal inclusion ($a_1=a_2=3 \cdot a_3$) or a spherical inclusion ($a_1 = a_2 = a_3$) will be considered at a certain depth 'c'. In order to make results dimensionless, dimension a_3 of those inclusions is defined by the theoretical contact radius 'a' found considering the Hertzian theory ($a_3=0.5a=10\mu\text{m}$). When the upper side of inclusions is touching the surface, depth 'c' is then half of the contact radius

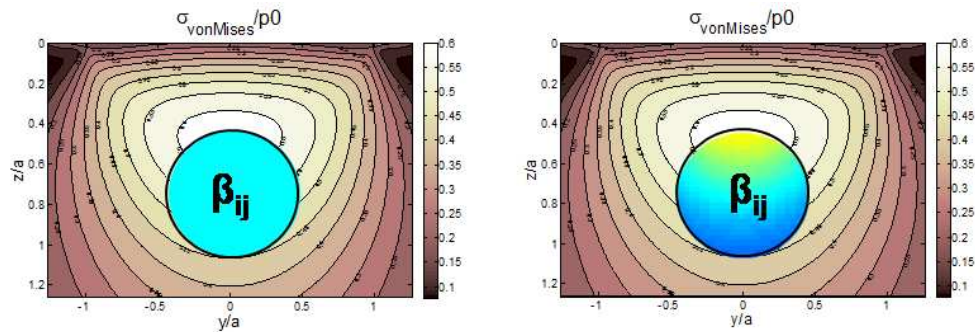


Figure 3.44: Spherical inclusion when considering central stress through the inclusion (left) or local stresses (right) in the misfit strain computation

($c=0.5a$), which is almost equal to the depth of maximum von Mises stress in an homogeneous contact problem. Another case will be considered ($c=a$), in this case, inclusions are located in a high gradients region and results could be sensibly different. Finally, inclusions will be considered harder or softer than the matrix and elastic modulus E_i is taken two times harder or softer than the matrix ($E_i=2.E$ or $E_i=0.5.E$). Finally, gradients will be taken into account or not, and results will be compared so the interest of such method should be highlighted. The Hertzian pressure has been set as a reference, meaning that stresses are dimensionless.

3.5 Conclusion

This chapter presents the main features of a fast semi-analytical three-dimensional method to treat the contact problem for a half-space containing multiple inhomogeneities. Analytical Eshelby solutions have been implemented in the contact solver to account for spherical inhomogeneities. It can be seen as a method to enrich the classical homogeneous solution of the contact problem. This technique is highly efficient in terms of computing time.

The numerical results given underline that most of the time it is not correct to assume a Hertzian pressure distribution for the contact problem in presence of soft or stiff inhomogeneities near the contacting surface, since the pressure distribution may exhibit a peak of pressure with a magnitude up to 1.75 times the Hertz solution. The peaks of pressure are located above stiff inhomogeneities while soft ones produce a local decrease of the contact pressure compared with that for the homogeneous half-space. The Poisson's ratio is also an important parameter which could increase significantly the contact pressure on the top of inhomogeneities when they tend to be incompressible (for example a cavity filled with a liquid). It is also noted that stiff inhomogeneity acts to toughen the surrounding material and reduce subsurface stress at the inclusion-matrix interface. This phenomenon is amplified when the inhomogeneities get closer.

Another way is to mesh an inclusion in many small cuboids. This method requires a finer mesh, but allows various shapes such as ellipsoidal inclusions, cubical, polyhedral and spherical inclusions. Using such technique, gradients inside the inclusion are considered. This technique has been validated considering results found for a spherical and an elliptical inclusion in [MUR 79].

Chapter 4

Coatings and other applications

Coating is a covering that is applied to the surface of an object, usually referred to as the substrate. In many cases coatings are applied to improve surface properties of the substrate, such as appearance, adhesion, wettability, corrosion resistance, wear resistance, and scratch resistance. In other cases, in particular in printing processes and semiconductor device fabrication (where the substrate is a wafer), the coating forms an essential part of the finished product.

Contents

4.1	Coatings	147
4.1.1	Elastic layers of uniform thickness using cubical inclusions	147
4.1.2	Enrichment techniques using spherical inclusions	149
4.1.3	Proposed technique for coating computations	153
4.1.4	Coatings under fully-sliding conditions	156
4.1.5	Coating thickness	161
4.1.6	Conclusion	163
4.2	Applications	164
4.2.1	Indentation of coated surfaces considering friction	164
4.2.2	Partial sliding over coated surfaces	167

4.2.3	Wear of coatings	175
4.2.4	Wear of coatings: fully sliding contacts	178
4.2.5	Fretting-wear of coatings: stick-slip conditions	185
4.2.6	Concrete used in civil engineering	194
4.2.7	Nano indentation of human bones	197
4.3	Conclusion	200

4.1 Coatings

Semi-analytical methods are a fast and simple tool for contact mechanics, running simulation with frictional, thermal and hardening aspects. Until now they have been mostly limited to homogeneous half-spaces. Removing this assumption could lead the way to many other applications such as (I) thermal softening, (II) damage for brittle materials and others, (III) coatings with complex mechanical properties – damage and plastic behavior, for instance - and many other applications considering different elastic properties in the media.

4.1.1 Elastic layers of uniform thickness using cubical inclusions

In previous studies, non-homogeneous aspects were applied to the whole domain, or to an ellipsoidal domain, but could also be applied to a thin layer so coating problems can be investigated. In this last part, stresses and pressure fields will be compared to numerical results found in the literature [O'S 88].

A rigid indenter is considered, with a spherical tip of radius R . It is pressed against an elastic material of properties (E_2, ν_2) covered by a layer (E_1, ν_1) — harder or softer than the substrate— and of thickness 'h' so that $R=10xh$. In order to normalize this problem, the normal load P will be applied so the contact radius is equal to h when unlayered (See Figure 4.9).

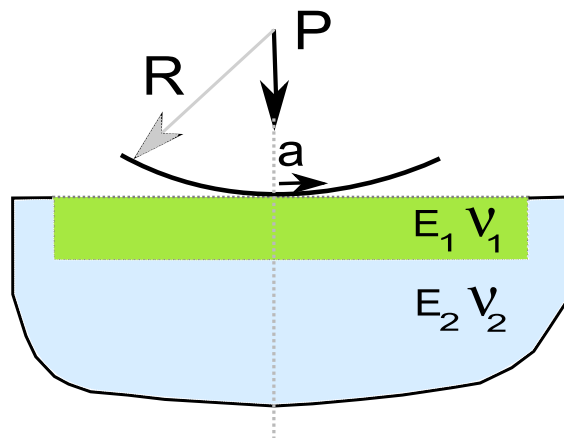


Figure 4.1: Spherical indentation of an elastic coating [O'S 88]

Five different coatings are investigated: $E_1 = 0.25E_2$ and $E_1 = 0.5E_2$ (softer coatings) $E_1 = E_2$ (same properties), $E_1 = 2E_2$ and $E_1 = 4E_2$ (harder coating). The contact radius increases with the softness of the coating, while the maximum pressure decreases (respectively, the contact radius decreases with the hardness of the coating, while the maximum pressure increases), according to numerical computations. However, pressure fields for each case are shown in Figure 4.2 and reveal a rough agreement between numerical and semi-analytical results, especially for hard coatings (See [O'S 88]).

When hard coatings are considered, the maximum pressure increases and may increase so that only one point remains in the contact ($E_1 = 4E_2$). This is a non-physical phenomenon and no

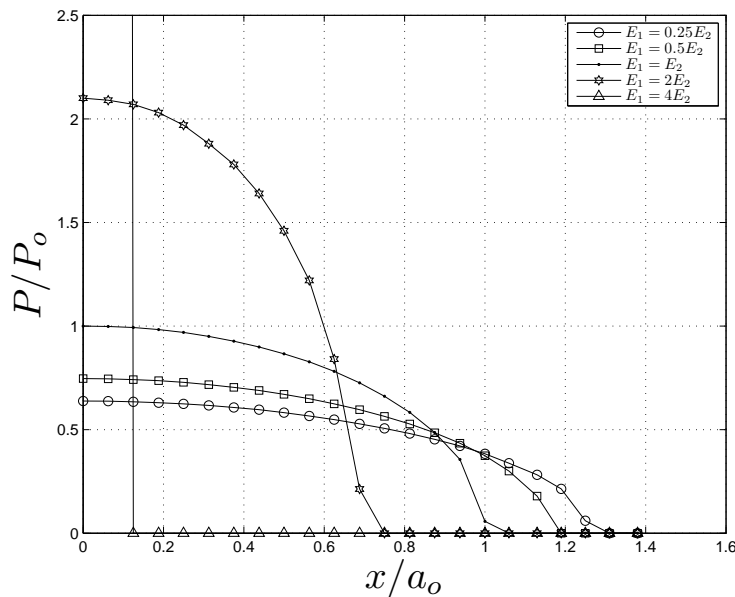


Figure 4.2: Pressure fields normalized by the Hertzian pressure for different coatings:
 $E_1 = 0.5E_2$, $E_1 = E_2$ and $E_1 = 2E_2$

valuable solution was found in order to prevent it. There is mainly two reasons that could cause such discrepancy:

- Non-homogeneities are typically close to the surface due to the film thickness and it must be reminded that elementary solutions and algorithm have been validated for spherical and cubical inclusions much deeper into the volume. Comparisons with numerical solutions would have fail with inclusions arising in the contact using a 3D-FFT algorithm. This numerical method is not adapted in this case because of the rough discretization of the pressure field σ_m (See section 2.3.7).
- Only the zero order of the Taylor's series has been considered for the cubical inclusions [MOS 75b]. It is a source of error that has been relatively small until now. But it could have an impact on the contact response when located in highly deformed volumes with high gradients. (See the note below)

note Very similar result were observed when enrichment functions used are relative to spherical inclusions. Despite the shape factor differences, the spherical inclusions have a great advantage over the cubical inclusions, their simplicity. Indeed, only the zero order of the Taylor's series has been considered for the cubical inclusions [MOS 75b], while spherical inclusions do not require such development and have an exact solution when in a uniform stress field. Some techniques were tested and little or no improvement was observed (See section 4.1.2). It was then concluded that even if the first and second order of the Taylor's series have a small impact on the results, it is not the source of such discrepancy.

	Solutions using a 2D-FFT	Solutions using a 3D-FFT
Cubical inclusion ($Z_0/2a \geq 5$)	If incompressible	
Spherical inclusion ($Z_0/2a \geq 5$)		
Cubical inclusion ($Z_0/2a < 5$)	If incompressible	<i>Reason^o 1</i>
Spherical inclusion ($Z_0/2a < 5$)		<i>Reason^o 1</i>

Table 4.1: Existing semi-analytical solutions when considering spherical or cubical inclusions at various depths Z_0 . The cube's size is $2b$ and its volume is equal to the sphere's volume

4.1.2 Enrichment techniques using spherical inclusions

The shape factor of a cube and a sphere are not the same. Strain fields induced by a cubical or a spherical inclusion are defined by the same equation, as shown below, where ϕ and ψ are bi-harmonic potentials.

$$\varepsilon_{ij} = \frac{1}{8\pi(1-\nu)} \cdot (\psi_{,ijkl} \cdot \beta_{kl} - 2\nu \phi_{,ij} \cdot \beta_{kk} - 2(1-\nu) \cdot (\phi_{,kj} \cdot \beta_{ik} + \phi_{,ki} \cdot \beta_{jk})) \quad (4.1)$$

with $\psi = \iiint_{\Omega} |x - x'| dx'$ and $\phi = \iiint_{\Omega} \frac{1}{|x - x'|} dx'$

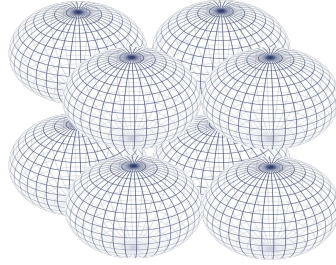
Bi-harmonic potentials ϕ and ψ are integral functions over the domain Ω , which is cubical or spherical depending on the geometry considered. This expression is valid outside of the domain Ω , and inside, defining the Eshelby's tensor 'S'. According to this, and because of the common sense, strain fields close to the inclusion considered is highly geometry-sensitive. When a spherical inclusion becomes close enough to the contact, its shape is no longer equivalent to a cubical inclusion, and the pressure field σ_m becomes different. Therefore, solutions of normal and tangential displacements become inaccurate.

	Stresses Inside	Stresses Outside ($Z_0/2b \geq 5$)	Stresses Outside ($Z_0/2b < 5$)
Sphere	Eshelby's tensor	Shape factor	Shape factor
	Eshelby's tensor	Shape factor	3D-FFT

Table 4.2: Validations of stress fields inside/outside of a spherical element

This lead to an over-estimation of normal and tangential displacements into the contact. For this reason, over-shooting of the real solution happened and non-physical solutions were found, especially when considering hard coatings because of the high stress levels close to the surface. The goal of this study is consider another geometry, based on an arrangement of spherical inclusions, in order to reduce the influence of the shape factor and verify that the 3D-FFT is the main source of error.

The shape factor of a cube and a sphere are not the same. When the influence coefficients obtained for a cube are compared to the coefficients of influence obtained for a unique sphere, differences may be observed, as seen in figures 4.3 and 4.4.



A technique was proposed to reduce the gap between both geometries using an enrichment technique, considering an arrangement of spheres, as seen herebelow. Obviously, the sum of all sphere's volume must be equal to the cube's volume. Similar arrangement are made considering 9 and 27 spherical inclusions. Because the relative size of inclusions is reduced, and the cubical volume is more correctly occupied, the shape factor differences are reduced. The coefficients of influence are then described as follow:

$$\varepsilon_{ij} = \sum_N \frac{1}{8 \cdot \pi \cdot (1 - \nu)} \cdot (\psi_{,ijkl} \cdot \beta_{kl} - 2 \cdot \nu \cdot \phi_{,ij} \cdot \beta_{kk} - 2 \cdot (1 - \nu) \cdot (\phi_{,kj} \cdot \beta_{ik} + \phi_{,ki} \cdot \beta_{jk})) \quad (4.2)$$

with $\psi = \iiint_{\Omega} |x - x'_N| dx'$ and $\phi = \iiint_{\Omega} \frac{1}{|x - x'_N|} dx'$ and $x'_N = x' + / - b$ where b is distance between the center of the cubical element and the center of each spherical inclusion N used to discretize this element.

Influence coefficients are computed only one time at the very beginning of the numerical procedure, and takes about 1 second for a domain of 60x60x60 elements. Depending on the refinement required, computing time of influence coefficients may be increased by the number of spheres used to refine one element. The computing time increase is negligible.

	Stresses Inside	Stresses Outside ($Z_0/2b \geq 5$)	Stresses Outside ($Z_0/2b < 5$)
N Spheres	Eshelby's tensor		3D-FFT

Table 4.3: Validations of stress fields inside/outside of an element made of 8 spheres

This technique highly increases the accuracy of the solution outside of the inclusion, as seen in figures 4.3 and 4.4 when 9 spheres are used instead of 1 cuboid or a large sphere of the same volume. However stresses inside the inclusion remain inaccurate since the Eshelby's tensor for a sphere has been used. Despite such improvement, discrepancies observed in 4.2 are still present, even when discretizing each cube in 27 spheres. This short study was necessary, and it now becomes clear that the 3D-FFT algorithm plays a key role in the creation of the instabilities observed.

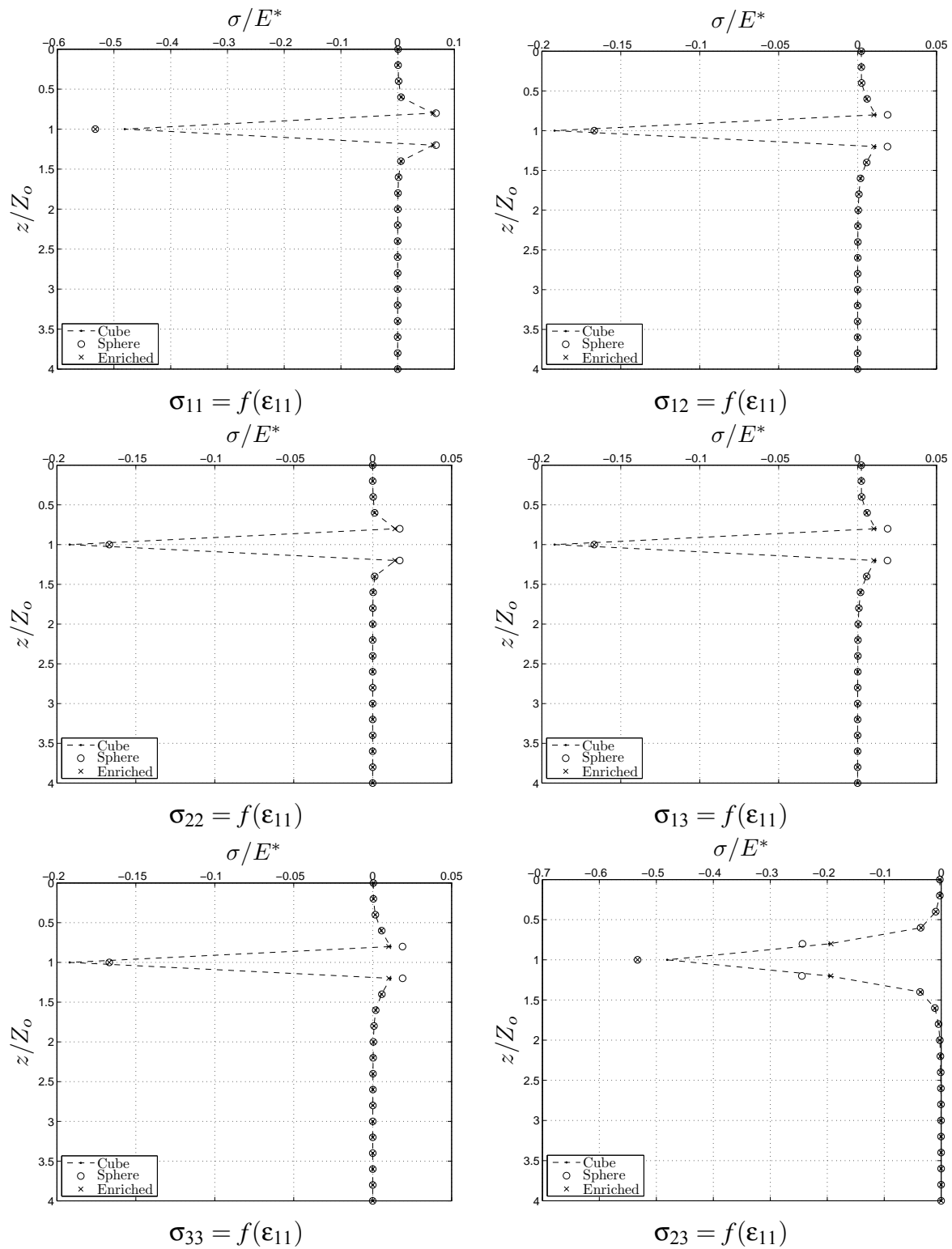


Figure 4.3: Validations of stress fields inside/outside of three elements considering $\epsilon_{11}^* = 1$ on the left and $\epsilon_{33}^* = 1$ on the right (other components are nil)

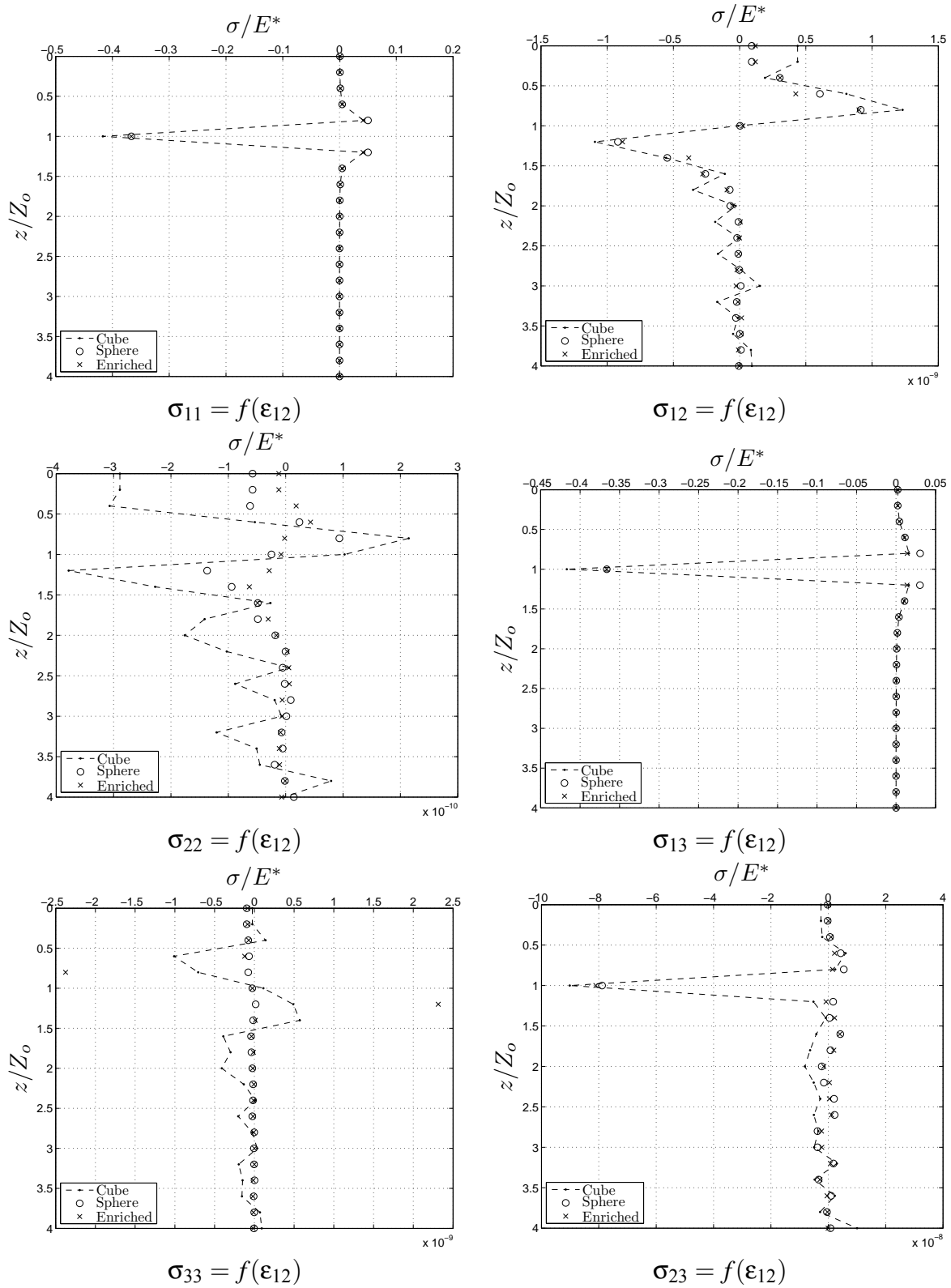


Figure 4.4: Validations of stress fields inside/outside of three elements considering $\epsilon_{12}^* = 1$ on the left and $\epsilon_{13}^* = 1$ on the right (other components are nil)

4.1.3 Proposed technique for coating computations

The last problem that remains is induced by the 3D-FFT algorithm and using such 3D-FFT algorithm is questionable. It must be reminded that no solution exists in an infinite half space for cubical inclusions that are compressible, and a combination of 2D and 3D-FFT is not possible as seen in Table 4.1. The development of a technique enabling cubical and spherical inclusions tangent to the contact surface is still required (and no solution has been found at this time). But a trick can be used for coating problems in order to overcome this issue.

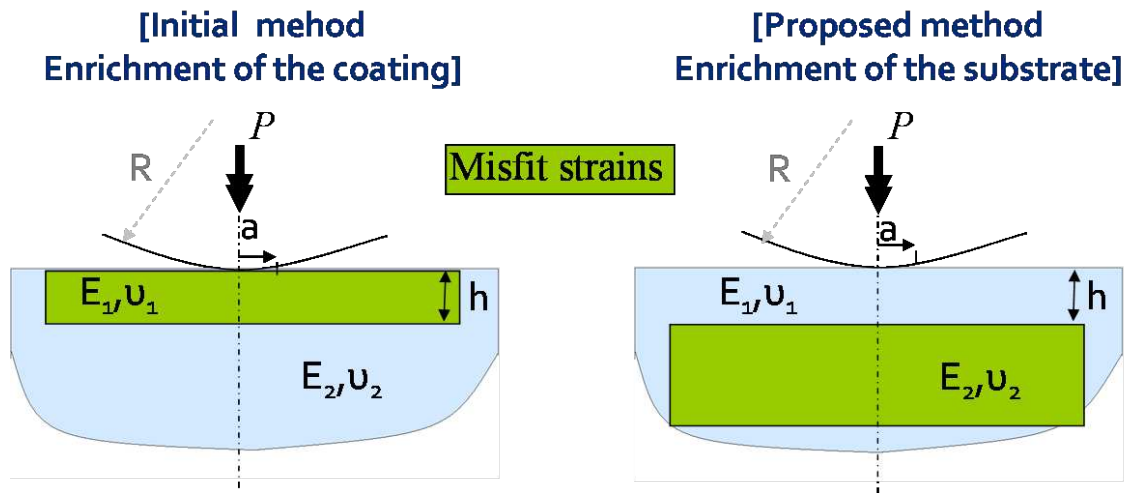


Figure 4.5: Proposed technique for coatings using an enrichment of the substrate

As seen in figure 4.5, the substrate will be enriched instead of the coating. This implies that the domain is large enough so it is equivalent to a half-space, since material properties out of the domain are now equal to the coating properties. Using this technique, all cubical inclusions are far enough from the surface so the 3D-FFT algorithm does not fail to predict stress fields and normal displacements.

	Stresses Inside	Stresses Outside ($Z_0/2b \geq 5$)	Stresses Outside ($Z_0/2b < 5$)
Cube proposed technique	No gradient	No gradient	None

Table 4.4: Validations of stress fields inside/outside of a cubical element while enriching the substrate

Stress issues when cubical or spherical inclusions are closed to the surface are not fixed when using this technique, but just avoided. Another method still have to be defined, so it would treat this issue in order to deal with fibers and inclusions close to the surface.

A much better agreement can be found using the actual method. The pressure field is normalized by the pressure P_0 found under the center of the indenter in the Hertz solution for a homogeneous medium when $a_0 = h$. When the Young's modulus of the coating E_1 differs significantly from the Young's modulus of the substrate E_2 , the radius of the contact zone and the pressure under the center of the indenter become quite different from the Hertzian case (See Figure 4.6).

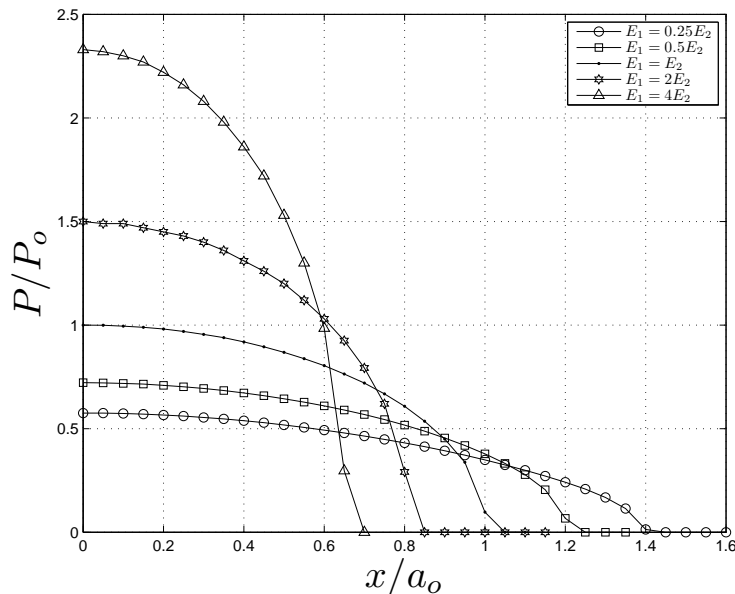


Figure 4.6: Pressure normalized by the Hertzian pressure for different coatings

Maximum of pressure and contact radii are equivalent to the results found in [O'S 88], except for the softest coating. In this case, the semi-analytical method predicts a maximum pressure $P = 0.56P$ while O'Sullivan predicts a maximum pressure $P_{O'Sullivan} = 0.5P$. This is due to the limited size of the domain considered, while contact radius increased from $a/a_0 = 1$ to about 1.4. A larger model, running on a 64-bits computer, can avoid such differences.

The indentation depth D is then plotted versus the applied load L acting on the indenter for different values of E_1 relative to E_2 (See figure 4.7). The load L is normalized by the Hertz loading L_0 which corresponds to $a_0 = h$. For low loads, $L \ll L_0$, the indentation depth versus the applied load curves are coincident with the corresponding Hertzian curves having the same layer elastic moduli. Because of the relative size of the contact radius compared to the coating thickness, the coating becomes virtually thick.

On the other hand, for highest load, $L \gg L_0$, the indentation depth versus the applied load curves become coincident with the Hertzian curves having the elastic moduli of the substrate. Because the contact radius becomes large compared to the coating thickness, the coating becomes virtually thinner.

Von Mises stresses below the surface using the actual method are successfully compared to stresses found using a numerical method. Von Mises stresses are shown in figure 4.8. It must be noticed that agreement is valid in both the coating and the substrate for $E_1 = 0.5E_2$, $E_1 = E_2$ and $E_1 = 2E_2$. It can be noticed that the homogeneous problem does not show any discontinuity between the substrate and the coating, according to the Hertz formulae. Those results will be

analysed in section 4.1.4 and will not be detailed in this section.

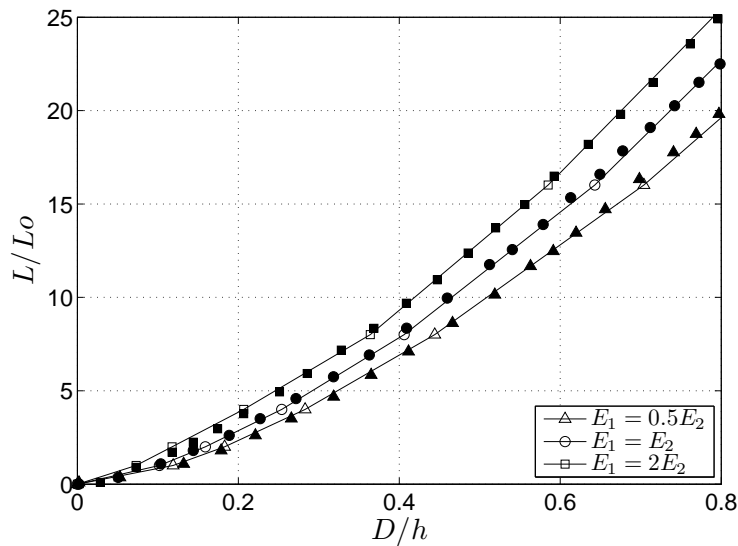


Figure 4.7: Normalized indentation curves for different coatings

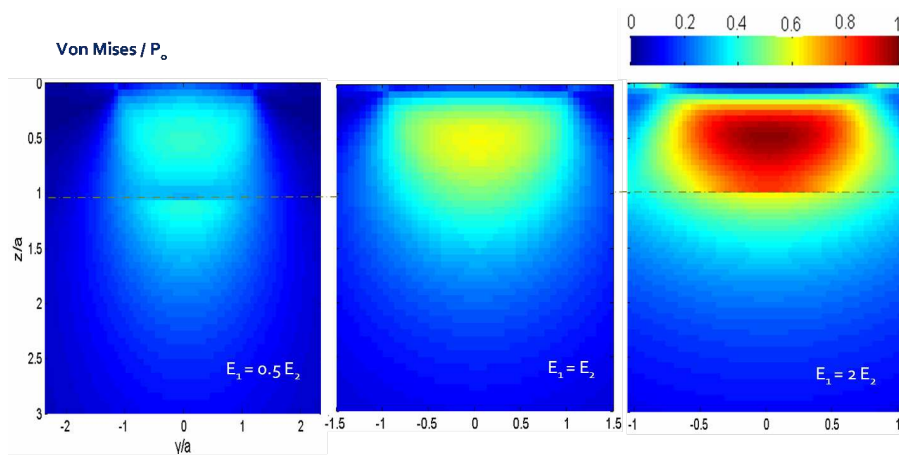


Figure 4.8: Actual Method: Von Mises stress normalized by the Hertzian pressure for different coatings: $E_1 = 0.5E_2$, $E_1 = E_2$ and $E_1 = 2E_2$

Finally, this proves the ability of such approach to deal with coatings and non-homogeneous aspects. Multiple coatings could even be considered using such technique. However, many other aspects still have to be validated, and that will be done in further sections. Validations under fully-sliding conditions will be presented next.

4.1.4 Coatings under fully-sliding conditions

The solutions of the sliding contact problem agrees with the Hertz solution in the normal contact case when the layer and substrate elastic properties are equal, while in the corresponding sliding contact case the stresses under the indenter agree with the exact solutions found in [JOH 85].

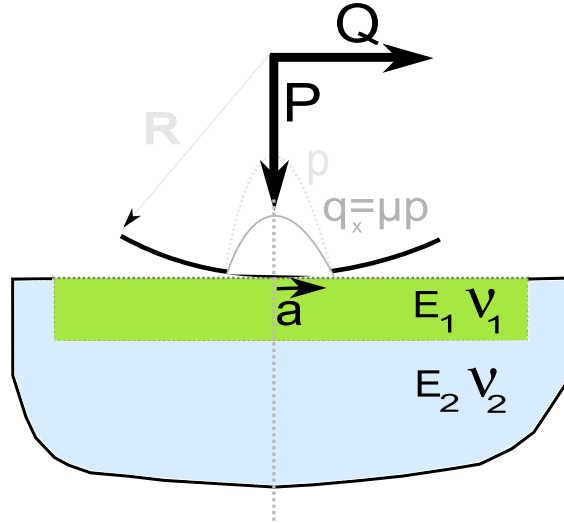


Figure 4.9: Sphere sliding over an elastic coating [O’S 88]

note: It must be noticed that O’Sullivan’s problem is uncoupled, for this reason simulations are also uncoupled. However, little difference was observed when considering the coupling between the normal and the tangential problem. In consequence, pressure profile shown in Figure 4.6 are still valid.

The indenter radius R was also taken to be $10.h$ and the indenter was assumed to be rigid. According to the previous section, the normal load applied P implies that the contact radius a is equal to the coating thickness h for the unlayered case. The very classical Hertz formula $a = \left(\frac{3PR}{4E^*}\right)^{1/3}$ is used to determine P . The coefficient of friction varies; $\mu = 0$ (see the previous section), $\mu = 0.25$ and $\mu = 0.5$ will be studied. For the layered case, material properties are recapped hereafter:

Geometries	Sphere of radius $200\mu\text{m}$	Substrate	Coating of $20\mu\text{m}$
Young’s modulus	$E = \infty$	$E_2 = 210\text{GPa}$	E_1
Poisson coefficient	$\nu = 0.3$	$\nu = 0.3$	$\nu = 0.3$

Table 4.5: Material properties used for coating simulations

The Young's modulus value of the layer E_1 varied. five cases are now considered:

- $E_1 = 1/4.E_2$
- $E_1 = 1/2.E_2$
- with no coating, $E_1 = 1.E_2$
- $E_1 = 2.E_2$
- $E_1 = 4.E_2$

The von Mises stresses normalized by the Hertzian pressure in the layer and substrate under the center of the indenter for normal contact with frictional sliding are shown in Figure 4.10, central row ($\mu = 0.25$) and right ($\mu = 0.5$) rows. The maximum von Mises stress value and location is also indicated. For soft and hard coatings, maximum Von Mises stress has been successfully compared to the results found by O'Sullivan. For hard coatings, significant discontinuities occur at the interface. The maximum von Mises stress increases with the Young's modulus of the coating, and also moves to the surface. For a coefficient of friction $\mu = 0.5$, the Von Mises stress is maximum at the surface for both the layered and unlayered case. For soft coatings, the Von Mises stress are lower than in the unlayered case, and is not moving away from the surface. For $E = 0.25E$ and $\mu = 0.25$ the maximum stress moves to the surface, but this result is supposedly disturbed by the high proximity of stresses with the model boundaries. Stress profiles are not available for $E = 0.25E$ in [O'S 88]. Finally, only mild discontinuity occurs at the interface since the substrate is also strained.

note: Simulations have been optimized, the region close to the contact is finely meshed and properly described, but stresses far from the contact approach the model boundaries and will virtually increase. It is due to the limited size of the domain, which is of about $70 \times 70 \times 70$ elements on a 32-bits computer. But model size could be much higher on a 64-bits computer.

The three stress components σ_{xx} , σ_{zz} and σ_{zx} are then plotted as a function of depth at $x = y = 0$ for a coefficient of friction $\mu = 0.25$ in Figure 4.11. The value of the three stress components increase when the layer is stiffer than the substrate. It can be explained because a stiffer thin layer acts like a plate attached to the half-space, then a large bending stress develops in the thin layer, resulting in an almost linear distribution of σ_{xx} through the layer. This is of a great importance, because stiffer coatings will have a large tensile component (σ_{xx}) at the interface, aiding the propagation of cracks at the base of layer in a direction orthogonal to the interface. The stresses are also much higher into the contact for stiff coatings because of σ_{xx} , σ_{zz} and σ_{zx} . However the shear stress σ_{zx} rapidly decays into the depth. Finally, it must be noticed that for soft coatings, the maximum stress values are smaller than in the corresponding unlayered case (See Figure 4.12). Those results show that the value of the Young's modulus of the layer relative to the substrate has a strong effect on stresses and yielding in both the layer and the substrate. The maximum tensile stress on the surface also depends strongly on both the friction coefficient and this Young's modulus ratio. But it also prove the accuracy of the SA method while dealing with frictional contact, even with domains of a relatively small size.

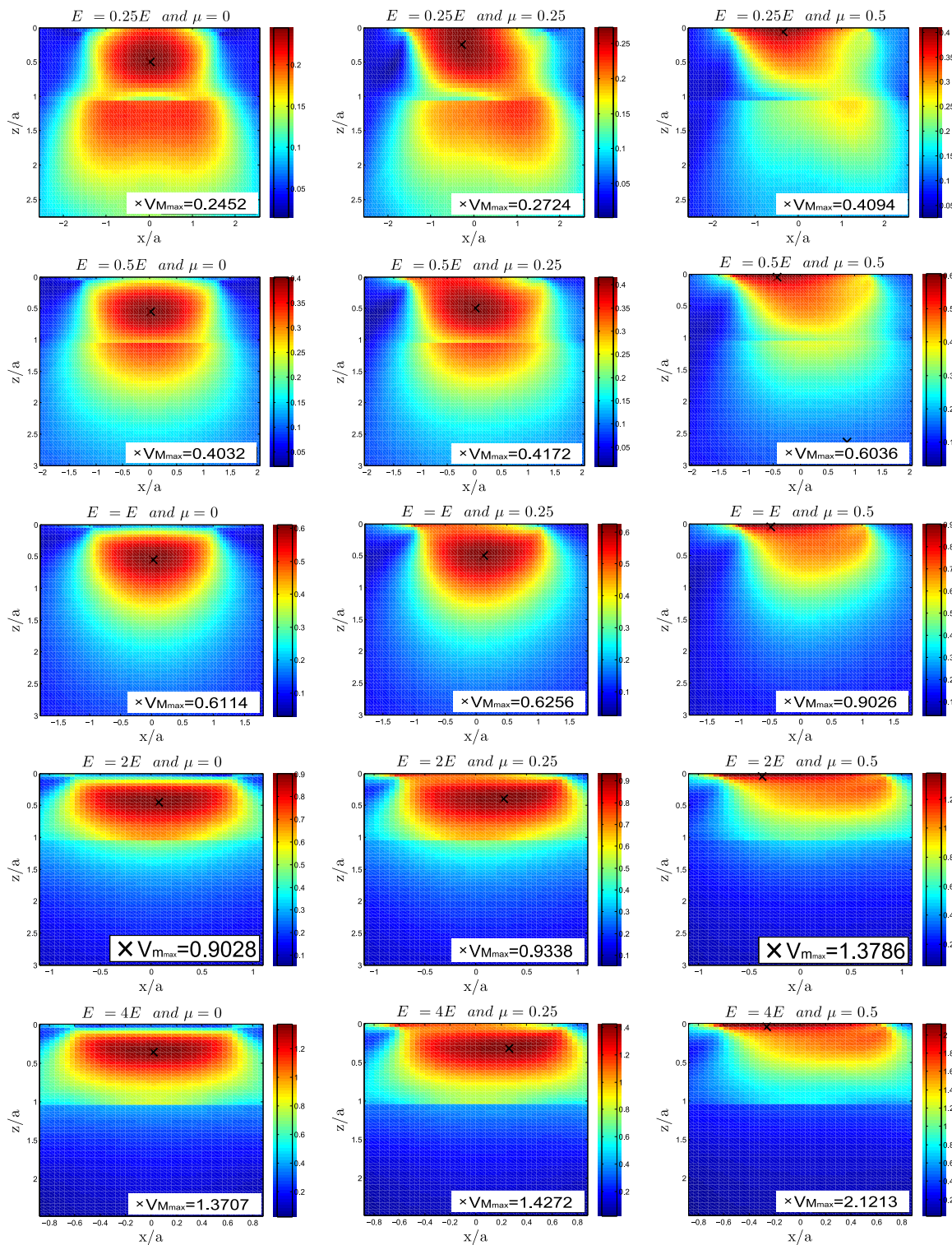


Figure 4.10: Actual Method: Von Mises stress normalized by the Hertzian pressure for different coatings and friction coefficients

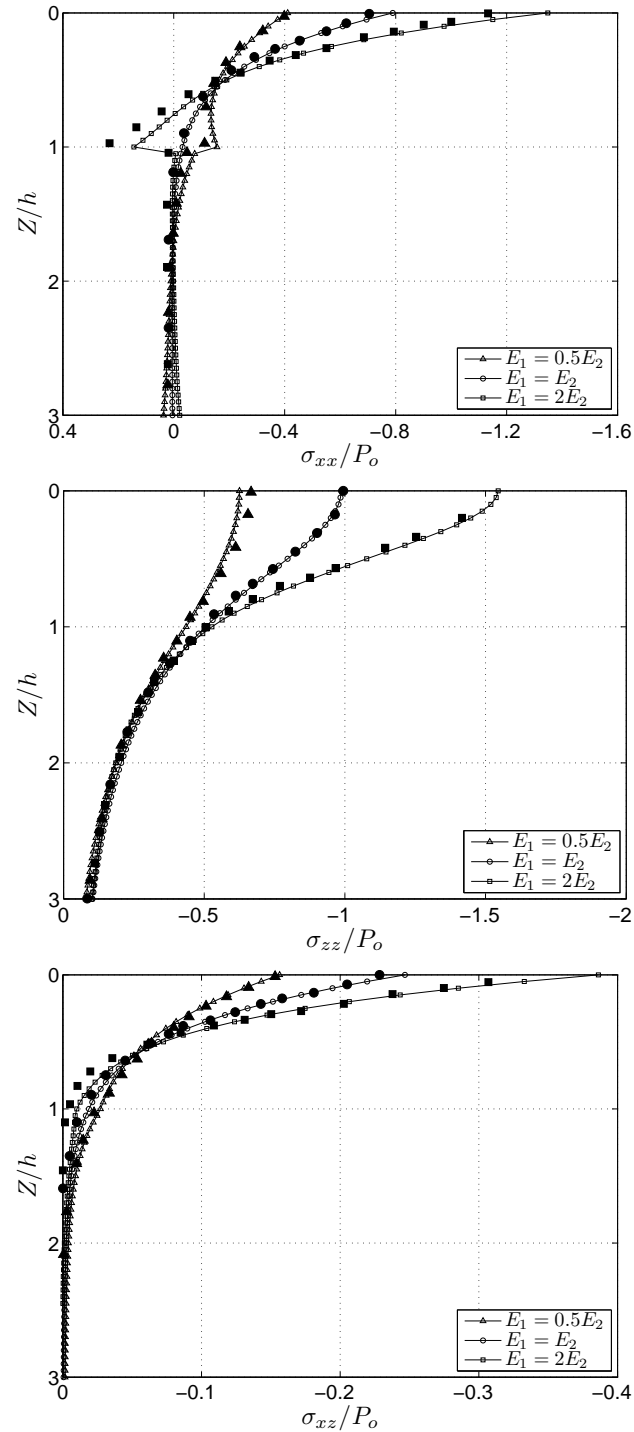


Figure 4.11: Stresses along the z-axis under combined normal loading and sliding contact $\mu = 0.25$. Large black symbols are numerical results [O'S 88] while small symbols and lines are found using the present semi-analytical method

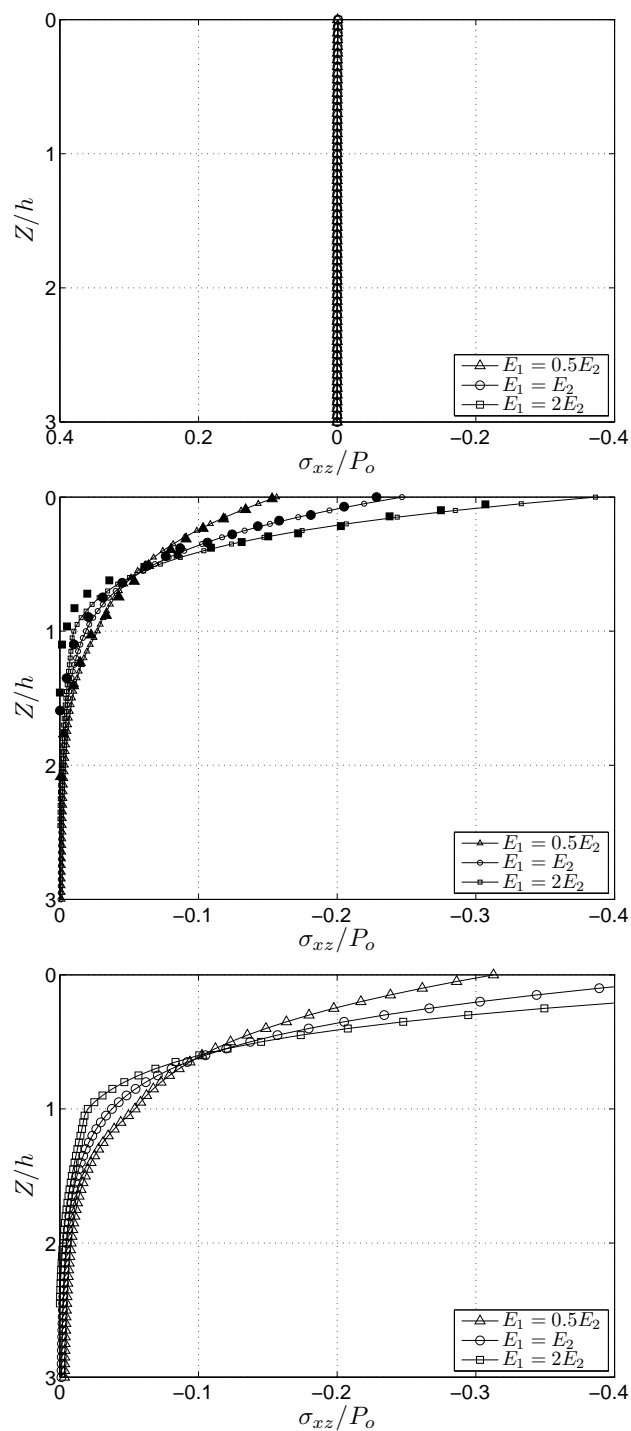


Figure 4.12: Stresses σ_{xz} along the z -axis under combined normal and tangential loading (gross-slip) for various coefficients of friction $\mu = 0$, $\mu = 0.25$ and $\mu = 0.5$.

4.1.5 Coating thickness

The problem described by O'Sullivan imposed a unique coating thickness, but it is well known that the coating thickness has a great impact on the contact conditions. This problem has been studied by Plumet and Al. in [PLU 98] and will be used to validate the present method for various coating thicknesses.

A configuration is defined by the coating finite thickness h_1 and the Young's modulus ratio between the coating and the substrate E_1/E_2 . Variations of P_{max} and the contact area A will be compared to those of the reference case (P_{maxO} and A_O). According to [PLU 98], $\frac{P_{max}}{P_{maxO}}$ and $\frac{A}{A_O}$ are presented versus $\frac{h_1}{A_O^{1/2}}$ (4.13 and 4.14).

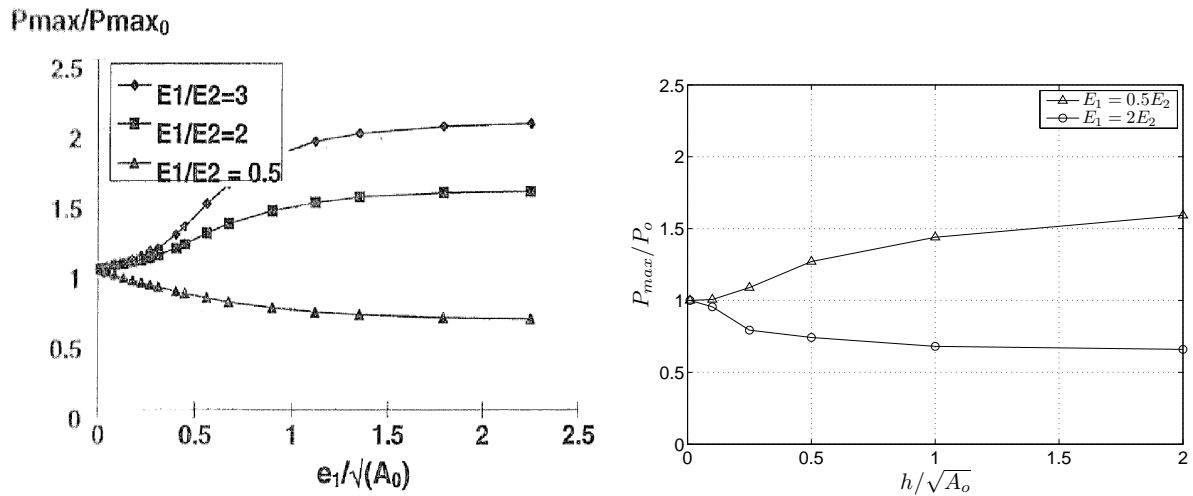


Figure 4.13: Maximal normal pressure variations depending on the coating thickness

When the coating is thin enough, the contact conditions are governed by the substrate behavior independently of the coating. P_{max}/P_{maxO} and A/A_O tend to values obtained without the coating.

$$\frac{P_{max}}{P_{maxO}} = 1 \quad \frac{A}{A_O} = 1$$

In contrario, when the coating becomes thick enough, the contact conditions are governed by the coating behavior independently of the substrate. P_{max}/P_{maxO} and A/A_O tend to values obtained without the substrate.

$$\frac{P_{max}}{P_{maxO}} = (E_o^*/E^*)^{2/3} \quad \frac{A}{A_O} = (E^*/E_o^*)^{1/3}$$

In Figure 4.14(a), the contact area A when considering a soft coating ($E_1/E_2=0.5$) tends to $A = 1.45A_o$. However, semi-analytical results shown in Figure 4.14(b) highlight a different asymptote with $A = 1.55A_o$. It has been concluded with the Authors that this last result was closer to the analytical solution given by Hertz: $A/A_o = (E_o^*/E^*)^{2/3} = 2^{2/3} = 1.5874$.

In fine, according to [LER 89], three configurations are possible depending on the coating thickness and contact area size:

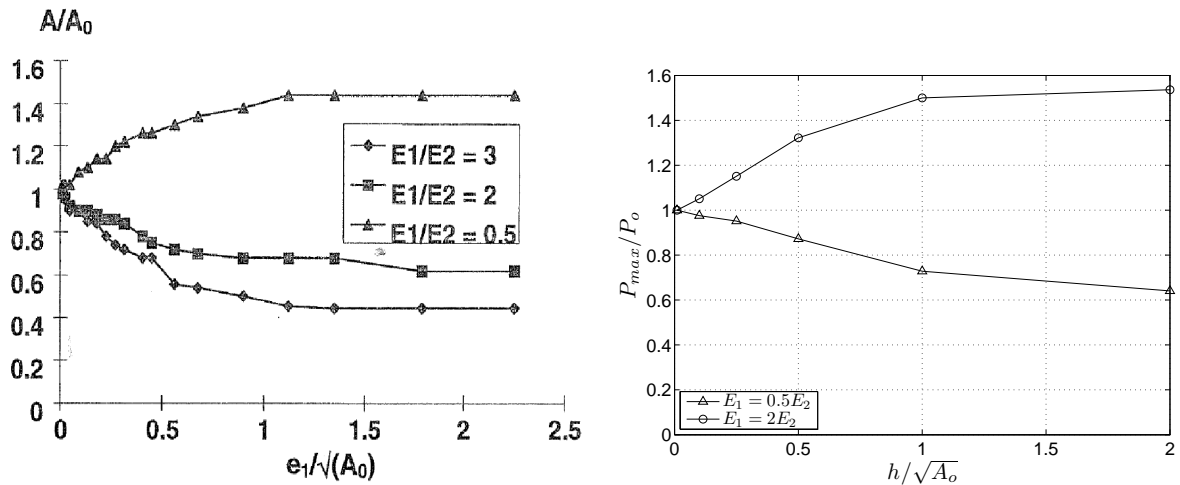


Figure 4.14: Contact area size variations depending on the coating thickness

- For $\frac{h_1}{A_0^{1/2}} \geq 0.05$, the layer is very thin and no significant influence of the coating on the contact solution should be noted. However, due to the limited size of the model, the coating thickness can not be smaller than few times the mesh size. In consequence, very thin layers are not possible using the actual code. Hopefully, because of their relative influence, very thin layers can be neglected.
- For $0.05 \geq \frac{h_1}{A_0^{1/2}} \geq 0.05$, the effect of the coating thickness on the pressure $\frac{P_{max}}{P_{max0}}$ and the contact area $\frac{A}{A_0}$ is important. This problem is accurately described by the present method.
- For $1.5 \geq \frac{h_1}{A_0^{1/2}}$, the layer is thick enough and the contact conditions are governed by the coating behavior independently of the substrate.

Those results show that the coating thickness relative to the contact radii has a strong effect on the contact conditions. The contact conditions for various coating thickness have been validated. Very thin layers have not been yet investigated. However, the actual method has a great advantage over other methods since it can consider layers of non-uniform thickness. This method can be used to study wear processes in sliding (See section 4.2.4) or partially sliding (See section 4.2.5) contacts for instance.

4.1.6 Conclusion

The method retained here is based on the Eshelby's theory also called the Equivalent Inclusion Method. It has been extended to cuboidal inclusions according to Chiu's solutions, describing the influence of a cubical inclusion on the surrounding infinite space [CHI 77] (note that solutions in a half-space implicitly consider an incompressible misfit strain [CHI 78]). The 3D-FFT has been used in order to account for any misfit strain tensor. The 3D-FFT technique used for stress computations has been extended to the tangential displacements calculation in order to permit the resolution of the tangential contact problem (solution in a half-space also considered implicitly an incompressible misfit strain [FUL 10]). Finally, this method is used as enrichment technique and suffers of some flaws. The substrate is then enriched instead of the coating in order to improve the contact stability. In fine, all elementary solutions have been validated using a Finite Element model. The frictionless coated contact and the fully sliding coated contact have been validated [O'S 88]. Various coating thickness have also been considered successfully [LER 89, PLU 98, O'S 88].

The method will now be used for partially-sliding coated contacts and wear of coated surfaces. However, wearing those coatings leads to many problems. (i) The coefficient of friction is assumed uniform and constant which is not compatible with a coating vanishing and a substrate appearing in the contact. (ii) Moreover coatings are described by a parallelepiped of the mesh, which means that coatings can not be worn on the surface when considering such method. However, a specific procedure will be drawn and coatings will remain slightly worn. Finally, the case of reinforced and brittle materials will be exposed briefly in the latest sections.

4.2 Applications

4.2.1 Indentation of coated surfaces considering friction

The solutions given by Hertz are defined for frictionless contacts. However, when dissimilar material properties are considered for two bodies pressed against together, a coupling exists between the normal and tangential problem. A radial shear appears and has been defined by Goodman for fully-sticking contacts [GOO 62], but does not verify the Coulomb's law locally at the edge of the contact zone. The solution has been extended to partially-slicking contacts by Spence [SPE 75] to verify the Coulomb's law locally. A sticking area appears in the center of the contact, and its radius depends on the coefficient of friction and the Dundurs [DUN 72] constant. This problem has been treated in the elastic regime in [GAL 07a, GAL 10] and in the elastic-plastic regime in section 2.4.2.

This problem is now briefly exposed when considering a uniform coating. A rigid ball ($R = 200\mu\text{m}$) is now pressed against a coated half space ($E_2 = 210\text{GPa}$, $\mu = 0.3$). The normal load applied P reaches a maximum value after 36 increments, so the contact radius for the uncoated case becomes equal to the coating thickness $a = h$ and $a = R/10$, as defined by O'Sullivan in (See section 4.1.3). Material properties are similar to the previous cases.

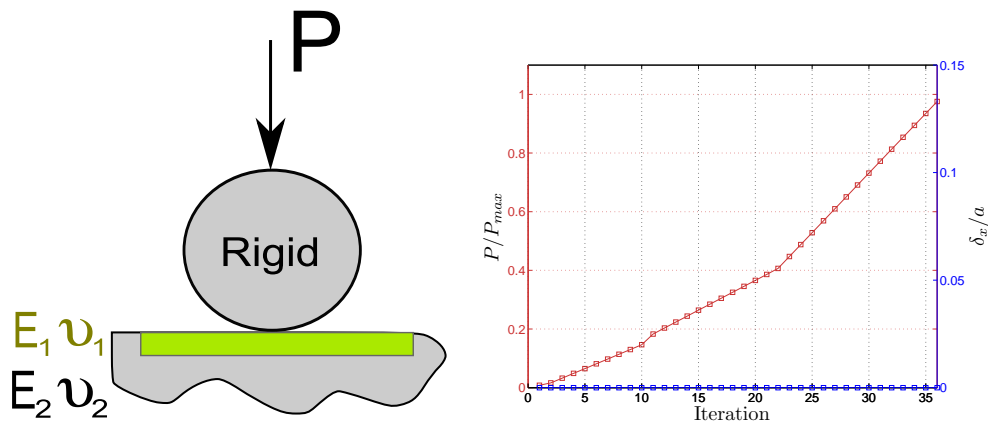


Figure 4.15: Normal loading applied to the sphere when indenting the coated surface

It is shown in figure 4.16 that the stress levels observed for frictionless and frictional indentations are different. For frictional contacts, the maximum von Mises stress is not as deeper as in frictionless contacts. This is due to the radial tractions observed into the contact. Because of those tractions, the stress level also increases for frictional contact. For soft coatings, the maximum Von Mises stress increases of about 22%, 17% for uncoated surfaces and 15% for the hard coating. The spatial discretization is not fine enough, and it is impossible to catch the correct value of the sticking radius. However, it is worth noting that in this case, contacts are almost fully-sticking. The shear distribution are radial and anti-symmetric, and are correctly described when the normal loading is imposed slowly (36 increments are required in this simulation).

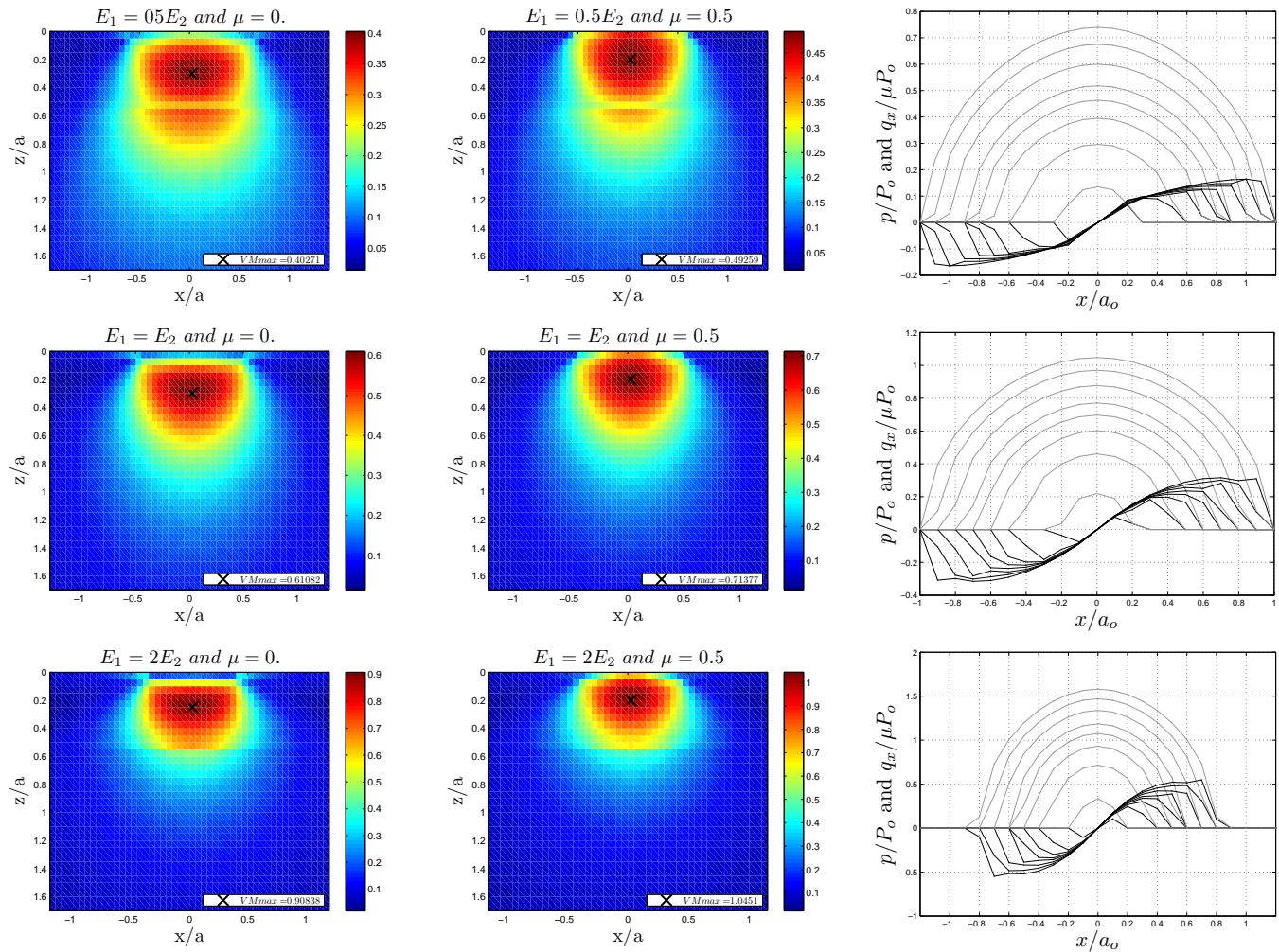


Figure 4.16: Von Mises stresses when considering no friction (left), a friction $\mu = 0.5$ (middle) and pressure and shears profiles for various normal loadings

It must be noticed that the maximum pressure increases for frictional contacts. Because of the coupling, the tangential problem will change the normal problem solution. In this case, pressures are reduced when shears are maximum, at the edge of the contact. Due to the load balance, the pressure increases at the center of the contact, where shears are minimum or nil because of their anti-symmetric properties.

Finally, many other coefficients of friction are now considered: $\mu = 0.1$, $\mu = 0.2$, $\mu = 0.25$, $\mu = 0.3$ and $\mu = 0.4$. For lower friction coefficients, the sticking radius c decreases according to Spence and becomes nil for frictionless contacts. Spence curves are then presented in figure 4.17 for three cases.

Surprisingly, Spence curves obtained when uncoated, with a hard or a soft coating are not similar. Even if β depends on the material properties considered, this has no effect here. Indeed, β is a constant defined by Dundurs and is expressed as follow:

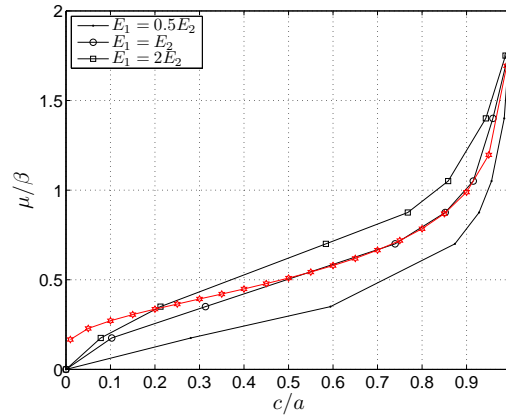


Figure 4.17: Evolution of the sticking radius c/a for various coatings

$$\beta = \frac{1}{2} \cdot \left[\frac{(1-2\nu)/G - (1-2\nu')/G'}{(1-\nu)/G + (1-\nu')/G'} \right] \quad (4.3)$$

where (G,ν) and (G',ν') are the material properties of both bodies. In this section, the second material is rigid. It comes that the Dundurs constant is independent of the Young's modulus of the material, and for $\mu = 0.3$ it comes $\beta = 0.2856$. In consequence, Spence curves highlight a new aspect of the problem.

For the uncoated case, numerical results are very similar to the theoretical results, even if it must be noted that the Spence formulation does not predict the vanishing sticking area for frictionless contacts. When the coating is thick enough, or thin enough, the problem becomes equivalent to the homogeneous problem as seen in section 4.1.5. However, for finite thickness, the Spence curves differ from the uncoated case. Soft coatings are sticking more than uncoated cases, while stiff coatings are slipping more than uncoated cases. This is caused by the coating/substrate interface, discontinuity in which interfacial tractions are important. In our case, the maximum von Mises stress is located in the coating, so it will be used for reference. Stress levels are still high at the interface so it will play a role in the contact problem. For hard coatings, the substrate is relatively softer and will increase the slipping area. In the same manner, for soft coatings, the substrate is relatively harder and will reduce the slipping area. This conclusion is very similar to the conclusions found in next sections, when sliding tangentially.

When von Mises stresses are mainly located below the coating/substrate interface, different results could be expected since the coating is no longer used for reference. Additional simulations should be run in order to highlight the influence of the coating thickness on the sticking radius.

4.2.2 Partial sliding over coated surfaces

A rigid ball ($R = 200\mu\text{m}$) is now sliding over a coated half space ($E_2 = 210\text{GPa}$, $\mu = 0.3$). Material properties, coating thickness and normal loading used hereafter have been used in previous sections (See section 4.1.3) and are defined by O'Sullivan. The normal load applied P generates a maximum Von Mises stress located in the coating. Because the sphere is rigid and the coated surface is not, a coupling exists between the normal and the tangential problem and the coupling will be considered in the contact code. A tangential displacement δ_x is now imposed, and the coefficient of friction is set equal to $\mu = 0.5$.

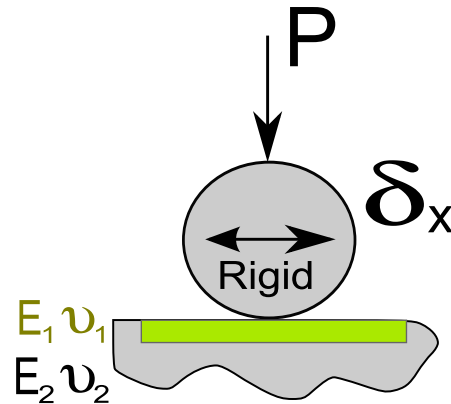


Figure 4.18: Fretting cycle considering a coated surface

According to the Cattaneo-Mindlin concept [CAT 38, MIN 49], Johnson [JOH 85] gives the solutions for Hertzian geometries loaded normally – P – and tangentially – $Q_x = \pm|Q_x|$ – and this problem is known as the first mode of fretting. This problem has been extensively studied experimentally, analytically and numerically. Very recently, Zhan-Jiang Wang and Al. [WAN 10] presented a similar work considering stick-slip in coated problems, however this approach is not based on enrichment elements but on the Papkovitch-Neuber potentials, and coatings considered are implicitly uniform. The work presented in this thesis permits non-uniform coatings so wear of coatings can be investigated. The goal of those studies is to predict shears and slips, slipping and sticking areas.

Two cases are now considered. First, the tangential displacement δ_x is kept small so the contact remain partially sliding during the fretting-cycle. Second, the tangential displacement δ_x is increased so the contact becomes fully sliding. Both cases will be investigated in next paragraphs. The response of the system will be studied and the fretting loops will be drawn. The von Mises stresses for the maximum amplitude of $+\delta_x$ and the contact pressures, shears and slips for various loadings are also presented.

4.2.2.1 Small amplitudes of sliding

The normal loading P and the tangential displacement $\delta_x/a = 0.025$ are exposed hereafter. The tangential displacement δ_x has been chosen arbitrarily. Letters A, AB, B, C, CD, D, E and F will be used later for reference.

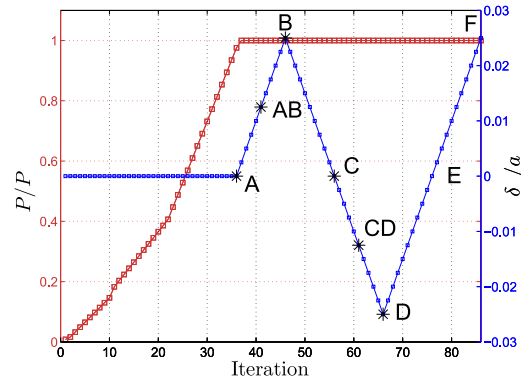


Figure 4.19: Normal loading and tangential displacements for a sphere moving over a coated surface, in the stick/slip regime

For small amplitudes of δ_x , the contact remains partially sliding and the fretting loops exposed in figure 4.20 are not widely opened. Since the tangential displacement δ_x is imposed, the maximum amplitude observed for $\delta_x/(\mu P)$ (mm/N) is independent of the coating properties. However, the tangential load Q_x is sensitive to the coating properties, and this load increases with the Young's modulus of the coating. This is due to higher shear stresses into the contact for hard coatings. It must be noted that the tangential force applied is not symmetric, which is a very classical result in partially slipping contacts. Moreover, the surface created by a fretting loop is related to the dissipated energy. It must be noticed that hard coatings dissipate more energy than softer coatings.

Von mises stress fields obtained during the fretting cycle (A,B,C,D,E and F) are shown in figure [?] for an uncoated case. It is shown that the maximum von Mises stress increases of about 4% with the application of the tangential loading from A to B. The location of the von Mises stress may eventually moves to the surface, depending on the coefficient of friction and the tangential displacement δ_x considered. However, it must be noticed that the maximum Von Mises stress will decrease from B to D, and then from D to F. Stress levels will finally stabilize around a certain value after few cycles. Obviously, stress levels remain higher than stress levels observed without friction.

Stress fields observed for B are now presented for various coatings in figure 4.22. It is shown that the dimension of stick region depends on the material properties, and increases with the softness of the coating in this case. For this reason, shears observed are lowered when considering soft coatings. On the opposite, the sticking area is reduced and shears increased for hard coatings. For this reason, compliant coatings need higher tangential forces to achieve the gross slip. Slips S_x along the x-direction and S_y along the y-direction are then presented. Slips amplitude are reduced by the softness of the coating, in both direction. Because the wear phenomenon is based on the energy balance, and the hard coating presents a higher shear and slip level, the wear rate observed for the hard coatings will be higher than the wear rate for soft coatings.

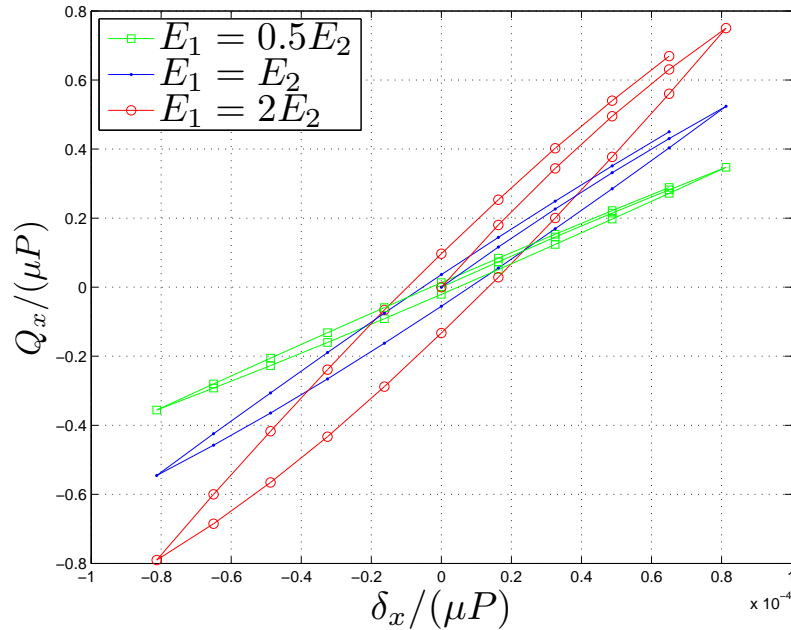


Figure 4.20: Fretting loop obtained for a circular contact partially sliding and various coating properties

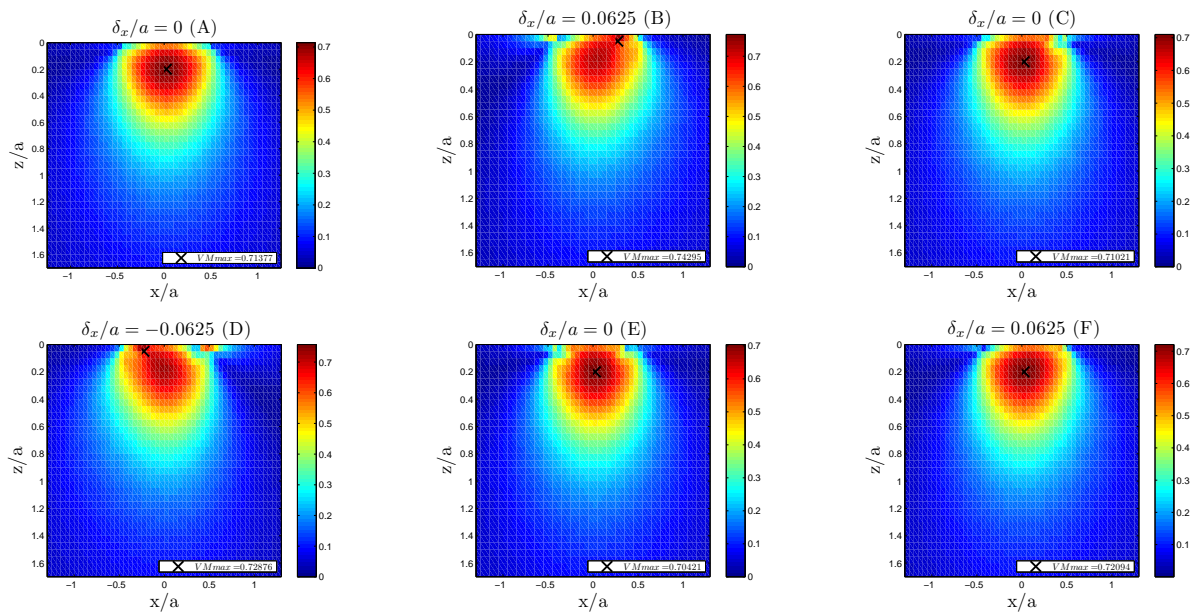


Figure 4.21: Von Mises stresses for an uncoated surface submitted to a fretting loading of small amplitude

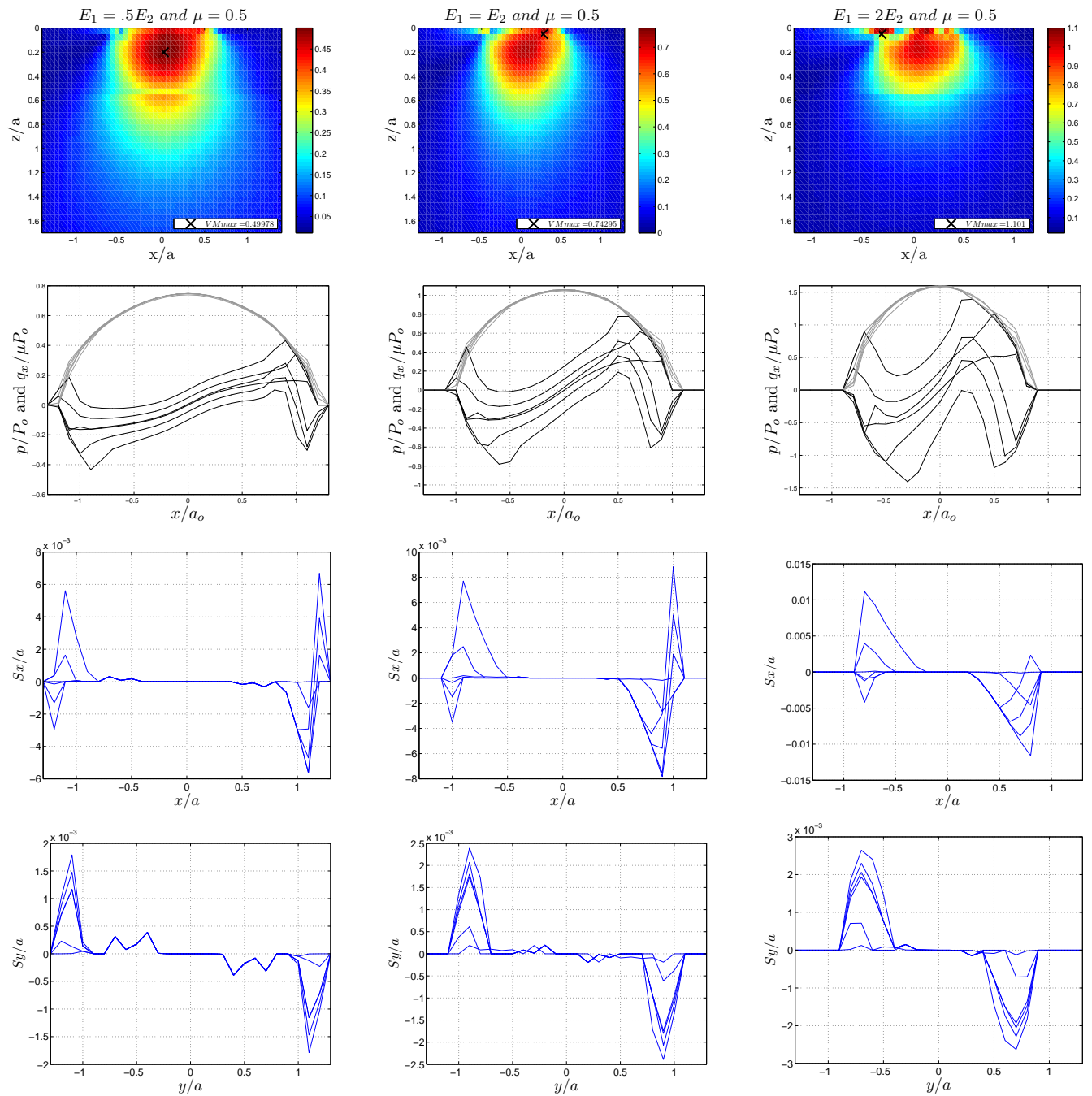


Figure 4.22: Von Mises stresses at the point B in figure 4.19 and pressures, shears and slips for various loadings when partially sliding

4.2.2.2 Large amplitudes of sliding

The normal loading P remains unchanged, while the tangential displacement $\delta_x/a = 0.125$ is increased by 5. This amplitude is quite interesting, since it is at the onset of the gross slip. The letters A, AB, B, C, CD, D, E and F are still used for reference.

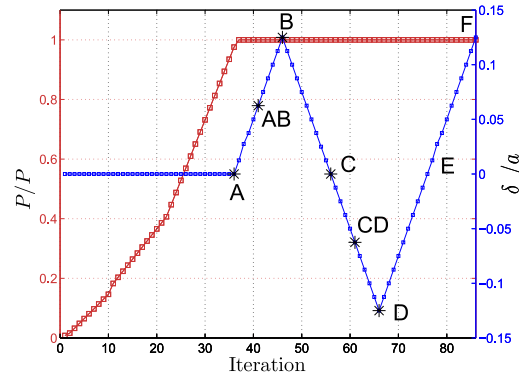


Figure 4.23: Normal loading and tangential displacements for a sphere moving over a coated surface, at the onset of gross slip

For larger amplitudes of $\delta_x/\mu P$ (mm/N), the contact may transit from the stick/slip regime to the gross-slip regime. In this case, all points of the contact zone are slipping and the Coulomb's law gives locally $q = \mu p$. The fretting loops are then widely opened and present two extrema, for $Q_x/(P) = \mp 1$. As seen in the previous paragraph, the gross slip regime is reached faster for stiffer coatings. Once again, the surface created by a fretting loop is related to the dissipated energy, and hard coatings are dissipating more energy than softer coatings, and will wear faster.

For larger amplitudes, just after the onset of the gross-slip regime, the solutions are very close to the fully sliding solution. Because the tangential problem is historic sensitive, the previous contact conditions will affect the current solution. The uncoated problem is a good example, since the solution in C and E is a transition between the stick-slip and the gross-slip regime. In this case, the maximum von Mises stress is slightly different ($VM_{max} = 0.921Po$) than the solution in B, D and F in figure 4.25 ($VM_{max} = 0.915Po$). Since the slopes of curves rapidly decrease when approaching the gross-slip regime, and this slope should tend continuously to zero, it is worth noting that difference observed are caused by a poor loading discretization.

Stress fields observed for B are now presented for various coatings in figure 4.26. It is shown that the sticking radius rapidly decreases with the coating stiffness. The pressure profiles are differs from the Hertz solution because of the coupling with the tangential problem, finally the contact area may slightly evolve for the same reason. More interesting is the evolution of the slip profiles. In the stick/slip regime, both slips S_x and S_y were lowered by the coating softness. The same conclusion can be made for S_x , however, slips along the transversal direction become much higher in the gross-slip regime because of the coating softness.

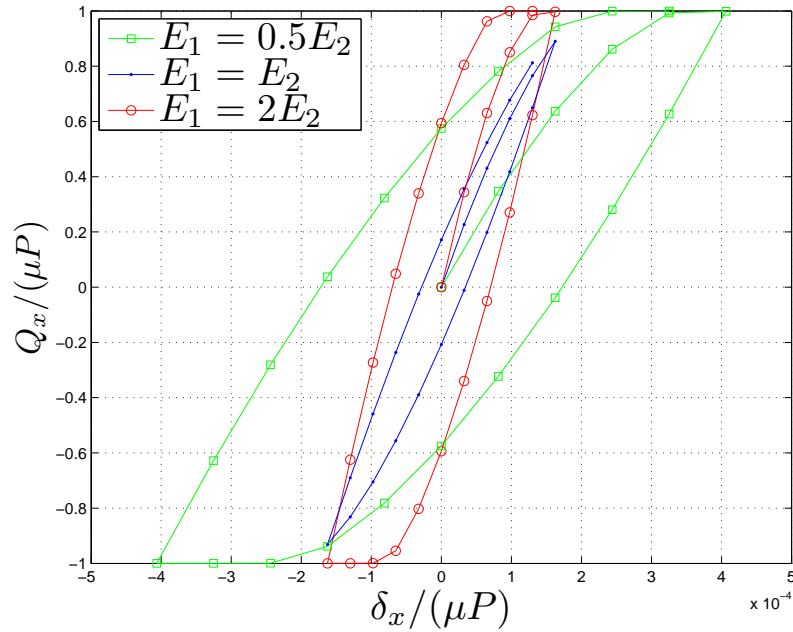


Figure 4.24: Fretting loop obtained for a circular contact at the onset of sliding and for various coating properties

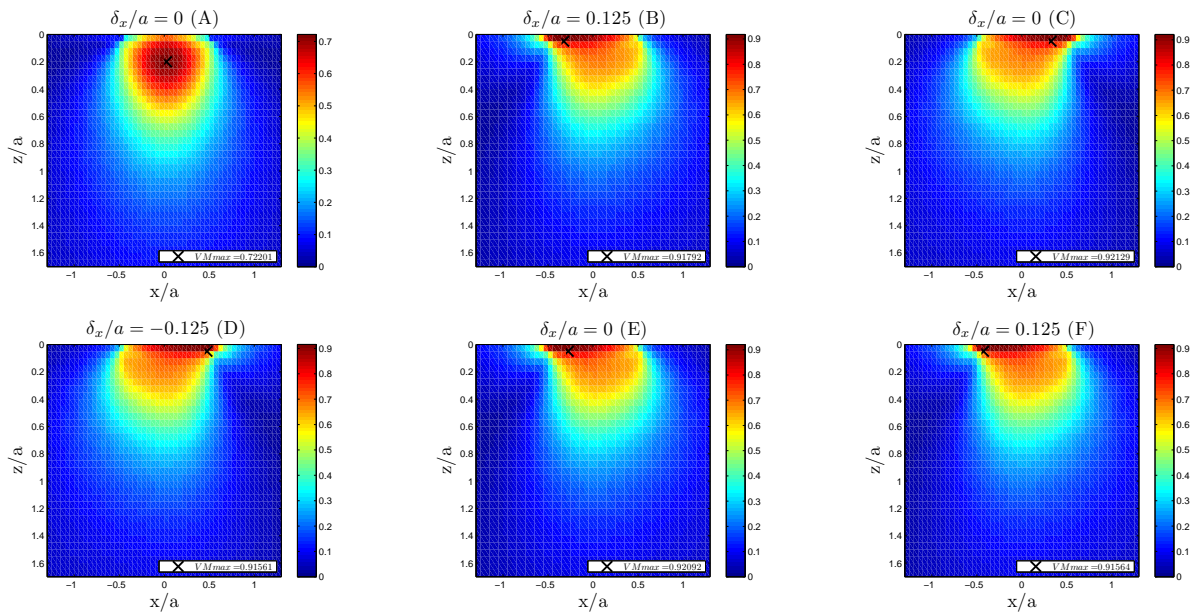


Figure 4.25: Von Mises stresses for an uncoated surface submitted to a fretting loading of large amplitude

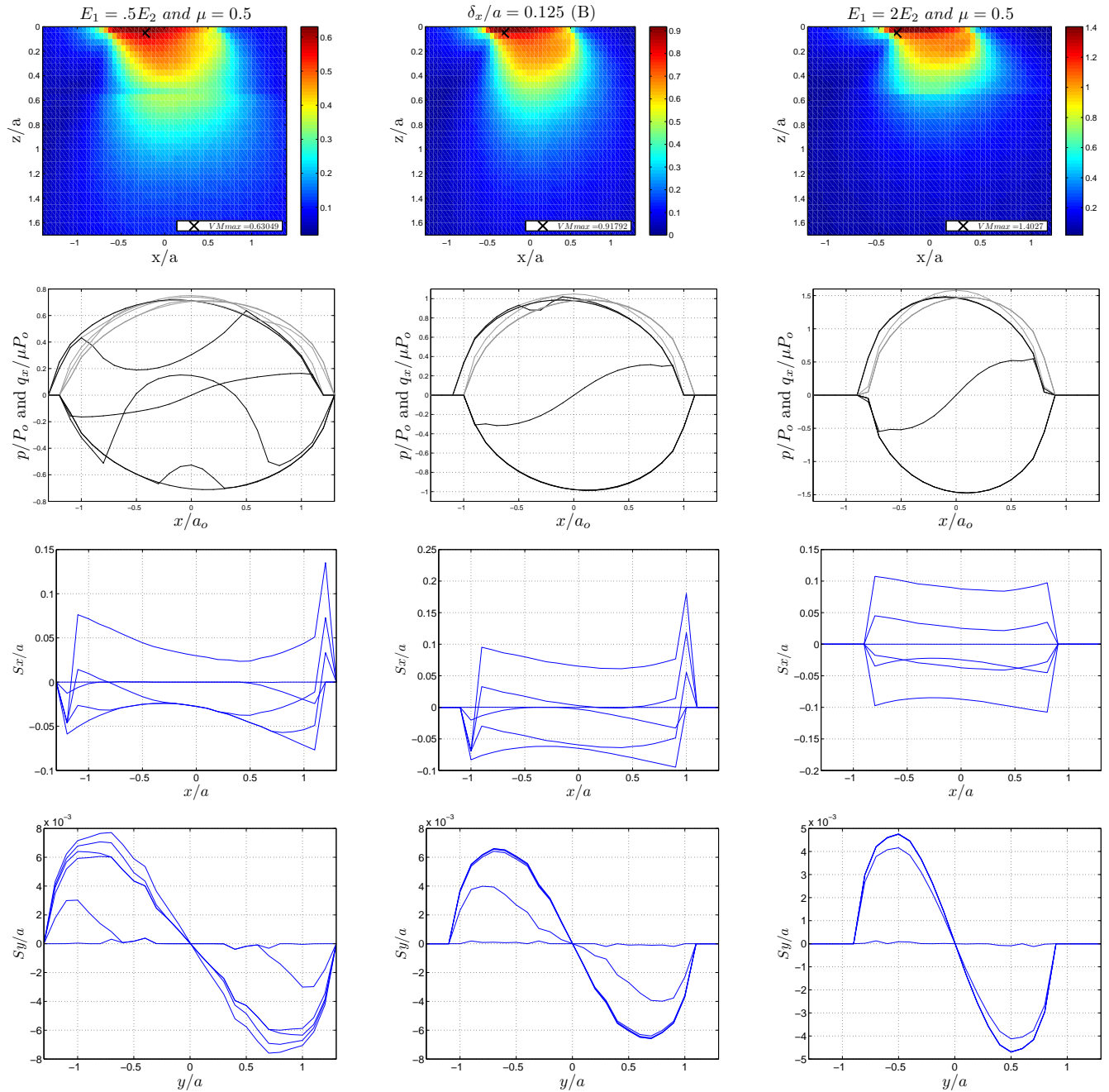


Figure 4.26: Von Mises stresses, pressures, shears and slips for various loadings at the onset of gross-slip

In the stick/slip regime, the sticking area is larger for soft coatings reducing shears amplitudes. Because of the reduced shear tractions on the surface, the tangential displacements and slips are reduced. However, when the gross-slip regime arises, because of the softness of the coating, transversal displacements and slips are increased and become more important than in stiff cases.

However, it would be awkward to draw a direct conclusion because S_x are still reduced by the softness of the coating. It must be reminded that slips are found by simple summation of slips computed between one loading step and the next one. Because the gross-slip regime was reached earlier when considering hard coatings, and slips are maximum in the gross-slip regime, the slips S_x are greater.

4.2.2.3 Word of caution about previous conclusions

Various simulations have been presented in previous sections, and prove the ability of this method to deal with frictional coated contacts included in the stick/slip regime. However, those simulations did consider a unique normal load P and a unique coating thickness h so the contact radius a is equal to h . In this case, the maximum Von Mises stress is located in the coating. Different results might be observed when the maximum Von Mises stress is located deeper into the volume.

When applying a normal load, the stress levels globally increases and move closer to the surface because of surface tractions. Radial shears and slips are also observed, however it is difficult to describe a smooth slip profile when the geometrical refinements are limited due to computer capabilities. The influence of the interface on the evolution of the sticking radius has been highlighted and should be investigated furthermore.

In the stick-slip and gross-slip regime, similar results are observed. The maximum von Mises stress progressively increases when applying the tangential displacement δ_x , until it reaches a maximum value in the gross-slip regime. The influence of coating properties have been highlighted, and it has been observed that the response of the system may significantly evolve depending on the coating properties. Since shears and slips are obtained precisely in both the stick/slip and the gross-slip regime, it is now possible to determine the wear rates for various coatings, based on the energy balance. The methodology will be defined in the next sections.

note: Some discontinuities can be observed for slips S_y in the transversal direction. It is due to the slips observed when loading, summed to the slips created while sliding. It is very difficult to obtain a good description of the radial slips when normally loaded, when the spatial discretization is limited by the computer capabilities. More globally, when the slip distribution is drastically changed from an increment to another, due to the poor loading or spatial discretization, such discontinuities are frequently observed in the slip profiles.

4.2.3 Wear of coatings

Motivations Because dovetail joints between fan blades and the disk of turbine engines are subjected to fretting, the objective of this research is to realize wear prediction using a fast-computational method. The goal is obviously the estimation of wear kinetics, but also to obtain worn surfaces, and permit the manufacturer to realize complementary design analyses with worn surfaces.

Actual method As seen in the previous sections, the actual method is based on an enrichment technique where non-homogeneous elements of the half-space are enriched using enrichment functions defined for a cuboidal inclusion. Enrichment functions are related to the Young's modulus, the Poisson's ratio of the matrix and the shape of the inclusion, and are calculated once at all at the beginning of the computation considering the actual parameters. The shape factor of an inclusion is classically defined by the ratios $\Delta y/\Delta x$ and $\Delta z/\Delta x$.

Considering a unique set of enrichment functions, it was assumed in [NEL 06] that based on a strain criterion, a volume of material where the equivalent plastic strain found exceeds a threshold value while located at the surface, will detach from the surface (See Figure 4.27a). This model requires a very fine mesh and increases the instabilities of the contact conditions because of rough wear profiles (mesh is never fine enough).

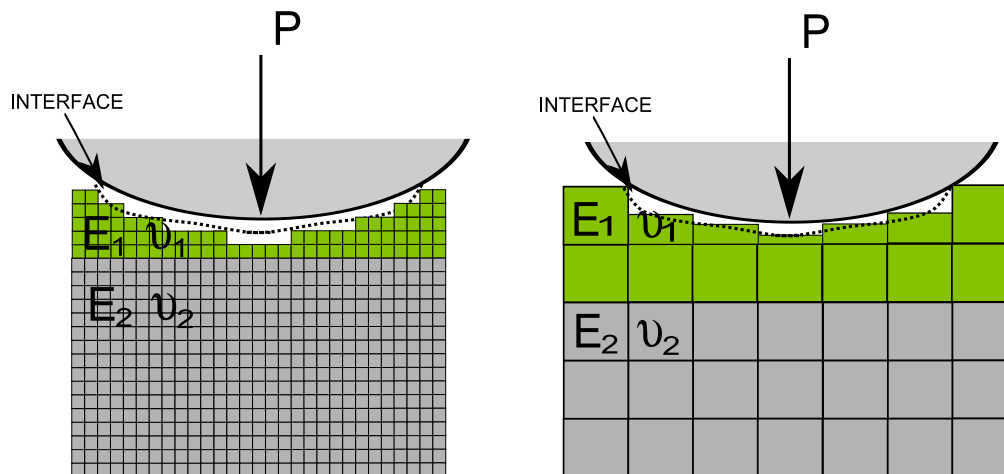


Figure 4.27: Techniques used to model rough surfaces

Fretting-wear problems require a much higher stability of the contact problem, since both the normal and the tangential problems are considered. It is important to define a smooth wear profile and use it in the non-homogeneous solver (See Figure ??b). However, this is not compatible with the unique shape factor used in the enrichment functions calculations. Obviously, it is not even imaginable to compute a set of enrichment functions for each size (worn geometry of the element). An homogenization method will be used to solve this issue, making wear profiles virtually smooth in the non-homogeneous stress-solver.

Wear modelling Initially, the contact surface was moving down when worn. This approach is incompatible with the half-space theory, since the surface must remain flat (large radius are assumed to be flat). It is commonly admitted that this problem is equivalent to another problem when the wear depth is kept small. In consequence, the coating/substrate interface will move up instead of the contact surface moving down, as seen in figure 4.51. Obviously, it must be noticed that shear tractions at the coating/substrate interface become obsolete for the most severe wear profiles.

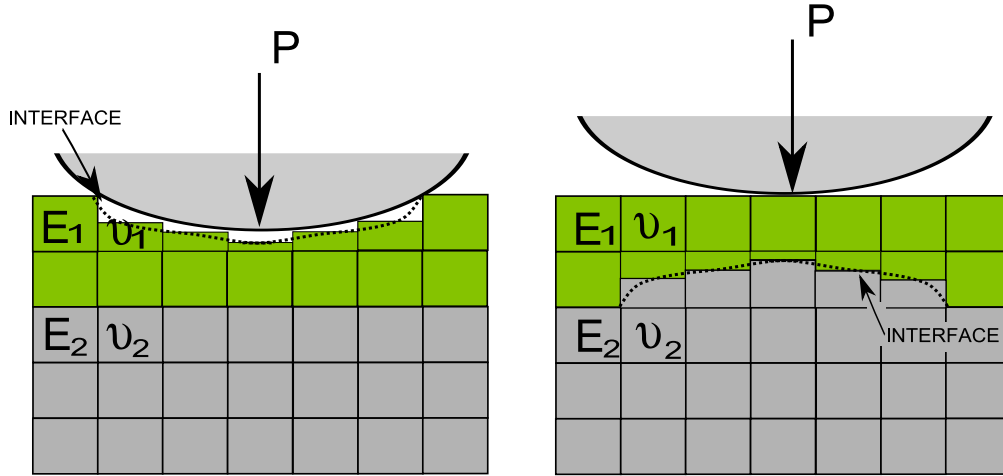


Figure 4.28: Worn coatings considering a moving surface or a moving interface

The coating/substrate interface is now moving in the elements of the grid. Once again, a parallel could be drawn between this technique and other enrichment techniques such as the X-FEM techniques. The originality consists in using an homogenization technique, based on a weighted mean technique.

$$\beta_{homogenized} = \frac{Vol_{coating}}{Vol_{substrate} + Vol_{coating}} \cdot \beta_{coating} \quad (4.4)$$

In finite element analysis, a weight tensor \mathbf{W} is used to describe the actual geometry. For each element of the domain Ω , divided in $\Omega_{substrate}$ and $\Omega_{coating}$, \mathbf{W} is defined by:

$$\mathbf{W} = \frac{Vol_{coating}}{Vol_{substrate} + Vol_{coating}} \quad (4.5)$$

Then, it comes:

$$\mathbf{W} = 0. \quad \text{for} \quad \text{elements} \in \Omega_{substrate} \quad (4.6a)$$

$$0. < \mathbf{W} < 1. \quad \text{for} \quad \text{elements} \in \Omega_{coating+substrate} \quad (4.6b)$$

$$\mathbf{W} = 1. \quad \text{for} \quad \text{elements} \in \Omega_{coating} \quad (4.6c)$$

Using this technique, the coating/substrate interface slowly moves inside the elements as the weight tensor \mathbf{W} decreases, as seen in figure 4.29. This helps to prevent the non-linearities induced by geometrical non-linearities.

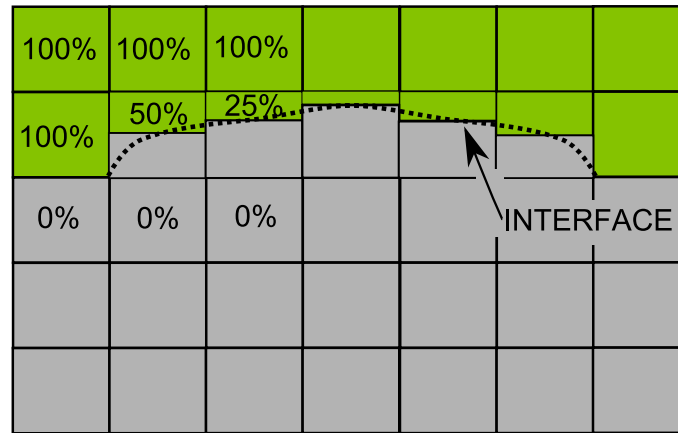


Figure 4.29: The weight tensor \mathbf{W} used to define the moving interface

Wear law Wear can be understood through the energetic balance [ARC 53]. Friction is a dissipative phenomenon, and a part of this energy is consumed by different processes (Material transformations such as plasticity [NEL 06], physical-chemical processes, third body formation) that conduct to wear. An empirical wear law that implicitly accounts for all those aspects will be used. The wear law is based on the Archard's law, modified by Fouvry and Paulin [PAU 05, PAU 06], and is based on the friction dissipated energy:

$$V = \alpha \sum_N Ed \quad (4.7)$$

Classically, the energy dissipated locally on a surface S is caused by the local shears q_x, q_y and slips s_x, s_y and can be defined by:

$$Ed = (s_x^2 + s_y^2)^{0.5} \cdot (q_x^2 + q_y^2)^{0.5} \cdot S \quad (4.8)$$

In fretting applications, the wear coefficient α is a consequence of debris formation and debris ejection. Because the fretting tangential displacement δ_o relative to the reference fretting test amplitude is responsible for the debris ejection, the wear law used derived from:

$$V = \alpha_{ref} \frac{\delta_o}{\delta_{ref}} \sum_N Ed \quad (4.9)$$

Because of equation 4.9, the wear law used in the partial sliding regime differs from the wear law used in the full sliding regime:

- In the sliding regime, the wear coefficient $\alpha_{sliding}$ is related to the wear volume (mm^3) due to a dissipated energy Ed and is expressed in mm^3/J . The wear law is very classical $V = \alpha \sum_N Ed$
- In the partial sliding regime, the wear coefficient $\alpha_{stick-slip}$ commonly used is equal to $\frac{\alpha_{ref}}{\delta_{ref}}$ and is expressed in mm^2/J . The wear law is then expressed locally and becomes $V = \alpha_{stick-slip} \cdot (s_x^2 + s_y^2)^{0.5} \cdot \sum_N Ed$

Obviously, it must be noticed that the wear coefficient was arbitrarily chosen. Therefore, the number of cycles obtained are arbitrary, but the wear profiles and contact conditions obtained remain valid. In the next sections, results will be presented as a function of the maximum wear depth.

4.2.4 Wear of coatings: fully sliding contacts

Material properties and contact conditions used hereafter are similar to the parameters used in section 4.1.4. However, the rigid indenter will be replaced by a coated elastic indenter sliding over a rigid flat. Indeed, a rigid sphere sliding over a coated flat would create a very small groove on the flat geometry, while looking at a coated sphere sliding over a rigid flat the wear depth will increase continuously.

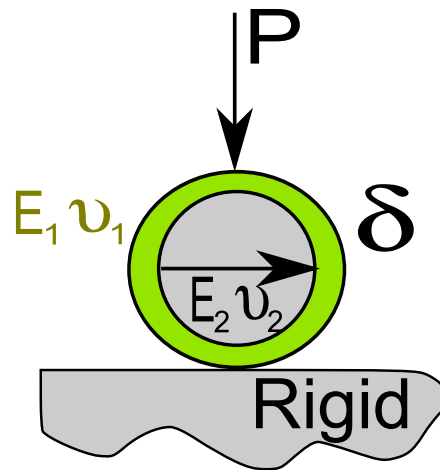


Figure 4.30: Coated sphere sliding over a rigid flat

The spherical indenter defined by (E_2, ν_2) and radius R is pressed against the rigid flat by a normal load P so the contact radius a_0 when unlayered is equal to the coating thickness $h = 10.R$ of material properties (E_1, ν_1) .

Geometries	Rigid flat	Sphere of radius $200\mu\text{m}$	Coating of $20\mu\text{m}$
Young's modulus	$E = \infty$	$E_2 = 210\text{GPa}$	E_1
Poisson coefficient	$\nu = 0.3$	$\nu = 0.3$	$\nu = 0.3$

Table 4.6: Material properties

Three different coatings are investigated: $E_1 = 0.5E_2$, $E_1 = E_2$ and $E_1 = 2E_2$. The coefficient of friction μ considered remains low $\mu = 0.25$ so the coating/substrate interface remains highly stressed (See Figure 4.10). Finally, the sliding amplitude for each cycle and the wear coefficient

are chosen arbitrarily, $\delta_x = 1m$ and $coeff_{wear} = 1\mu m^3/J$. Both parameters have an influence on the number of cycles calculation only. Wear increments are defined by the maximum wear depth $wear_{max}$ normalized by the contact radius a_0 . Since the wear phenomenon is based on the energy balance, it is necessary to verify that all simulations have the same energy balance. The wear volume $Wear_{vol}$ is determined using the worn geometry by: $Wear_{vol} = \Delta_x \Delta_y Wear_{depth}$. Finally, the wear volume $Wear_{vol}$ versus the number of cycles N_{cycles} curves are plotted in figure 4.31 and validate the equivalence of the energy balances.

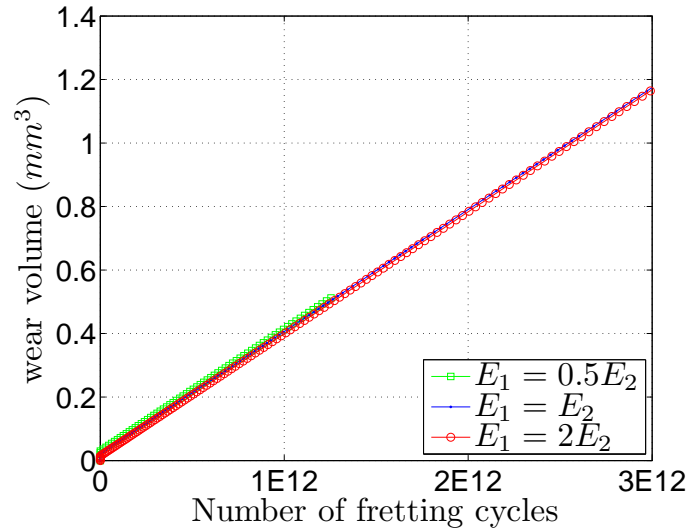


Figure 4.31: Dissipated energy: Wear volume vs. the number of cycles

Coatings are used in mechanical engineering to improve the wear resistance of the material. The maximum wear depth $max.wear_{depth}$ is first investigated. Figure 4.32 presents the influence of the Young's modulus of the coating on the maximum wear depth obtained after a certain number of cycles. Obviously, those comparisons are limited since the coefficients of friction used are similar for various coatings, which is not necessarily true for real materials.

The coating properties obviously have a great impact on the evolution of the maximum wear depth during the first cycles. The slope of the curve is 1.5 times steeper for the hard coating compared to the uncoated surface, while the slope is less than 1.5 times more gentle than the uncoated case.

In fact, it is due to the maximum pressures found by O'Sullivan. Since the problem is fully sliding, shears and pressures are linked together by the coefficient of friction $\mu = 0.25$. Because slips are arbitrarily taken equal to $1m$, wear profiles are driven by the shears profiles only.

As seen in figure 4.33 the maximum pressures tend to diminish rapidly, which is consistent with the wear phenomenon. Wear acts in decreasing the stress level at the surface. Maximum pressures drop and finally converge to approximately the same solution.

This is believed to be caused by the very particular geometry obtained after a certain time. This geometry is supposed to be optimized for the wear resistance. Because wear is governed by the shears only (so the pressure) in this model, the pressure profiles become particularly flat,

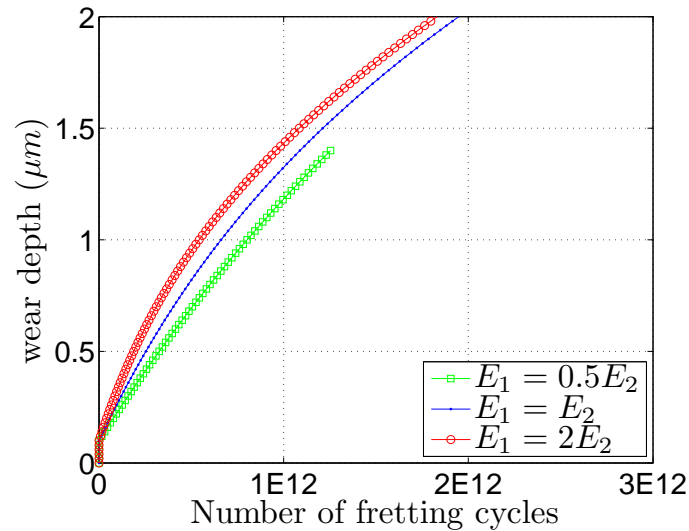


Figure 4.32: Maximum wear depth vs. the number of cycles

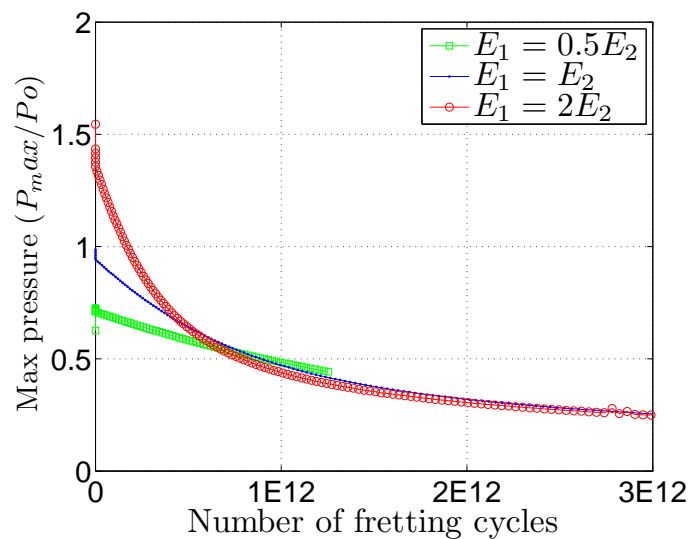


Figure 4.33: Maximum pressure vs. the number of cycles

as seen in figure 4.34(right). Regardless of the material properties, the pressure profile becomes similar for such geometry. The wear profiles are also exposed on the left for various wear depth. The contact area increases with the maximum wear depth, as seen in figure 4.35.

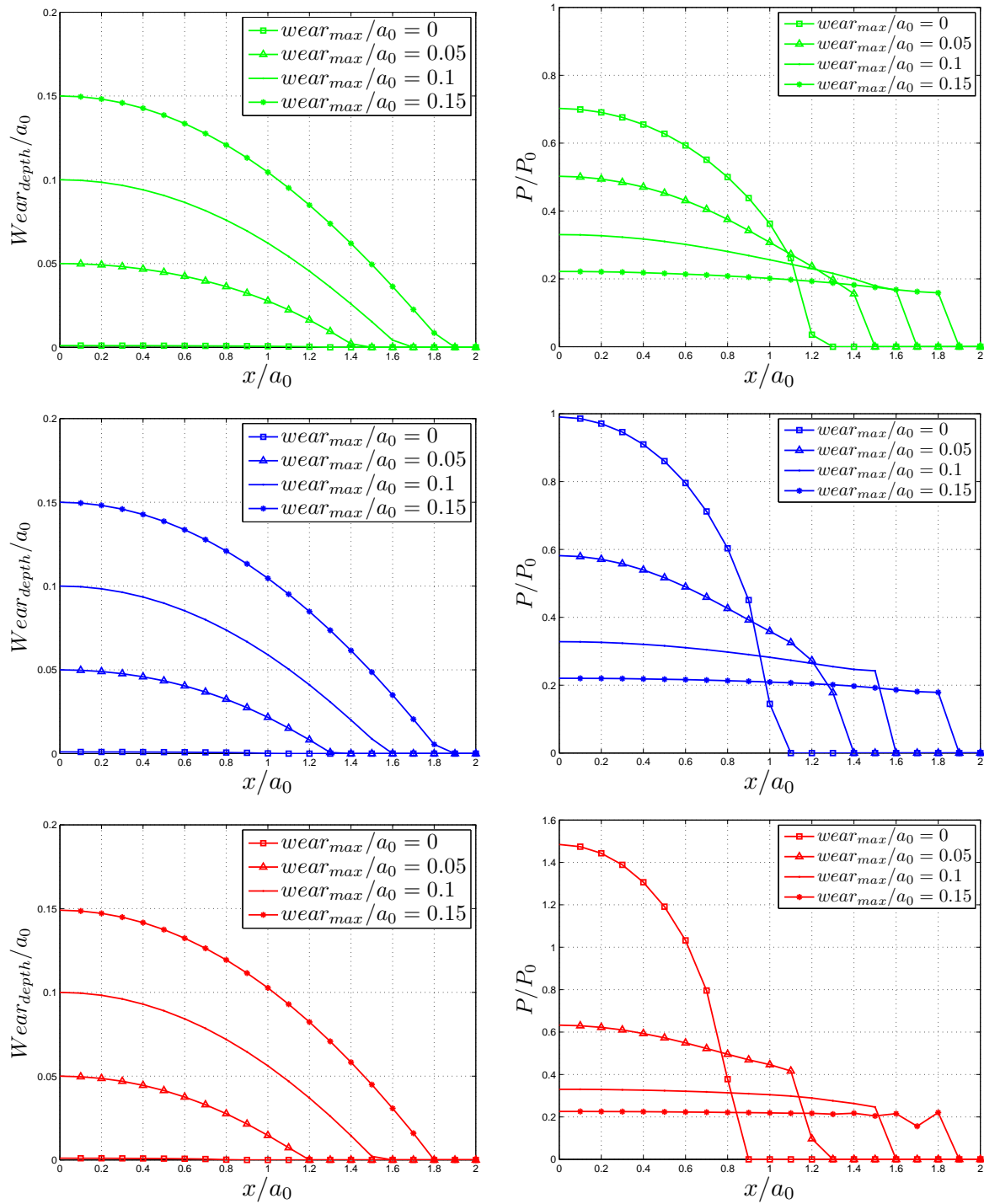


Figure 4.34: Wear depth normalized by the contact radius (left) and associated pressure fields (right)

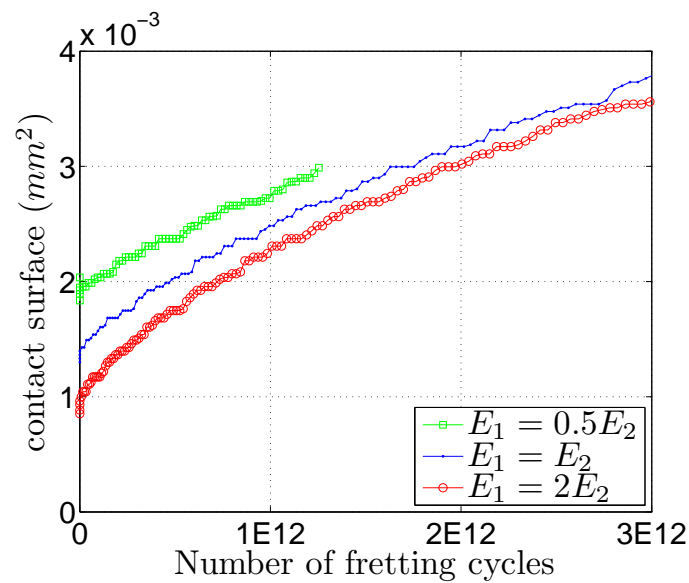


Figure 4.35: Contact surface vs. the number of cycles

The worn geometries are easily found and an example is shown in figure 4.36. In this case, the geometry considered is a sphere of radius $R = 0.2\text{mm}$ layered with a thin coating of 0.02mm ($E_1 = 0.5E_2$). The geometry is shown as it was initially (left) and for $wear_{max}/a_0 = 2$ or $wear_{max} = 2\mu\text{m}$. Since the initial geometry is similar for all cases considered, the worn geometry has little interest. The wear profiles exposed in figure 4.34 (right) are much more interesting.

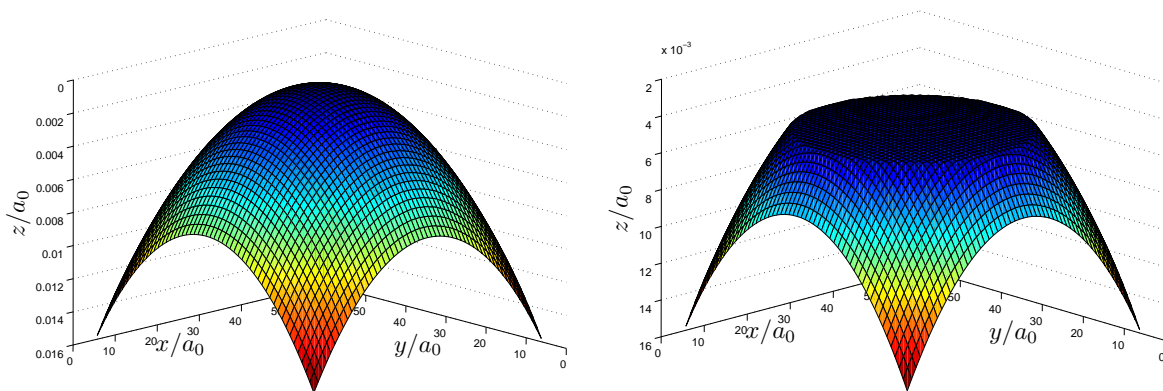


Figure 4.36: Sphere of radius 0.2mm (left) and worn (right) for $max.wear_{depth}/a_0 = 2$

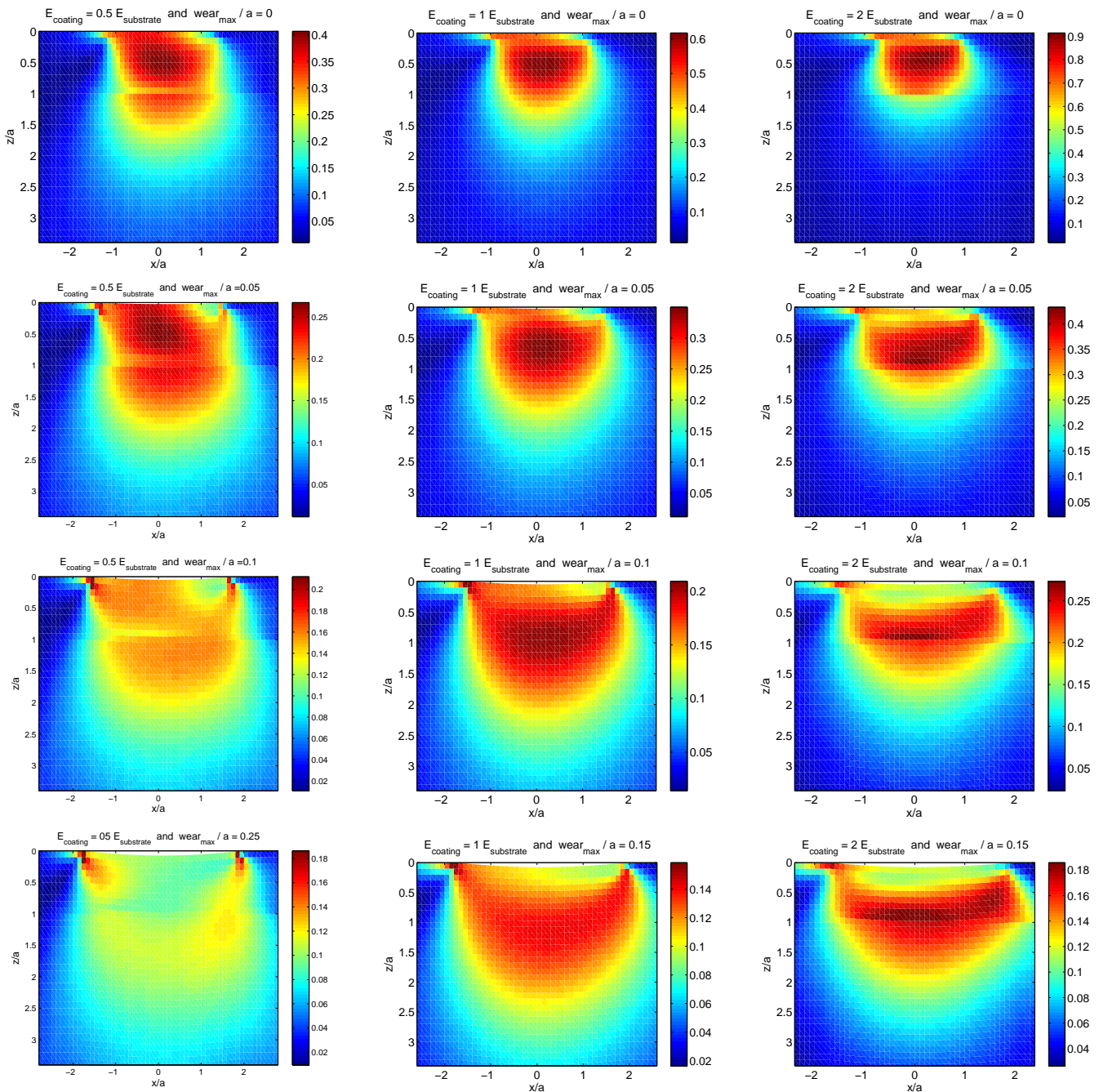


Figure 4.37: Von Mises stress normalized by the Hertzian pressure, for various coatings ($E_1 = 0.5E_2, E_1 = E_2$ and $E_1 = 2E_2$) and wear rates, for a sphere sliding over a rigid flat

Finally, the Von Mises stresses normalized by the Hertzian pressure is shown in figure 4.38. Because the contact zone increases, the stress levels drop significantly by almost one order of magnitude for $wear_{max}/a_0 = 2$. The location of the maximum stress is found deeper into the half-space, and the conditions at the interface may also evolve when wear is considered, however the

stress level at the interface is also significantly reduced. Wear is presented in this figure since the contact surfaces go down when ratios $wear_{max}/a_0$ go up.

issues for highly worn surfaces In previous simulations, it was decided to update the geometry when $wear_{step} \geq 0.02\mu\text{m}$ or $wear_{step}/a_0 \geq 0.001$ considering the contact size. If wear rates are way too important, the results may differ significantly at the edge of the contact and below the surface because of the geometrical non-linearities. In figure 4.38 the wear step used is $wear_{step} \geq 0.05\mu\text{m}$, only two and half times greater, but the stresses are located at the edge of the contact and the shape of the stress profiles are quite modified. The wear step will have to be defined carefully, and the stability must be verified using a lower wear rate. Another issue observed when profiles are highly worn, as seen in the last figure. It is only due to numerical noise and errors caused by the large contact. On the first hand, the contact touches the boundaries of the domain, on the second hand the domain is no longer a half-space since high stress levels are observed at the boundaries of the domain. Both reasons are responsible for instabilities observed on the surface, that are slowly transmitted from an element to the element next to it onto the surface.

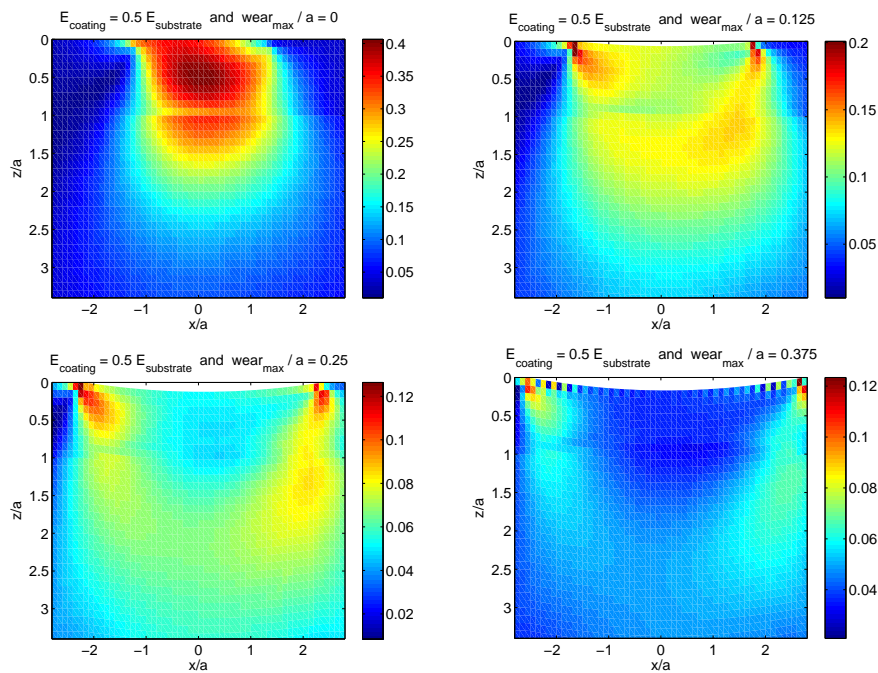


Figure 4.38: Von Mises stress normalized by the Hertzian pressure for a soft coating $E_1 = 0.5E_2$ highly worn.

4.2.5 Fretting-wear of coatings: stick-slip conditions

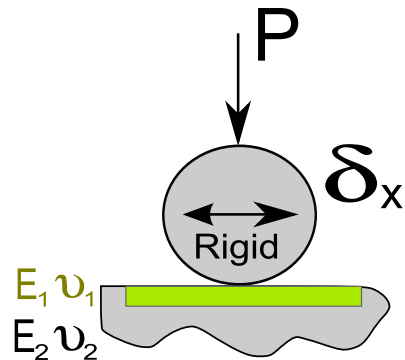


Figure 4.39: Fretting cycle considering a coated surface

Previous results are now extended to the stick-slip regime, considering the normal and tangential loadings defined in section 4.2.2. The first loading (Figure 4.40 on the left) is known to be in the stick-slip regime, and fretting loops created are relatively narrow. On the other hand, the second loading (Figure 4.40 on the right) is at the onset of the gross-slip regime and finally become fully slipping. Fretting loops created in this case are wide opened.

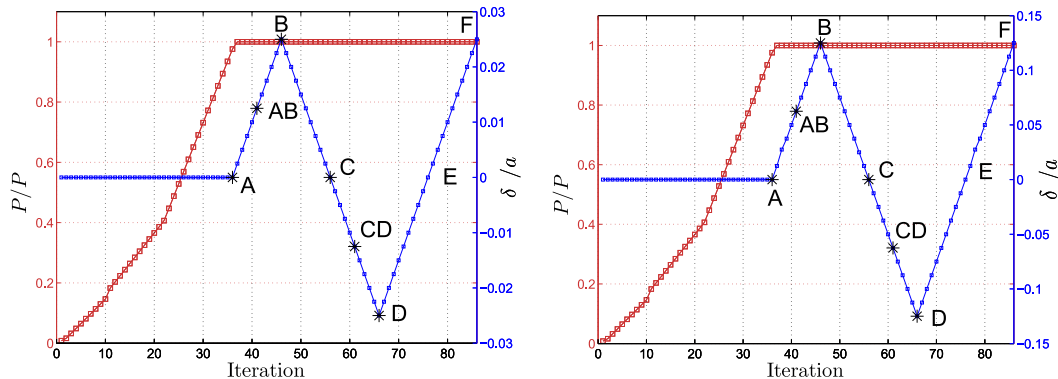


Figure 4.40: Normal loading and tangential displacements for a sphere moving over a worn coating

Both cases will be studied hereafter, however it must be noticed that the normal load P (Rigid sphere of radius $R = 200\mu\text{m}$, $P = 12.3\text{N}$, substrate properties $E_2 = 210\text{GPa}$, $\nu = 0.3$, contact radius $a = 20\mu\text{m}$) and coating thickness h ($h = 20\mu\text{m}$) have been defined in section 4.2.2 and are the same in the following simulations. Further studies will have to estimate the influence of the coating thickness on the system response. Moreover, it is worth noting that considering a fine discretization of the tangential loading (20 increments per fretting cycle), and a fine discretization of the wear phenomenon, the wear depth obtained after 20 fretting cycles (400 increments) are still limited to a few microns.

Note Wear criterion is now based on a wear coefficient arbitrarily chosen and is set equal to $1.10^4 \text{mm}^3/\text{J.mm}$ for simulations in the stick-slip regime and $1.10^1 \text{mm}^3/\text{J.mm}$ for simulations at the onset of the gross-slip regime. However, wear kinetics could be increased by changing this wear criterion, performing fast computation with a reduced accuracy of the solution.

4.2.5.1 Small amplitudes of sliding

Wear coefficient is arbitrarily chosen and is set equal to $1.10^4 \text{mm}^3/\text{J.mm}$, and amplitude of sliding considered is small, so the contacts remain in the stick-slip regime. As seen in previous sections, considering such amplitude, the soft coating will stick longer and wear less than stiff coatings, as seen in figure 4.41. It must be observed that the stiffer coating is wearing much more than other cases, and influence of wear after 15 fretting cycles (300 increments) will be significant. However, in other cases, this influence is limited.

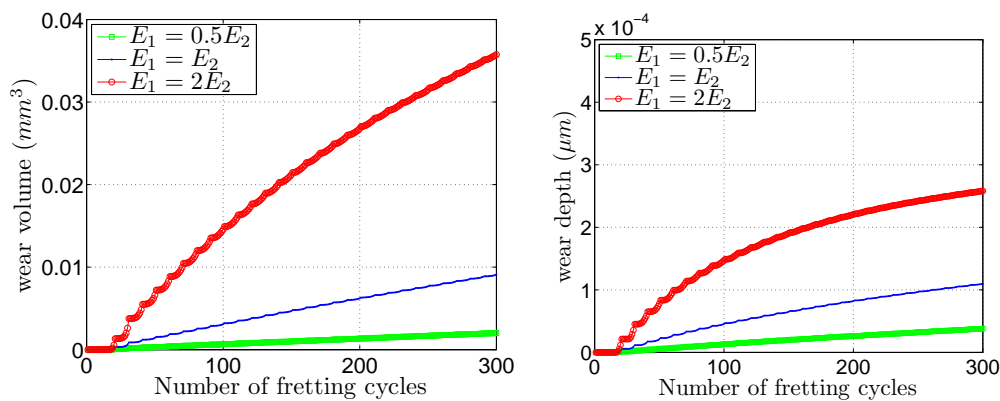


Figure 4.41: Dissipated energy: Wear volume vs. the number of increments (left) and Maximum wear depth vs. the number of increments (right)

For all cases considered, the partial-slip regime is the only source of dissipation and the slipping annulus observed in section 4.2.2 causes the wear profiles to be strongly discontinuous, as seen in figure 4.42. It must be observed that wear profiles are not totally symmetric and can be explained as follow: (i) the stick-slip problem is not totally symmetric, even when considering a symmetric loading, because of anti-symmetric shear profiles created by the normal loading P and (ii) because this wear profiles is actually observed at the loading step B. However, after a long time it is currently observed that wear profiles are becoming symmetric.

Because of wear, the maximum pressure observed will increase for all cases (see figure 4.43a). For the soft coating case this evolution is not even visible because of the very low wear rates, but it is more clear for the hard coating case. In this last case, two slopes can be observed. The first slope can be explained by the elevation of the contact pressure observed in the center of the contact because of the wear annulus surrounding it. Oddly, the second slope is much more important. It could be explained by the shear and pressure profiles observed in figure 4.45, where maximum pressures are observed just at the edge of the sticking zone. Obviously this is due to geometrical non-linearities created by the wear annulus, becoming sharp enough to create an annulus peak of pressure at the edge of the sticking zone.

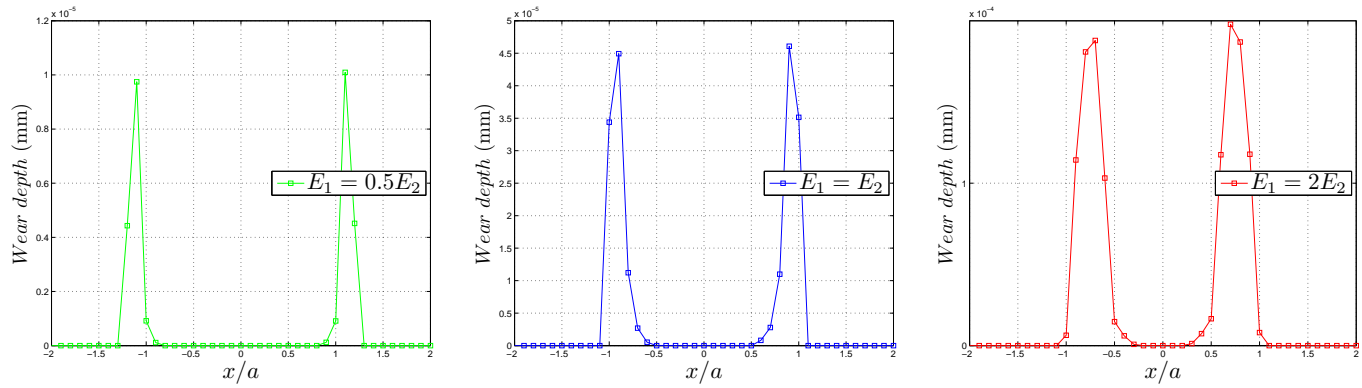


Figure 4.42: Wear profiles observed after 15 fretting cycles for various coatings

The surface area slowly increases because of wear, but it is also observed that variations of the contact area due to the fretting loading are also visible in figure 4.43b. It is shown that for the hard coating and the uncoated case, the variations of the contact surface are much more important for worn geometries. Once again, it can be explained by the pressure profiles observed in figure 4.45. It can be observed in figure 4.45c ($E_1 = 2E_2$) that the contact pressures at the edges of the contact are very low. As a matter of fact, points at the edges of the contact may easily jump from the contact zone to an exterior point during the fretting cycle, explaining the variations of the contact surface observed during the fretting cycle.

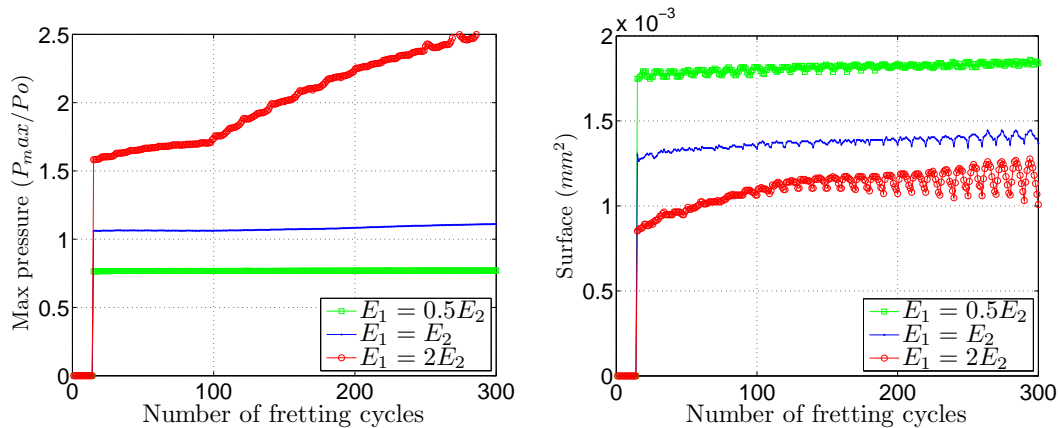


Figure 4.43: Maximum pressure vs. the number of increments (left) and contact surface vs. the number of increments (right)

The global response of the system is presented in figure 4.44. Energy dissipation causes the fretting loops to move clock-wise, which is easily observed for stiffer cases according to figure 4.41c. Since the maximum pressure, contact area and global response are changing, it is expected a significant change in terms of von Mises stresses, pressure and shears (See figure 4.44). It is observed that the stress levels globally increase when compared to von Mises stresses shown in

figure 4.21, due to the geometrical singularities observed at the edge of the contact.

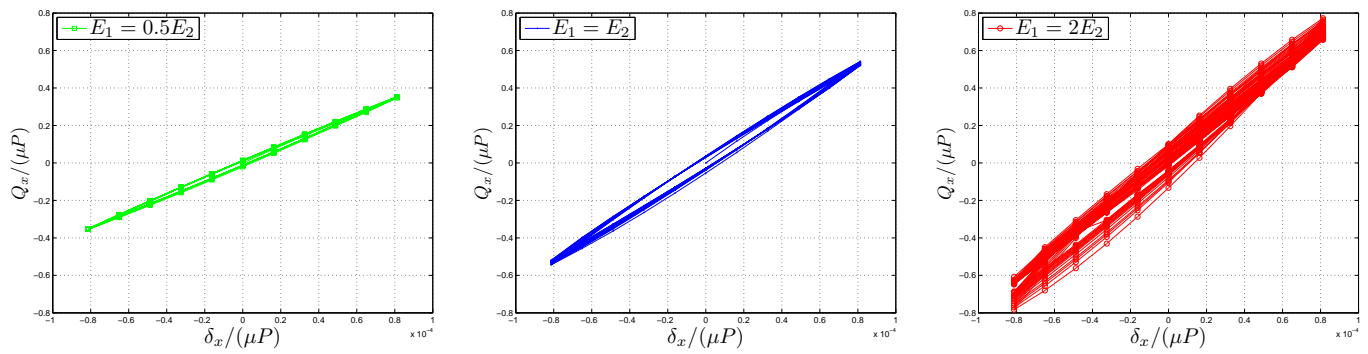


Figure 4.44: Fretting loops obtained for various worn coatings in the stick slip regime

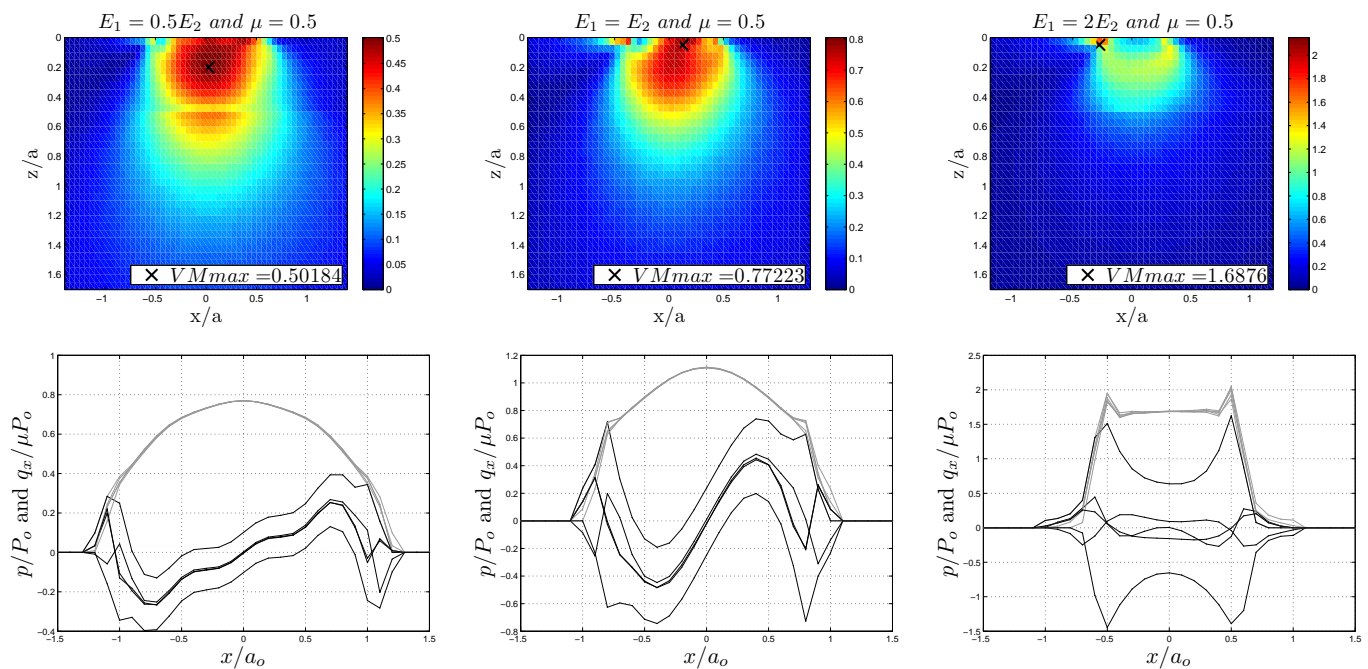


Figure 4.45: Von Mises stress, pressure and shear stress distributions normalized by the Hertz pressure, for various coatings ($E_1 = 0.5E_2$, $E_1 = E_2$ and $E_1 = 2E_2$) after 15 fretting cycles, for a sphere sliding over a rigid flat in the stick-slip regime

4.2.5.2 Large amplitudes of sliding

The wear coefficient is arbitrarily chosen and is set equal to $1.10^1 \text{mm}^3/\text{J.mm}$, and amplitude of sliding considered are relatively large just after the onset of the gross-slip regime. As seen in previous sections, considering such amplitude, the soft coating will stick longer than stiff coatings. It implies that the wear volume, related to the dissipated energy, increases with the stiffness of coatings (See figure 4.46). It must be observed that the stiff and uncoated cases are wearing much more than the soft coating. This is due to the importance of the partial-slip regime for the soft coating case.

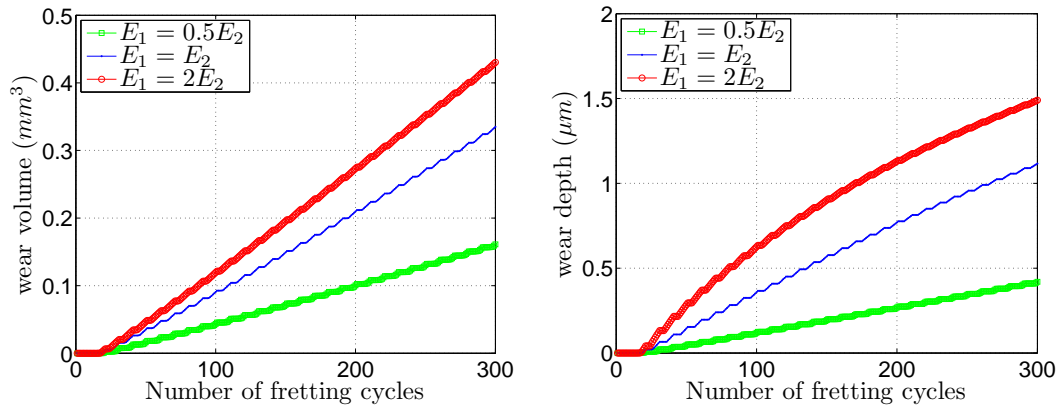


Figure 4.46: Dissipated energy: Wear volume vs. the number of increments (left) and Maximum wear depth vs. the number of increments (right)

The maximum wear depth is also logically higher for stiffer cases, since the contact pressure increases with the stiffness of coatings and the gross-slip regime is reached. However, the maximum depth is observed in the middle of the contact if the gross-slip regime is the principal mode of dissipation, which is observed for uncoated and stiff cases.

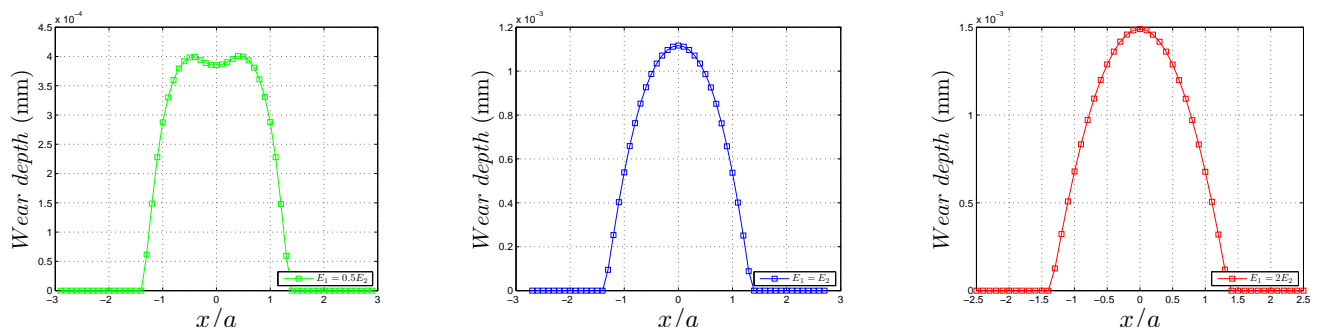


Figure 4.47: Wear profiles observed after 15 fretting cycles for a soft, uncoated and stiff coating

However, considering the soft case, the partial-slip regime remains an important source of dissipation when compared to the gross-slip regime. In this case, wear profiles are different and an annulus of maximum wear is observed, as seen in figure 4.47.

Because of wear, the maximum pressure observed will significantly drop for all cases, except for the soft coating which has a different wear kinetic because of the stick-slip regime importance. Oddly, the maximum pressure of the stiffest case will rapidly become the less severe case, which is consistent with the variations of contact surfaces, as seen in figure 4.48b.

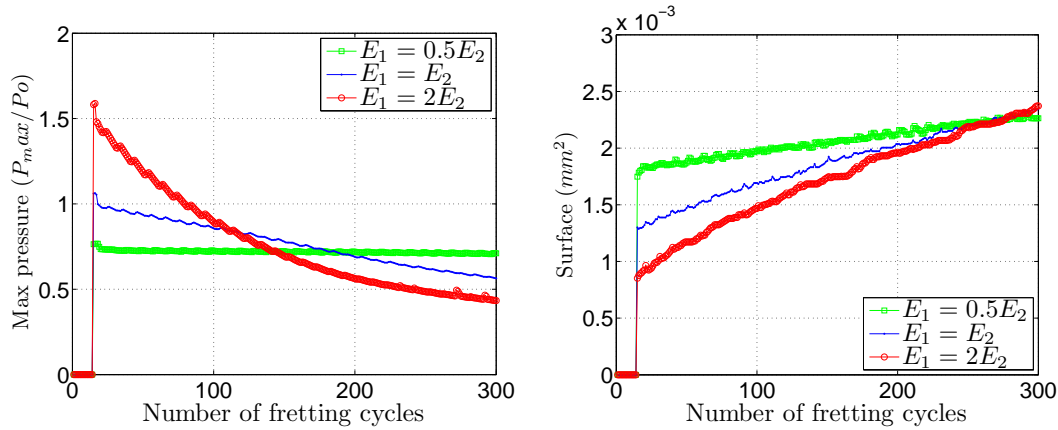


Figure 4.48: Maximum pressure vs. the number of increments (left) and contact surface vs. the number of increments (right)

The global response of the system is presented in figure 4.49. Energy dissipation causes the fretting loops to slowly close, which is easily observed for stiffer cases according to figure 4.46. Since the maximum pressure, contact area and global response are changing, it is expected a significant change in term of von Mises stresses, pressure, shears and slip profiles. However, it is observed that the stress levels become similar after 15 fretting cycles (See figure 4.50).

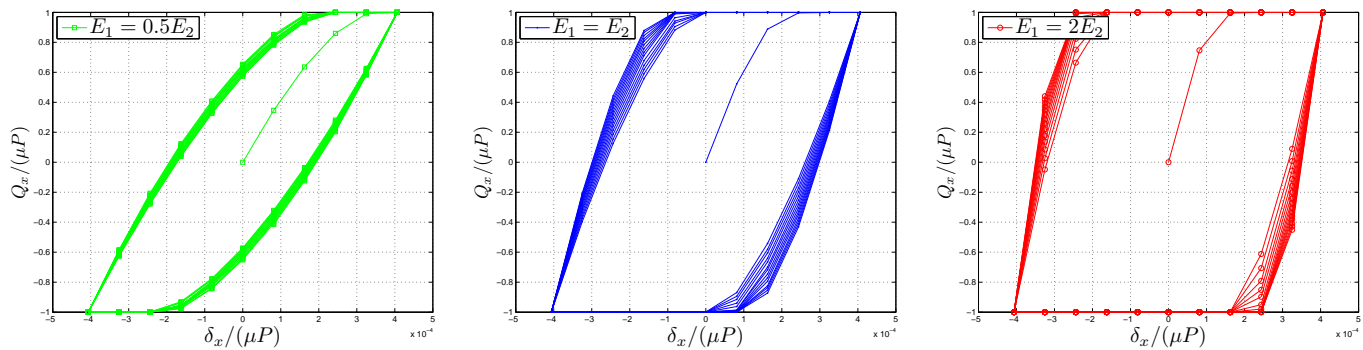


Figure 4.49: Fretting loops obtained for various worn coatings in the gross slip regime

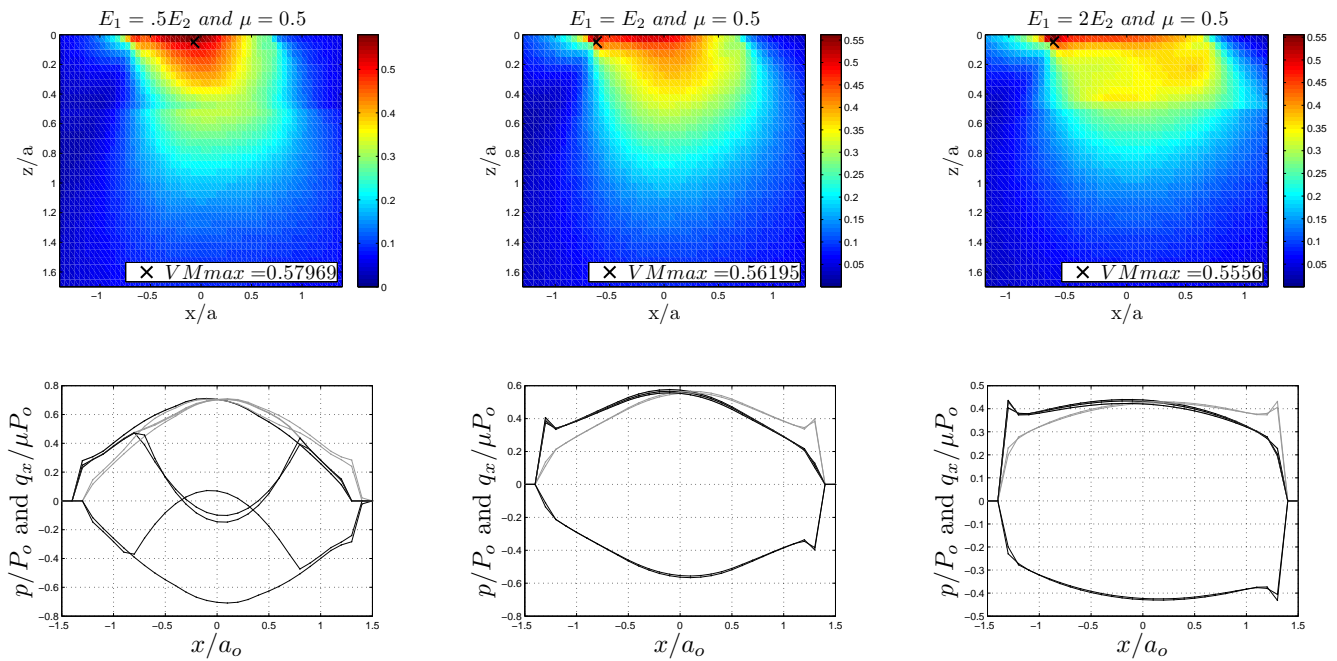


Figure 4.50: Von Mises stress, pressure and shear distributions normalized by the Hertz pressure, for various coatings ($E_1 = 0.5E_2, E_1 = E_2$ and $E_1 = 2E_2$) after 15 fretting cycles, for a sphere sliding over a rigid f at at the onset of the gross slip regime

4.2.5.3 Evolution of fretting loops

The wear-coefficient is now different for each case, and is globally increased significantly so the wear depth are of about $6\mu\text{m}$ after 30 fretting cycles (600 loading increments). Worn surfaces are presented and corresponding fretting loops are shown. It is observed that evolutions of the fretting cycles observed previously are confirmed for all cases (See figures 4.51 and 4.53). Some explanations are also proposed.

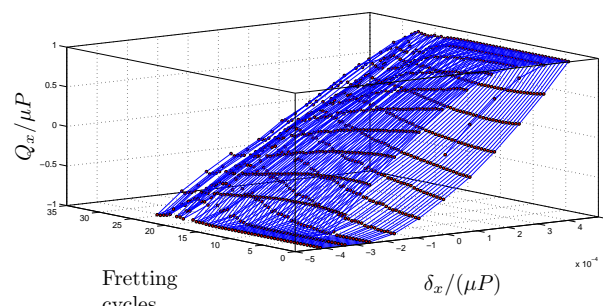


Figure 4.51: Fretting cycle considering a coated surface ($E_1 = 0.5E_2$) highly worn

Two cases will be considered:

- The sliding amplitude is large enough and the gross-slip regime is reached. Wear profiles are of the shape of an hyperbolic cosine function if the gross-slip regime is the principal mode of dissipation, which is not the case for $E_2 = 0.5E_1$. However the evolutions of fretting loops are very similar for all cases considered. From an initial state, wear will cause the fretting loops to close progressively. The surface covered by each fretting cycle is progressively diminished, meaning that the dissipation of energy has been globally reduced. Finally, the fretting loops may close enough so the partial-slip regime is reached (for $E_2 = 0.5E_1$).
- The sliding amplitude is small enough and the gross-slip regime is not reached. In this case, an annulus of wear is observed, and this annulus is different from a coating to another since it was observed previously that a soft coating tends to stick longer and has a larger sticking radius than a stiff coating. Fretting loops remain globally unchanged, however two aspects can be considered. First of all, the surface covered by each fretting cycle is also progressively diminished, proving that wear is still defining an optimized geometry for its wear resistance, which is commonly admitted. In addition, the inclination of fretting loops is progressively reduced (fretting loops are moving clock-wise). Moreover, this inclination is more important during the first fretting cycle, while it seems to be relatively stable after a few cycles. It was observed that the inclination is modified by the ellipticity ratio of the contact, which is consistent with observations since the wear profiles are not axi-symmetric. It can be seen that the wear profile is not axi-symmetric after the first fretting cycle, but wear profiles become axi-symmetric after a few fretting cycles (See figure 4.52). More classically, it is caused by the changes in compliance of the contact.

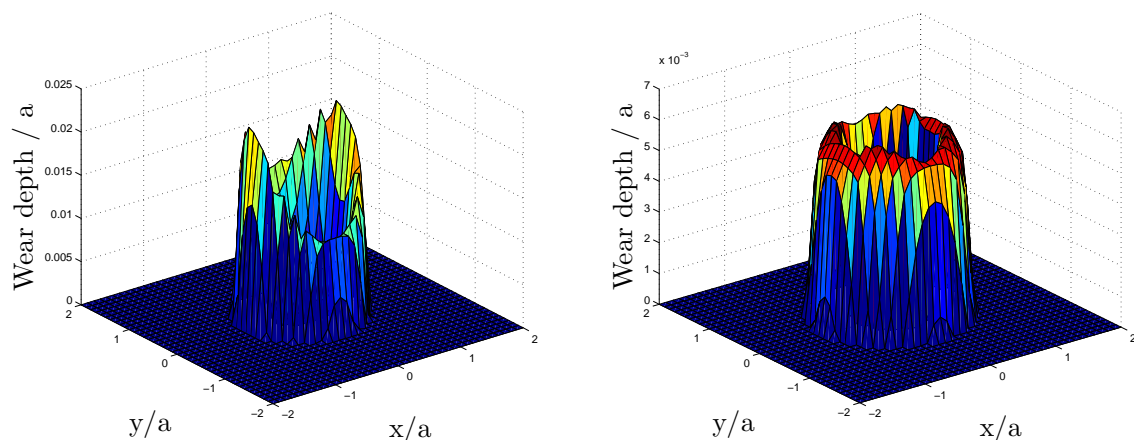


Figure 4.52: Comparison between the wear depth induced by the first fretting cycle (left) and the tenth fretting cycle (right)

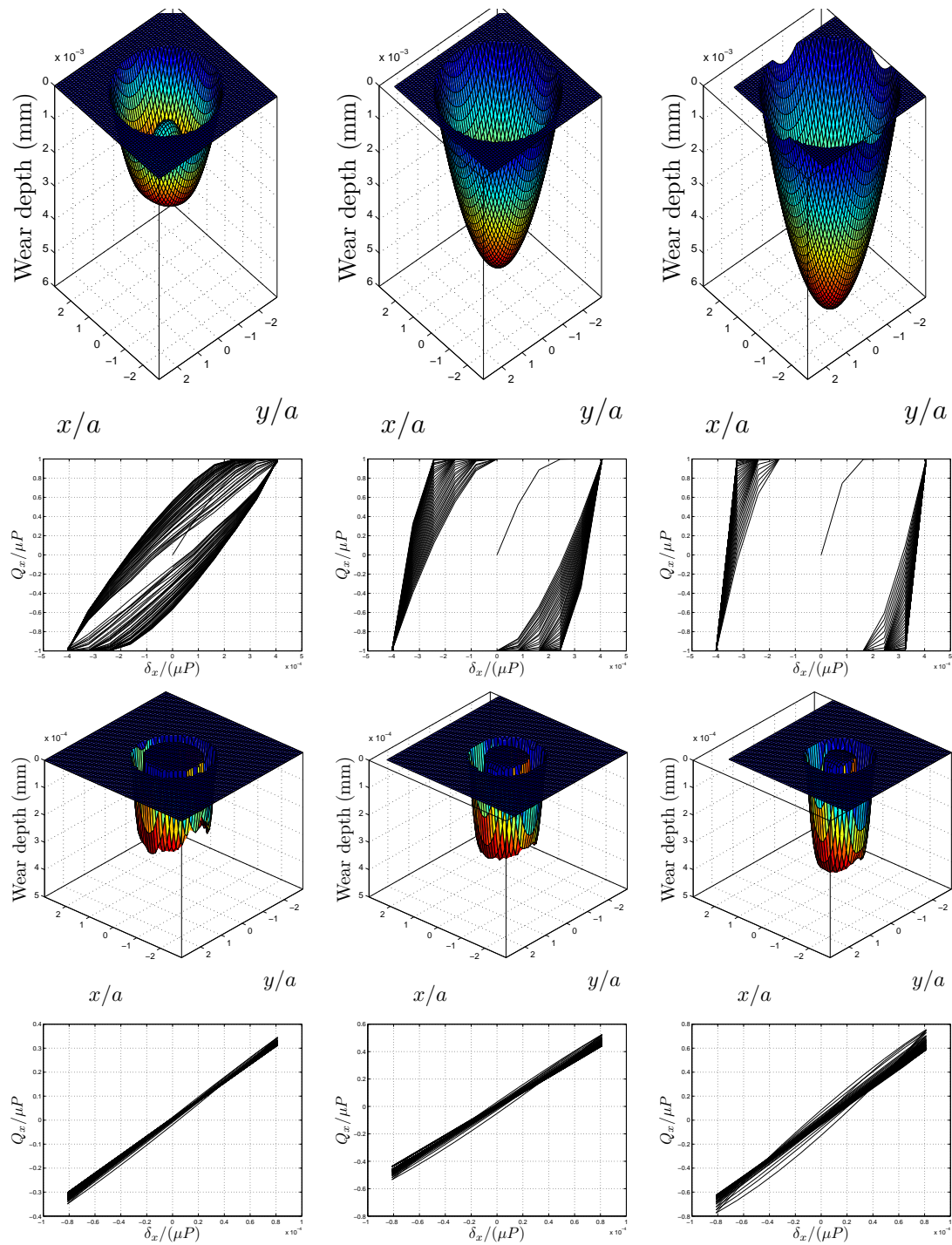


Figure 4.53: Evolution of fretting loops considering severe wear depth for various coatings ($E_1 = 0.5E_2$ (left), $E_1 = E_2$ (middle) and $E_1 = 2E_2$ (right)) and for both amplitudes of sliding (Large amplitudes (up) and small amplitudes (down))

4.2.6 Concrete used in civil engineering

Mechanical properties of concrete Concrete has a relatively high compressive strength, but significantly lower tensile strength, and as such is usually reinforced with materials that are strong in tension (often steel). Those reinforcements may be prestressed, as a method for overcoming concrete's natural weakness in tension, for use in beams, floors or bridges with a long span (See Figure 4.54). Prestressed steels or fibers are used to provide a clamping load which produces a compressive stress that offsets the tensile stress that concrete would otherwise experience. Such reinforcement could be considered using an alignment of non-homogeneities. Debonding between non-homogeneities and the matrix are not taken into account in the actual form of the code. However it would be useless for two major reasons:

- when the cement paste within the concrete hardens this conforms to the surface details of the steel, permitting any stress to be transmitted efficiently between the different materials;
- Usually steel bars are rough or corrugated to further improve the bond or cohesion between the concrete and steel;

Pre-stress of steel bars would be easily treated by simply adding a pre-strain ε^p along the bars' direction (see equation 3.1).

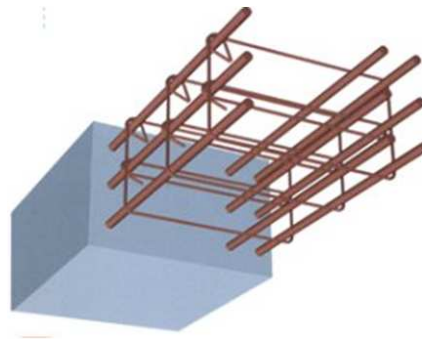


Figure 4.54: Structure of a reinforced or prestressed concrete

Another major property is a relatively constant elasticity at low stress levels, which starts decreasing at higher stress levels as matrix crackings develop. A closer look at it would highlight such crackings, and would require a much finer analysis. However, this loss of yield stress can also be generalized throughout the matrix and a damage behavior based on some mechanical criterion, such as the von Mises yield criterion, could be considered.

Case of a pre-stressed bar In this part, both the steel bar and the concrete are purely elastic. Approximate material properties of steel ($E_1 = 210GPa, \nu = 0.3$) and concrete ($E_2 = 50GPa, \nu = 0.3$) are used. The contact is not loaded at this time, but the steel bar is then pre-stressed by considering an additional strain field $\varepsilon^p = 1\%$, in the direction of the bar and for the bar's volume, in the heterogeneous solver. This additional strain is arbitrarily chosen. Results obtained are presented in figure 4.55. Obviously, stress levels observed are purely theoretical and are linearly proportional to ε^p at this time. (Note that the results are normalized by P_o , the same Hertzian pressure as used in the next paragraph)

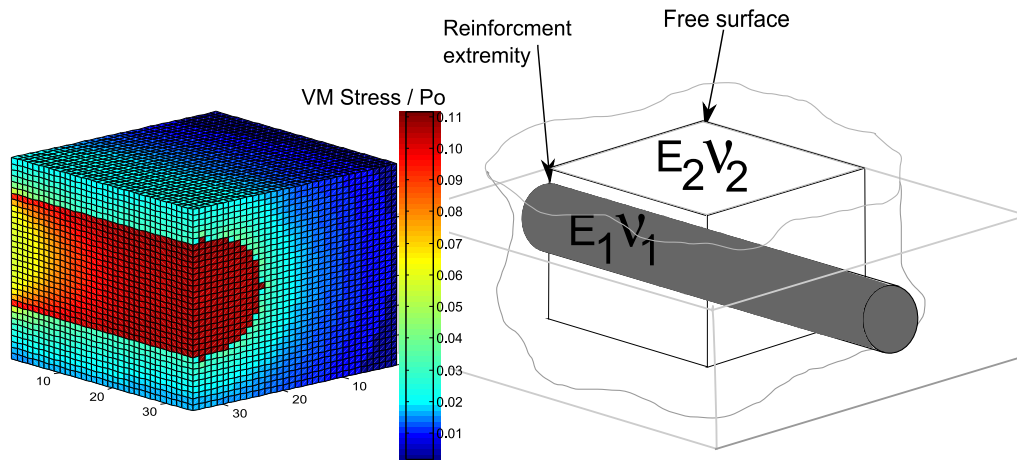


Figure 4.55: Von Mises stress around a pre-stressed steel bar of finite dimensions and located below a free surface

The pre-stress is transmitted to the concrete through the steel-concrete interface which is considered perfectly bonded. This problem should be two dimensional when considering a bar of infinite length. However, because of the finite length of the steel bar, the stress field may vary at the tip of this bar, while it is two dimensional far away. This proves the ability of the method to deal with fiber reinforcements at this stage.

Case of an arrangement of bars under contact loading A normal loading is then applied using a spherical indenter. The normal load P is applied so the Hertz pressure P_o and contact radius a_o are found in the homogeneous case.

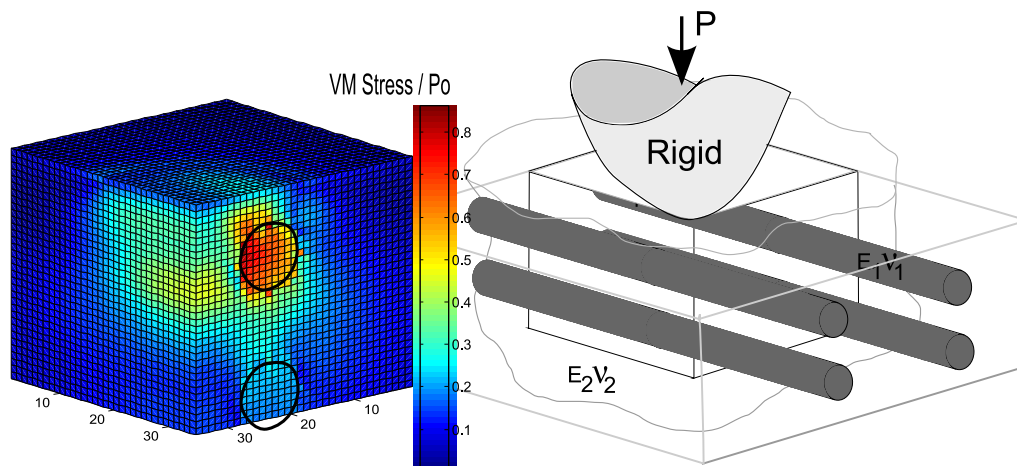


Figure 4.56: Von Mises stress around two pre-stressed steel bars of finite dimensions and located below a free surface, normally loaded

Parameters are chosen arbitrarily, and results shown hereafter are normalized by this Hertz pressure. However, it must be noticed that fibers of radius $R_{fiber} = 0.625a_o$ are here located at a depth $z_1 = a_o$ and $z_2 = 2.2a_o$ for $y = \pm 0.625a_o$. Bars are still pre-stressed, but stress levels caused by the contact loading are much higher than the pre-stress field observed in the previous paragraph. The von Mises stress field normalized by P_o is shown in figure 4.56.

A coupling exists between the normal, tangential and non-homogeneous problem so the contact pressure changes because of the steel bars existence. This pressure field is shown in figure 4.57 and normalized by the Hertzian pressure P_o , while the Hertzian pressure is also shown for reference. It can be seen that the presence of both steel bars close to the surface will significantly modify the pressure field, and two extrema are now observed.

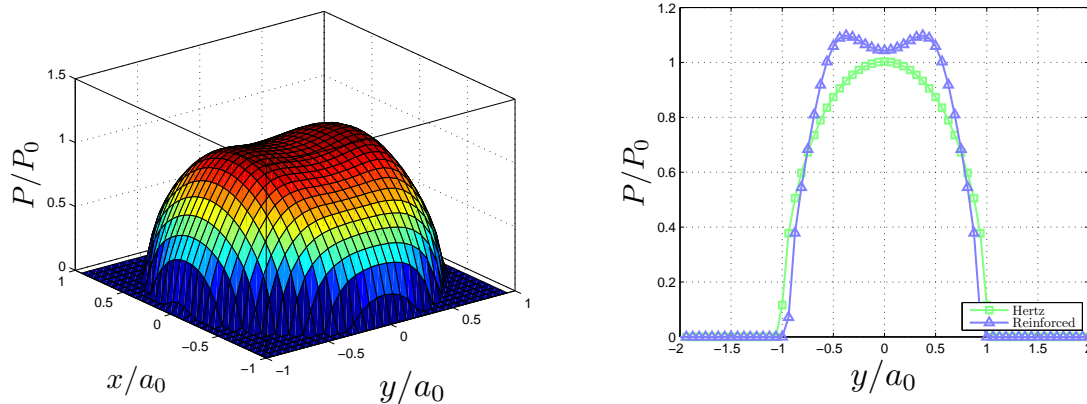


Figure 4.57: Pressure field normalized by the maximum Hertz pressure (left) and compared to the Hertz solution (right) for a loaded contact on a pre-stressed concrete

Conclusion In this short example, the Young's modulus of a cylindrical volume is accounting for fiber reinforcements. The fiber-matrix interface is perfectly bonded, and may eventually lead to some non-physical solutions. The case of a pre-stressed concrete is briefly exposed, and the von Mises stress observed at the steel-concrete interface are presented.

A contact loading is then considered. Four pre-stressed steel bars are placed below a spherical contact. The pressure profiles are significantly modified because of the presence of non-homogeneities below the surface, and the resultant von Mises stress field is presented.

This approach could be generalized, and the reinforcement fibers could account for composite materials. However, the size of the domains and refinement required in such analysis should be carefully considered. Many improvements are still required in order to account for complete composite structures. However, this approach is an example of the kind of application that could be dealt with a semi-analytical solver that is no longer limited to the homogeneous case.

4.2.7 Nano indentation of human bones

Overview of bone structure Bone is a relatively hard and lightweight composite material, and its structure is very complex since it is a multi-scale composite material, so multi-scale experiments are necessary to describe macro, micro and nano-mechanical properties. The primary tissue of bone, osseous tissue, is mostly formed of calcium phosphate in the chemical arrangement termed calcium hydroxyl apatite. It has a relatively high compressive strength of about 1800 MPa, but poor tensile strength of 104-120 MPa. It is also brittle and damage may occur at higher stress levels, even if it does have a significant degree of elasticity, contributed chiefly by collagen fibers.

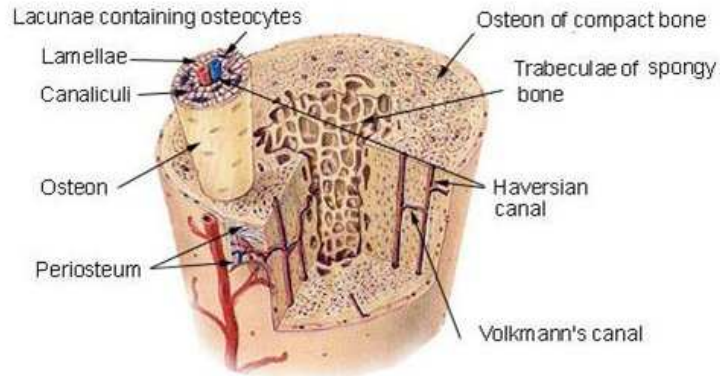


Figure 4.58: Trabecular and cortical bone structure

At a higher level, bone structure can be simplified in two main regions (See Figure 4.58):

- The outer layer of bones is much harder than the inner bone. Its structure is relatively compact and its porosity is 5-30%. This layer will be called cortical bone. This tissue gives bones their smooth, white and solid appearance, and accounts for 80% of the total bone mass of an adult skeleton.
- The inner bone is the trabecular bone or spongy bone. It is an open cell porous network of rod and plates which accounts for the remaining 20% of total bone mass while its porosity is 30-90%. It is lighter and allows room for blood and marrow.

Numerical modelling Cortical bone has been extensively studied at the Notre-Dame University by Timothy Ovaert, because of its importance in mechanical resistance of bones. Both experimental and numerical work can be found in [ZHA 08]. Typical load vs. indentation depth curves have been obtained using a finite-element model and considering a visco-elastic plastic-damage behavior, using a set of parameters defined experimentally. However, because of the viscous aspect, the indentation speed were increased and viscous properties are found while holding. This is obviously incompatible with the actual semi-analytical model. Moreover, the Berkovitch tip used is not ideal for the Semi-analytical method. For this reason, an indentation test was specifically realized by T. Ovaert using a spherical indenter and low indentation speeds (See Figure 4.60b).

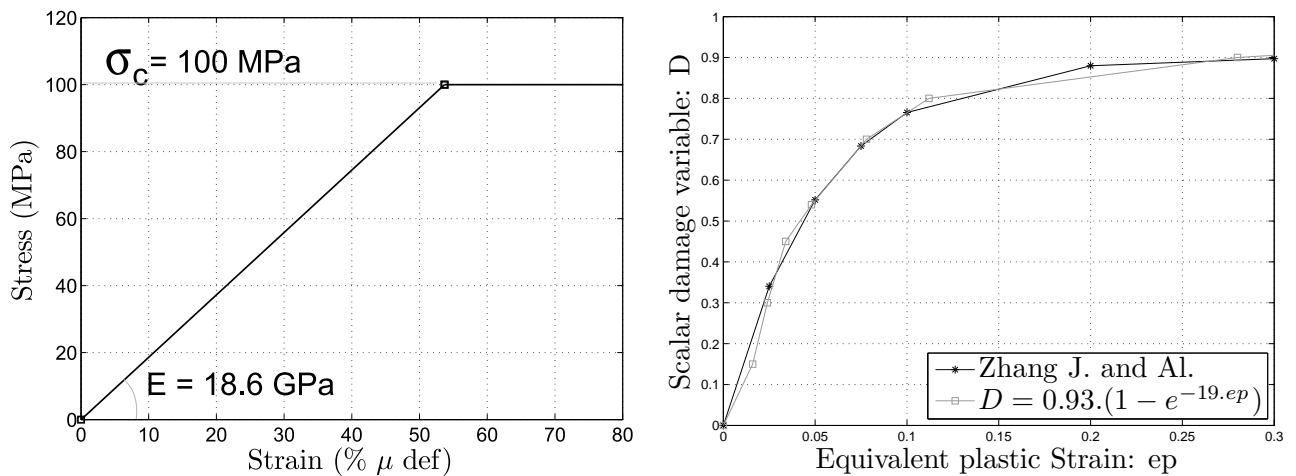


Figure 4.59: Elastic-plastic damage properties of cortical bone [ZHA 08]

It was assumed by Zhang and al. that the constitutive response of bones was characterized by an elastic-plastic-damage model defined by the material parameters described hereafter. First of all, the cortical bone is supposed to be perfectly plastic. The Young's modulus E is equal to 18.6 GPa . The compressive yield stress σ_c is set equal to 100 MPa . Finally, an empirical plastic-damage curve is defined in [ZHA 08] and will be used to define the damage-rate d_c related to the equivalent plastic strain e^p . This plastic-damage curve has been interpolated and an analytical form is used in the computations (See Figure 4.59). Actually, this kind of model is very similar to the cohesive models used for concrete in civil engineering.

Semi-analytical modelling Ordinary elastic-plastic constitutive models based on linear or power law hardening are not able to capture the complete unloading response during indentation of bone, particularly near the end of unloading, due to the decrease in stiffness. A rigid sphere of radius $R = 2 \mu\text{m}$ was progressively pressed against the material until it reaches $P = 10 \mu\text{N}$, and then unloaded. Damage is related to the equivalent plastic strain and modifies the strain level because of the stiffness degradation. The strain level will directly impact on the addition of plastic deformation, that are irreversible. In consequence it is of a great importance to couple both problem using a very low coefficient of relaxation on the plastic strains in order to target the physical solution, the risk would be to over-shoot this solution.

In fine, the actual model highlights a stiffness degradation at the end of unloading, which is experimentally quite characteristic while indenting cortical bones, as seen in figure 4.60 (radius of the indenter used here is unknown). The plastic-damage behavior clearly modifies the unloading response, especially at the end of unloading. Moreover, it must be noticed that the maximum depth remains close for both the plastic and the plastic-damage model which has been numerically observed by Zhang et al. However, a damage level of 90% was obtained by Zhang, which seems to be far from the constitutive equations of the SAM which is based on the

small strain theory. Finally, the equivalent plastic strain e^p for the plastic and plastic-damage are compared in figure 4.61.

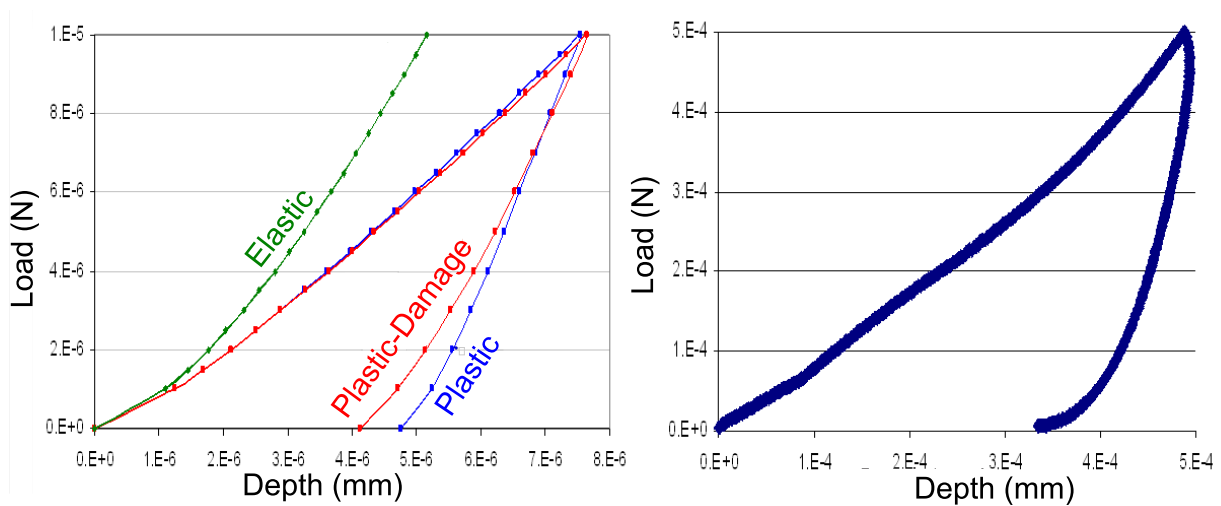


Figure 4.60: Plastic-damage model compared to a typical bone micro-indentation experimental curve [ZHA 08]

Conclusion In this short example, the Young's modulus of the matrix changed progressively and was based on a plastic criterion. This elastic-plastic-damage model has been used in order to perform a spherical indentation simulation. Almost no difference can be observed while loading and unloading, until the end of unloading, when compared to the elastic-plastic case. The maximum depth remains almost unchanged, while the final print is greatly reduced in the elastic-plastic-damage case.

This approach could be generalized, and the criterion used could be changed in order to treat other behaviors. However, this approach is an example of the kind of application that could be run with a semi-analytical solver that is no longer limited to the homogeneous case. Concrete presented in previous subsection and ceramics described in section 1.5.2 are brittle and could also be treated using such approach, in addition to the effect of their fiber reinforcements.

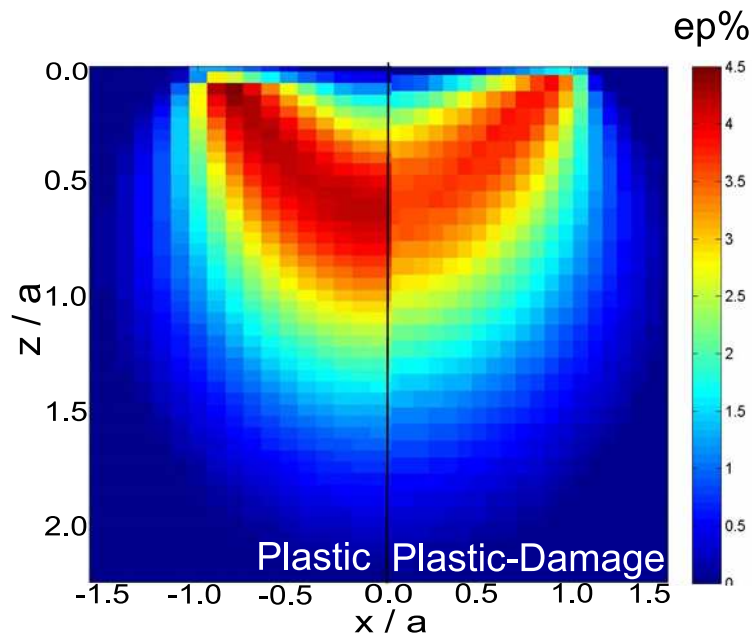


Figure 4.61: Plastic-damage model results compared to Plastic model results

4.3 Conclusion

The Equivalent Inclusion Method has been extended in order to consider many other inhomogeneous aspects. A 3D-FFT algorithm has been used to perform such computations in a reduced computing time. Stress and pressure fields for a coated surface obtained using such method are compared to numerical results found in the literature. The rigid sphere is (i) indented and then (ii) fully sliding over the coated surface [O'S 88]. Results are also compared to numerical results [PLU 98] for various coating thickness. Coupling is then added, and the stick/slip regime is first investigated for a normal loading. It is observed that the coating has a great influence on the contact regime while normally loaded. The ratio c/a , where c is the sticking radius and a is the contact radius, significantly changes while considering different coatings. The very particular stress state at the coating/substrate interface is believed to have a great influence on the contact conditions. A tangential displacement is then imposed, and pressure, shear and stress fields are observed. Two cases have been considered: (I) the stick/slip regime and (II) at the onset of the gross slip regime. It is shown that soft coatings are sticking more than hard coatings and should wear less than hard coatings when considering the same wear coefficient. A technique has been proposed so that wear of coatings become possible. This is of a great importance since coatings are no longer of uniform thickness. Wear is first investigated in the fully-sliding regime using simulation (ii). Wear significantly reduces the maximum pressure and increases the contact area. Pressure profiles are progressively flattened after many cycles regardless of the coating properties. However, wear kinetics are different depending on the coating properties. This study is extended to the stick-slip regime. Previous simulations ((I) and (II)) are then used while considering a wear coefficient chosen arbitrarily. As supposed in previous experiments, soft coatings tend to wear

less than hard coatings in the stick-slip regime while imposing a tangential displacement. But, more interesting is that surfaces covered by fretting loops in the gross-slip regime are reduced after many cycles. The energy dissipated after each cycle is reduced by wear. Previous analysis were considering a unique elastic coating of uniform or non-uniform thickness. But many elastic-plastic coatings could be considered without any difficulty. This technique can be used for many other non-homogeneities. In order to prove the interest of this method, two cases are considered and results are presented without going any further. The case of a pre-stressed concrete is considered with a unique pre-stressed steel-bar. Stress observed at the interface are presented. Then, an arrangement of four steel bars is considered under contact loading and stresses observed below the surface prove that fiber reinforcements play a key role in the determination of stress levels in the matrix. Moreover, it is shown that the contact pressure may be significantly modified because of fiber reinforcements. In order to deal with brittle materials, enrichment of elements can be based on a plastic criterion in order to account for damage. Results are compared to the elastic and elastic-plastic case and a great difference has been observed. It is shown that brittle materials tend to have the same loading curve than plastic materials, and the same slope at the onset of unloading. However, the residual print is greatly reduced while considering a plastic-damage model. Despite real numerical comparisons, same tendencies are observed both experimentally and numerically.

Conclusion and perspectives

Conclusion

Contact solvers based on the semi-analytical method need elementary analytical solutions to compute. Love [LOV 52] and Cerruti [CER 82] solutions used in elastic contact solver are elementary solutions relating the surface pressure and shear distributions to the subsurface stress state and surface displacements for homogeneous and isotropic media. New elementary solutions are required when plasticity is involved. While Chiu [CHI 78, CHI 77] described the effect of a unique plastic zone on the residual stress and strain states, Jacq et al. [JAC 01, JAC 02] related analytically the subsurface plastic strains to the normal surface displacements. All these elementary solutions have been used in a three-dimensional semi-analytical elastic-plastic contact code. A special attention to the tangential effects involved by plasticity should be paid since it has not been properly considered until now. Analytical expressions that relate the components of the strain tensor of an incompressible cuboid of uniform strain on the tangential displacements of any point of the free surface of a half-space is then expressed [FUL 10]. Both normal and tangential solutions have been compared to a finite element analysis and a very good agreement was found, which validates the analytical solutions. Those solutions have been implemented into an elastic-plastic contact solver to investigate frictional contact problems.

In order to highlight the influence of plasticity on the contact regime, three fretting modes have been investigated in the second section of this manuscript: (i) indentation and (ii) incipient motion have been more carefully studied. However, (iii) the torsional mode is studied without going any further. Considering FEM non-linearities encountered in contact problems, which generate cumbersome computations, models based on semi-analytical methods, with such new ingredients to account for plasticity, could be an interesting alternative.

The third part is related to the Eshelby's theory dealing with spherical non-homogeneities. Using such method, spherical non-homogeneities made of a different material are considered equivalent to a spherical inclusion with the same elastic properties. This transition is possible using a tensor, related to the shape of the inclusion considered, known as the Eshelby's tensor. Because spherical inhomogeneities are easy to use and require limited numerical computations, this shape has been first studied here. Influence on the contact has been investigated for a unique or a cluster of non-homogeneities of various properties.

The Eshelby's tensor for a cube is determined, and spherical inclusions are then discretized in many cubical inclusions. Solutions obtained are then compared to the analytical solutions, and a reasonably good agreement is found. Any shape of inclusion is now possible, considering such

discretization. A short example is then proposed, considering a large inclusion and a fretting loading.

The fourth part shows that such approach can be extended in order to deal with other in-homogeneous aspects. A 3D-FFT algorithm has been successfully implemented in the contact solver, allowing much larger models in about the same computing time, making computing time affordable in conjunction of an elastic-plastic analysis. It was also the unique possibility in the non-homogeneous case. A 2D-FFT was available in the elastic-plastic case.

Stress and pressure fields for a coated surface indented by a rigid sphere were compared to numerical results given by O'Sullivan [O'S 88]. Fully sliding contacts were then studied when the coupling is temporarily neglected. A good agreement is observed and studies have been extended farther. Elastic-plastic properties can be defined in those non-homogeneities and lead to much complicated problems, among which are (i) elastic-plastic coatings, (ii) elastic-plastic inclusions, (iii) brittle materials with damageable media and many other applications.

A technique is then proposed in order to wear coatings. Wear of coatings is first studied in the fully-sliding regime. It is then extended to the stick-slip regime, considering a partially sliding contact and a contact at the onset of the gross-slip regime. Variation of the contact regime is then investigated.

In fine, two examples are presented without going any further. (i) The case of a pre-stressed concrete is then considered with a unique steel bar pre-stressed. An arrangement of four steel bars is considered under contact loading. (ii) Enrichment of elements is then based on a plastic criterion in order to account for damage. Results are compared to the elastic and elastic-plastic case. It is shown that despite real experimental and numerical validations, same tendencies are observed both experimentally and numerically.

To conclude, the gap between numerical and semi-analytical methods has to be reduced. Many improvements have been made in this field and friction is now taken into account with hardening problems. Moreover, spherical non-homogeneities can be considered with elastic-plastic properties allowing further study on the influence of metallic purity on crack initiation and propagation. A complete study presents the influence of a unique or a cluster of inclusions of various elastic properties on the contact conditions. Coatings are then considered, results obtained are successfully compared to the literature. Those results are extended to the stick-slip regime, considering a full coupling of all problems. The simulation of the coating wear becomes possible and few results are presented, among other applications. Many developments in this field can now be carried on.

This work can be extended in order to study the influence of fiber reinforcements on the local stress levels and the contact response. Elementary solutions for a cubical inclusion presented in this work will have to be extended to the first and the second order, so that gradients could be taken into account and solution's accuracy improved. Using such technique, fibers will be explicitly meshed. Other coefficients of influence can also be extended from the isotropic to the anisotropic half-space. Fiber reinforcements are no longer considered explicitly, but the anisotropic behavior accounts for the reinforcement structure. If the contact area is large enough compared to the fibers' size, results obtained using the first method could be faced to the results obtained using the second one.

Various techniques should be found in order to consider a coating particularly thin, which becomes important for severe wear rates. In some cases, the substrate may appear into the contact, another coefficient of friction could be defined locally, and wear kinetics could be investigated.

Acknowledgment

Thanks go to Snecma for its technical and financial support. This work takes place in the framework of the MAIA mechanical research and technology program sponsored by CNRS, ONERA and SAFRAN Group.

Bibliography

- [AI 99] AI X., SAWAMIPHAKDI K.
Solving elastic contact between rough surfaces as an unconstrained strain energy minimization by using CGM and FFT Techniques. *ASME J. Tribol.*, vol. 121, 1999, p. 639–647.
- [ALE 86] ALEXANDROV V., ROMALIS B.
Contact problems in mechanical engineering. Mashinostroenie, 1986.
- [AMB 00] AMBRICO J.M. B. M.
Plasticity in fretting contact. *Journal of the mechanics and physics of solids*, vol. 48, 2000, p. 2391-2417.
- [AMB 01] AMBRICO J.M. B. M.
The role of macroscopic plastic deformation in fretting fatigue life predictions. *International journal of fatigue*, vol. 23, 2001, p. 121-128.
- [ANT 04] ANTALUCA E., NÉLIAS D., CRETU S.
A three-dimensional friction model for elastic-plastic contact - Application to dented surfaces. *ASME/STLE International Joint Tribology Conference*, 2004. paper TRIB2004-64331.
- [ANT 05] ANTALUCA E.
Contribution à l'étude des contacts élasto-plastiques - effet d'un chargement normal et tangential. PhD Thesis, INSA Lyon, 2005.
- [ANT 08] ANTALUCA E., NÉLIAS D.
Contact fatigue analysis of a dented surface in a dry elastic-plastic circular point contact. *Trib. Lett.*, vol. 29, 2008, p. 139-153.
- [ARC 53] ARCHARD J. F.
Contact and rubbing of f at surfaces. *J. Appl. Phys.*, vol. 24, 1953, p. 981–988.
- [BEN 06] BENEDIKT B., LEWIS M., RANGASWAMY P.
On elastic interactions between spherical inclusions by the equivalent inclusion method. *Computational Materials Science*, vol. 37, 2006, p. 380-392.
- [BOU 85] BOUSSINESQ J.
Application des potentiels à l'étude de l'équilibre et du mouvement des solides élastiques. Gauthier-Villars, Paris, 1885.

- [BOU 04] BOUCLY V.
Modélisation semi-analytique du contact thermo-élasto-plastique. Master's thesis, INSA de Lyon, 2004.
- [BOU 05] BOUCLY V., NÉLIAS D., LIU S., WANG Q. J., KEER L. M.
Contact Analyses for Bodies with Frictional Heating and Plastic Behavior. *ASME J. Tribol.*, vol. 127, 2005, p. 355–364.
- [BOU 07] BOUCLY V., NELIAS D., GREENWOOD I.
Modeling of the rolling and sliding contact between two asperities. *ASME J. Tribol.*, vol. 129, 2007, p. 235-245.
- [BOU 08] BOUCLY V.
Semi-analytical modeling of transient thermal-elastic-Plastic contact and its application to asperity collision, wear and running-in of surfaces. PhD Thesis, INSA Lyon, 2008.
- [CAT 38] CATTANEO C.
Sul contatto di due corpi elastici : distribuzione locale degli sforzi. *Accademia Nazionale Lincei, Rendiconti, Ser. 6*, vol. XXVII, 1938, p. 342–348, 434–436, 474–478.
- [CER 82] CERRUTI V.
Ricerche intorno all'equilibrio de' corpi elastici isotropi. *Rend. Accad. Lincei*, vol. 3, n° 13, 1882, p. 81–122.
- [CHA] CHAISE T., NELIAS D., SADEGHI F.
On the effect of isotropic hardening on the coefficient of restitution for single or repeated impacts using a semi analytical method. *Tribology Transactions*, to appear.
- [CHA 90] CHANG T., CHENG H., CHOU W., SPROUL W.
A comparison of Fatigue Failure Morphology between TiN Coated and Uncoated Lubricated Rollers. *ASME Journal of Tribology*, vol. 121, 1990, Page 1.
- [CHI 77] CHIU Y.
On the stress field due to initial strains in a cuboid surrounded by an infinite elastic space. *ASME J. Appl. Mech.*, vol. 44, 1977, p. 587-591.
- [CHI 78] CHIU Y. P.
On the stress field and surface deformation in a half-space with a cuboidal zone in which initial strains are uniform. *ASME J. Appl. Mech.*, vol. 45, 1978, p. 302-306.
- [CIA 98a] CIAVARELLA M.
The generalized Cattaneo partial slip plane contact problem. I–Theory. *International Journal of Solids and Structures*, vol. 35, n° 18, 1998, p. 2349–2362.
- [CIA 98b] CIAVARELLA M.
The generalized Cattaneo partial slip plane contact problem. II–Examples. *International Journal of Solids and Structures*, vol. 35, n° 18, 1998, p. 2363–2378.
- [COU 03] COURBON J., AL.
Influence of inclusion pairs, clusters and stringers on the lower bound of the endurance limit of bearing steels. *Tribology International*, vol. 36, 2003, p. 921-928.

- [DIN 05] DINTWA E., ZEEBROECK M. V., TIJSKENS E., RAMON H.
Torsion of viscoelastic spheres in contact. *Granular Matter*, vol. 7, n° 2, 2005, p. 169–179.
- [DUN 72] DUNDURS J., LEE M. S.
Stress concentration at a sharp edge in contact problems. *Journal of Elasticity*, vol. 2, 1972, p. 109–112.
- [DUV 72] DUVAUT G., LIONS J. L.
Les inéquations en mécanique et en physique. Dunod, Paris, 1972.
- [ESH 06] ESHELBY J.
Collected works of J.D. Eshelby. The mechanics of defects and inhomogeneities, elastic inclusions and inhomogeneities. Springer, 2006.
- [FOT 96] FOTIU P., NEMAT-NASSER S.
A universal integration algorithm for rate dependant elasto-plasticity. *Comput. Struct.*, vol. 59, 1996, p. 1173-1184.
- [FUL 10] FULLERINGER B., NELIAS D.
On the tangential displacement of a surface point due to a cuboid of uniform plastic strain in a half-space. *ASME J. Appl. Mech.*, vol. 77, 2010, p. 021014-1-021014-7.
- [GAL 53] GALIN L. A.
Contact Problems in the Theory of Elasticity. Moscow-Leningrad, October 1953. English translation by H. Moss, edited by I. N. Sneddon, North Carolina State College, Departments of Mathematics and Engineering Research, NSF Grant No. G16447, 1961.
- [GAL 06] GALLEGO L., NÉLIAS D., JACQ C.
A comprehensive method to predict wear and to define the optimum geometry of fretting surfaces. *ASME J. Tribol.*, vol. 128, 2006, p. 476–485.
- [GAL 07a] GALLEGO L.
Fretting et Usure des Contacts Mécanique: Modélisation Numérique. PhD Thesis, INSA-Lyon, 2007.
- [GAL 07b] GALLEGO L., FULLERINGER B., DEYBER S., NELIAS D.
Multiscale computation of fretting wear at the blade/disk interface. *Proceedings of the 5th Int. Symp. on Fretting Fatigue (ISFF5), Montreal, Quebec, Canada, April 21-23 2007*.
- [GAL 07c] GALLEGO L., NELIAS D.
Modeling of Fretting Wear Under Gross Slip and Partial Slip Conditions. *Journal of Tribology*, vol. 129, n° 3, 2007, p. 528-535, ASME.
- [GAL 10] GALLEGO L., NELIAS D., DEYBER S.
A fast and efficient contact algorithm for fretting problems applied to fretting modes I, II and III. *Wear*, vol. 268, 2010, p. 208-222.
- [GLA 80] GLADWELL G.
Contact problems in the classical theory of elasticity. Sijthoff & Noordhoff, Alphen aan den Rijn, The Netherlands, 1980.

- [GOO 62] GOODMAN L. E.
Contact stress analysis of normally loaded rough spheres. *J. Appl. Mech.*, vol. 29, 1962, Page 515.
- [GRE 66] GREENWOOD J. A., WILLAMSON J. B. P.
Contact of normally f at surfaces. *Proc. R. Soc. London, Ser. A*, vol. 295, 1966, p. 300–319.
- [HAM 63] HAMILTON G. M., GOODMAN L. E.
The stress f eld created by a circular sliding contact. *Journal of Applied Mechanics*, vol. 33, n° MAR, 1963, Page 371.
- [HER 82] HERTZ H.
On the contact of elastic solids. *J. Reine Angew. Math.*, vol. 92, 1882, p. 156–171.
- [JAC 01] JACQ C.
Limite d'endurance et duree de vie en fatigue de roulement du 32CrMoV13 nitrure en presence d'indentations. PhD Thesis, INSA Lyon, 2001.
- [JAC 02] JACQ C., NELIAS D., LORMAND G., GIRODIN D.
Development of a Three-Dimensional Semi-Analytical Elastic-Plastic Contact Code. *Journal of Tribology International*, vol. 124, n° 4, 2002, p. 653–667, ASME.
- [JAE 04] JAEGER J.
New Solutions in Contact Mechanics. Witpress, Southampton, Boston, 2004.
- [JOH 85] JOHNSON K. L.
Contact Mechanics. Cambridge University Press, London, 1985.
- [JU 96] JU Y., FARRIS T. N.
Spectral Analysis of Two-Dimensional Contact Problems. *ASME J. Tribol.*, vol. 118, 1996, p. 320–328.
- [KAB 04] KABO E., EKHBERG A.
Material defects in rolling contact fatigue of railways wheels: the influence of defect size. *Internation Journal of Wear*, vol. 1, 2004.
- [KAL 90] KALKER J. J.
Three dimensional elastic bodies in rolling contact. Kluwer Academic Publishers, Dordrecht, 1990.
- [KOM 88] KOMVOPOULOS K.
Finite Element Analysis of a Layered Elastic Solid in Normal Contact with a Rigid Surface. *ASME journal of tribology*, vol. 110, 1988, p. 477-485.
- [LEM 90] LEMAINTRE J., CHABOCHE J.
Mechanics of solid materials. Cambridge University Press, 1990.
- [LER 89] LEROY J., FLOQUET A., VILLECHAISE B.
Thermomechanical Behavior for Multilayered Media: Theroy. *ASME journal of Tribology*, vol. 111, 1989, p. 538-544.

- [LER 10] LEROUX J., FULLERINGER B., NELIAS D.
Contact analysis in presence of spherical inhomogeneities within a half-space. *International journal of solid and structures*, vol. 47, 2010, p. 3034-3049.
- [LIU 00] LIU S., WANG Q., LIU G.
A versatile method of discrete convolution and FFT (DC-FFT) for contact analyses. *Wear*, vol. 243, 2000, p. 101–111.
- [LIU 01] LIU G., WANG Q., LIU S.
A Three-Dimensional Thermal-Mechanical Asperity Contact Model for Two Nominally Flat Surfaces in Contact. *J. Tribol.*, vol. 123, n° 3, 2001, p. 595–602, ASME.
- [LIU 02] LIU S., WANG Q.
Studying contact stress fields caused by surface tractions with a discrete convolution and fast Fourier transform algorithm. *ASME J. Tribol.*, vol. 124, 2002, p. 36–45.
- [LIU 05a] LIU S., WANG Q.
Elastic fields due to eigenstrains in a half-space. *ASME J. Appl. Mech.*, vol. 72, 2005, p. 871-878.
- [LIU 05b] LIU S., PEYRONNEL A., WANG Q., KEER L.
An extension of the Hertz theory for the three-dimensionnal coated bodies. *Tribology letter*, vol. 18, 2005, p. 303-314.
- [LIU 07] LIU Y., CHEN W., ZHU D., LIU S., WANG Q.
An elastohydrodynamic lubrication model for coated surfaces in point contacts. *ASME Journal of Tribology*, vol. 129, 2007, p. 509-516.
- [LOV 52] LOVE A. E. H.
A Treatise on the Mathematical Theory of Elasticity. Cambridge University Press, London, 4th edition, 1952.
- [MAN] MANZHIROV A. V.
The Wear Contact Problem for an Elastic Foundation with an Inhomogeneous Coating. *Proceedings of WTC IV conference, Kyoto, 2009*, vol. Department for Modeling in Solid Mechanics, Ishlinsky Institute for Problems in Mechanics, Russian Academy of Sciences, Moscow, Russia, p. I-145.
- [MCE 49] MCEWEN E.
Stress in elastic cylinders in contact along a generatrix. *Philosophical Magazine*, vol. 40, 1949, p. 454–459.
- [MEI 68] MEIJERS P.
The contact problem of a rigid cylinder on an elastic layer. *Applied Science Research*, vol. 18, 1968, Page 353.
- [MIK 57] MIKHLIN S.
Integral equations. Pergamon press, London, 1957.
- [MIN 49] MINDLIN R. D.
Compliance of elastic bodies in contact. *ASME J. Appl. Mech.*, vol. 16, 1949, p. 259–268.

- [MIN 53] MINDLIN R. D., DERESIEWICZ H.
Elastic spheres in contact under varying oblique forces. *Journal of Applied Mechanics*, vol. 20, 1953, p. 327–344.
- [MOH 95] MOHRBACHER H., CELIS J. P., ROOS J. R.
Laboratory testing of displacement and load induced fretting. *Tribology International*, vol. 28, 1995, p. 269–278.
- [MOS 75a] MOSCHOVIDIS Z., MURA T.
Two ellipsoidal inhomogeneities by the equivalent inclusion method. *ASME J. Appl. Mech.*, vol. 42, 1975, p. 847-852.
- [MOS 75b] MOSCHOVIDIS Z.
Two ellipsoidal inhomogeneities and related problems treated by the equivalent inclusion method. PhD Thesis, Northwestern University, 1975.
- [MUR 77] MURA T., CHENG D.
The elastic field outside an ellipsoidal inclusion. *ASME J. Appl. Mech.*, vol. 44, 1977, p. 591-594.
- [MUR 79] MURA T., SEO K.
The elastic field in a half space due to ellipsoidal inclusion inclusions with uniform dilatational eigenstrains. *ASME J. Appl. Mech.*, vol. 46, 1979, p. 568-572.
- [MUS 53] MUSKHELISHVILI N.
Singular integral equations. P. Nordhoff N.V., Gronnigen, 1953.
- [NEL 06] NELIAS D., BOUCLY V., BRUNET M.
Elastic-Plastic Contact Between Rough Surfaces: Proposal for a Wear or Running-in Model. *J. Tribol.*, vol. 128, n° 2, 2006, p. 236–244, ASME.
- [NEL 07a] NELIAS D., ANTALUCA E., BOUCLY V.
Rolling of an elastic ellipsoid upon an elastic-plastic flat. *ASME J. Tribol.*, vol. 129, 2007, p. 791-800.
- [NEL 07b] NELIAS D., ANTALUCA E., BOUCLY V., CRETU S.
A three dimensional semi-analytical model for elastic-plastic sliding contacts. *ASME J. Tribol.*, vol. 129, 2007, p. 761-771.
- [O'S 88] O'SULLIVAN T., KING R.
Sliding contact stress field due to a spherical indenter on a layered elastic half-space. *ASME J. of Trib.*, vol. 127, 1988, p. 494-502.
- [PAN 75] PANAGIOTOPOULOS P. D.
A nonlinear programming approach to the unilateral contact and friction-boundary value problem in the theory of elasticity. *Ingenieur-Archiv*, vol. 44, 1975, p. 421–432.
- [PAU 05] PAULIN C., FOUVRY S., DEYBER S.
Wear kinetics of Ti-6Al-4V under constant end variable fretting sliding conditions. *Wear*, vol. 259, 2005, p. 292–299.

- [PAU 06] PAULIN C.
Etude de l'endommagement du contact multicouche aube/disque sous chargement de fretting : impact des sollicitations variables et de la dimension du contact. PhD Thesis, Ecole Centrale de Lyon, 2006.
- [PLU 98] PLUMET S. D. M.-C.
A 3-D Model for a Multilayered Body Loaded Normally and Tangentially Against a Rigid Body: Application to Specific Coatings. *Journal of Tribology*, vol. 120, 1998, p. 668-676.
- [POL 99] POLONSKY I. A., KEER L. M.
A numerical method for solving rough contact problems based on the multi-level multi-summation and conjugate gradient techniques. *Wear*, vol. 231, 1999, p. 206-219.
- [POL 00a] POLONSKY I. A., KEER L. M.
Fast methods for solving rough contact problems: a comparative study. *ASME J. Tribol.*, vol. 122, 2000, p. 36-40.
- [POL 00b] POLONSKY I., KEER L.
A fast and accurate method for numerical analysis of elastic layered contacts. *ASME Journal of Tribology*, vol. 122, 2000, p. 30-35.
- [POL 01] POLONSKY I. A., KEER L. M.
Stress analysis of layered elastic solids with cracks using the fast Fourier transform and conjugate gradient techniques. *ASME J. Appl. Mech.*, vol. 68, 2001, p. 708-714.
- [ROU 81] ROUTH E.
Dynamics of a system of rigid bodies. Mac Millan and co., 1981.
- [SAC 83] SACKFIELD A., HILLS D. A.
Some Useful Results In The Classical Hertz Contact Problem. *Journal Of Strain Analysis For Engineering Design*, vol. 18, n° 2, 1983, p. 101-105.
- [SAI 02] SAINSOT P., JACQ C., NELIAS D.
A numerical model for elastoplastic rough contact. *Cmes-Computer Modeling In Engineering & Sciences*, vol. 3, n° 4, 2002, p. 497-506.
- [SIN 69] SINGLETON R. C.
An Algorithm for Computing the Mixed Radix Fast Fourier Transform. *IEEE Transactions on Audio and Electroacoustics*, vol. AU-17, n° 2, 1969, p. 93-103.
- [SNE 51] SNEDDON I.
Fourier transforms. McGraw-Hill, New York, 1951.
- [SPE 75] SPENCE D. A.
The hertz contact problem with finite friction. *Journal of Elasticity*, vol. 5, n° 3, 1975, p. 297-319.
- [VER 85] VERGNE F.
Calcul des déplacements et des contraintes dans un demi-espace élastique chargé en surface par des actions distribuées normales ou tangentielles quelconques. Master's thesis, INSA Lyon, 1985.

- [WAN 10] WANG Z., WANG W., H. WANG, ZHU D., HU Y.
Partial Slip contact analysis on three dimensional elastic layered half space. *Journal of Tribology*, vol. 132, 2010, p. 1-12.
- [WES 39] WESTERGAARD H. M.
Bearing pressures and cracks. *ASME Journal of Applied Mechanics*, vol. 6, 1939, Page 49.
- [ZHA 08] ZHANG J., MICHALENKO M., KUHL E., OVAERT T.
Characterization of Indentation Response and Stiffness Reduction of Bone using a Continuum Damage Model, accepted for publication in the Journal of the Mechanical Behavior of Biomedical Materials. *accepted for publication in the Journal of the Mechanical Behavior of Biomedical Materials*, , 2008.
- [ZHO 06] ZHOU K., CHEN W.
A fast method for solving three-dimensional arbitrarily shaped inclusions in a half space-normal. *Comput. Methods Appl. Mech. Engrg.*, vol. 128, 2006, p. 236-244.